

EFFECTS OF TARGET PROPERTIES ON THE FORMATION OF LUNAR IMPACT
CRATERS IN THE SIMPLE-TO-COMPLEX TRANSITION

By

Mitali Chandnani

A Dissertation Submitted in Partial Fulfillment of the Requirements

For the Degree of

Doctor of Philosophy

in

Geology

University of Alaska Fairbanks

December 2019

APPROVED:

Dr. Robert Herrick, Committee Chair

Dr. Georgiana Kramer, Committee Member

Dr. Jessica Larsen, Committee Member

Dr. Jonathan Dehn, Committee Member

Dr. Paul McCarthy, Chair

Department of Geosciences

Dr. Kinchel Doerner, Dean

College of Natural Science and Mathematics

Dr. Michael Castellini, *Dean of the Graduate School*

ABSTRACT

The transition from simple to complex crater morphology in impact craters with increase in crater size has been modelled and observed in planetary bodies across the Solar System. The transition diameter depends upon the strength and gravity of the planetary body. On the Moon, this transition takes place over a diameter range of several kilometers. This range spans a diversity of crater morphologies including simple, transitional and complex craters. The diameter range of 15-20 km falls within the lunar simple-to-complex transition. All other impactor properties held constant, the 15-20 km range corresponds to a factor of three in the magnitude of impact kinetic energy. I conducted detailed geologic investigation of 244 well-preserved craters in this diameter range to elucidate the root causes of morphological variations. I used panchromatic data for observing crater and surface morphology, Digital Elevation Models (DEMs) for evaluating crater morphometry and topographic variation of pre-impact terrain, near-infrared (NIR) bands for determining the composition of crater cavity and surrounding terrain, thermal infrared bands for examining rock abundance, and Synthetic Aperture Radar (SAR) data for detecting impact melt deposits. The results of my investigation indicate that the morphological differences are primarily governed by target properties. Simple craters are confined to the highlands, and the mare are more abundant in complex craters. The mare are composed of solidified basaltic lava flows interlayered with regolith. The layering creates vertical strength heterogeneities that drive the destabilization of the transient cavity and its collapse, causing the transition to complex craters at smaller diameters in the mare. The non-layered highlands are more vertically homogeneous in strength and therefore favor simple crater formation.

Eight atypically deep simple craters were identified in the highlands near the mare-highlands boundaries, the most porous terrains on the lunar surface. After detailed examination of these craters in comparison to their normal-depth counterparts, I conclude that part of the energy from impact on porous target was spent in target compaction. The higher the porosity of the target, the deeper the crater and greater its volume, due to increased compaction. That only some of the craters in the high porosity terrains are deep suggests that those craters are on locally extreme-high porosity patches. However, an unusual impactor property, such as a high velocity impact, a high-density impactor, or a near-vertical impact may also be a contributor.

The simple craters in the highlands were observed to be located on flat or gradually sloping surfaces or degraded rims and terraces of pre-existing craters. Most craters with localized slumps superpose sharp topographic breaks such as well-developed rims and terraces of pre-existing craters. However, the topographic settings of 35% of the craters with localized slumps appeared to be similar to that of the simple craters. More detailed topographic study of the pre-impact terrains of these two morphologies revealed that the pre-impact terrains of 35% of the craters with localized slumps are gradually sloping or have subtle topographic breaks. Both sharp and subtle breaks are characterized with similar sloping directions as the adjacent craters' walls, which led to over steepening of the transient cavity walls around this part of the rim and their collapse, thereby causing the accumulation of localized slumped material. Several simple craters were also identified to have formed on pre-impact topographic breaks. However, the simple craters' walls that superpose these breaks were observed to be sloping in directions opposite to that of the breaks. So the ejecta around these walls was deposited along the break slopes, and thus syn-impact mass wasting occurred external (and not internal) to the crater cavity.

TABLE OF CONTENTS

	Page
ABSTRACT	iii
LIST OF FIGURES	xi
LIST OF TABLES	xv
LIST OF APPENDICES	xvii
ACKNOWLEDGEMENTS	xix
CHAPTER 1 INTRODUCTION	1
1.1 Chapter 2: Geologic Analyses of the Causes of Morphological Variations in Lunar Craters Within the Simple-to-Complex Transition.....	2
1.2 Chapter 3: Geologic Investigation of Deep Simple Craters in the Lunar Simple-to-Complex Transition.....	3
1.3 Chapter 4: Influence of Target Properties on Wall Slumping in Lunar Craters within the Simple-to-Complex Transition	
1.4 References.....	3
CHAPTER 2 GEOLOGIC ANALYSES OF THE CAUSES OF MORPHOLOGICAL VARIATIONS IN LUNAR CRATERS WITHIN THE SIMPLE-TO-COMPLEX TRANSITION	7
Abstract.....	7
2.1 Introduction.....	8
2.1.1 Lunar Simple-to-Complex Impact Crater Transition.....	8
2.1.2 Objectives	13
2.2 Methods and Data	14
2.2.1 Morphological Characterization	14
2.2.2 Close-Proximity Analyses	17
2.2.3 Data Sets Used.....	18

2.3 Results.....	18
2.3.1 Morphological Characterization	18
2.3.1.1 Simple Crater	19
2.3.1.2 Crater with Localized Slumps.....	20
2.3.1.3 Crater with Localized Slumps and Terraces	24
2.3.1.4 Crater with Localized Slumps and Central Uplift.....	26
2.3.1.5 Crater with Localized Slumps, Terraces, and Central Uplift.....	27
2.3.1.6 Floor-Fractured Crater	28
2.3.1.7 Concentric Crater	28
2.3.2 Highlands Versus Mare Craters	29
2.3.3 Close-Proximity Craters.....	34
2.4 Discussion.....	40
2.4.1 Mare-Highlands Differences.....	40
2.4.2 Unusually Deep Craters	45
2.4.2.1 Impact into a high-porosity target.....	45
2.4.2.2 The highlands are more coherent in these locations and less susceptible to minor slumping of the transient cavity	46
2.4.3 Potential Impactor-Caused Variations	47
2.4.4 Comparison with Other Planets	49
2.5 Conclusions.....	50
2.6 Acknowledgments.....	52
2.7 References.....	52
APPENDIX A.....	68

CHAPTER 3 GEOLOGIC INVESTIGATION OF DEEP SIMPLE CRATERS IN THE LUNAR SIMPLE-TO-COMPLEX TRANSITION	91
Abstract	91
3.1 Introduction	92
3.1.1 Deep Simple Craters	92
3.1.2 Objectives	97
3.1.2.1 Greater compaction of target with increase in porosity results in larger crater depths	97
3.1.2.2 The highlands are more coherent in these locations and more resistant to minor slumping of the transient cavity	98
3.2 Methods and Data Sets.....	99
3.2.1 Crater Depths from SLDEM and LOLA tracks.....	99
3.2.2 Depths of Proximity Craters	100
3.2.3 Trends in Crater Morphometry	101
3.2.4 Impact Melt Deposits.....	105
3.2.5 Visual Examinations of Crater Cavities.....	107
3.3 Results.....	107
3.3.1 Crater Depths from SLDEM and LOLA Tracks.....	107
3.3.2 Depths of Proximity Craters	109
3.3.3 Trends in Crater Morphometry	111
3.3.3.1 Association of Crater Depth with Porosity	111
3.3.3.2 Rim Height.....	113
3.3.3.3 Wall Slope.....	113
3.3.3.4 Floor Size	115
3.3.3.5 Cavity Profiles	117

3.3.3.6 Ejecta-Cavity Volume Ratio	118
3.3.4 Impact Melt Deposits	119
3.3.5 Visual Examinations of Crater Cavities	119
3.4 Discussion	123
3.4.1 Greater compaction of target with increase in porosity results in larger crater depths	126
3.4.2 The highlands are more coherent in these locations and more resistant to minor slumping of the transient cavity	130
3.5 Conclusions	131
3.6 Acknowledgements	132
3.7 References	133
APPENDIX B	148
CHAPTER 4 INFLUENCE OF TARGET PROPERTIES ON WALL SLUMPING IN LUNAR CRATERS WITHIN THE SIMPLE-TO-COMPLEX TRANSITION	157
Abstract	157
4.1 Introduction	158
4.1.1 Wall Slumping	158
4.1.2 Objectives	162
4.1.2.1 Localized slumping occurred post-crater formation	162
4.1.2.2 Localized slumping occurred on weaker target	163
4.1.2.3 Impact cratering on a slope causes the localized slumping	163
4.2 Methods and Data Sets	164
4.2.1 Testing hypothesis 1: Comparison of crater densities on slumps and ejecta units of craters with localized slumps	164

4.2.2 Testing hypothesis 2: Frequencies of proximal simple craters and craters with localized slumps.....	166
4.2.3 Testing hypothesis 3: Topographic variation in pre-impact terrains of the simple craters and craters with localized slumps along with rim circularity.....	168
4.3 Results.....	170
4.3.1 Comparison of crater densities on slumps and ejecta units of craters with localized slumps.....	170
4.3.2 Frequencies of proximal simple craters and craters with localized slumps.....	173
4.3.3 Topographic variation in pre-impact terrains of the simple craters and craters with localized slumps along with rim circularity.....	175
4.4 Discussion.....	180
4.5 Conclusions.....	184
4.6 Acknowledgements.....	185
4.7 References.....	185
APPENDIX C.....	194
CHAPTER 5 CONCLUSION.....	211
5.1 Target Properties.....	211
5.2 Impactor Properties.....	213

LIST OF FIGURES

	Page
Figure 2.1. Illustration of two similar-sized lunar craters with differing morphologies.....	11
Figure 2.2. List of the adopted morphological classification criteria within the 15–20-km size range.....	16
Figure 2.3. Examples of topographic measurements from LOLA tracks and LOLA gridded data superposed on LROC WAC images	17
Figure 2.4. Global lunar WAC mosaic showing the locations of simple craters (purple circles) and craters with localized slumps (dark blue circles).....	19
Figure 2.5. Examples of well-preserved simple lunar craters in the simple-to-complex transition zone and their topographic profiles along specific transects	21
Figure 2.6. WAC illustrations of unusually deep lunar craters in the simple-to-complex transition, with their cross-sectional profiles along orthogonal azimuths	22
Figure 2.7. WAC images and LOLA DEM topographic profiles of four lunar craters that bear localized slumped material	24
Figure 2.8. Mapped distributions of crater morphologies other than simple craters and craters with localized slumps.....	26
Figure 2.9. WAC illustrations and LOLA profiles of crater morphologies other than simple craters and craters with localized slumps.....	27
Figure 2.10. WAC images and LOLA profiles of (a) floor-fractured crater and (b) concentric crater	29
Figure 2.11. Crater depth versus diameter plots for the five major crater morphologies.....	30
Figure 2.12. LOLA DEM superposed on WAC images of simple craters and overlain by prominent elevation contours.....	32
Figure 2.13. Illustrations of pre-impact topography and cavity features of highland crater morphologies other than simple craters	33
Figure 2.14. Wide Angle Camera images of craters in mare. All craters are characterized by layering on walls.....	35
Figure 2.15. Mapped coordinates of craters that were eliminated from close-proximity analyses (red circles) and the craters that qualify for the analyses (green circles).....	37

Figure 2.16. Wide Angle Camera images of craters that are alike in morphology and occur on uniformly sloping highland terrain devoid of any distinguishable topographic or other geologic differences.....	37
Figure 2.17. WAC images of close-proximity Group E: Simple crater and crater with localized slumped material.....	39
Figure 2.18. WAC images of groups of close-proximity craters that differ in morphology but whose geologic settings appear to be similar.....	40
Figure 2.19. WAC image of a pair of close-proximity craters, which comprises a crater bearing localized slumped material and a floor-fractured crater.....	41
Figure 2.20. Mapped locations of simple craters with impact melt deposits and unusually deep craters on the lunar surface porosity distribution map.....	47
Figure A-1. WAC and NAC illustrations of floor melts and melt features in two simple craters.....	68
Figure A-2. Investigation of the timing of deposition of localized slumped material relative to deposition of ejecta for craters Coriolis S and Bode.....	69
Figure A-3. WAC image illustrations of craters that were discarded from the close-proximity analysis.....	71
Figure A-4. WAC images of close proximity groups that were not shown in the article.....	72
Figure A-5. WAC images of more close proximity groups that were not shown in the article.....	73
Figure 3.1. WAC images and orthogonal cross-sectional profiles of deep simple craters that were identified using LOLA gridded topography data.....	97
Figure 3.2. WAC images of simple craters surrounding the 15-20 km-sized deep simple craters, in order of increasing diameter.....	102
Figure 3.3. Illustration of rim height, slope measurement and volume calculation methods for a simple crater.....	106
Figure 3.4. Mapped distribution of well-preserved 15-20 km-sized simple craters that are superposed on the lunar highlands porosity map.....	108
Figure 3.5. Stacked bar chart that depicts the % distribution of crater d/D ranges corresponding to each porosity range (or each bar).....	112
Figure 3.6. Scatter plot of rim height scaled to crater diameter (h/D) against depth/diameter (d/D) ratio for 117 well-preserved 15-20 km-sized simple craters.....	114

Figure 3.7. Scatter plot of wall slopes (θ) against depth/diameter (d/D) ratio for 117 well-preserved 15-20 km-sized simple craters.....	115
Figure 3.8. Scatter plot of crater d/D against floor diameter scaled to crater diameter (f/D) for 117 well-preserved 15-20 km-sized simple craters	116
Figure 3.9. Scatter plot of crater wall slope (θ) against floor diameter scaled to crater diameter (f/D) for 117 well-preserved 15-20 km-sized simple craters	117
Figure 3.10. Cavity profiles of two normal-depth craters and two deep craters.....	118
Figure 3.11. Scatter plot of crater ejecta-cavity volume ratio (E/C) against d/D for 53 well-preserved 15-20 km-sized simple craters.....	119
Figure 3.12. Impact melt flows outlined in red surrounding deep crater Polybius A and normal-depth crater Planck W	120
Figure 3.13. Illustration of cavity morphologies of the craters whose profiles have been displayed in Figure 3.10	125
Figure B-1. Mapped distribution of impact melt flows around the rims of deep crater Hill and normal-depth crater Unnamed27	148
Figure 4.1. LOLA elevation contours superposed on WAC images of 15-20 km-sized simple craters and craters with localized slumps on highlands terrains	162
Figure 4.2. Slump and ejecta units mapped on the Kaguya TC image of crater Swann C that has localized slumped material	167
Figure 4.3. Log-log CSFD plots corresponding to ejecta and slump units of four craters with localized slumps.....	171
Figure 4.4. LOLA topographic profiles (center) of craters whose CSFD plots are shown in Figure 4.3.....	173
Figure 4.5. Mapped distribution of percentages of transitional craters relative to simple craters in the proximity of 83 15-20 km diameter simple craters.....	174
Figure 4.6. Mapped distribution of percentages of transitional craters relative to simple craters in the proximity of 24 15-20 km diameter craters with localized slumps.....	176
Figure 4.7. LOLA elevation contours superposed over WAC images of simple craters and aspect-slope maps of their pre-impact terrains and crater cavities	177

Figure 4.8. LOLA elevation contours superposed over WAC images of craters with localized slumps and aspect-slope maps of their pre-impact terrains and crater cavities	178
Figure 4.9. Box plots of PP scores of simple craters and craters with localized slumps	179
Figure 4.10. Scatter plots of PP score vs simple crater floor diameter scaled to crater diameter for various topographic heterogeneities and presence/absence of layering in the pre-impact terrains	179
Figure 4.11. Demonstration of transient cavity formation on a slope	182
Figure 4.12. 3D illustrations of crater morphologies on pre-existing slopes	183
Figure C-1. Log-log CSFD plots corresponding to ejecta and slump units of remaining 16 craters with localized slumps	194

LIST OF TABLES

	Page
Table 2.1. Relative abundance of crater morphological classes in mare and highlands.....	25
Table 2.2. Summarized details of close-proximity crater groups shown in Figures 2.16 through 2.19.....	42
Table A-1. List of the 244 well-preserved lunar impact craters in the 15-20 km diameter range, their geographic locations, morphologies and evaluated morphometric parameters.....	74
Table A-2. Data on layering, floor melt, elevation variation of pre-impact terrains of highlands craters, and crater selection for close-proximity analyses for the 244 well-preserved lunar craters within the simple-to-complex transition	80
Table A-3. List of the groups of close proximity craters. This table also includes the locations, diameters, d/D s of the craters and discussion of observed similarities or differences in the morphologies and geologic settings of the craters in each group	88
Table 3.1. List of 15-20 km-sized simple craters, whose d/D s were re-evaluated using SLDEM (and LOLA RDRs in case of craters located beyond 60° latitudes)	109
Table 3.2. The list of percentages of smaller deep simple craters surrounding (within 100 km from crater center) each of the selected 28 simple craters in the 15-20 km size range	110
Table B-1. Data on the morphometric parameters of 15-20 km-sized 117 simple impact craters	149
Table B-2. Results from one-way ANOVA of the three d/D groups classified by porosity ranges	155
Table B-3. Results from Tukey Kramer HSD test that are indicative of the pairs among the d/D groups (classified by porosity) that are significantly different from each other.....	155
Table B-4. Results from one-way ANOVA of the three crater wall slope groups classified by porosity ranges	155
Table B-5. Results from Tukey Kramer HSD test that are indicative of the pairs among the crater wall slope groups (classified by porosity) that are significantly different from each other	155
Table 4.1. List of cumulative crater densities at D of 1 km (N(1)) along with error bar values for the slump and ejecta units of the selected 20 craters with localized slumps in the 15-20 km diameter range.....	172

Table C-1. Tabulated statistics of proximal well-preserved transitional craters relative to well-preserved simple craters for each of the 15-20 km-sized simple craters and craters with localized slumps197

Table C-2. List of slopes and respective sloping directions (relative to sloping directions of adjacent craters' walls) of topographic breaks adjoining the walls of the 15-20 km diameter simple craters and craters with localized slumps202

LIST OF APPENDICES

	Page
APPENDIX A.....	68
APPENDIX B.....	148
APPENDIX C.....	194

ACKNOWLEDGEMENTS

I wish to express a heartfelt thanks to my advisor, Professor Robert Herrick, without whom this dissertation would not have been possible. Professor Herrick presented his idea of the first chapter to me and then let me structure my dissertation. He offered to help me only when I had consistently tried to solve a problem, which ensured that by the end of my PhD I graduated as an independent and creative researcher. The financial assistance provided by him throughout most of my semesters helped me focus completely on my own research. Because of his polite and affable nature, I was able to discuss my ideas and concerns with him in a comfortable manner. I am immensely thankful to my family in India for their immense courage in sending me so far away, and their consistent support in favor of my career choices. My committee member, friend and co-author, Dr. Georgiana Kramer, was instrumental in educating me about the geology of the Moon and providing valuable feedback on my manuscripts. Professor Jonathan Dehn and Professor Jessica Larsen who are renowned volcanologists and my committee members ensured the compliance of rules pertaining to my program and guided me with constructing my thesis for readers with expertise outside planetary science. My colleagues from the remote sensing suite, specifically Professor Franz Meyer and Dr. David McAlpin guided me with remote sensing concepts and statistical tests that contributed significantly to my research. I am grateful to Professor Catherine Hanks who gave me an opportunity to explore my leadership skills through the Imperial Barrel Award Competition. The UAF International Program Officers and Graduate School staff were instrumental in helping me smoothly maintain my standing as an international graduate student. Lastly, wish to thank my friends from India and Fairbanks for boosting my confidence and keeping me stress-free through the PhD program.

CHAPTER 1 INTRODUCTION

The study of impact craters is critical for obtaining insights into the surface and near-surface attributes of a planetary body and the characteristics of the projectiles that impact the body. An impact crater is formed by a hypervelocity impact of a projectile on a surface followed by three stages (Melosh, 1989b; Melosh & Ivanov, 1999). In the first stage, the contact and compression stage, the projectile transfers a large portion of its kinetic energy into the target in the form of shock waves that travel radially outward from the target-projectile interface, fracturing and compressing the target. This stage leads to the excavation stage in which the pressure release from the passage of shock waves induces outward and upward movement in the target material thereby creating a hollow parabolic transient cavity from the ejection of the material. The third stage, the modification stage, involves cavity collapse under the action of gravity (Melosh, 1989a). For smaller craters (or impacts with lower energy), minor wall slumping causes the formation of simple craters whose cavities have a roughly parabolic shape (Melosh, 1989a). In larger craters (or higher energy impacts), the rim and wall collapse causes slumping and deposition of unconsolidated material and discrete blocks (in the form of terraces), and is accompanied by the uplift of the floor in the form of central peaks which results in a complex crater morphology (Hargitai & Öhman, 2014; Kenkmann et al., 2012; Melosh, 1989a; Pike, 1980a, 1980b; Quaide et al., 1965). The size-dependent morphologic progression from small simple craters to larger increasingly complex craters has been hypothesized to result from transient strength degradation of impacted target rocks (Melosh, 1977, 1989a; Quaide et al., 1965). As impactor kinetic energy increases, the volume of the excavated “transient cavity” increases until the hydrostatic pressure at its base exceeds the transient strength, precipitating cavity collapse.

The Moon was the first well-imaged planetary body with an abundance of uneroded impact craters. The latest high-resolution lunar image and topography data is aiding in the exploration of lunar surface properties through studies of lunar impact crater morphologies. The simple-to-complex transition diameters are governed by the gravity and strength of a planetary body (Herrick & Lyons, 1998; Pike, 1988). On the Moon, the simple-to-complex transition takes place over a 15—20 km diameter range (Croft, 1985; Pike, 1977, 1980a, 1980b, 1988). For fixed impactor composition and impact angle, impact energy triples if diameter is increased from 15 km to 20 km. (Holsapple & Schmidt, 1982; Holsapple, 1993; Melosh, 1989c; Schmidt & Housen, 1987) and spans simple, transitional and complex crater morphologies. Transitional craters have the wall collapse features of complex craters while lacking a well-defined central peak (Cintala et al., 1977; Cintala & Grieve, 1998; Howard, 1974; Kalynn et al., 2013; Pike, 1974, 1977, 1988; Plescia, 2015; Robbins & Hynes, 2012; Smith & Sanchez, 1973). This dissertation focuses on the determination of the factors responsible for the morphological variations in lunar craters occurring in the 15-20 km diameter range.

1.1 Chapter 2: Geologic Analyses of the Causes of Morphological Variations in Lunar Craters Within the Simple-to-Complex Transition

A multitude of target properties (lithology, porosity, topography, layering) and/or impactor properties (impact velocity, impact angle, impactor density, impactor size) could influence the cratering process in creating the morphological difference between the 15-20 km diameter craters. In Chapter 2, a survey of the craters and their terrains was conducted to understand the influence of highlands and mare terrains on the crater morphologies, and variations of crustal structure within highlands that could further contribute to the diversity of intra-highland crater morphologies.

1.2 Chapter 3: Geologic Investigation of Deep Simple Craters in the Lunar Simple-to-Complex Transition

In Chapter 2, a handful of simple craters were found to be deeper than most simple craters that have been modelled and observed in planetary bodies across the Solar System. They occur around the mare-highlands contacts. I conducted detailed geologic studies of these craters in comparison to the normally deep craters to determine the target and/or impactor properties that could produce the stable larger-than-normal depths.

1.3 Chapter 4: Influence of Target Properties on Wall Slumping in Lunar Craters within the Simple-to-Complex Transition

In Chapter 2, it was observed that 35 transitional craters in the highlands were formed on terrains with similar topographic variation as the terrains of simple craters. This chapter unravels the subtle differences in the properties of the pre-impact terrains of the transitional and simple craters that were not noticeable in the preliminary examination of the terrains in Chapter 2.

1.4 References

- Cintala, M., Wood, C., and Head, J. (1977). *The effects of target characteristics on fresh crater morphology-Preliminary results for the moon and Mercury*. Paper presented at 8th Lunar and Planetary Science Conference Proceedings, Houston, TX.
- Cintala, M. J., and Grieve, R. A. (1998). Scaling impact melting and crater dimensions: Implications for the lunar cratering record. *Meteoritics & Planetary Science*, 33(4), 889-912. doi:<https://doi.org/10.1111/j.1945-5100.1998.tb01695.x>.
- Croft, S. K. (1985). The scaling of complex craters. *Journal of Geophysical Research: Solid Earth*, 90(S02). doi:<https://doi.org/10.1029/JB090iS02p0C828>.

- Hargitai, H., and Öhman, T. (2014), Complex Crater, In *Encyclopedia of Planetary Landforms*, pp. 1-17, Springer, New York, NY, doi:https://doi.org/10.1007/978-1-4614-9213-9_429-2.
- Herrick, R. R., and Lyons, S. N. (1998). Inversion of crater morphometric data to gain insight on the cratering process. *Meteoritics & Planetary Science*, 33(1), 131-143. doi:<https://doi.org/10.1111/j.1945-5100.1998.tb01615.x>
- Holsapple, K. A. (1993). The scaling of impact processes in planetary sciences. *Annual review of earth and planetary sciences*, 21(1), 333-373. doi:<https://doi.org/10.1146/annurev.ea.21.050193.002001>.
- Holsapple, K. A., and Schmidt, R. M. (1982). On the scaling of crater dimensions: 2. Impact processes. *Journal of Geophysical Research: Solid Earth*, 87(B3), 1849-1870. doi:<https://doi.org/10.1029/JB087iB03p01849>
- Howard, K. A. (1974). *Fresh lunar impact craters-Review of variations with size*. Paper presented at 2nd Lunar and Planetary Science Conference Proceedings, Houston, TX.
- Kalynn, J., Johnson, C. L., Osinski, G. R., and Barnouin, O. (2013). Topographic characterization of lunar complex craters. *Geophysical Research Letters*, 40(1), 38-42. doi:<https://doi.org/10.1029/2012GL053608>
- Kenkmann, T., Collins, G. S., and Wünnemann, K. (2012), The modification stage of crater formation, In Gordon R Osinski et al. (Eds.), *Impact cratering: Processes and products*, pp. 60-75, John Wiley & Sons, Oxford, U.K.
- Melosh, H. J. (1977). *Crater modification by gravity-A mechanical analysis of slumping*. Paper presented at Impact and Explosion Cratering: Planetary and Terrestrial Implications, Flagstaff, AZ.

- Melosh, H. J. (1989a), Cratering Mechanics: Modification Stage, In *Impact cratering: A geologic process*, pp. 126-161, Oxford University Press, New York.
- Melosh, H. J. (Eds.) (1989b). *Impact cratering: A geologic process*, New York: Oxford University Press.
- Melosh, H. J. (1989c), Scaling of Crater Dimensions, In *Impact cratering: A geologic process*, Oxford University Press, New York.
- Melosh, H. J., and Ivanov, B. (1999). Impact crater collapse. *Annual Review of Earth and Planetary Sciences*, 27(1), 385-415. doi:<https://doi.org/10.1146/annurev.earth.27.1.385>.
- Pike, R. J. (1974). Depth/diameter relations of fresh lunar craters: Revision from spacecraft data. *Geophysical Research Letters*, 1(7), 291-294. doi:<https://doi.org/10.1029/GL001i007p00291>.
- Pike, R. J. (1977), Size-dependence in the shape of fresh impact craters on the Moon, In D.J. Roddy et al. (Eds.), *Impact and Explosion Cratering: Planetary and Terrestrial Implications*, pp. 489-509, Pergamon Press, New York.
- Pike, R. J. (1980a). *Control of crater morphology by gravity and target type-Mars, Earth, Moon*. Paper presented at 11th Lunar and Planetary Science Conference Proceedings, Houston, TX.
- Pike, R. J. (1980b), Geometric interpretation of lunar craters. *USGS Professional Paper*, Rep. 1046-C, C1-C77, Washington: US Govt. Print. Off.
- Pike, R. J. (1988), Geomorphology of impact craters on Mercury, In F Vilas et al. (Eds.), *Mercury*, pp. 165-273, University of Arizona Press, Tucson, AZ.

- Plescia, J. B. (2015), Transitional Crater (Simple/Complex), in *Encyclopedia of Planetary Landforms*, edited, pp. 1-5, Springer, New York, NY, doi:https://doi.org/10.1007/978-1-4614-9213-9_407-2.
- Quaide, W. L., Gault, D. E., and Schmidt, R. A. (1965). Gravitative effects on lunar impact structures. *Annals of the New York Academy of Sciences*, 123(1), 563-572. doi:<https://doi.org/10.1111/j.1749-6632.1965.tb20388.x>.
- Robbins, S. J., and Hynek, B. M. (2012). A new global database of Mars impact craters ≥ 1 km: 2. Global crater properties and regional variations of the simple-to-complex transition diameter. *Journal of Geophysical Research: Planets*, 117(E6). doi:<https://doi.org/10.1029/2011JE003967>.
- Schmidt, R. M., and Housen, K. R. (1987). Some recent advances in the scaling of impact and explosion cratering. *International Journal of Impact Engineering*, 5(1-4), 543-560. doi:[https://doi.org/10.1016/0734-743X\(87\)90069-8](https://doi.org/10.1016/0734-743X(87)90069-8).
- Smith, E. I., and Sanchez, A. G. (1973). Fresh lunar craters: Morphology as a function of diameter, a possible criterion for crater origin. *Modern Geology*, 4, 51-59.

CHAPTER 2 GEOLOGIC ANALYSES OF THE CAUSES OF MORPHOLOGICAL VARIATIONS IN LUNAR CRATERS WITHIN THE SIMPLE-TO-COMPLEX TRANSITION¹

Abstract

The diameter range of 15 to 20 km is within the transition from simple to complex impact craters located on the Moon. This range spans roughly a factor of three in impact energy for the same impactor speed, composition, and trajectory angle. We analyzed the global population of well-preserved craters in this size range in order to assess the effects of target and impactor properties on crater shapes and morphologies. We observed that within this narrow diameter range, simple craters are confined to the highlands, and complex craters are more abundant in the mare. We found unusually deep craters around the highlands-mare boundaries and favor the hypothesis that they form by impact cratering on high-porosity terrain. We infer that target properties primarily contribute to the observed morphological variations in the craters. Simple crater formation is favored by a terrain that is more homogeneous in strength and topography, while transitional and complex crater formation is aided by heterogeneity in lithology, topography, or strength, or a combination of these parameters. Clearly visible impact melt deposits in a small percentage of simple craters, and two cases of craters differing in morphologies from their nearest neighbors in similar geologic settings, suggest that variation in impactor properties such as impact velocity and impactor size may have some role in causing morphological differences between similar-sized craters.

¹Chandnani, M., Herrick, R. R., and Kramer, G. Y. (2019), Geologic Analyses of Causes for Morphological Variations in Lunar Craters within the Simple-to-Complex Transition, *Journal of Geophysical Research: Planets*, 1238-1265, doi:<https://doi.org/10.1029/2018JE005729>.

2.1 Introduction

Understanding impact cratering mechanics is critical for using craters to study the history of a planetary body. The Moon was the first well-imaged planetary body to possess an abundance of impact craters, and a variety of new high-resolution satellite data are reinvigorating lunar crater studies. With the increase in crater size, simple, bowl-shaped craters are unable to sustain their shape; the walls collapse and the crater center rebounds upward, forming a central peak and resulting in a complex crater (Hargitai & Öhman, 2014; Kenkmann et al., 2012; Melosh, 1989a; Melosh & Ivanov, 1999; Pike, 1980a, 1980b; Quaide et al., 1965). For larger craters, the crater center transitions to more complex structures, such as a peak ring (peak-ring basins) or multiple rings (multi-ring basins) (Melosh, 1989a, 1989b; Melosh & Ivanov, 1999; Pike, 1980a, 1980b).

2.1.1 Lunar Simple-to-Complex Impact Crater Transition

The progression from simple to complex crater morphology on the Moon takes place gradually over a diameter range. In this range are simple, complex and transitional craters. Transitional craters have morphologies that are intermediate between simple crater and complex crater morphologies. They are characterized by slumped material at the base of the crater walls in the form of unconsolidated debris and/or terraces that may either be localized or extended across the floor, while lacking a well-defined central peak (Cintala et al., 1977; Cintala & Grieve, 1998; Howard, 1974; Kalynn et al., 2013; Pike, 1974, 1977b, 1988; Plescia, 2015b; Robbins & Hynek, 2012; Smith & Sanchez, 1973). The diameters for the simple-to-complex crater transition are primarily governed by the surface gravity and strength of the target material (Herrick & Lyons, 1998; Pike, 1988). For the Moon, depending upon the resolution of the data and the methodology, several transition diameters have been estimated: 17.5 km based on appearances of central peaks, flat floors, terraces and swirl texture, and ratio-level variations of rim-crest diameter with crater depth, rim height, flank width, wall slope,

floor diameter, circularity, and rim-crest evenness in craters that appeared fresh in the Apollo data (Pike, 1977b); 16 km for the mare (Pike, 1980a) and 21 km for the highlands from revised morphological observations and re-evaluated d/D ratios of well-preserved craters (Pike, 1980b); 19 km as recalculated from the intersection of d/D and rim height/ D regression lines of simple and complex craters (Pike, 1988); 15 km based on the transient crater diameter/final crater diameter ratio measuring unity at the transition diameter (Croft, 1985; Melosh & Ivanov, 1999); and 20.1 km for the highlands as well as 17.7 km for the mare as determined from the intersection of regression lines corresponding to the empirical relation between d and D of simple and complex craters, separately for the highlands and mare, with the help of the Lunar Reconnaissance Orbiter Camera Wide Angle Camera (LROC WAC) and Kaguya Terrain Camera (TC) Digital Terrain Model (DTM) data (Krüger et al., 2018). Differences in the simple-to-complex transition diameters for the highlands and mare have been hypothesized to be due to differences in crustal strength between the regolith-dominated highlands (Soderblom et al., 2015) and the more coherent mare (Cintala et al., 1977; Pike, 1980b; Smith & Hartnell, 1978). The coherent but layered nature of mare (Pike, 1980a; Quaide & Oberbeck, 1968) and their relatively younger ages (Hiesinger et al., 2000; Shoemaker & Hackman, 1962) may aid in uniform cavity collapse in the form of terraces, hence a smaller transition size, as opposed to non-pervasive slumping of material in craters formed on the older, more fragmented, and weaker highlands. Based on the above values, the transition size range varies with the morphometric criteria used to define it. However, a range of 15–20 km overlaps with most of the published values. In an ideal situation, we could learn about the complexities of planetary-scale crater formation by observing kilometer-scale impacts of a variety of projectiles over a span of velocities into multiple geologic targets. In reality, multi-kilometer craters form rarely on the planets relative to the timescale of human recorded history, and we are limited to comparing existing craters where our selection criteria are designed to minimize the number of

free parameters. Choosing a relatively narrow range of crater diameters that is still large enough to provide a reasonably good sample size of well-preserved craters is the best empirical approach to control for total impactor energy. Choosing to study craters in a diameter range associated with a major morphological transition, in our case the simple-to-complex transition, maximizes the sensitivity of crater morphology to target conditions.

For a fixed impact speed, impact angle, and impactor composition, the volume of the transient crater cavity scales with impact energy to the power 0.78 (Holsapple, 1993; Holsapple & Schmidt, 1982; Melosh, 1989c; Schmidt & Housen, 1987). Consequently, a diameter range of 15–20 km corresponds to a factor of three in the magnitude of impact kinetic energy for impacts that occur at a similar velocity and impact angle. Variations in impactor velocity, angle, and composition could potentially raise the differences in kinetic energy between crater-forming events in this diameter range to over an order of magnitude (Silber et al., 2017). Within this 5-km-diameter range, lunar craters can have significantly different appearances. For example, Figure 2.1 shows that a simple crater was formed in the highlands with nearly the same size as a crater with localized slumps and terraces at the base of the walls at another location in the lunar mare. In this paper we assess craters in this diameter range and attempt to evaluate whether the morphological differences observed are due to impactor properties (e.g., density and velocity) or target differences (e.g., cohesion, layering, and porosity).

Remote sensing studies, field analyses, numerical modeling, and experimental impacts have furthered our understanding that target properties (lithology, porosity, layering, and topography) and impactor properties (impact velocity, impact angle, impactor density, and impactor size) have a significant influence on the final morphology of a crater. It is well established that the formation of complex craters from transient cavity collapse is a result of weakening of target rocks fractured and displaced by impact (Kenkmann et al., 2012; Melosh, 1977; Melosh & Ivanov, 1999). An observational and numerical modeling study of central peak

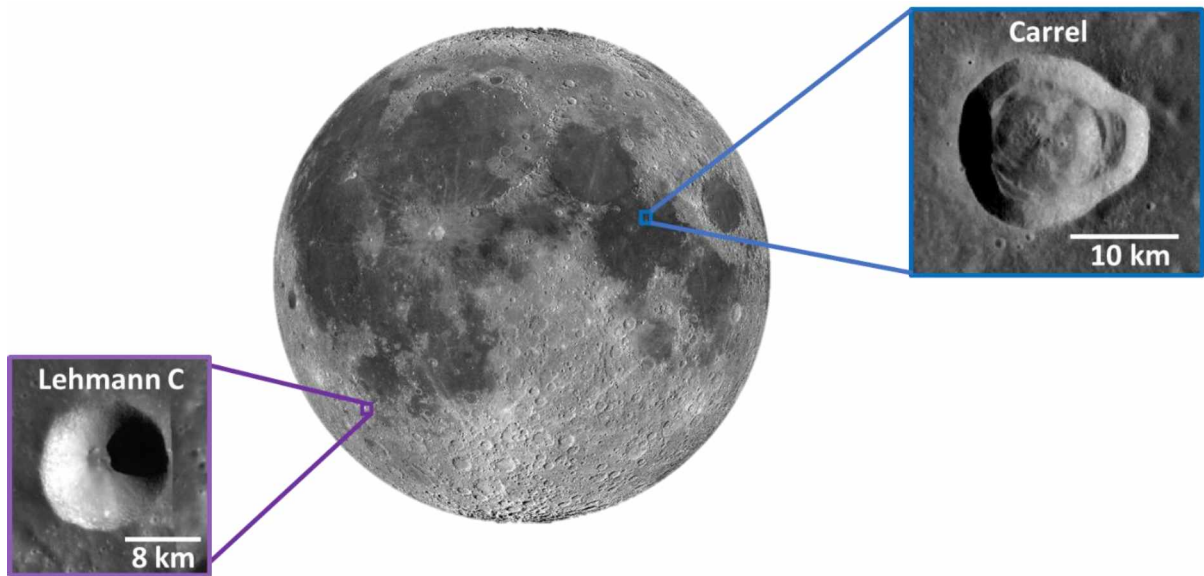


Figure 2.1. Illustration of two similar-sized lunar craters with differing morphologies. Lehmann C (-35.57°N , 309.83°E), a simple crater, is nearly the same size (15.1 km) as Carol (10.66°N , 26.68°E), a crater with localized slumps and terraces, both occurring within the simple-to-complex transition diameter range. Lehmann C occurs on highland terrain and shows a breccia lens/melt deposit. Carrel occurs in the mare and shows a large flat floor with slumped material and a single terrace.

craters on the Moon and Ganymede (Bray et al., 2008) inferred similar weakening mechanisms and hence similar strength model parameters during impact in both icy and rocky targets. Boyce et al. (2006) discovered unusually deep simple impact craters in restricted units of the northern lowlands of Mars and suggested that the unusually high material strength of the geological units inhibited the collapse of the transient cavities, thereby causing these cavities to retain their large depths and simple crater morphologies. From the examination of lunar craters with sharp rims and negligible degradation (class 1 craters as per the definition by Arthur et al., 1964) on terrains differing in lithology and strength, more coherent but layered substrates were found to be more abundant in complex craters (Cintala et al., 1977).

Numerical simulations (Housen & Holsapple, 2000; Milbury et al., 2015; Wünnemann et al., 2006; Wünnemann et al., 2008) and hypervelocity impact experiments (Housen et al., 1999; Housen & Holsapple, 2003; Housen & Voss, 2001) have revealed that impacts into high-porosity targets result in anomalously deep craters because a large fraction of the impact energy is spent in crushing of pore spaces, thus leading to the compaction of target material. Housen

and Holsapple (2012), Housen et al. (1999), and Prieur et al. (2017) reported that for targets with porosity up to ~35% (or possibly larger values), whose grains are densely packed, the creation of crater volume by ejection of material and displacement of material toward the cavity walls dominates volume creation by compaction. From numerical modeling and observation, it is well known that impacts into layered targets can produce shallower craters and earlier onset of complex craters (Collins et al., 2008; Dence, 1972; Pike, 1980a; Quaide & Oberbeck, 1968; Senft & Stewart, 2008; Stewart & Valiant, 2006). Craters formed from experimental impacts on slopes were observed to contain higher amounts of slumped material than the craters formed on flat surfaces (Aschauer & Kenkmann, 2017).

Crater-scaling laws state that crater size depends upon a combination of impactor and target properties (Holsapple, 1993; Holsapple & Schmidt, 1982; Melosh, 1989c; Schmidt & Housen, 1987). Thus, similar-sized craters on targets with similar properties can be formed from a similar combination of impactor properties. However, impactor density, size, velocity, impact angle, and other potentially relevant parameters can vary significantly within that combination (see Table 2 in Silber et al., 2017) and possibly influence the shape and morphology of the craters. It is known from impact simulations and experimental studies that highly oblique impacts (12° or less; Bottke et al., 2000) create elliptical craters (Elbeshausen et al., 2013; Gault & Wedekind, 1978; Herrick, 2014) with asymmetric ejecta patterns and downrange offset of the central peak (Elbeshausen et al., 2009; Shuvalov & Dypvik, 2004). A numerical modeling study suggested that the transition from simple to complex crater morphologies occurs at smaller diameters with an increase in impactor size or decrease in impactor velocity for acoustically fluidized targets (Silber et al., 2017). While a general idea has been established about the attributes controlling the various crater morphologies, little attention has been given to the factors responsible for the diverse morphologies of similar-sized lunar craters within the simple-to-complex transition. A similar investigation was performed

recently on craters spanning the simple-to-complex transition on Mars (Herrick & Hynek, 2017). Clayton et al. (2013) noted an earlier onset of terraces in mare craters as compared to the highlands from their observational study of fresh transitional lunar impact craters. Silber et al. (2017) and Wünnemann and Ivanov (2003) focused on determining impactor and target properties, respectively, that are responsible for threshold diameter of transition from simple to complex morphology.

2.1.2 Objectives

We seek to determine the causes of the morphological diversity of lunar craters measuring 15–20 km in diameter. Inferred target and/or impactor properties will advance our understanding of simple and complex cratering mechanics along with providing additional information on the regional crustal variations beyond the well-established mare-highlands dichotomy on the Moon (Kalynn et al., 2013; Osinski et al., 2018; Pike, 1980a, 1980b; Smith & Hartnell, 1978). In general terms, a strong correlation of crater morphology with geologic settings, based on target parameters such as lithology, topography, strength, and porosity, would be an indicator that some property of the lunar surface (the target) is causing the observed morphological differences. Differing morphologies in a similar geologic setting indicates that the cause is probably differences in the impactor. Quantitative assessment of specific impactor properties from remotely sensed data can be challenging. The higher simple-to-complex transition diameter on Mercury relative to Mars (Barnouin et al., 2011; Garvin & Frawley, 1998; Schultz, 1988) has been attributed to higher impact velocities on Mercury (Le Feuvre & Wieczorek, 2008) because laboratory experiments (Barnouin et al., 2011; Schultz, 1988) and a recent impact simulation study (Silber et al., 2017) determined that lower velocity impacts cause more transient cavity collapse and hence the possibility of the formation of shallow, complex craters. However, Susorney et al. (2016) suggested that difference in impact velocity is not sufficient to justify the difference in values of transition diameter because of

statistically similar d/D values for simple craters on Mercury and Mars. Impact angle and direction have also been roughly estimated from asymmetric ejecta patterns (Herrick & Forsberg-Taylor, 2003; Herrick & Hessen, 2006) or the offset of central uplift and the internal structure of eroded floor (Kenkmann et al., 2009; Kenkmann & Poelchau, 2009; Scherler et al., 2006) using existing modeling and experimental results discussed in section 1.1. Here we attribute crater morphologies to impactor properties only in the case of encountering identical-sized craters with different morphologies that are in close proximity and in inferred similar geologic settings.

2.2 Methods and Data

2.2.1 Morphological Characterization

We compiled a database of 244 well-preserved lunar craters in the diameter range of 15–20 km. We used the most recent and complete catalog of craters greater than or equal to 8 km in size (Bandeira et al., 2014) and the database of well-represented near side craters (Losiak et al., 2009). We classified craters based on their degradation state on a scale of 1 to 4 (Arthur et al., 1964). Class 1 comprises craters with sharp rims, distinctly visible features (such as terraces, central peaks, and floor fractures) and no apparent post-impact filling or degradation. Class 2 craters have slightly softened rims and some modest degradation. The craters with substantially degraded rims fall in Class 3. The most shallow, degraded craters with little or no rims occur in class 4. We selected all identifiable class 1 craters in the 15–20-km size range for our database. We also discarded the craters that are completely shadowed in the images, especially ones at greater than 80° latitudes because we could not verify the preservation state or observe the crater features. Large secondary craters that were identifiable through crater chains were not included.

We classified the craters into various morphological categories based on the shapes of their cavities and the features (unconsolidated slumped material, terraces, central uplift, floor fractures, and so on) that are visible in their panchromatic imagery and topographic profiles. Figure 2.2 summarizes the classification scheme for every category. We calculated the rim-floor depth by independently measuring the rim and floor elevations and subtracting the latter from the former. For the rim elevation, we averaged the elevations along the rim outline where the standard deviation would account for topographic variability along the rim. The floor elevation was evaluated from within a polygon whose boundaries were delineated at the crater wall-crater floor contact. We measured the minimum value in case of a parabolic cavity or in craters where slumped material filled in most of the floor area. The standard deviation for the depth in this case can be assumed to come from rim elevation because the only measurement error in minimum floor elevation would be caused by the minimal geolocation error value (10 cm) for the Lunar Orbiter Laser Altimeter (LOLA; Smith et al., 2011). For craters with flat floors, we averaged the floor elevation within the polygon so that uncertainty in the depth would be contributed by both rim and floor elevations. The evaluation of mean elevations was automated through the Zonal Statistics tool in ArcGIS. Although this tool selected a variable number of points for each rim outline or floor area, most of the statistics show a scatter around ~1,000 points. We used the “Circle by Points” method of the CraterTools in ArcGIS (Kneissl et al., 2010) in outlining each crater rim to obtain the crater diameter, also ensuring that each circle encompasses the largest area for noncircular craters. The central uplifts, if any, were narrow enough so that we selected the maximum elevation value from a small area outlined around the peak and then subtracted the floor elevation from this value to derive the central uplift height for identifying complex craters. The above morphometry measurement techniques were first devised by Herrick and Sharpton (2000) for Venusian impact craters spanning simple

to peak-ring morphologies. Next, we analysed the relative global abundance of these classes and their global distribution with respect to the geology of the terrains they occur in.


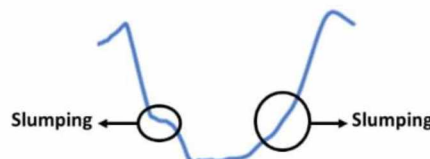
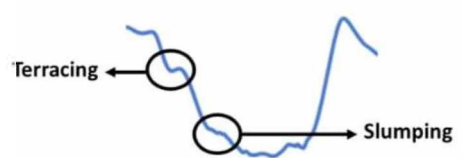
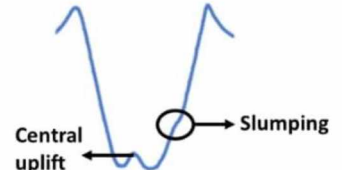
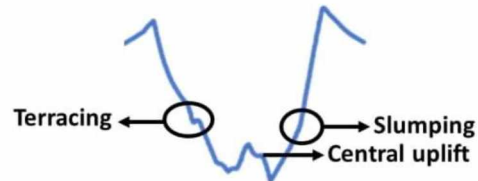
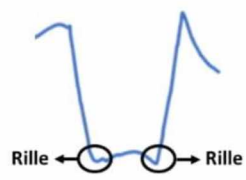
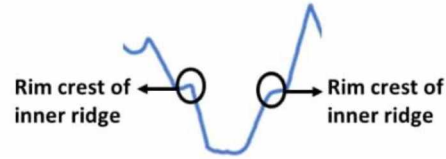
	Morphological Class	Characteristics in planform	Topographic profile
	Simple crater	Bowl-shaped cavity with breccia lens-covered floor; smooth, uniformly sloping walls	
Transitional Craters	Crater with localized slumps	Flat floor partly or completely covered with slumped debris; gradual decrease in wall slope at the position of the slumped material to values as low as $\sim 5^\circ$	
	Crater with localized slumps and terraces	Flat floor partly or fully covered with slumped material; step-like slump features along crater wall marked by a sharp, step-like break in wall slope to $\sim 0^\circ$	
Complex Craters (Hargitai & Öhman, 2014)	Crater with localized slumps and central uplift	Flat floor partly or fully covered with localized slumped material; visible mound of rocky, high albedo material on the center of the floor	
	Crater with localized slumps, terraces and central uplift	Flat floor partly or fully covered with debris that slumped along the walls; step-like slump features in the form of terraces along the walls; visible mound of rocky, high albedo material on the center of the floor	
	Floor-fractured crater	Shallow floor marked with narrow channels that appear to be annular fractures	
	Concentric crater	Inner concentric ridge nested inside the outer crater cavity	

Figure 2.2. List of the adopted morphological classification criteria within the 15–20-km size range.

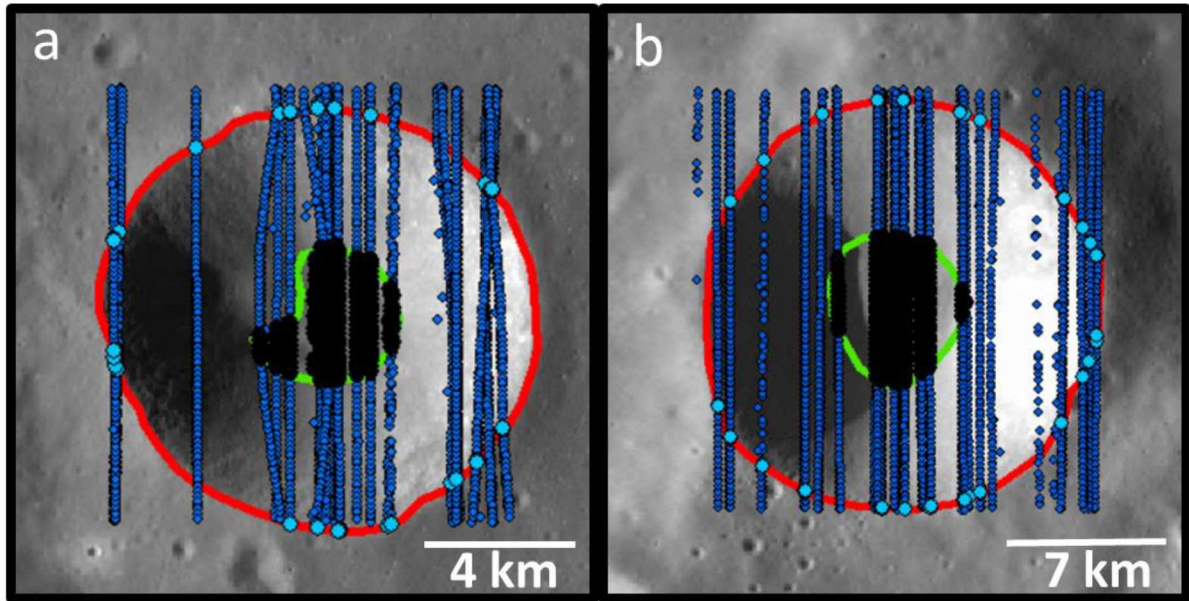


Figure 2.3. Examples of topographic measurements from LOLA tracks and LOLA gridded data superposed on LROC WAC images. (a) Theon Senior (-0.8°N , 15.42°E) and (b) Coriolis G (-0.03°E , 174.54°E). Dotted blue lines show LOLA altimetry tracks. The red and green lines correspond to rim outlines and floor area, respectively. The data points of the tracks intersecting the rim and the floor area are shaded in sky blue and black, respectively. Despite a gap of few kilometers between tracks, rim-floor depth estimations from gridded data and tracks measure ~ 3.4 km for Theon Senior and differ by ~ 100 m for Coriolis G (~ 2.9 km from reduced data record and ~ 3 km from gridded data record). Both images are 26 km wide. North is up in both images.

2.2.2 Close-Proximity Analyses

To look for differences within a similar geologic setting that might indicate an impactor-caused difference in morphology, we compiled groups of craters in closest proximity to each other. For example, if crater A and crater B occur nearest to each other, A and B form a pair. However, if A is the nearest neighbor of a crater C, then A, B, and C form a group. The craters that occur on topographically smooth surfaces (do not superpose a topographic discontinuity) were selected to minimize the variability of target properties owing to the effect of topography. Additionally, the craters that are diagnostic of oblique impacts (elliptical craters) were eliminated. We continued compiling crater groups with increasing nearest neighbor distance until we encountered clusters that comprise craters occurring in terrains marked with prominent differences in geology, such as a pair in which one crater is located in the highlands and another in the mare, or a group comprising craters that occur on well-

developed units of a larger crater (floor, ejecta, and terraces) that may differ in attributes such as lithology, strength, and porosity. The morphological variations in these terrains were evidently attributable to the association with differences in target properties. We terminated our compilation with the group that consisted of craters separated by 124 km. This value also turned out to be the maximum distance between any two craters in a close-proximity cluster.

2.2.3 Data Sets Used

We used the LROC WAC global mosaic (processed to 100 m per pixel) and Narrow Angle Camera (NAC) images (0.5 m per pixel; Robinson et al., 2010) to observe crater morphologies and their terrains. We obtained topographic profiles and elevation measurements from the gridded topography (gridded data record [GDR]) data from the Lunar Orbiter Laser Altimeter Digital Elevation Model (LOLA DEM) of ~1-m vertical resolution (Smith et al., 2011; Smith et al., 2017). The 512 ppd DEM provided sufficiently high spatial resolution to locate the crater rim and other crater features. We compared the rim-floor depths obtained from the GDR data with those estimated from individual LOLA altimetry tracks (reduced data record [RDR]), paying particular attention to craters located at the equator where the tracks can be separated by distances up to 2–4 km. We determined that the results were consistent with each other. The GDR-derived depths differed from the RDR-derived depths by values up to 100 m, which falls within the ranges of standard deviation values that we calculated for the crater depths from both GDRs and RDRs. An example of the LOLA tracks covering two simple craters at the equator and superposing the rim and floor outlines used for gridded data measurements is illustrated in Figure 2.3.

2.3 Results

2.3.1 Morphological Characterization

Based on crater features and average topographic profile, we classified the 244 well-

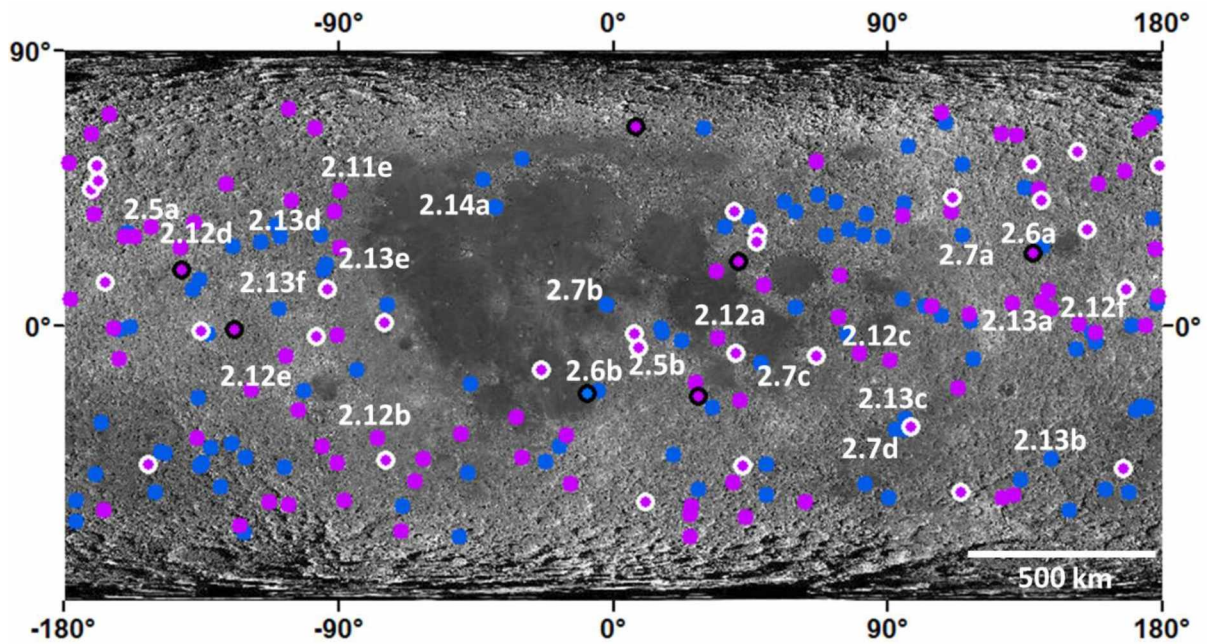


Figure 2.4. Global lunar WAC mosaic showing the locations of simple craters (purple circles) and craters with localized slumps (dark blue circles). The black outlines refer to unusually deep craters. Simple craters with identified impact melt deposits on the floors are denoted by white outlines. The alphanumeric labels represent the craters displayed in Figures 2.5, 2.6, 2.7, 2.12, 2.13 and 2.14. North is up.

preserved craters into the following morphological categories (a comprehensive list along with morphometric and observational data is available in Tables A-1 and A-2 of Appendix A):

2.3.1.1 Simple Crater

This morphology is characterized by a smooth-walled, roughly bowl-shaped cavity (Figures 2.5a and 2.5b). The floors of these craters usually show a breccia lens, containing a mixture of fallback ejecta and slump material of the steep crater walls along with small visible amounts of impact melt on the floors of 32 craters (Cintala & Grieve, 1998; Grieve et al., 1977; Melosh, 1989a). In Figure 2.4, the circles shaded in purple correspond to simple craters, and the purple circles outlined in white shade represent simple craters with visible impact melt-lined floors. Using LROC NAC images, we identified impact melts based on smooth surfaces, lower albedo in comparison to the breccia boulders, sharper contact with the breccia blocks and crater walls as opposed to more gradual change in slope from the walls to the floor due to slumped material, and presence of palimpsests (if any) that are characteristic of crater

morphology formed on melt surfaces (Fink et al., 1982; Greeley et al., 1980; Howard & Wilshire, 1973; Plescia, 2015a; Plescia & Cintala, 2012). Examples of simple craters containing clearly visible impact melt on their floors are shown in Figure 2.5b, and some melt features that form the identification criteria have been illustrated in Figure A-1 of Appendix A. Floors of eight craters could not be verified for the presence of impact melt because these craters are located at and beyond 60° latitudes and their floors are partially obscured by shadow in both NAC images. The simple craters form the most abundant category (49%) in our database and are concentrated exclusively in the highlands (see locations of purple circles in Figure 2.4).

A d/D ratio of ~ 0.20 was determined by several studies in the past for well-preserved simple craters (Kenkmann et al., 2012; Melosh, 1989a; Melosh & Ivanov, 1999; Pike, 1974). However, the d/D ratios of six simple craters exceed this value after accounting for the uncertainty values (purple circles outlined in black in Figure 2.4, example in Figure 2.6a), and our measurements of d/D ratios for the remaining simple craters span a broad range from 0.14 to 0.20. An example of a crater with a d/D ratio of ~ 0.15 has been shown in Figure 2.5a. The unusually deep craters are located near the mare-highlands contacts within the regions that encompass the ejecta blankets of the mare basins. The 32 craters whose floors contain visible impact melt deposits, include two unusually deep craters (Hill at 20.91°N, 40.81°E and Unnamed31 at 18.32°N, 218.59°E).

2.3.1.2 Crater with Localized Slumps

Craters with this morphology contain unconsolidated material that slumped down the walls under gravity and collected locally at the base of the walls. At the position of the localized slumped material, their profiles show a gradual decrease in wall slopes to values that cover a wide range and can also be as low as $\sim 5^\circ$ (Figures 2.7a–2.7d). Such a morphology qualifies for

the definition of a transitional crater (Cintala et al., 1977; Cintala & Grieve, 1998; Howard, 1974; Kalynn et al., 2013; Osinski et al., 2018; Pike, 1974, 1977b, 1988; Plescia, 2015b;

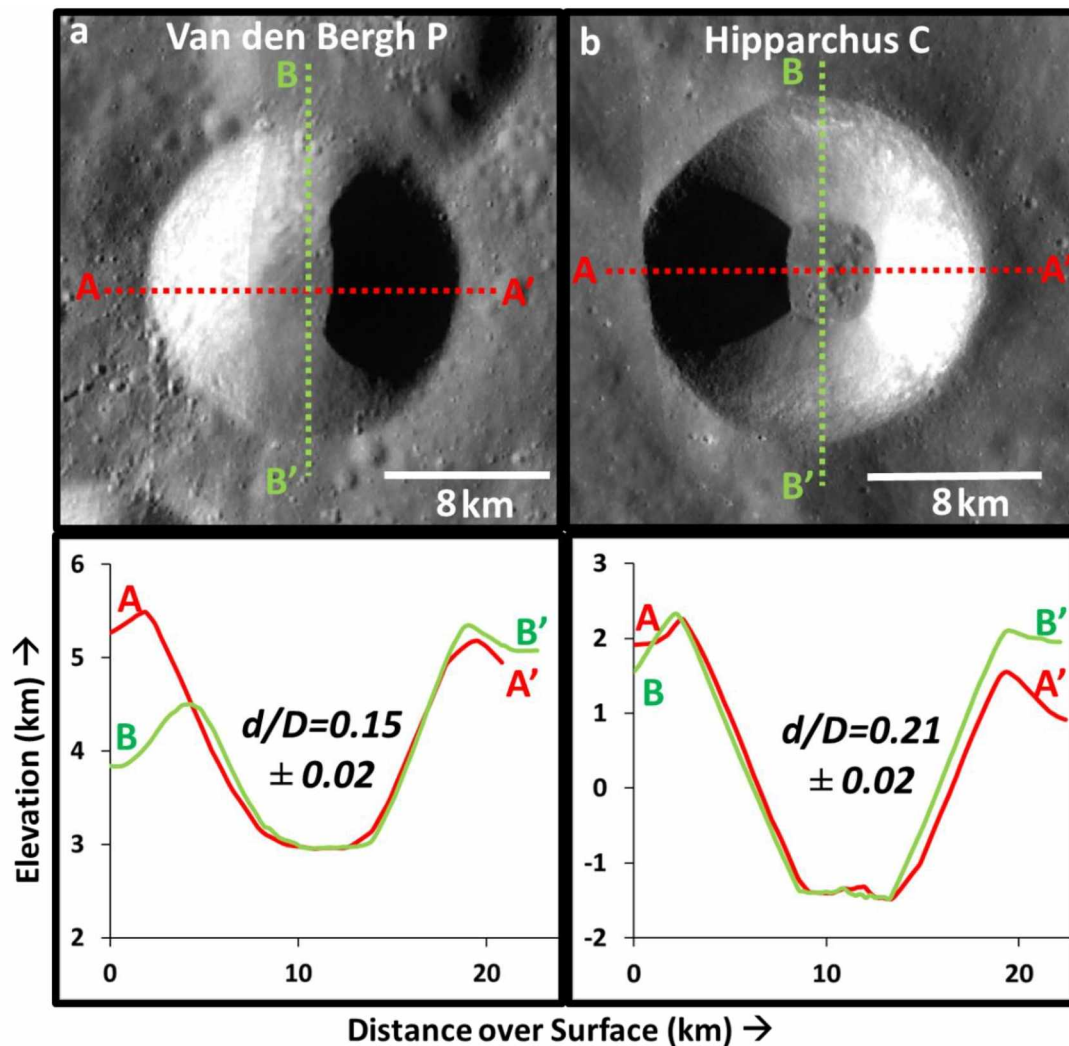


Figure 2.5. Examples of well-preserved simple lunar craters in the simple-to-complex transition zone and their topographic profiles along specific transects. The geographic coordinates of their centers are (a) 29.2°N, 199.81°E; (b) -7.41°N, 8.21°E. The geographic locations of these craters are marked on the Wide Angle Camera mosaic in the form of their figure labels in Figure 2.4. Note that the profiles are characteristic of uniformly sloping walls. The floors of crater in (b) are covered with identifiable impact melts and breccia lens. North is up in both images.

Robbins & Hynek, 2012; Smith & Sanchez, 1973). The craters whose wall slopes exhibit a change due to accumulated material that was primarily contributed by ejecta of impact craters on or adjoining the rims would be classified as simple craters. This is because this debris originated from excavation of material from a different impact and not from collapse of the parent crater's walls. The ejecta flows can be generally seen emanating from the rim of the

younger crater. They could also be lined along the older crater's walls. Their albedo is similar to that of the material deposited by them and higher than the floor debris that accumulated from

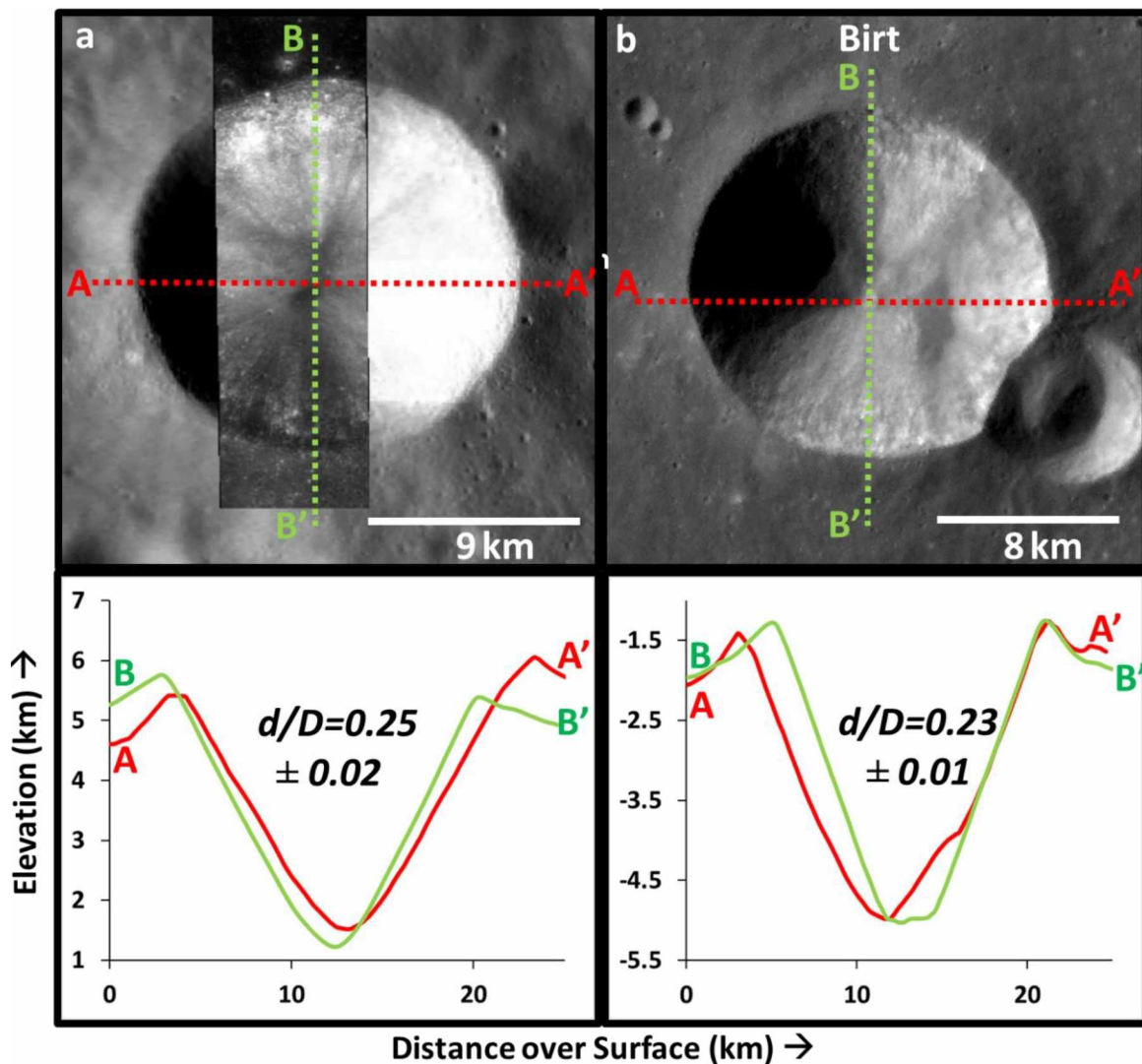


Figure 2.6. WAC illustrations of unusually deep lunar craters in the simple-to-complex transition, with their cross-sectional profiles along orthogonal azimuths. The locations of the craters on the lunar surface ((a) 23.62°N , 137.65°E ; (b) -22.36°N , 351.4°E) are labeled on the WAC mosaic in Figure 2.4. Narrow Angle Camera M1102659336R in (a) has been used to highlight the crater floor. The calculated d/D ratios are given within every profile. We noticed that this category constitutes simple craters except for (b), which is a crater with localized slumped material. We found all unusually deep craters to occur around the rims or within the ejecta coverage of mare basins. North is up in both images.

slumping during crater formation. However, we could not find any craters with such signatures of localized floor material. It could be possible that the change in wall slope is caused by localized slumping that could occur immediately after transient cavity formation as part of the modification phase of crater formation (Melosh, 1989a; Quaide et al., 1965; Settle & Head,

1979), or material could potentially slump off the walls much later, triggered by some process such as seismic shaking from a later impact (Brunetti et al., 2015; Izenberg, 2010; Kumar et al., 2013; Scaioni et al., 2018). To test whether our database consists of crater structures characteristic of both the processes, we performed crater counting on the ejecta and slumped material of few randomly selected, though similar-sized craters to compare the relative ages of the unconsolidated floor material with that of the ejecta. This procedure has been demonstrated in supporting information A-2 of Appendix A. We observed that the ejecta and the unconsolidated debris for one out of the three analyzed craters could differ in relative ages. This difference indicates that this class may also include craters whose unconsolidated material may result from slumping off the walls by processes occurring later than the modification stage. It is beyond the scope of this study to conduct crater counts for all 114 craters with localized slumped material, so here we do not separate syn- and post-impact slumping within these craters.

After the final characterization, we observed that craters with localized slumps (see examples in Figure 2.7) are distributed globally across the lunar surface (Figure 2.4), forming the second most abundant group of morphologies (Table 2.1) within the lunar simple-to-complex transition zone. We calculated their d/D ratios and found them to occur in the range of 0.11 to 0.19 with only one crater Birt that was observed to have an anomalously deep cavity ($d/D = 0.23 \pm 0.01$). Birt is in the mare near the mare-highlands boundary and cuts against the rim of a smaller crater. Its location is marked in dark blue and outlined in black in Figure 2.4. Figure 2.6b shows its WAC image and topographic profile. After a preliminary examination of the geology of Birt for the determination of syn- or post-impact slumping, we infer that impact against a pre-existing crater's rim in the southeast may have triggered the slumping in this crater and the collection of ejecta (visible unconsolidated material) in the cavity of the smaller crater. If the smaller crater had formed from impact against the rim of Birt, impact-induced seismic

shaking (post-impact slumping) and ejecta from the smaller crater would have caused the accumulation of the localized debris. However, this case is unable to justify the presence of unconsolidated material inside the smaller crater. Also, post-impact slumped material is younger than the crater's ejecta and therefore must have a higher albedo. In case of Birt, although we see younger and brighter flows on its walls that do lead to the high albedo material on the floor, the debris on the southeast is distinctly darker (possibly older) and shows a sharp contact with the brighter flows. Further investigation is required to determine the relative ages of Birt and its floor material. Therefore, for this study, we classify it as an unusually deep crater with localized slumps. It shares a common location with the unusually deep simple craters, that is, proximity to the mare-highlands contact.

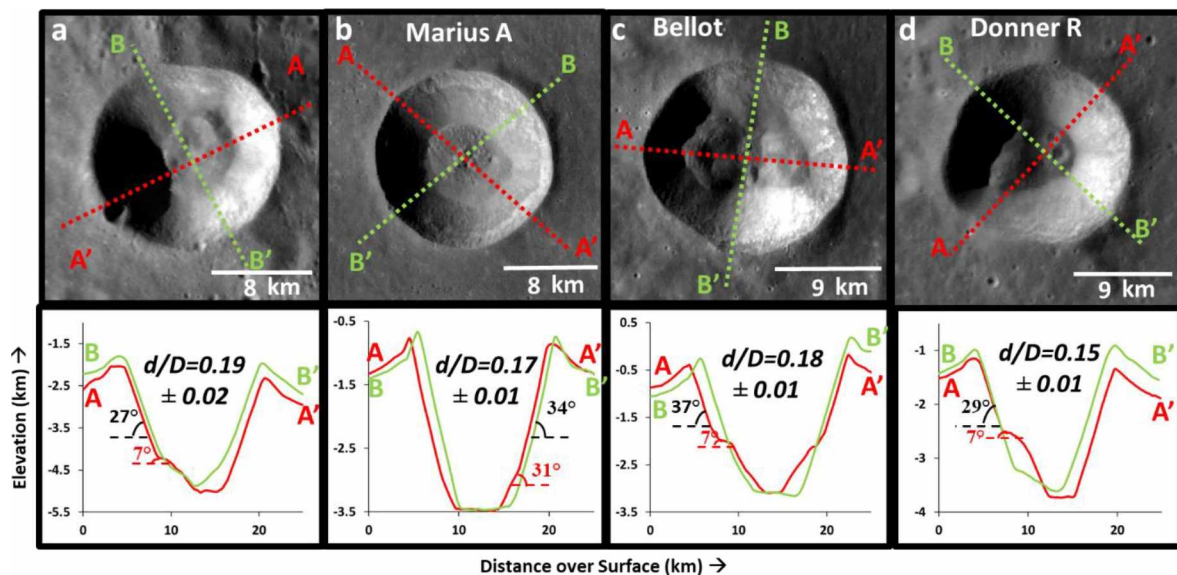


Figure 2.7. WAC images and LOLA DEM topographic profiles of four lunar craters that bear localized slumped material. The geographic coordinates of their centers are as follows: (a) 29.73°N, 114.29°E (highlands); (b) 12.59°N, 313.95°E (mare); (c) -12.47°N, 48.19°E (highlands); (d) -34.34°N, 92.28°E (mare-highlands boundary). The locations of these craters are labeled on the WAC mosaic in Figure 2.4. Crater profiles were selected to get the best measurements of the examined features. In the profiles, the slope values in black represent the wall slope of the region above the location of the slumped material, whereas the slope values in red refer to the wall slope at the position of the slumped debris. North is up in all images.

2.3.1.3 Crater with Localized Slumps and Terraces

These craters are characterized by single terrace patterns (Figure 1.9b) and occasionally a couple of concentric (Figure 2.9a) terraces (Cintala et al., 1977; Collins, 2014; Pearce &

Melosh, 1986; Pike, 1988) formed by discrete blocks that slid down the crater walls in addition to slumping of unconsolidated material (Melosh, 1989a; Quaide et al., 1965 ; Settle & Head,

Table 2.1. Relative abundance of crater morphological classes in mare and highlands.

Crater Class	Highlands	Mare	Boundary
Simple Crater	117	0	0
Crater with localized slumps	97	15	2
Crater with localized slumps and terraces	3	4	0
Crater with localized slumps and central uplift	1	1	0
Crater with localized slumps, terraces and central uplift	0	2	0
Floor-fractured crater	0	1	0
Concentric crater	1	0	0

1979). Their WAC images and cross-sectional profiles also exhibit a decrease in wall slope due to terracing, but unlike a gradual slope change from slumped material along with flat floors, terraces appear as step-like breaks in the profile such that the slope can drop to $\sim 0^\circ$ at the position of the terrace. The terraces are not as continuous around the crater floor as observed in larger complex craters and can be called partial terraces. The craters containing localized slumped material, partial terraces, and flat floors have also been recognized as transitional craters. We observed seven lunar craters in our survey that qualify for this class. Three of these were formed on the highland surface out of which two craters are situated in the South Pole Aitken Basin region near the mare patches (Figure 2.8). The d/D ratios range from 0.09 up to 0.17. A power law relation between the depths (d) and diameters (D) of all transitional craters (craters in this section and section 2.3.1.2), excluding the only unusually deep crater Birt whose depth could influence the power law exponent representative of the ordinarily deep craters that are in majority, was derived by means of least squares fit:

$$d = (0.290 \pm 0.121) D^{0.784 \pm 0.146}$$

The depth versus diameter of transitional craters follows a nonlinear relationship. The power law exponent for these morphologies is less than ~ 1 that has been estimated for lunar simple craters spanning nearly all sizes (Pike, 1974, 1977a, 1980a; Salamunićcar et al., 2012; Wood & Anderson, 1978) and greater than the exponent determined from global studies of lunar

complex craters (~0.3; Kalynn et al., 2013; Pike, 1974, 1977a, 1980a, 1981; Salamunićcar et al., 2012; Williams & Zuber, 1998; Wood & Anderson, 1978). The depths of transitional craters

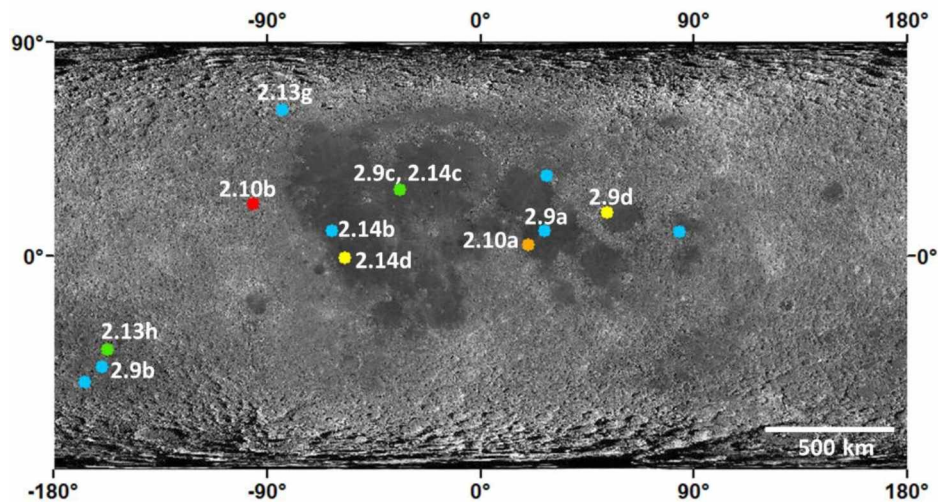


Figure 2.8. Mapped distributions of crater morphologies other than simple craters and craters with localized slumps. WAC mosaic has been used to display locations of craters with localized slumps and terraces (light blue circles), craters with localized slumps and central uplift (green circles), crater with localized slumps, terraces, and central uplift (yellow circle), floor-fractured crater (orange circle), and concentric crater (red circle). The alphanumeric labels refer to the locations of the craters shown in Figures 2.9, 2.10, 2.13 and 2.14. North is up.

increase at a lower rate relative to depths of simple craters and at a higher rate as compared to depths of complex craters, which is possibly due to higher amount of slumping than in simple craters but still lower than the amount of modification that yields continuous terraces and central peaks in complex craters. We did not come across any craters in our survey with terraces that exist without the presence of slumped debris. The crater Virchow in our database has also been catalogued as a floor-fractured crater by virtue of the numerous fractures on its floor (Jozwiak et al., 2012).

2.3.1.4 Crater with Localized Slumps and Central Uplift

We found two complex craters (Hargitai & Öhman, 2014; Melosh, 1989a; Melosh & Ivanov, 1999) in our survey that contain a small central rise (and hence are complex craters) and localized slumped material. Their geographic locations are labelled in Figure 2.8. The central uplifts are also visible in their topographic profiles. One of the craters was formed in the mare (Figure 2.9c), and the second crater is located on the highland surface that transitions

into the mare terrain on the north and south of the crater. These craters were formed with d/D ratios measuring 0.16 ± 0.01 and central uplifts of heights ~ 145 and ~ 202 m, respectively. The

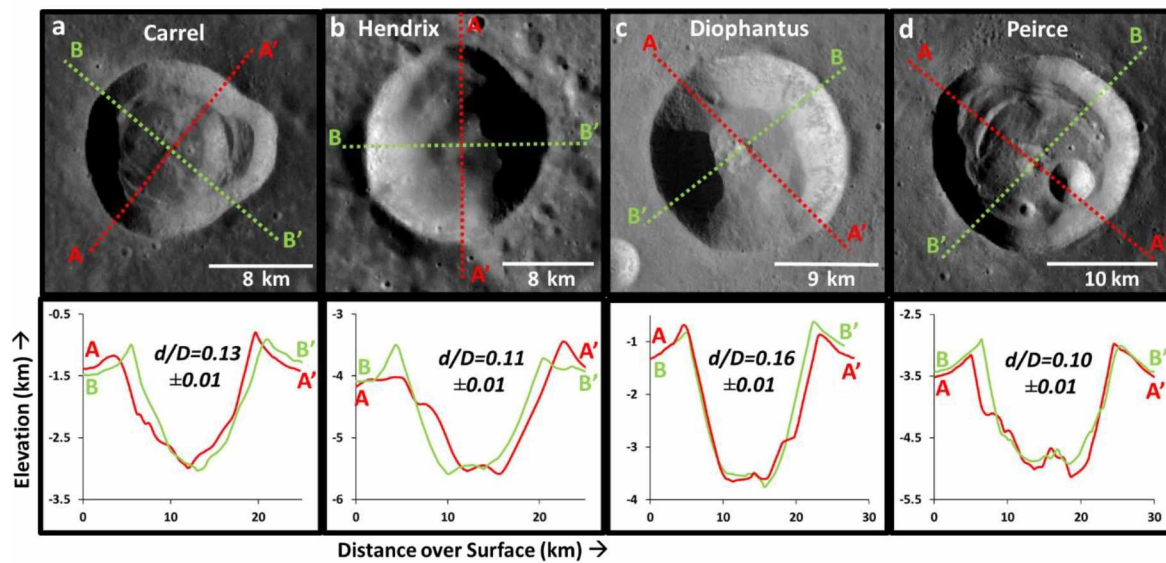


Figure 2.9. WAC illustrations and LOLA profiles of crater morphologies other than simple craters and craters with localized slumps. (a) Crater bearing localized slumps and terraces in the mare (10.66°N , 26.68°E); (b) crater bearing localized slumps and terraces in the highlands (46.86°N , 200.06°E); (c) crater with localized slump and central uplift in the mare (27.62°N , 325.7°E), and (d) crater with localized slumps, terraces, and central uplift in the mare (18.26°N , 53.35°E). Crater profiles were selected to get the best measurements of the examined features. In the red-lined profiles of craters in (a), (b) and (d), the step-like breaks in slope close to the edge A correspond to terraces. The green-lined profiles of craters in (a) and (d) and the red-lined profile of crater in (c) clearly illustrate the position of localized slumped material indicated by a gradual decrease in wall slope. The rocky, high albedo features on the floors of craters in (c) and (d) are the emergent central uplifts. The locations of these craters are labelled in Figure 2.8. North is up in all images.

d/D values are greater than the values reported for complex craters by previous studies (Howard, 1974; Melosh, 1989a; Pike, 1977a). This difference is probably because of the absence of terraces that are indicative of wall collapse (Quaide et al., 1965; Settle & Head, 1979) and could have further contributed to reduction in crater depth (Melosh & Ivanov, 1999; Pike, 1977b, 1980b).

2.3.1.5 Crater with Localized Slumps, Terraces, and Central Uplift

This morphology is characterized by components of a well-developed complex crater, primarily central uplift (Hargitai & Öhman, 2014; Melosh, 1989a; Melosh & Ivanov, 1999), in the lunar simple-to-complex transition: central uplift, localized slumped material, and discrete

partial terraces. We observed only two craters of this morphology. They are located in the mare (Figure 2.8). Their d/D ratios measure 0.10 ± 0.01 each (one example in Figure 2.9d), and the heights of central mounds measure $\sim 106\text{--}116$ m. The presence of terraces in these craters can perhaps justify the smaller d/D values relative to the d/D values of craters in section 2.3.1.4.

2.3.1.6 Floor-Fractured Crater

We found one crater, Manners, whose floor is characterized with arcuate narrow depressions that look like annular fractures (Figure 2.10a). Its dome-like uplifted, shallow floor (d/D ratio of 0.11) is evident from its topographic profile. It is surrounded by arcuate rilles in Mare Tranquillitatis (see location in Figure 2.8). Lunar arcuate rilles have been suggested to be of a tectonic origin, resulting from the sinking of solidified lava under its own weight (McGill, 1971; Quaide, 1965; Smith, 1966). Manners has not been included in the catalog of floor-fractured craters compiled by Jozwiak et al. (2012). However, owing to its floor morphology, it can be termed a floor-fractured crater as defined by Schultz (1976). Due to the identification of only one such crater in the 15–20-km size range, we were not able to perform detailed analyses on the causes behind its formation. Therefore, we suggest the most recent hypothesis postulated on the basis of a comprehensive examination of lunar floor-fractured craters that the presence of shallow magmatic intrusions underneath the crater floor yielded these fractures (Jozwiak et al., 2012, 2015, 2017; Thorey & Michaut, 2014; Wilson & Head, 2018).

2.3.1.7 Concentric Crater

As seen in the WAC image and LOLA topographic profile in Figure 2.10b, this crater is composed of an inner concentric ridge. It has an anomalously shallow floor (d/D ratio of 0.08) and is located near the mare terrain (Figure 2.8). It was formed on the buried floor of an older crater on the highlands. However, we could not find any other well-preserved crater of a similar morphology within the 15–20-km size range for comparison. We therefore defer to the

interpretation of Trang et al. (2016) that magmatic intrusions from underneath the crater may have uplifted the floor to form a concentric ridge. It is one of the few craters greater than 15 km in size that exhibit this morphology.

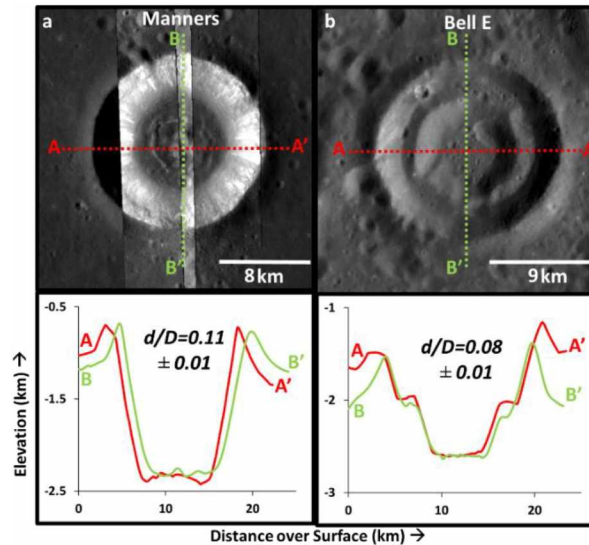


Figure 2.10. WAC images and LOLA profiles of (a) floor-fractured crater (4.57°N, 19.99°E) and (b) concentric crater (22.06°N, 264.06°E). The profiles in (a) show that the fractures are deeper by ~125 m on the east and west ends of the floor as compared to the northern and southern edges. For obtaining a more illuminated view of the fractures in (a), we used Narrow Angle Cameras M1169394997L, M1096365414L, and M1096365414R. The locations of (a) and (b) are marked in Figure 2.8. North is up in both images.

2.3.2 Highlands Versus Mare Craters

Of the five premier morphological categories belonging to the lunar simple-to-complex transition diameter range identified, 219 craters are in the highlands, 23 craters occur in the mare, and 2 craters are on the mare-highlands boundary. Table 2.1 summarizes the abundance of all crater classes in the highlands, the mare, and the mare-highlands boundary. As evident from the depth versus diameter plot in Figure 2.11, the distribution of most of the groups is skewed toward either terrain. All 117 simple craters are concentrated on the highland surface, whereas craters bearing localized slumped material are scattered across the lunar surface (15 in mare, 97 in highlands, and 2 on boundary). With the development of more units like terraces and central uplifts, the craters show a sharp decline in the numbers but a shift in their concentration to the mare terrain. The two complex craters with localized slumps, terraces, and

central rise are located only in the mare. The higher percentage of surface area covered by the highlands and the significantly high abundance of highland craters relative to mare craters could factor into the strong association of certain morphologies with certain terrains (for example, simple crater concentration in highlands). However, we also examined the geology of the terrains that correspond to craters of each morphological class and investigated common attributes among them that could correlate with that class.

Figure 2.11 illustrates that the diameters of all morphologies, regardless of whether they are in the highlands or on mare terrain, are spread across the 15–20-km size range and are not confined to a size or a subrange within this range. There is a shift in the depths to smaller values with transition from simple to complex morphologies, a result of additional material to the floor in the form of slumps and terraces and/or the presence of central uplift. The shallowest craters have transitional and complex crater morphologies and are in the mare. However, there is a significant overlap of the depths of shallow simple craters and the depths of transitional and complex craters. We also noticed an earlier development of terraces and central uplift in the mare, which implies earlier onset of complex craters in the mare (15–16 km) as compared to the highlands (19–20 km).

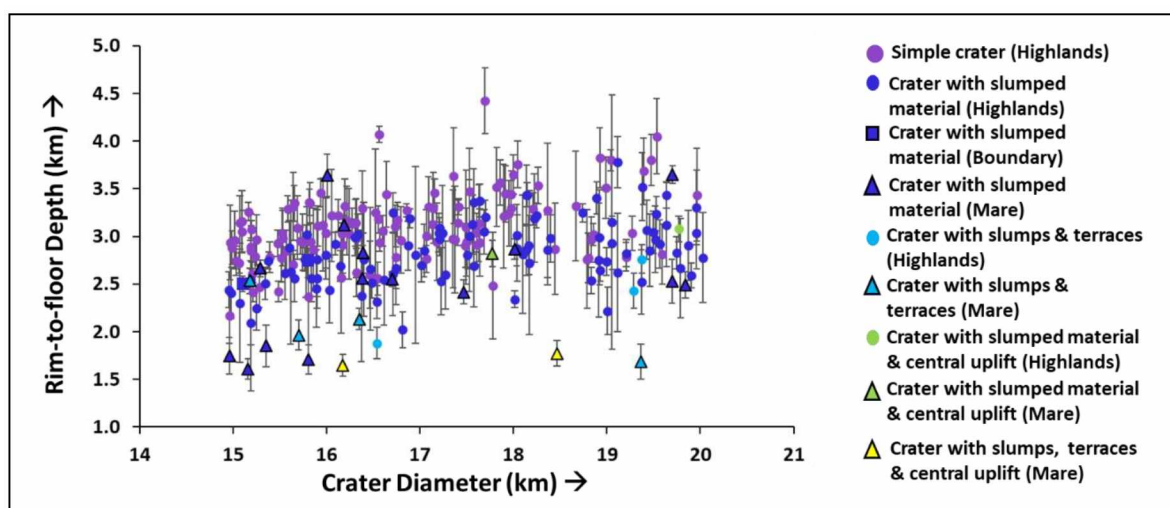


Figure 2.11. Crater depth versus diameter plots for the five major crater morphologies. Dots refer to the highlands, triangles represent the mare, and squares have been used for the two craters with localized slumped material that occur on the highlands-mare boundary. Note that while all simple craters are concentrated in the highlands, with the development of complex

craters, the location shows a gradual shift to the mare. The depths of the shallower simple craters show a significant overlap with the other morphologies.

We examined the terrain exterior of the craters located in the lunar highlands. For estimating the elevation variation of the pre-impact terrains around the craters, we extracted LOLA GDR profiles across transects that pass through the crater center and extend to two crater radii on each end from the center. Six such profiles at azimuthal intervals of 30° were obtained for each crater. The pre-impact terrain elevation value was recorded at the position where the ejecta profile started flattening. The terrain elevation variation across each profile was obtained from the difference of terrain elevation on both ends of that profile. An average of the six values obtained from the six profiles across each crater was calculated to derive the mean terrain elevation variation around each crater. A list of these elevation variation values for simple craters and craters with localized slumps is available in Table A-2 of Appendix A. The elevation variation of the terrains around simple craters ranges from flat to 1 km and from 200 m to 4 km around craters with localized slumps. Such elevation differences exist globally for the heavily cratered highlands and can be larger in several regions. However, the immediate surroundings, or the surfaces on which the simple craters occur, are relatively flat (Figure 2.12a) or uniformly sloping (see the red-lined profiles in Figures 2.5b, 2.12b, and 2.12c), or the craters display a slight overlap with the rim of a subdued or buried crater (Figures 2.5a and 2.12d–2.12f). Craters bearing localized slumped material, including the two craters on the mare-highlands boundaries, were predominantly formed by impacts on sharp topographic boundaries such as the terrace of a well preserved, larger crater (Figure 2.13a) or the developed rim of a pre-existing crater (Figures 2.7a, 2.7c, 2.7d, 2.13b, and 2.13c). However, there are 35 craters (Figures 2.13d–2.13f) with localized slumps that either occur on gradually sloping surfaces or superpose degraded crater rims but are not reflective of impact against a prominent topographic discontinuity in the panchromatic images. In the South Pole Aitken region, where

the mare basalts occur in isolated patches and have also penetrated the highlands, we encountered a crater with localized slumps and central uplift and two craters with localized

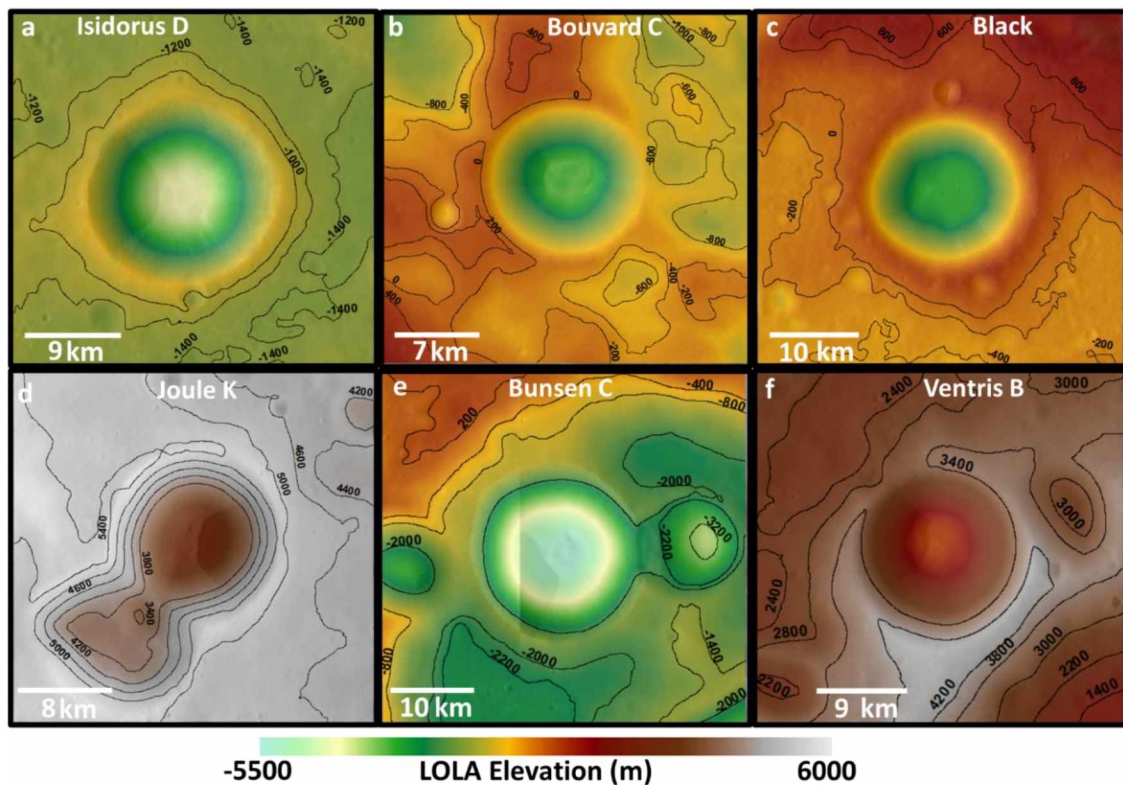


Figure 2.12. LOLA DEM superposed on WAC images of simple craters and overlain by prominent elevation contours. The contours highlight the elevation variation and the direction of slope, if any, of pre-impact terrain. The elevation values are in meters. (a) Simple crater on a flat surface (-4.27°N , 34.07°E); (b) simple crater on a surface that gradually slopes from southwest to northeast and whose maximum elevation variation was evaluated to be ~ 1 km (-37.05°N , 282.52°E); (c) simple crater on a surface that gradually slopes from north to south and whose maximum elevation variation was evaluated to be ~ 0.7 km (-9.19°N , 80.39°E); simple crater that truncates against the rim of smaller, pre-existing crater in (d) 25.64°N , 218.15°E (pre-existing crater is in the southwest) and (e) 44.2°N , 270.18°E (pre-existing crater is in the east); (f) simple crater (-2.22°N , 158.08°E) that superposes the subdued rim of smaller, pre-existing crater to the east. North is up in all images. The legend at the bottom refers to the elevations represented by the different shades.

slumps and terraces. Each of these craters is located adjacent to a mare patch. The complex crater (Figure 2.13h) is located on a flat highland terrain and possesses layering on its walls. One of the two terraced craters (Bose D in Figure A-3 pf Appendix A) superposes the rim of a larger pre-existing crater, whereas the other crater with localized slumps and terraces (Hendrix in Figure 2.9b) occurs on relatively flat terrain. The third crater with localized slumps and

terraces (Figure 2.13g) is in the highlands to the extreme north at ~245 km from the nearest mare-highlands contact (Figure 2.8).

The mare are smooth plains formed by basaltic lava flows (Head, 1975; Smith et al.,

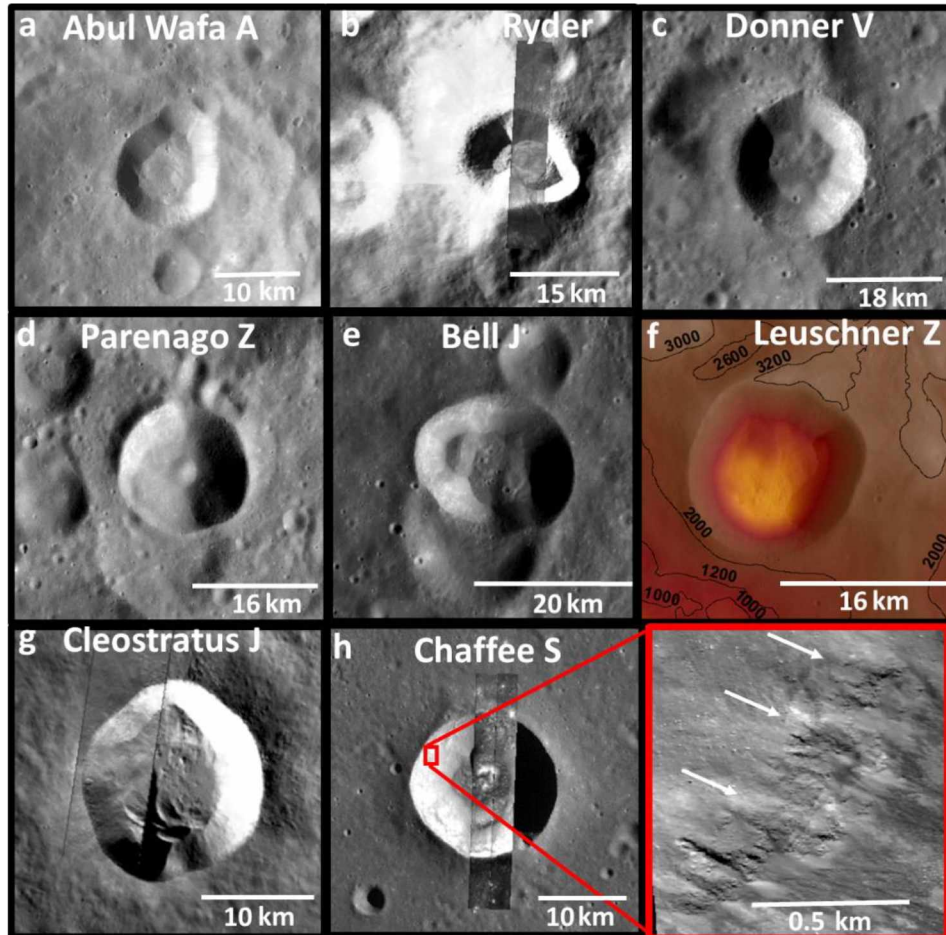


Figure 2.13. Illustrations of pre-impact topography and cavity features of highland crater morphologies other than simple craters. WAC images show (a) crater with localized slumped material, which superposes the well-preserved terrace of a larger crater (1.39°N, 116.86°E); (b) crater with localized slumped material, which superposes the well-developed rim of an older crater (−43.87°N, 143.29°E; NAC108292443L and NAC108292443R highlight the slumped debris); (c) crater with localized slumped material, which superposes the well-preserved rims of two smaller craters and a bigger pre-existing crater (−30.56°N, 95.58°E); crater with localized slumped material, which intersects the subdued rim of a smaller crater to the south in (d) 28.96°N, 250.71°E, and (e) 19.88°N, 265.88°E; (f) crater bearing localized slumped material and located on a surface that slopes from northeast to southwest (depicted by the contours superposed on the LOLA DEM) whose maximum elevation variation was evaluated to be ~2 km (5.24°N, 250.43°E); (g) crater with localized slumps and terraces with layering on the southwest wall (61.39°N, 276.34°E; NAC1117105565R used for enhanced visibility); and (h) crater with localized slumped material and central uplift whose walls are characterized with layering that is indicated by white arrows in the NAC1165856567R inset outlined in red. Please refer to the legend in Figure 2.12 for looking up the elevation values in meters represented by the contours in the LOLA DEM in (f). The crater locations are also labelled in Figures 2.4 and 2.8. North is up in all images.

1970; Taylor, 1989). Thus, craters in this terrain primarily occur on flat surfaces, the exception being few craters that formed on pre-existing basin rims. However, all morphologies are characterized by prominent layering on the crater walls. From the limited sample size of terraced craters, we noticed that the terraces increase in number with increasing distance from the highland terrain. Craters in the highlands (Figures 2.9b and 2.13g) or near mare-highlands boundaries (Figure 2.9d) have one terrace as compared to two or three terraces in craters that occur further in the mare (Figures 2.9a, 2.14b, and 2.14d) as far as a few hundred kilometers from the highlands. The distribution of the number of terraces appears to be random with respect to the increase in crater diameter. Figure 2.14 demonstrates layering on walls of mare craters.

2.3.3 Close-Proximity Craters

To investigate impactor-caused differences of nearest neighbor crater morphologies within similar geologic settings, we required only those craters that occur on even surfaces to minimize the effect of target properties. We also discarded the craters that appeared to have formed from highly oblique impacts. Therefore, from 244 craters, we eliminated the craters that

- [1] Superpose a crater's rim (81 craters),
- [2] Truncate against a crater's rim (11 craters),
- [3] Superpose a crater's terrace (16 craters),
- [4] Superpose a crater's outer wall (2 craters), and
- [5] Are elliptical due to possibly highly oblique impacts (1 crater).

Craters of type 1 are illustrated in Figures 2.5a, 2.7a, 2.7c, 2.7d, 2.12f, 2.13b, 2.13c and 2.14a. Figures 2.6b, 2.12d and 2.12e show craters of type 2. An example of a crater formed on a larger crater's terrace (type 3) is displayed in Figure 2.13a.

Figure A-3 of Appendix A demonstrates more examples corresponding to each type of discarded crater. Figure 2.15 shows a global map of the distribution of discarded craters (red circles) and the craters selected for close-proximity analyses (green circles). After eliminating

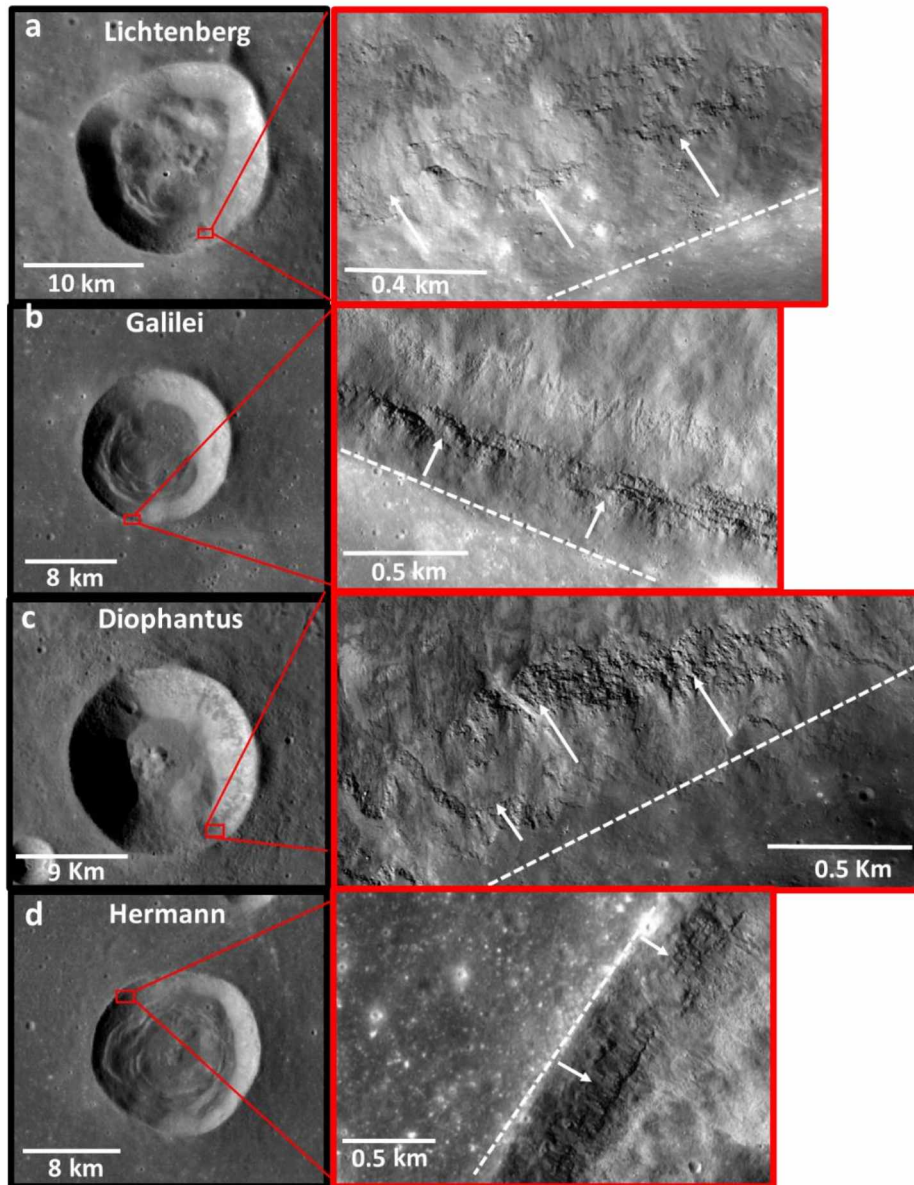


Figure 2.14. Wide Angle Camera images of craters in mare. All craters are characterized by layering on walls (magnified using the NAC insets outlined in red). (a) Crater with localized slumped material that superposes the rim of a mare-filled crater to the northwest (31.85°N , 292.28°E ; NAC M183975919L), (b) crater with localized slumps and terraces (10.48°N , 297.16°E ; NAC M150931890L), (c) crater with localized slumped material and central uplift (27.62°N , 325.7°E ; NAC M183754268L), (d) crater with localized slumps, terraces, and central uplift (-0.87°N , 302.53°E ; NAC M1114547048R). The dashed white lines in the NAC insets refer to rim outlines, and the white arrows indicate layering. The locations of the above craters are shown in Figures 2.4 and 2.8. North is up in all images.

111 craters, we generated groups of craters that are nearest neighbors of each other and obtained the maximum distance between two crater centers to be 124 km (section 2.2.2). Thus, we analyzed 27 craters in total. For craters of the same morphology, we compared their d/D values and inferred similar depths if the differences in the d/D values fell within their standard deviations. We generated a table (Table A-3 of Appendix A) of all the close proximity groups, which is available in the supporting information. The morphologic details of some of the groups are displayed in Figures 2.16–2.19 and summarized in Table 2.2, with their locations labeled in Figure 2.15. We have labeled all groups in Table A-3 and referenced them in the following discussion. The images of the groups that are not shown in this paper are available in Figures A-4 and A-5 of Appendix A.

We noticed that five pairs and one triplet comprise craters that exhibit simple crater morphologies and similar rim-floor depths. Craters belonging to four pairs (Group G in Figure 2.16a, Groups H, I, and L) and the triplet (Group A) are simple craters that are located on either topographically flat highland surfaces or superpose rims and terraces of buried craters. Craters from the remaining pair (Group K) have localized minor wall slumping and are located on highland surfaces with topographic variations that are similar to those corresponding to the terrains of the simple craters. Due to their close proximity to impact basins, the pre-impact substrate is likely comprised of fragmented ejecta up to a depth of at least a few kilometres (Fassett et al., 2011; McGetchin et al., 1973; Thompson et al., 1979, 2009). The low strength of the target material and/or hidden heterogeneities in the basin ejecta may be responsible for the minor localized slumping observed (Aschauer & Kenkmann, 2017). Furthermore, the possibility of slumping from post-crater modification (Kumar et al., 2013; Scaioni et al., 2018) cannot be ruled out.

Group C (Figure 2.16b) is composed of craters that bear localized slumped material but statistically differ in depth. Their target settings resemble those of Group K due to their location

on potential ejecta material of the impact basin beneath adjacent mare, hence the possibility of similar causes of slumping. The variation in depths could be due to a higher amount of slumping in crater 2, which could stem from the possible origins of these craters: lower strength

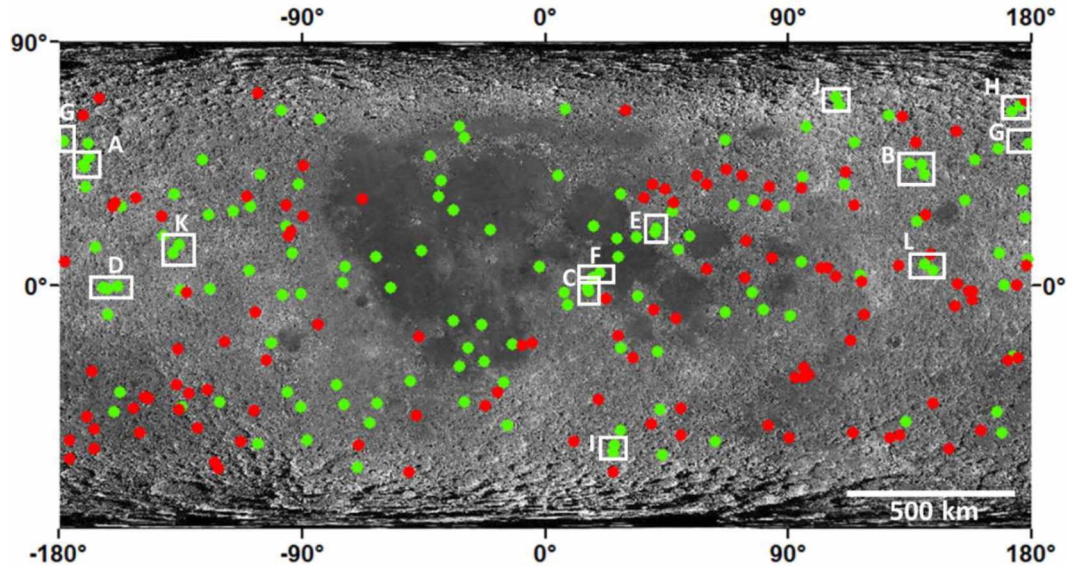


Figure 2.15. Mapped coordinates of craters that were eliminated from close-proximity analyses (red circles) and the craters that qualify for the analyses (green circles). The white boxes refer to the close-proximity crater groups that we used for the analyses. The white letter labels correspond to the respective groups listed in Table A-3 of Appendix A. The global lunar WAC mosaic has been used in the background. North is up.

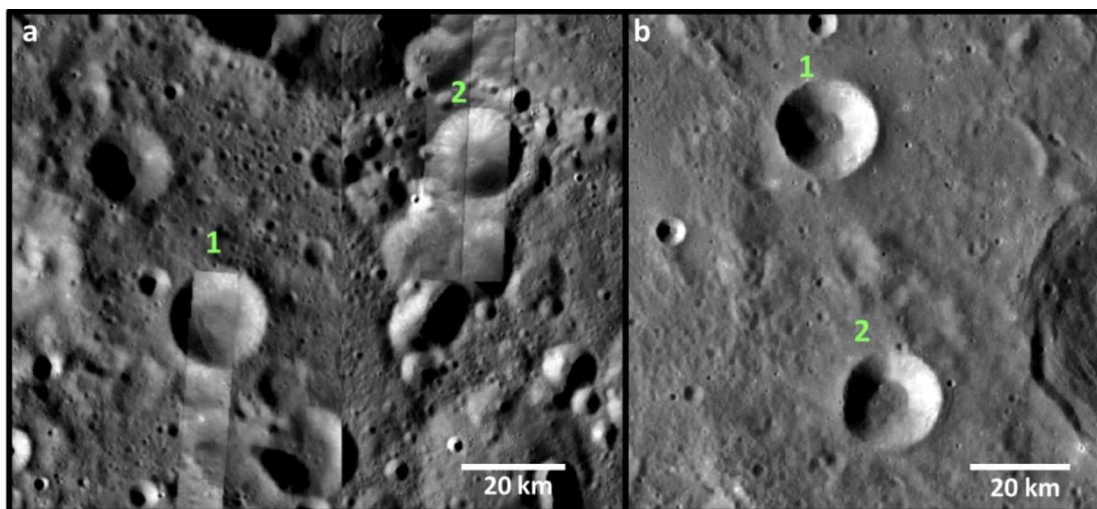


Figure 2.16. Wide Angle Camera images of craters that are alike in morphology and occur on uniformly sloping highland terrain devoid of any distinguishable topographic or other geologic differences. (a) Group G of simple craters that have similar rim-to-floor depths; NAC M1146003042R and NAC M1181309951R&L were used for the visibility of floors of craters 1 and 2, respectively. (b) Group C of craters with localized slumped material that statistically differ in rim-to-floor depths. The locations of their centers are marked in Figure 2.15, and their geometric details are listed in Table 2.2. North is up in both images.

of the target material that resulted in more slumping syn- or post-crater formation, or a more abrupt, obscured topographic hindrance that enabled more slumping to destabilize the cavity. We identified three pairs and two triplets that contain craters with differing morphologies. For one triplet (Group D), we observed the highland terrains of the simple crater to be gradually sloping and those associated with the craters with localized slumps to be marked by slightly more abrupt topographic contacts (weathered terrace and peak ring of buried crater), which was a globally observed terrain correlation for these morphologies in our survey. One pair of craters was observed to be located along the highlands-mare boundary (Group E in Figure 2.17). Both craters are characterized with mare layering on their walls. However, the simple crater is located primarily on the highland surface that abruptly transitions to the mare on the east and west, whereas the crater with localized slumps is predominantly located on the mare surface. We hypothesize that some measure of the higher strength homogeneity of the highlands crust by virtue of being non-layered could have been responsible for a more stable transient cavity, thereby resulting in less slumping and a simple crater morphology, hence two neighboring craters with differing morphologies. For the second triplet (Group B in Figure 2.18b) and another pair (Group J in Figure 2.18a) of close proximity craters, it can be observed that the simple craters and those containing localized slumped material were formed on rugged, gradually sloping highland surface. Any prominent difference in the geology of the terrains is indistinguishable in the optical images. The rim of Crater 1 in Figure 2.18b appears to be elongated and intersecting the rim of a smaller, buried crater. This local topographic discontinuity might have played a role in triggering slumping during crater formation. However, we noticed similar terrain geology in the case of many simple craters (Figures 2.5a and 2.12d–2.12f). Thus, we suggest that differences in impactor properties may have caused the differences among crater morphologies in Groups B and J (see discussion on impactor properties in section 2.4.3).

A crater bearing localized slumps and a floor-fractured crater, separated by ~98 km, comprise the last crater pair (Figure 1.19; Group F in Table A-3). Both craters occur in Mare Tranquillitatis but the former (Dionysius) is a rayed crater with layering on its walls and was formed by an impact adjacent to the highlands-mare boundary, whereas the latter (Manners)

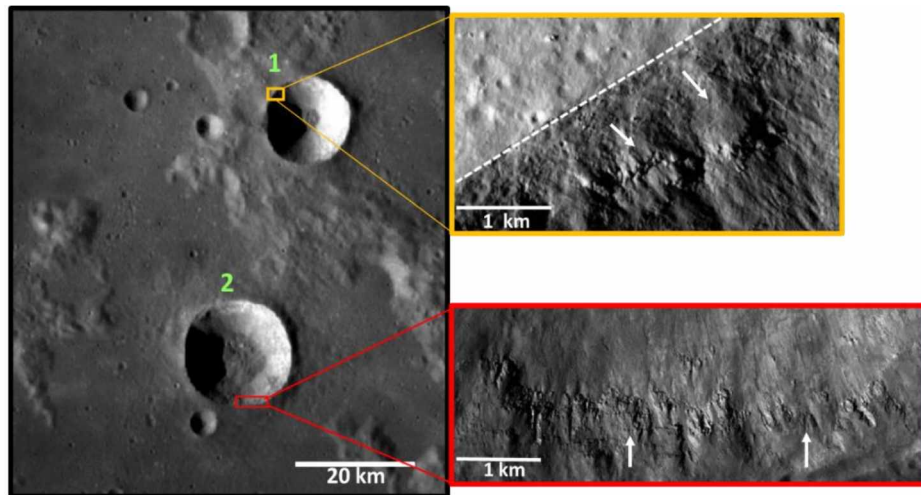


Figure 2.17. WAC images of close-proximity Group E: Simple crater (Crater 1) and crater with localized slumped material (Crater 2). The layering on both craters' walls is displayed in the Narrow Angle Camera insets: M1249268566L (yellow outline) for crater 1 and M104254490R (red outline) for crater 2. The white dashed line refers to the rim crest, and the white arrows indicate layering. North is up in all images.

was formed further in the middle of the mare near large arcuate rilles. Based on these observations, we hypothesize that the layering on the walls of Dionysius implies a terrain made of a thinner and more cohesive mare layer over a thicker and weaker highland layer (hence layering on walls) that influenced cavity collapse and excavated the mare layer as the bright ejecta rays (Hawke et al., 2004; Schmitt et al., 1967; Shoemaker & Hackman, 1962). Manners was also formed on the smooth surface of Mare Tranquillitatis but in the presence of arcuate rilles around the crater that are indicative of tectonic processes (McGill, 1971; Quaide, 1965). Additionally, fractures on the crater floor suggest the presence of subsurface magmatic intrusions (Jozwiak et al., 2012, 2015, 2017; Thorey & Michaut, 2014; Wilson & Head, 2018) that could have caused the annular fractures to develop, thereby resulting in the visible floor morphology syn- or post-crater formation.

Overall, we saw little evidence of morphological variations that could not be attributed to local terrain differences and would therefore suggest that an impactor property was responsible. However, the craters that qualified for the close-proximity analyses comprise only a small portion (11%) of the craters that we studied. It may be that uncommon extremes in impactor properties are necessary to produce easily identifiable differences in morphology of

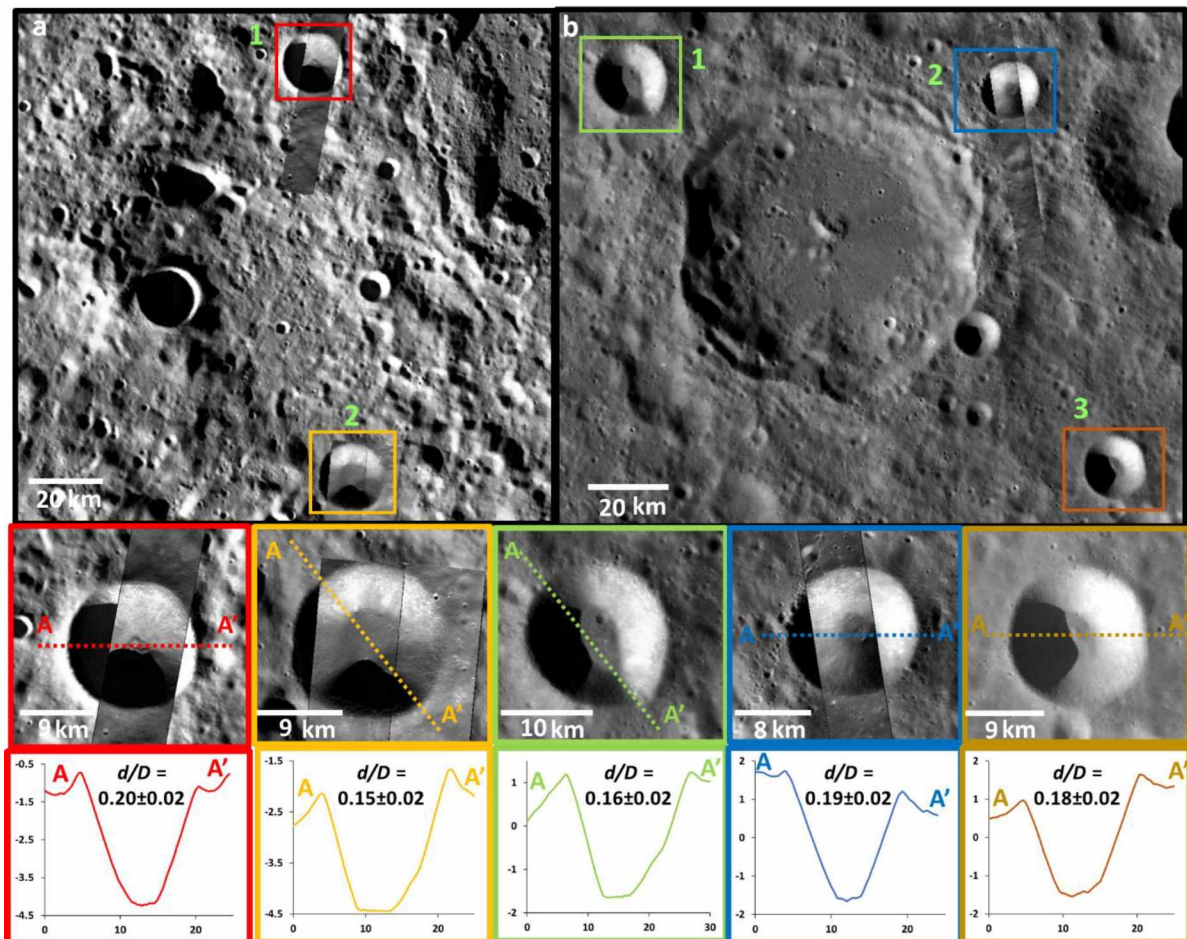


Figure 2.18. WAC images of groups of close-proximity craters that differ in morphology but whose geologic settings appear to be similar. (a) Group J: Simple crater (Crater 1) and crater with localized slumped material (Crater 2). Narrow Angle Camera (NAC) 1148856132R in Crater 1 and NAC 187557854 pairs in Crater 2 enable the visibility of the floor and walls. (b) Group B: Crater 1 contains localized slumped material. Crater 2 (NAC M1166245732L used for floor visibility) and Crater 3 are simple craters. The boxes around the craters refer to their magnified images at the bottom of (a) and (b). The slumping in Crater 2 of (a) and Crater 1 of (b) occurred along the southeast walls, as depicted by a slight change in wall slopes in their respective topographic profiles. North is up in all images.

craters occurring in similar settings (such as the craters in Groups B and J). The reader is referred to section 2.4.3 for a more elaborate discussion on impactor-caused variations.

2.4 Discussion

2.4.1 Mare-Highlands Differences

The number of representative craters observed for each of the seven crater morphologies sharply declines with increasing morphological complexity as summarized in

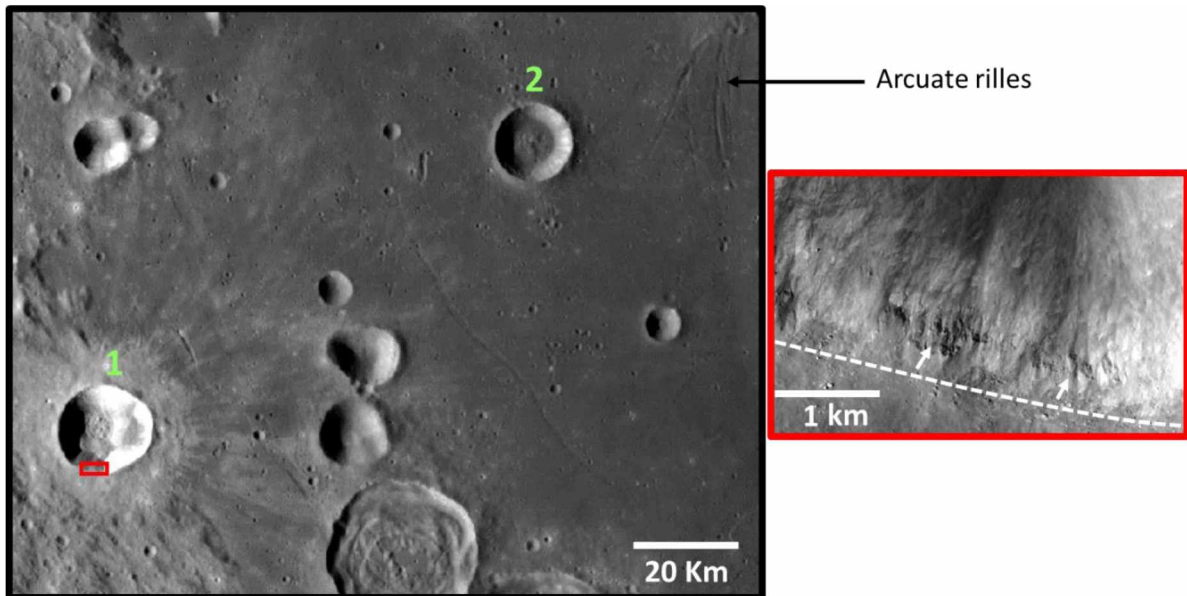


Figure 2.19. WAC image of a pair of close-proximity craters (Group F of Table A-3), which comprises a crater bearing localized slumped material (crater 1: Dionysius) that formed adjacent to the highlands-mare boundary and a floor-fractured crater (crater 2: Manners) that is located at a distance of ~98 km from Crater 1 in Mare Tranquillitatis. The locations of their centers are marked in Figure 2.15, and their geometric details are listed in Table 2.2. North is up in both images. Dionysius' walls are characterized with layering (indicated by white arrows in magnified NAC M1098737669L on the right that is outlined in red). Manners' floor morphology may have been influenced by subsurface magmatic intrusions.

Table 2.1. This could be a caveat behind the observation that simple craters (most abundant) are concentrated on the highlands, craters with localized slumps are scattered across the lunar surface, and the majority of the complex craters (least abundant) occur in the geographically limited, less-cratered, layered mare. However, these target associations on the Moon were also reported in the past. Additionally, our observations are analogous to previously reported findings on terrestrial craters (Dence, 1972): terrestrial complex craters occur at smaller diameters on layered sedimentary targets as compared to crystalline targets. Robbins and Hynek (2012) and Herrick and Hynek (2017) published a similar association of terraced craters

with layered volcanic flows in their studies of Martian simple-to-complex transition craters. The presence of layering on the walls of all craters in the mare reflects a significant contribution of a layered substrate to complex crater morphology. In one case of close-proximity analyses (Group E), despite layering on both craters' walls, the crater with localized slumps occurs

Table 2.2. Summarized details of close-proximity crater groups shown in Figures 2.16 through 2.19. The group numbers are as per the sequence in Table A-3.

Group	Figure	Crater Number	Crater Name	Latitude (°N)	Longitude (°E)	Diameter (km)	Morphology	d/D	STD (d/D)
G	2.16a	1	Cooper G	52.42	178.76	19.2	Simple crater	0.15	0.01
	2.16a	2	-	53.45	181.38	17.2	Simple crater	0.17	0.02
C	2.16b	1	Theon Senior	-0.81	15.42	17.6	Crater with localized slumps	0.19	0.01
	2.16b	2	Theon Junior	-2.41	15.79	17.7	Crater with localized slumps	0.17	0.01
E	2.17	1	Hill	20.91	40.81	15.7	Simple crater	0.21	0.01
	2.17	2	Carmichael	19.53	40.36	19.7	Crater with localized slumps	0.19	0.01
J	2.18a	1	Shwarzschild T	69.82	107.63	16.2	Simple crater	0.19	0.02
	2.18a	2	Shwarzschild Q	66.24	108.83	17.6	Crater with localized slumps	0.15	0.02
B	2.18b	1	-	44.88	134.77	19.4	Crater with localized slumps	0.16	0.02
	2.18b	2	-	44.52	139.37	15.3	Simple crater	0.20	0.02
	2.18b	3	Kurchatov X	41.18	140.07	16.8	Simple crater	0.18	0.02
F	2.19	1	Dionysius	2.77	17.29	18.0	Crater with localized slumps	0.16	0.01
	2.19	2	Manners	4.57	19.99	15.0	Floor-fractured crater	0.11	0.01

predominantly on the mare surface as compared to the simple crater whose surface is mostly highland terrain.

Basaltic lava flows erupted and deposited in layers over a period of at least 2 Ba (Hiesinger et al., 2000; Shoemaker & Hackman, 1962), filling the older highland impact basins to form the lunar mare (Head, 1975; Philpotts & Schnetzler, 1970; Smith et al., 1970; Taylor, 1989). Thus, the layers could be interleaved with regolith over hiatuses of nondeposition, resulting in heterogeneity in strength spatially and vertically, which may be a major factor in weakening the transient cavity and causing an earlier cavity collapse in comparison with highland craters (Cooper, 1977; Kalynn et al., 2013; Pike, 1980a; Quaide & Oberbeck, 1968; Roddy, 1977; Smith & Hartnell, 1978). Also, because the mare are more cohesive than the fractured highlands, the transient cavity is likely to undergo a more uniform collapse along

discrete faults, causing terracing at smaller crater sizes (Cintala et al., 1977). This theory is supported by our observation of an increasing number of terraces in the four representative mare craters with increasing distance from the highlands. Results of global studies on craters in various planetary bodies have reported an increase in number of terraces with increase in crater diameter in the simple-to-complex transition (Clayton et al., 2013; Osinski et al., 2018; Pike, 1977b, 1980a, 1988). Our survey is limited by only seven terraced craters. Therefore, a larger number of terraced transitional and complex craters (that can be included by expanding the transition diameter range) is required to draw a conclusion about the distribution of the number of terraces with respect to locations in the mare and change in crater size.

We also noticed a complex crater (Figure 2.13h) and two craters with localized slumps and terraces in the South Pole Aitken Basin, and a crater with localized slumps and terraces in the highlands to the north (Figure 2.13g). The walls of these craters exhibit layering, which we did not find on most highland crater walls. This may reflect cryptomare, thinner mare cover around the mare-highlands boundaries, mafic melt products, or layered mafic lower crustal material (e.g., Clegg-Watkins et al., 2016; Pieters et al., 2001). The extensive mare cover in the South-Pole Aitken Basin region and the scarcity of simple crater populations suggests a heterogeneity in lithology, strength, and/or topography that generated cavity-weakening forces, thus causing a higher number of transitional and complex craters to form. The lunar highlands crust is postulated to have been formed earlier than the mare (Wilhelms et al., 1987) by separation of plagioclase from a magma ocean followed by bulk crystallization, unlike the layered deposition of mare basalts (Smith et al., 1970; Taylor & Bence, 1975; Wood et al., 1970). This massive crust has been battered by impacts ever since its formation and is weaker owing to fracturing of rocks by shock waves and accumulation of impact ejecta and regolith over time. Though the highland material is less coherent than the younger mare, the homogeneity in its strength relative to the layered mare seems to be the primary factor in

stabilizing the transient cavity, resulting in simple craters at larger diameters than in the mare (Krüger et al., 2018; Osinski et al., 2018).

The heavily cratered highlands are characterized by a rough surface whose topographic variation around the craters in our database can reach ~4 km. We seldom encountered regions that are as flat as the mare. The simple craters are located on gradually sloping highland surfaces, subdued crater rims or terraces, or nearly flat highland terrain. Surfaces with sharp topographic breaks, such as well-preserved rims or terraces of craters, in the highlands favor the formation of most craters bearing localized slumped material. A transient cavity created on or against a sharp topographic boundary is more likely to be over steepened, causing the wall slope angle to exceed the angle of repose and thus undergo collapse in the modification stage (Aschauer & Kenkmann, 2017). As discussed before, without extensive analysis and sub-kilometer crater counting, we cannot assess the extent to which post-impact processes may have contributed to some of the slumped material in these craters. Conversely, the absence of a prominent topographic hindrance could lessen the probability of over steepening, thus driving the stabilization of the cavity and resulting in simple craters. These terrain correlations are demonstrated by close-proximity group D. The geologic settings of simple craters and of 35% of the craters bearing localized slumped material in the highlands appear to be similar, supported by our observations on terrains of close-proximity groups B, C, J, and K. The morphological differences in similar geologic settings could be the result of multiple causes: relatively older craters undergoing slumping post crater formation from seismic shaking (Brunetti et al., 2015; Izenberg, 2010; Kumar et al., 2013; Scaioni et al., 2018), abrupt topographic variation obscured by regolith or ejecta blankets of surrounding craters, unrecognized target properties (such as highland material of strength that is low enough to facilitate sliding under gravity), or impactor properties such as impact velocity, impactor size, and density. The similar target geology of craters in Groups B and J suggests the primary

involvement of impactor properties that result in the observed morphological differences among craters in each group (see section 2.4.3 for discussion on impactor properties).

The d/D s of several simple craters drop to as low as 0.14 because the 15–20-km size range spans the transition from simple to complex crater morphology, which means more unstable transient cavities and higher amounts of gravity-driven collapse. This suggests that the simple craters in this range must also have formed from larger amounts of slumping relative to smaller simple craters and hence the existence of simple craters with smaller d/D s that also overlap with the d/D s of transitional and complex craters. Ejecta from impacts on the crater rims could also have contributed to the shallow depths of some simple craters.

2.4.2 Unusually Deep Craters

We encountered six simple craters and one crater with localized slumps that are unusually deep ($d/D > 0.20$). The simple craters are in the highland regions that are within the coverage of ejecta blanket of mare basins. The crater with localized slumps occurs in the mare in the vicinity of the highlands-mare contact. Owing to the similarity in target settings, our emphasis is on target properties as the potential cause for the abnormally large crater depths. Although detailed investigation is required to ascertain the reasons for the large depths, we hypothesize two possible explanations:

2.4.2.1 Impact into a high-porosity target

The porosity in highland regions adjacent to most mare has been observed to be higher than average (~17–20%) in the lunar surface porosity map generated by Besserer et al. (2014) from the Gravity Recovery and Interior Laboratory (GRAIL) bouguer anomaly data (Zuber et al., 2013). The high porosity values are also evident from the red-orange regions on the map in Figure 2.20. Because most mare fill large impact basins, fracturing by impact generated shock waves and deposition of impact ejecta possibly produced the 17–20% porosity around the basin margins. Numerical simulations (Housen & Holsapple, 2000; Milbury et al., 2015;

Wünnemann et al., 2006) and hypervelocity impact experiments (Housen et al., 1999; Housen & Holsapple, 2003; Housen & Voss, 2001) on materials with significant porosity, hence low crushing strength, have revealed that a certain proportion of the impact energy is spent in crushing out the pore space, thereby causing compaction of target material and the generation of a narrow, deep transient cavity. The creation of unusually deep crater volume predominately by compaction and to a smaller extent by excavation of material, however, was reported to occur for impact on surfaces with porosity values greater than 35% (Housen et al., 1999; Housen & Holsapple, 2012; Prieur et al., 2017).

The global lunar porosity values have been derived by averaging over few hundreds of kilometers, such that it is conceivable that local porosity could vary considerably about the mean. Therefore, it is possible that impacts into only the highest-porosity spots produced the identified unusually deep craters. Local variability of porosity is also a potential explanation for why not every simple crater located in the high-porosity (17–20%) regions (red-orange shaded regions in Figure 1.20) or even in the maximum porosity (~20%) terrains (red areas in Figure 2.20 in closest proximity to mare margins) is unusually deep. We are not proposing impact cratering completely dominated by compaction, with no material ejected; such processes occur on targets with anomalously high porosities (80–97%) as simulated by Housen and Holsapple (2003). More detailed investigation is required in probing the factors behind the large depths of the craters and determining the local porosities around these craters. However, because of the strong association of the unusually deep craters with high-porosity terrains, we propose that locally high porosity influenced the formation mechanism of these craters.

2.4.2.2 The highlands are more coherent in these locations and less susceptible to minor slumping of the transient cavity

Mafic intrusions filled the cracks in the highlands terrain around the mare basin margins (Gong et al., 2016; Kiefer, 2013), thereby enhancing the coherence of the highlands, similar to

the proposed contribution of ultramafic lithologies to the formation of unusually deep simple craters in Utopia Planitia on Mars (Boyce et al., 2006). However, this hypothesis is not consistent with the observation that the craters are occurring in a high-porosity terrain. Therefore, we favor the hypothesis that attributes the larger-than-normal depths to impact cratering on high-porosity terrain.

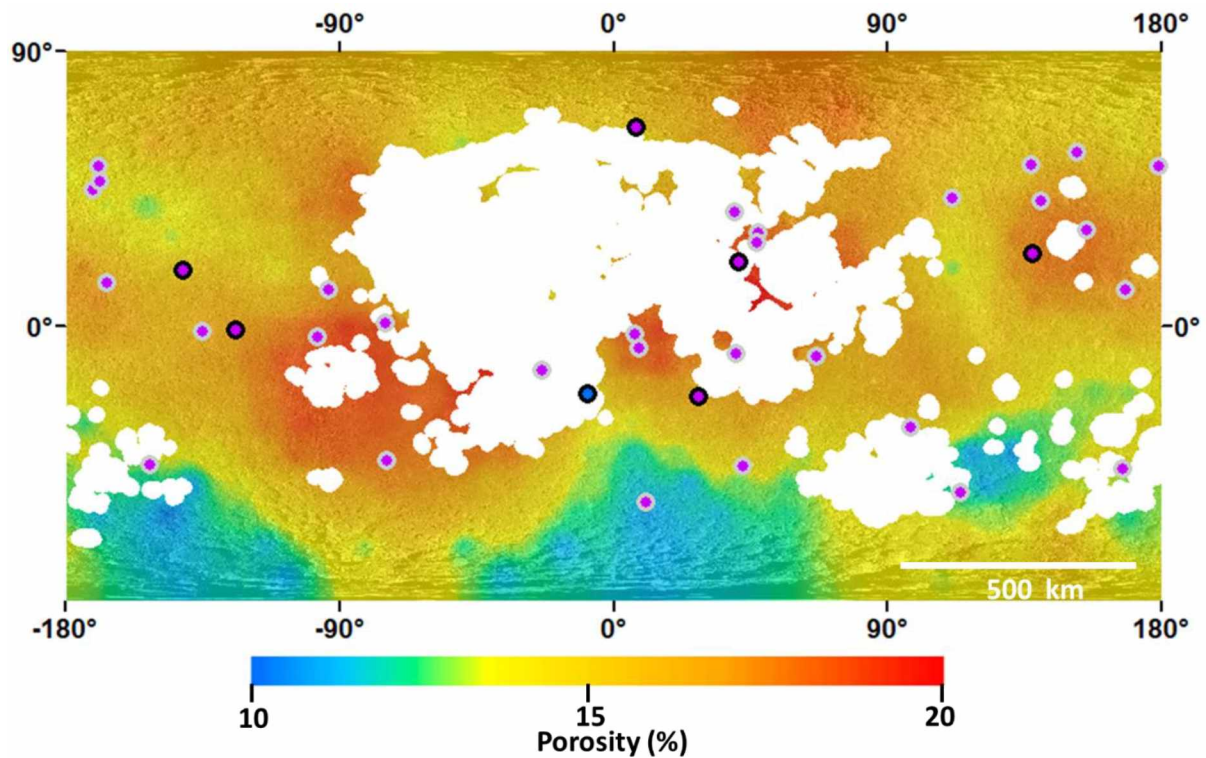


Figure 2.20. Mapped locations of simple craters with impact melt deposits (purple circles outlined in gray) and unusually deep craters (circles outlined in black) on the lunar surface porosity distribution map in Besserer et al. (2014). The white mask over the map was added to exclude the mare basalts from the porosity model.

2.4.3 Potential Impactor-Caused Variations

For a crater size range of 15–20 km corresponding to a narrow range in impact energy, we looked for signatures of various other impactor parameters that could significantly contribute to crater morphologies. The only direct indication of the influence of one impactor property on crater morphology within the lunar simple-to-complex transition zone was provided by an elliptical crater (Figure A-3(d) of Appendix A) that suggests a highly oblique impact at an angle of 12° or less (Bottke et al., 2000; Elbeshausen et al., 2013; Gault &

Wedekind, 1978; Herrick & Hessen, 2006). Both simple craters and 35% of craters with localized slumps are in similar highland terrains that are characteristic of flat or gradually sloping surfaces or degraded rims of craters. Close-proximity groups B and J further exemplify that nearest neighbor craters in these settings differ in morphologies. Morphological variations of craters in targets with similar properties can be potentially attributed to large variations in impactor parameters such as impactor size and velocity. From experimental impacts, Schultz (1988) and Barnouin et al. (2011) deduced that lower impact velocities can produce deeper transient cavities that collapse to form more shallow craters that can possibly have the form of transitional or complex craters. Silber et al. (2017) modeled craters of similar sizes around the lunar simple-to-complex transition diameter range by varying impactor size and velocity and observed that large/slow impactors result in an early onset of complex craters as compared to small/fast impactors if acoustic fluidization is the primary weakening mechanism. Therefore, it is possible that the craters with localized slumps occurring in similar targets as simple craters could have formed by projectiles that were larger and/or slower as compared to the impactors that formed the simple craters.

We could only identify impact melts on the floors of 32 out of 109 simple craters whose floors were visible in the NAC images. This is a small subset of simple craters that are scattered across the lunar highland surface. Their melt deposits co-occur with debris on the floors. There might be unidentifiable melt deposits potentially hidden beneath the slumped material on the floors of several of the remaining simple craters. Both higher target porosity (Wünnemann et al., 2008) and impact velocity (Ahrens & O'Keefe, 1977; Pierazzo et al., 1997) have been shown to result in higher melt production. A combined modeling and observational study by Silber et al. (2018) found that, keeping the target lithology constant, craters in the simple-to-complex transition size range produced by simulations on impacts of projectiles traveling at velocities of around 10–20 km/s contained higher volumes of impact melt than those formed

by lower velocity impacts. These melt volumes were modeled by Silber et al. (2018) to be similar to those evaluated by (Plescia et al., 2014) in lunar craters of diameter greater than 10 km. Although additional impactor parameter variations could contribute to the melt deposits, based on the work of Silber et al. (2018), we hypothesize that the 32 craters that contain visible impact melt deposits may have formed from higher velocity impacts relative to the craters whose floors are devoid of melt deposits. The calculation of volumes of impact melts in our craters would be able to constrain the range of impact velocity on comparison with the impact melt simulation results of Silber et al. (2018).

2.4.4 Comparison with Other Planets

We compared the results from the geologic investigation of our craters with the published results on craters within the simple-to-complex transition on Mercury and Mars. The simple-to-complex transition diameter range (15–20 km) for the Moon is at a larger diameter than on Mercury (~10–12 km from Barnouin et al. (2012); Pike (1988); Susorney et al., 2016) and Mars (~5–9 km from Garvin and Frawley (1998); Pike (1980a); Robbins and Hynes (2012)). This is primarily due to the lower value of gravitational acceleration of the Moon (1.6 m/s^2) relative to Mercury and Mars (3.7 m/s^2). On Mercury, the depths of craters in both smooth plains and the cratered terrain were observed to be similar (Susorney et al., 2016). The smaller age difference and possible volcanic origin of both the cratered terrain and smooth plains of Mercury may contribute to similar depths of craters in the two terrains (Susorney et al. (2016)), and these two terrain types are not analogous to the lunar mare-highlands differences.

Our study is similar in design to that of Herrick and Hynes (2017), which analyzed the geology of Martian craters within the simple-to-complex transition size range of 7–9 km for possible target or impactor influences on the crater morphologies. That study found compelling associations between crater morphology and geologic settings. The largest simple craters on Mars (and thus the deepest in the 7–9 km diameter range) occur preferentially in areas that are

likely to be vertically homogenous and well consolidated, such as selected areas of the northern plains (Boyce et al., 2006). This observation is similar to the findings of Robbins and Hynek (2012) for Martian craters in the simple-to-complex transition and also corroborates our inference that simple craters in the lunar simple-to-complex transition are favored by terrains (non-layered highlands) that are vertically more homogeneous in strength than the layered targets (mare). The complex and transitional craters preferentially occur in places that are likely to have less consolidated material in the subsurface. Terracing in this diameter range corresponded with areas thought likely to be composed of layered volcanic flows (Herrick & Hynek, 2017), analogous to our observations of lunar mare craters.

2.5 Conclusions

We compiled a database of 244 well-preserved lunar impact craters in the simple-to-complex transition diameter range of 15–20 km. Morphological classification of the craters was performed using the global LROC WAC mosaic, high-resolution NAC data, and topographic profiles from LOLA gridded data processed to a spatial resolution of 512 ppd. We studied the geology of the terrains that favor certain morphologies in the highlands and mare. We also conducted close-proximity analyses to look for impactor-caused differences in appearance of craters located in similar geologic settings. We drew the following conclusions: [1] The mare, composed of layered basaltic flows, experience the onset of complex craters at smaller diameters as compared to the highlands, which is consistent with published literature on layered, hence weaker targets (Cintala et al., 1977; Cooper, 1977; Dence, 1972; Pike, 1980a; Quaide & Oberbeck, 1968; Roddy, 1977; Senft & Stewart, 2008; Smith & Hartnell, 1978; Stewart & Valiant, 2006). We propose that the layering on the walls of the craters creates strength heterogeneities, perhaps regolith layers between lava flows, that enable complex crater

formation. The higher coherence of mare basalts also enables a more pervasive collapse along discrete faults resulting in earlier onset of terraces, as suggested by Cintala et al. (1977).

[2] Although weaker and more fractured than the mare, the highland terrain lacks layering, with exceptions of thin mare cover around the mare-highlands boundary. This is probably the reason that as compared to the mare, the highlands have a significantly smaller percentage of complex craters within the 15–20-km diameter range. Within the highlands, regions that are characterized by homogeneity in topography favor the formation of simple craters, whereas impacts on places with sharp topographic discontinuities experience oversteepening of the cavity, thus destabilizing it and resulting in craters with localized slumps. Without extensive additional work, we cannot rule out the possibility that some of the craters we classified as having localized slumped material may have been simple craters immediately post impact, with slumping occurring at some later date.

[3] We observed six unusually deep simple craters and one unusually deep crater with localized slumped material. These craters preferentially occur in the immediate vicinity of the mare-highlands contacts within the regions covering the ejecta blanket of mare basins. Our favored hypothesis is that these craters form by impact in high-porosity areas associated with the rim and ejecta materials of the large basins that contain the mare.

[4] The generation of visible impact melt on the floors of several simple craters is potentially a result of impacts at velocities ranging from 10 to 20 km/s (Silber et al., 2018). Also, the similar geologic settings of two close-proximity groups, each comprising craters that differ in morphologies, are indicative of the potential contribution of large variations in impactor properties. For example, larger projectiles traveling at lower velocities could have produced transitional craters as compared to smaller and faster objects that generated similar-sized simple craters. This inference is followed by the caveat that there may be unobserved near-

surface differences in target attributes overlain by ejecta/regolith and/or the wall slumping could be a result of modification post-crater formation.

2.6 Acknowledgements

This work was funded by a grant to R. R. H. from the NASA Lunar Advanced Science and Exploration Research (LASER) Program. We are thankful to an anonymous reviewer, Tim Krüger, and the Associate Editor for their constructive comments that helped in improving the manuscript.

2.7 References

- Ahrens, T. J., & O'Keefe, J. D. (1977). Equations of state and impact-induced shock-wave attenuation on the moon. In D. J. Roddy, R. Pepin, & R. Merrill (Eds.), *Impact and explosion cratering: Planetary and terrestrial implications*, (pp. 639–656). New York: Pergamon Press.
- Arthur, D., Agnieray, A. P., Horvath, R. A., Wood, C., & Chapman, C. (1964). The system of lunar craters, quadrant I, *Communications of the Lunar and Planetary The Laboratory*, 2, 71-78.
- Aschauer, J., & Kenkmann, T. (2017). Impact cratering on slopes. *Icarus*, 290, 89–95. <https://doi.org/10.1016/j.icarus.2017.02.021>
- Bandeira, L., Salamuniccar, G., & Hare, T. (2014). Global crater catalogues of the Moon, Mars and Phobos. Paper presented at 45th Lunar and Planetary Science Conference, Houston, TX.

- Barnouin, O., Ernst, C., Heinick, J., Sugita, S., Cintala, M., Crawford, D., & Matsui, T. (2011). Experimental results investigating the impact velocity effects on crater growth and the transient crater diameter-to-depth ratio. Paper presented at 42nd Lunar and Planetary Science Conference.
- Barnouin, O. S., Zuber, M. T., Smith, D. E., Neumann, G. A., Herrick, R. R., Chappelow, J. E., et al. (2012). The morphology of craters on Mercury: Results from MESSENGER flybys. *Icarus*, 219(1), 414–427. <https://doi.org/10.1016/j.icarus.2012.02.029>
- Besserer, J., Nimmo, F., Wieczorek, M. A., Weber, R. C., Kiefer, W. S., McGovern, P. J., et al. (2014). GRAIL gravity constraints on the vertical and lateral density structure of the lunar crust. *Geophysical Research Letters*, 41, 5771–5777. <https://doi.org/10.1002/2014GL060240>
- Bottke, W. F. Jr., Love, S. G., Tytell, D., & Glotch, T. (2000). Interpreting the elliptical crater populations on Mars, Venus, and the Moon. *Icarus*, 145(1), 108–121. <https://doi.org/10.1006/icar.1999.6323>
- Boyce, J. M., Mougini-Mark, P. J., Garbeil, H., & Tornabene, L. L. (2006). Deep impact craters in the Isidis and southwestern Utopia Planitia regions of Mars: High target material strength as a possible cause. *Geophysical Research Letters*, 33, L06202. <https://doi.org/10.1029/2005GL024462>
- Bray, V. J., Collins, G. S., Morgan, J. V., & Schenk, P. M. (2008). The effect of target properties on crater morphology: Comparison of central peak craters on the Moon and Ganymede. *Meteoritics & Planetary Science*, 43(12), 1979–1992. <https://doi.org/10.1111/j.1945-5100.2008.tb00656.x>
- Brunetti, M. T., Xiao, Z., Komatsu, G., Peruccacci, S., & Guzzetti, F. (2015). Large rock slides in impact craters on the Moon and Mercury. *Icarus*, 260, 289–300. <https://doi.org/10.1016/j.icarus.2015.07.014>

- Cintala, M., Wood, C., & Head, J. (1977). The effects of target characteristics on fresh crater morphology—Preliminary results for the Moon and Mercury. Paper presented at 8th Lunar and Planetary Science Conference Proceedings, Houston, TX.
- Cintala, M. J., & Grieve, R. A. (1998). Scaling impact melting and crater dimensions: Implications for the lunar cratering record. *Meteoritics & Planetary Science*, 33(4), 889–912. <https://doi.org/10.1111/j.1945-5100.1998.tb01695.x>
- Clayton, J., Osinski, G., Tornabene, L., Kalynn, J., & Johnson, C. (2013). Fresh transitional lunar impact craters. Paper presented at 44th Lunar and Planetary Science Conference, Houston, TX.
- Clegg-Watkins, R., Jolliff, B., Petro, N., & Lawrence, S. (2016). The distribution of mare and cryptomare in the South Pole-Aitken Basin: New perspectives from multiple datasets. Paper presented at 47th Lunar and Planetary Science Conference, Houston, TX.
- Collins, G. S. (2014). Terraced crater wall (mass wasting). In *Encyclopedia of planetary landforms*, Edited, pp. 1–6, Springer, New York, NY, https://doi.org/10.1007/978-1-4614-9213-9_361-1
- Collins, G. S., Kenkmann, T., Osinski, G., & Wünnemann, K. (2008). Mid-sized complex crater formation in mixed crystalline-sedimentary targets: Insight from modeling and observation. *Meteoritics & Planetary Science*, 43(12), 1955–1977. <https://doi.org/10.1111/j.1945-5100.2008.tb00655.x>
- Cooper, H. (1977). A summary of explosion cratering phenomena relevant to meteor impact events. In D. J. Roddy, R. O. Pepin, & R. B. Merrill (Eds.), *Impact and explosion cratering*, (pp. 11–44). New York: Pergamon Press.
- Croft, S. K. (1985). The scaling of complex craters. *Journal of Geophysical Research*, 90(S02), C828–C842. <https://doi.org/10.1029/JB090iS02p0C828>

- Dence, A. (1972). The nature and significance of terrestrial impact structures. Paper presented at 24th International Geological Congress, Section 15, Montreal, Canada.
- Elbeshausen, D., Wünnemann, K., & Collins, G. S. (2009). Scaling of oblique impacts in frictional targets: Implications for crater size and formation mechanisms. *Icarus*, 204(2), 716–731. <https://doi.org/10.1016/j.icarus.2009.07.018>
- Elbeshausen, D., Wünnemann, K., & Collins, G. S. (2013). The transition from circular to elliptical impact craters. *Journal of Geophysical Research: Planets*, 118, 2295–2309. <https://doi.org/10.1002/2013JE004477>
- Fassett, C. I., Head, J. W., Smith, D. E., Zuber, M. T., & Neumann, G. A. (2011). Thickness of proximal ejecta from the Orientale Basin from Lunar Orbiter Laser Altimeter (LOLA) data: Implications for multi-ring basin formation. *Geophysical Research Letters*, 38, L17201. <https://doi.org/10.1029/2011GL048502>
- Fink, J., Greeley, R., & Gault, D. (1982). Impact cratering experiments in Bingham materials and the morphology of craters on Mars and Ganymede. Paper presented at 12th Lunar and Planetary Science Conference Proceedings, Houston, TX.
- Garvin, J. B., & Frawley, J. J. (1998). Geometric properties of Martian impact craters: Preliminary results from the Mars Orbiter Laser Altimeter. *Geophysical Research Letters*, 25(24), 4405–4408. <https://doi.org/10.1029/1998GL900177>
- Gault, D. E., & Wedekind, J. A. (1978). Experimental studies of oblique impact. Paper presented at 9th Lunar and Planetary Science Conference Proceedings, Houston, TX.
- Gong, S., Wieczorek, M. A., Nimmo, F., Kiefer, W. S., Head, J. W., Huang, C., et al. (2016). Thicknesses of mare basalts on the Moon from gravity and topography. *Journal of Geophysical Research: Planets*, 121, 854–870. <https://doi.org/10.1002/2016JE005008>

- Greeley, R., Fink, J., Snyder, D., Gault, D., Guest, J., & Schultz, P. (1980). Impact cratering in viscous targets—Laboratory experiments. Paper presented at 11th Lunar and Planetary Science Conference Proceedings, Houston, TX.
- Grieve, R. A., Dence, M., & Robertson, P. (1977). Cratering processes—As interpreted from the occurrence of impact melts. Paper presented at Impact and Explosion Cratering: Planetary and Terrestrial Implications, Flagstaff, AZ.
- Hargitai, H., & Öhman, T. (2014). Complex crater. In Encyclopedia of planetary landforms, Edited, pp. 1–17, Springer, New York, NY. https://doi.org/10.1007/978-1-4614-9213-9_429-2
- Hawke, B. R., Blewett, D. T., Lucey, P. G., Smith, G., Bell, J. F. III, Campbell, B. A., & Robinson, M. S. (2004). The origin of lunar crater rays. *Icarus*, 170(1), 1–16. <https://doi.org/10.1016/j.icarus.2004.02.013>
- Head, J. (1975). Lunar mare deposits: Areas, volumes, sequence, and implication for melting in source areas. Paper presented at Conference on Origins of Mare Basalts and their Implications for Lunar Evolution, Lunar Science Institute, Houston, TX.
- Herrick, R. R. (2014). Elliptical crater (oblique impact). In Encyclopedia of planetary landforms, Edited, pp. 1–6, Springer, New York, NY. https://doi.org/10.1007/978-1-4614-9213-9_135-2
- Herrick, R. R., & Forsberg-Taylor, N. K. (2003). The shape and appearance of craters formed by oblique impact on the Moon and Venus. *Meteoritics & Planetary Science*, 38(11), 1551–1578. <https://doi.org/10.1111/j.1945-5100.2003.tb00001.x>
- Herrick, R. R., & Hesse, K. K. (2006). The planforms of low-angle impact craters in the northern hemisphere of Mars. *Meteoritics & Planetary Science*, 41(10), 1483–1495. <https://doi.org/10.1111/j.1945-5100.2006.tb00431.x>

- Herrick, R. R., & Hynek, B. M. (2017). Investigating target versus impactor influences on Martian crater morphology at the simple-complex transition. *Meteoritics & Planetary Science*, 52(8), 1722–1743. <https://doi.org/10.1111/maps.12884>
- Herrick, R. R., & Lyons, S. N. (1998). Inversion of crater morphometric data to gain insight on the cratering process. *Meteoritics & Planetary Science*, 33(1), 131–143. <https://doi.org/10.1111/j.1945-5100.1998.tb01615.x>
- Herrick, R. R., & Sharpton, V. L. (2000). Implications from stereo-derived topography of Venusian impact craters. *Journal of Geophysical Research*, 105(E8), 20,245–20,262. <https://doi.org/10.1029/1999JE001225>
- Hiesinger, H., Jaumann, R., Neukum, G., & Head, J. W. (2000). Ages of mare basalts on the lunar nearside. *Journal of Geophysical Research*, 105(E12), 29,239–29,275. <https://doi.org/10.1029/2000JE001244>
- Holsapple, K. A. (1993). The scaling of impact processes in planetary sciences. *Annual Review of Earth and Planetary Sciences*, 21(1), 333–373. <https://doi.org/10.1146/annurev.ea.21.050193.002001>
- Holsapple, K. A., & Schmidt, R. M. (1982). On the scaling of crater dimensions: 2. Impact processes. *Journal of Geophysical Research*, 87(B3), 1849–1870. <https://doi.org/10.1029/JB087iB03p01849>
- Housen, K. R., & Holsapple, K. A. (2000). Numerical simulations of impact cratering in porous materials. Paper presented at 31st Lunar and Planetary Science Conference, Houston, TX.
- Housen, K. R., & Holsapple, K. A. (2003). Impact cratering on porous asteroids. *Icarus*, 163(1), 102–119. [https://doi.org/10.1016/S0019-1035\(03\)00024-1](https://doi.org/10.1016/S0019-1035(03)00024-1)
- Housen, K. R., & Holsapple, K. A. (2012). Craters without ejecta. *Icarus*, 219(1), 297–306. <https://doi.org/10.1016/j.icarus.2012.02.030>

- Housen, K. R., Holsapple, K. A., & Voss, M. E. (1999). Compaction as the origin of the unusual craters on the asteroid Mathilde. *Nature*, 402(6758), 155–157. <https://doi.org/10.1038/45985>
- Housen, K. R., & Voss, M. E. (2001). Ejecta from impact craters in porous materials. Paper presented at 32nd Lunar and Planetary Science Conference, Houston, TX.
- Howard, K. A. (1974). Fresh lunar impact craters—Review of variations with size. Paper presented at 2nd Lunar and Planetary Science Conference Proceedings, Houston, TX.
- Howard, K. A., & Wilshire, H. G. (1973). Flows of impact melt at lunar craters. Paper presented at 4th Lunar and Planetary Science Conference, Houston, TX.
- Izenberg, N. (2010). Seismic shaking experiments in milligravity environments. Paper presented at Next-Generation Suborbital Researchers Conference, Boulder, Colorado.
- Jozwiak, L., Head, J. III, Neumann, G., & Wilson, L. (2017). Observational constraints on the identification of shallow lunar magmatism: Insights from floor-fractured craters. *Icarus*, 283, 224–231. <https://doi.org/10.1016/j.icarus.2016.04.020>
- Jozwiak, L. M., Head, J. W., & Wilson, L. (2015). Lunar floor-fractured craters as magmatic intrusions: Geometry, modes of emplacement, associated tectonic and volcanic features, and implications for gravity anomalies. *Icarus*, 248, 424–447. <https://doi.org/10.1016/j.icarus.2014.10.052>
- Jozwiak, L. M., Head, J. W., Zuber, M. T., Smith, D. E., & Neumann, G. A. (2012). Lunar floor-fractured craters: Classification, distribution, origin and implications for magmatism and shallow crustal structure. *Journal of Geophysical Research*, 117, E11005. <https://doi.org/10.1029/2012JE004134>
- Kalynn, J., Johnson, C. L., Osinski, G. R., & Barnouin, O. (2013). Topographic characterization of lunar complex craters. *Geophysical Research Letters*, 40, 38–42. <https://doi.org/10.1029/2012GL053608>

- Kenkmann, T., Collins, G. S., & Wünnemann, K. (2012). The modification stage of crater formation. In G. R. Osinski, & E. Pierazzo (Eds.), *Impact cratering: Processes and products*, (pp. 60–75). Oxford, UK: John Wiley.
- Kenkmann, T., & Poelchau, M. H. (2009). Low-angle collision with Earth: The elliptical impact crater Matt Wilson, Northern Territory, Australia. *Geology*, 37(5), 459–462. <https://doi.org/10.1130/G25378A.1>
- Kenkmann, T., Reimold, W., Khirfan, M., Salameh, E., Konsul, K., Lehmann, T., & Khoury, H. (2009). The impact crater Jebel Waqf as Suwwan in Jordan: Effects of target heterogeneity and impact obliquity on central uplift formation. Paper presented at 40th Lunar and Planetary Science Conference, Houston, TX.
- Kiefer, W. S. (2013). Gravity constraints on the subsurface structure of the Marius Hills: The magmatic plumbing of the largest lunar volcanic dome complex. *Journal of Geophysical Research: Planets*, 118, 733–745. <https://doi.org/10.1029/2012JE004111>
- Kneissl, T., van Gasselt, S., & Neukum, G. (2010). New software tool for map-projection-independent crater size-frequency determination in ArcGIS. Paper presented at 41st Lunar and Planetary Science Conference, Houston, TX.
- Krüger, T., Hergarten, S., & Kenkmann, T. (2018). Deriving morphometric parameters and the simple-to-complex transition diameter from a new, high resolution database of fresh lunar impact craters ≥ 3 km. *Journal of Geophysical Research: Planets*, 123, 2667–2690. <https://doi.org/10.1029/2018JE005545>
- Kumar, P. S., Keerthi, V., Kumar, A. S., Mustard, J., Gopala Krishna, B., Ostrach, L. R., et al. (2013). Gullies and landslides on the Moon: Evidence for dry-granular flows. *Journal of Geophysical Research: Planets*, 118, 206–223. <https://doi.org/10.1002/jgre.20043>
- Le Feuvre, M., & Wieczorek, M. A. (2008). Nonuniform cratering of the terrestrial planets. *Icarus*, 197(1), 291–306. <https://doi.org/10.1016/j.icarus.2008.04.011>

- Losiak, A., Wilhelms, D., Byrne, C., Thaisen, K., Weider, S., Kohout, T., et al. (2009). A new lunar impact crater database. Paper presented at 40th Lunar and Planetary Science Conference, Houston, TX.
- McGetchin, T. R., Settle, M., & Head, J. (1973). Radial thickness variation in impact crater ejecta: Implications for lunar basin deposits. *Earth and Planetary Science Letters*, 20(2), 226–236. [https://doi.org/10.1016/0012-821X\(73\)90162-3](https://doi.org/10.1016/0012-821X(73)90162-3)
- McGill, G. E. (1971). Attitude of fractures bounding straight and arcuate lunar rilles. *Icarus*, 14(1), 53–58. [https://doi.org/10.1016/0019-1035\(71\)90101-1](https://doi.org/10.1016/0019-1035(71)90101-1)
- Melosh, H. J. (1977). Crater modification by gravity—A mechanical analysis of slumping. Paper presented at Impact and Explosion Cratering: Planetary and Terrestrial Implications, Flagstaff, AZ.
- Melosh, H. J. (1989a). Cratering mechanics: Modification stage. In *Impact cratering: A geologic process*, pp. 126–161, Oxford University Press, New York.
- Melosh, H. J. (1989b). Multiring basins. In *Impact cratering: A geologic process*, pp. 163–183, Oxford University Press, New York.
- Melosh, H. J. (1989c). Scaling of crater dimensions. In *Impact cratering: A geologic process*, pp. 112–125, Oxford University Press, New York.
- Melosh, H. J., & Ivanov, B. (1999). Impact crater collapse. *Annual Review of Earth and Planetary Sciences*, 27(1), 385–415. <https://doi.org/10.1146/annurev.earth.27.1.385>
- Milbury, C., Johnson, B., Melosh, H., Collins, G., Blair, D., Soderblom, J., et al. (2015). Preimpact porosity controls the gravity signature of lunar craters. *Geophysical Research Letters*, 42, 9711–9716. <https://doi.org/10.1002/2015GL066198>
- Osinski, G. R., Silber, E. A., Clayton, J., Grieve, R. A., Hansen, K., Johnson, C. L., et al. (2018). Transitional impact craters on the Moon: Insight into the effect of target lithology

- on the impact cratering process. *Meteoritics & Planetary Science*.
<https://doi.org/10.1111/maps.13226>
- Pearce, S. J., & Melosh, H. (1986). Terrace width variations in complex lunar craters. *Geophysical Research Letters*, 13(13), 1419–1422.
<https://doi.org/10.1029/GL013i013p01419>
- Philpotts, J. A., & Schnetzler, C. (1970). Potassium, rubidium, strontium, barium, and rare-earth concentrations in lunar rocks and separated phases. *Science*, 167(3918), 493–495.
<https://doi.org/10.1126/science.167.3918.493>
- Pierazzo, E., Vickery, A., & Melosh, H. (1997). A reevaluation of impact melt production. *Icarus*, 127(2), 408–423. <https://doi.org/10.1006/icar.1997.5713>
- Pieters, C., Head, J., Gaddis, L., Jolliff, B., & Duke, M. (2001). Rock types of South Pole-Aitken basin and extent of basaltic volcanism. *Journal of Geophysical Research*, 106(E11), 28,001–28,022. <https://doi.org/10.1029/2000JE001414>
- Pike, R. J. (1974). Depth/diameter relations of fresh lunar craters: Revision from spacecraft data. *Geophysical Research Letters*, 1(7), 291–294.
<https://doi.org/10.1029/GL001i007p00291>
- Pike, R. J. (1977a). Apparent depth/apparent diameter relation for lunar craters. Paper presented at 8th Lunar and planetary science conference proceedings, Houston, TX.
- Pike, R. J. (1977b). Size-dependence in the shape of fresh impact craters on the Moon. In D. J. Roddy, R. Pepin, & R. Merrill (Eds.), *Impact and explosion cratering: Planetary and terrestrial implications*, (pp. 489–509). New York: Pergamon Press.
- Pike, R. J. (1980a). Control of crater morphology by gravity and target type—Mars, Earth, Moon. Paper presented at 11th Lunar and Planetary Science Conference Proceedings, Houston, TX.

- Pike, R. J. (1980b). Geometric interpretation of lunar craters, USGS Professional Paper Rep. 1046-C, C1-C77 pp, US Govt. Print. Off., Washington.
- Pike, R. J. (1981). Target-dependence of Crater depth on the Moon. Paper presented at 12th Lunar and Planetary Science Conference, Houston, TX.
- Pike, R. J. (1988). Geomorphology of impact craters on Mercury. In F. Vilas, C. Chapman, & M. Matthews (Eds.), *Mercury*, (pp. 165–273). Tucson, AZ: University of Arizona Press.
- Plescia, J., Barnouin, O., & Stopar, J. (2014), Impact melt volumes in simple lunar craters: Constraints on modeling. Paper presented at 45th Lunar and Planetary Science Conference, Houston, TX.
- Plescia, J. B. (2015a). Lunar crater forms on melt sheets—Origins and implications for self-secondary cratering and chronology. Paper presented at 46th Lunar and Planetary Science Conference, Houston, TX.
- Plescia, J. B. (2015b). Transitional crater (simple/complex), in *Encyclopedia of planetary landforms*, Edited, pp. 1–5, Springer, New York, NY, doi: https://doi.org/10.1007/978-1-4614-9213-9_407-2
- Plescia, J. B., & Cintala, M. (2012). Impact melt in small lunar highland craters. *Journal of Geophysical Research*, 117, E00H12. <https://doi.org/10.1029/2011JE003941>
- Prieur, N., Rolf, T., Luther, R., Wünnemann, K., Xiao, Z., & Werner, S. (2017). The effect of target properties on transient crater scaling for simple craters. *Journal of Geophysical Research: Planets*, 122, 1704–1726. <https://doi.org/10.1002/2017JE005283>
- Quaide, W. L. (1965). Rilles, ridges, and domes—Clues to maria history. *Icarus*, 4(4), 374–389. [https://doi.org/10.1016/0019-1035\(65\)90041-2](https://doi.org/10.1016/0019-1035(65)90041-2)
- Quaide, W. L., Gault, D. E., & Schmidt, R. A. (1965). Gravitative effects on lunar impact structures. *Annals of the New York Academy of Sciences*, 123(2), 563–572. <https://doi.org/10.1111/j.1749-6632.1965.tb20388.x>

- Quaide, W. L., & Oberbeck, V. R. (1968). Thickness determinations of the lunar surface layer from lunar impact craters. *Journal of Geophysical Research*, 73(16), 5247–5270. <https://doi.org/10.1029/JB073i016p05247>
- Robbins, S. J., & Hynek, B. M. (2012). A new global database of Mars impact craters ≥ 1 km: 2. Global crater properties and regional variations of the simple-to-complex transition diameter. *Journal of Geophysical Research*, 117, E06001. <https://doi.org/10.1029/2011JE003967>
- Robinson, M., Eliason, E., Hiesinger, H., Jolliff, B., McEwen, A., Malin, M., et al.. (2010). Lunar reconnaissance orbiter camera: First results. Paper Presented at European Planetary Science Congress 2010, Rome, Italy.
- Roddy, D. (1977). Tabular comparisons of the Flynn Creek impact crater, United States, Steinheim impact crater, Germany and Snowball explosion crater, Canada. Paper presented at Impact and Explosion Cratering: Planetary and Terrestrial Implications, Flagstaff, AZ.
- Salamunićcar, G., Lončarić, S., & Mazarico, E. (2012). LU60645GT and MA132843GT catalogues of lunar and Martian impact craters developed using a crater shape-based interpolation crater detection algorithm for topography data. *Planetary and Space Science*, 60(1), 236–247. <https://doi.org/10.1016/j.pss.2011.09.003>
- Scaioni, M., Yordanov, V., Brunetti, M. T., Melis, M. T., Zinzi, A., Kang, Z., & Giommi, P. (2018). Recognition of landslides in lunar impact craters. *European Journal of Remote Sensing*, 51(1), 47–61. <https://doi.org/10.1080/22797254.2017.1401908>
- Scherler, D., Kenkmann, T., & Jahn, A. (2006). Structural record of an oblique impact. *Earth and Planetary Science Letters*, 248(1–2), 43–53. <https://doi.org/10.1016/j.epsl.2006.05.002>

- Schmidt, R. M., & Housen, K. R. (1987). Some recent advances in the scaling of impact and explosion cratering. *International Journal of Impact Engineering*, 5(1–4), 543–560. [https://doi.org/10.1016/0734-743X\(87\)90069-8](https://doi.org/10.1016/0734-743X(87)90069-8)
- Schmitt, H. H., Trask, N. J., & Shoemaker, E. M. (1967). Geologic map of the Copernicus quadrangle of the Moon, Map I-515(LAC-558), US Geological Survey.
- Schultz, P. H. (1976). Floor-fractured lunar craters. *The Moon*, 15(3–4), 241–273. <https://doi.org/10.1007/BF00562240>
- Schultz, P. H. (1988). Cratering on Mercury—A relook. In F. Vilas, C. Chapman, & M. Matthews (Eds.), *Mercury*, (pp. 274–335). Tucson, Arizona: University of Arizona Press.
- Senft, L. E., & Stewart, S. T. (2008). Impact crater formation in icy layered terrains on Mars. *Meteoritics & Planetary Science*, 43(12), 1993–2013. <https://doi.org/10.1111/j.1945-5100.2008.tb00657.x>
- Settle, M., & Head, J. W. (1979). The role of rim slumping in the modification of lunar impact craters. *Journal of Geophysical Research*, 84(B6), 3081–3096. <https://doi.org/10.1029/JB084iB06p03081>
- Shoemaker, E. M., & Hackman, R. J. (1962). Stratigraphic basis for a lunar time scale. In Z. Kopal, & Z. Mikhailov (Eds.), *The Moon*, (pp. 289–300). New York: Academic Press.
- Shuvalov, V., & Dypvik, H. (2004). Ejecta formation and crater development of the Mjølner impact. *Meteoritics & Planetary Science*, 39(3), 467–479. <https://doi.org/10.1111/j.1945-5100.2004.tb00105.x>
- Silber, E. A., Osinski, G. R., Johnson, B. C., & Grieve, R. A. (2017). Effect of impact velocity and acoustic fluidization on the simple-to-complex transition of lunar craters. *Journal of Geophysical Research: Planets*, 122, 800–821. <https://doi.org/10.1002/2016JE005236>
- Silber, E. A., Zanetti, M., Osinski, G. R., Johnson, B. C., & Grieve, R. A. F. (2018). A combined modeling and observational study of the effect of impact velocity on

- production of melt in simple-to-complex lunar craters. Paper presented at 49th Lunar and Planetary Science Conference, Houston, TX.
- Smith, D. E., Zuber, M. T., Neumann, G. A., Mazarico, E., Head, J., & Torrence, M. H. (2011). Results from the Lunar Orbiter Laser Altimeter (LOLA): Global, high resolution topographic mapping of the Moon. Paper presented at 42nd Lunar and Planetary Science Conference, Houston, TX.
- Smith, D. E., Zuber, M. T., Neumann, G. A., Mazarico, E., Lemoine, F. G., Head, J. W. III, et al. (2017). Summary of the results from the Lunar Orbiter Laser Altimeter after seven years in lunar orbit. *Icarus*, 283, 70–91. <https://doi.org/10.1016/j.icarus.2016.06.006>
- Smith, E. I., & Hartnell, J. A. (1978). Crater size-shape profiles for the Moon and Mercury: Terrain effects and interplanetary comparisons. *The Moon and the Planets*, 19(4), 479–511. <https://doi.org/10.1007/BF00901976>
- Smith, E. I., & Sanchez, A. G. (1973). Fresh lunar craters: Morphology as a function of diameter, a possible criterion for crater origin. *Modern Geology*, 4, 51–59.
- Smith, G. I. (1966). A comparison of two terrestrial grabens with the lunar rilles Rima Ariadaeus and Rimae Hypatia I and II, U.S. Geol. Survey Astrogeol. Studies Rep., 65-86 pp, Washington, DC.
- Smith, J., Anderson, A., Newton, R., Olsen, E., Crewe, A., Isaacson, M., et al. (1970). Petrologic history of the moon inferred from petrography, mineralogy and petrogenesis of Apollo 11 rocks. *Geochimica et Cosmochimica Acta*, 1, 897–925.
- Soderblom, J. M., Evans, A. J., Johnson, B. C., Melosh, H. J., Miljković, K., Phillips, R. J., et al. (2015). The fractured Moon: Production and saturation of porosity in the lunar highlands from impact cratering. *Geophysical Research Letters*, 42, 6939–6944. <https://doi.org/10.1002/2015GL065022>

- Stewart, S. T., & Valiant, G. J. (2006). Martian subsurface properties and crater formation processes inferred from fresh impact crater geometries. *Meteoritics & Planetary Science*, 41(10), 1509–1537. <https://doi.org/10.1111/j.1945-5100.2006.tb00433.x>
- Susorney, H. C., Barnouin, O. S., Ernst, C. M., & Johnson, C. L. (2016). Morphometry of impact craters on Mercury from MESSENGER altimetry and imaging. *Icarus*, 271, 180–193. <https://doi.org/10.1016/j.icarus.2016.01.022>
- Taylor, S., & Bence, A. (1975). Evolution of the lunar highland crust. Paper presented at 6th Lunar and Planetary Science Conference Proceedings, Houston, TX.
- Taylor, S. R. (1989). Growth of planetary crusts. *Tectonophysics*, 161(3–4), 147–156. [https://doi.org/10.1016/0040-1951\(89\)90151-0](https://doi.org/10.1016/0040-1951(89)90151-0)
- Thompson, T. W., Campbell, B. A., Ghent, R. R., & Hawke, B. R. (2009). Rugged crater ejecta as a guide to megaregolith thickness in the southern nearside of the Moon. *Geology*, 37(7), 655–658. <https://doi.org/10.1130/G25565A.1>
- Thompson, T. W., Roberts, W. J., Hartmann, W. K., Shorthill, R. W., & Zisk, S. H. (1979). Blocky craters: Implications about the lunar megaregolith. *The Moon and the Planets*, 21(3), 319–342. <https://doi.org/10.1007/BF00897360>
- Thorey, C., & Michaut, C. (2014). A model for the dynamics of crater-centered intrusion: Application to lunar floor-fractured craters. *Journal of Geophysical Research: Planets*, 119, 286–312. <https://doi.org/10.1002/2013JE004467>
- Trang, D., Gillis-Davis, J. J., & Hawke, B. R. (2016). The origin of lunar concentric craters. *Icarus*, 278, 62–78. <https://doi.org/10.1016/j.icarus.2016.06.001>
- Wilhelms, D. E., John, F., & Trask, N. J. (1987). The geologic history of the Moon. Rep.
- Williams, K. K., & Zuber, M. T. (1998). Measurement and analysis of lunar basin depths from Clementine altimetry. *Icarus*, 131(1), 107–122. <https://doi.org/10.1006/icar.1997.5856>

- Wilson, L., & Head, J. W. (2018). Lunar floor-fractured craters: Modes of dike and sill emplacement and implications of gas production and intrusion cooling on surface morphology and structure. *Icarus*, 305, 105–122. <https://doi.org/10.1016/j.icarus.2017.12.030>
- Wood, C., & Anderson, L. (1978). New morphometric data for fresh lunar craters. Paper presented at 9th Lunar and Planetary Science Conference Proceedings, Houston, TX.
- Wood, J. A., Dickey, J. Jr., Marvin, U. B., & Powell, B. (1970). Lunar anorthosites and a geophysical model of the moon. *Geochimica et Cosmochimica Acta. Supplement.*, 1, 965–990.
- Wünnemann, K., Collins, G., & Melosh, H. (2006). A strain-based porosity model for use in hydrocode simulations of impacts and implications for transient crater growth in porous targets. *Icarus*, 180(2), 514–527. <https://doi.org/10.1016/j.icarus.2005.10.013>
- Wünnemann, K., Collins, G., & Osinski, G. (2008). Numerical modelling of impact melt production in porous rocks. *Earth and Planetary Science Letters*, 269(3–4), 530–539. <https://doi.org/10.1016/j.epsl.2008.03.007>
- Wünnemann, K., & Ivanov, B. (2003). Numerical modelling of the impact crater depth–diameter dependence in an acoustically fluidized target. *Planetary and Space Science*, 51(13), 831–845. <https://doi.org/10.1016/j.pss.2003.08.001>
- Zuber, M. T., Smith, D. E., Watkins, M. M., Asmar, S. W., Konopliv, A. S., Lemoine, F. G., et al. (2013). Gravity field of the Moon from the Gravity Recovery and Interior Laboratory (GRAIL) mission. *Science*, 339(6120), 668–671. <https://doi.org/10.1126/science.1231507>

APPENDIX A

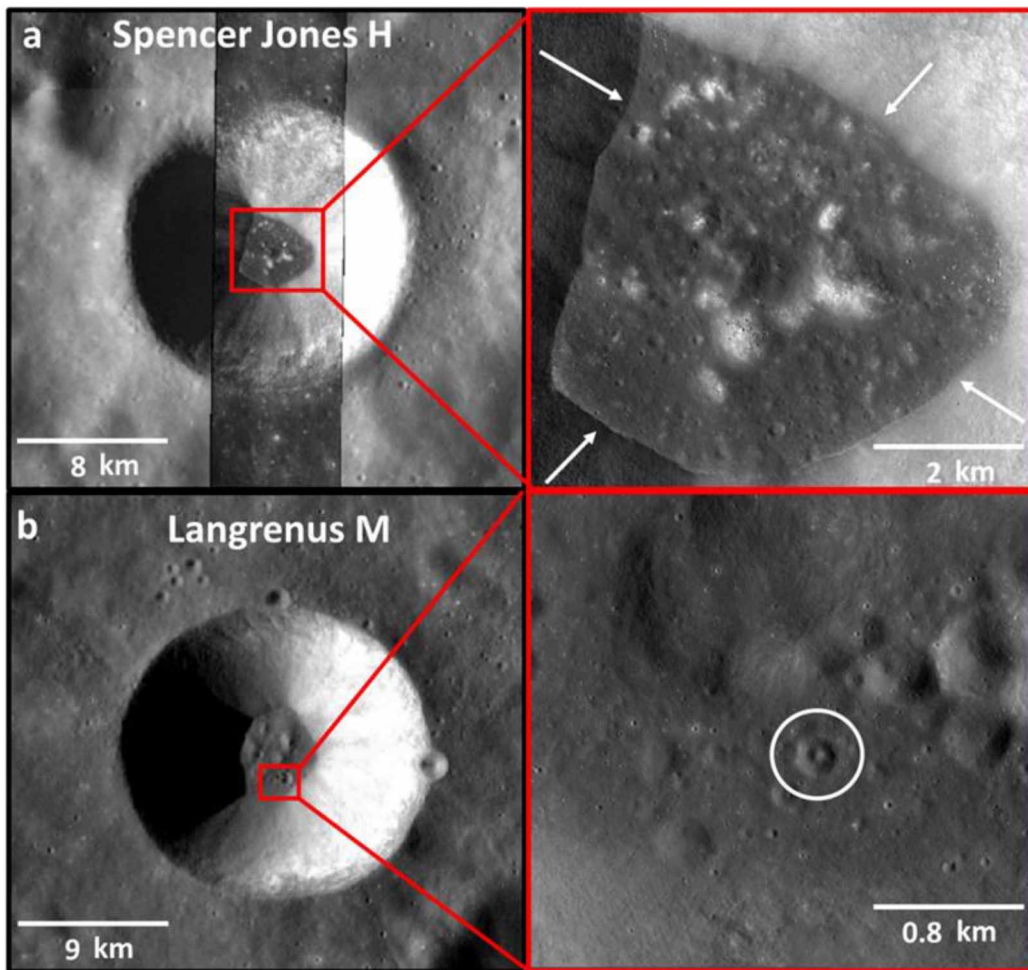


Figure A-1. WAC and NAC illustrations of floor melts and melt features in two simple craters. The craters are located at (a) 11.93°N , 168.12°E and (b) -9.81°N , 66.41°E . NAC M105772705L in (a) and NAC M1138475944R in (b) highlight the impact melt-lined floors of the craters. The surface of the melt is smoother as compared to the bright breccia boulders. Also, the melt has a darker albedo relative to the surrounding crater walls and the breccia boulders on the floor. The melt displays a sharp contact with the walls (white arrows) and the boulders. The circle outlined in white in the NAC inset of (b) encompasses a crater of the morphology of a palimpsest that is formed from impact on the surface of a melt deposit.

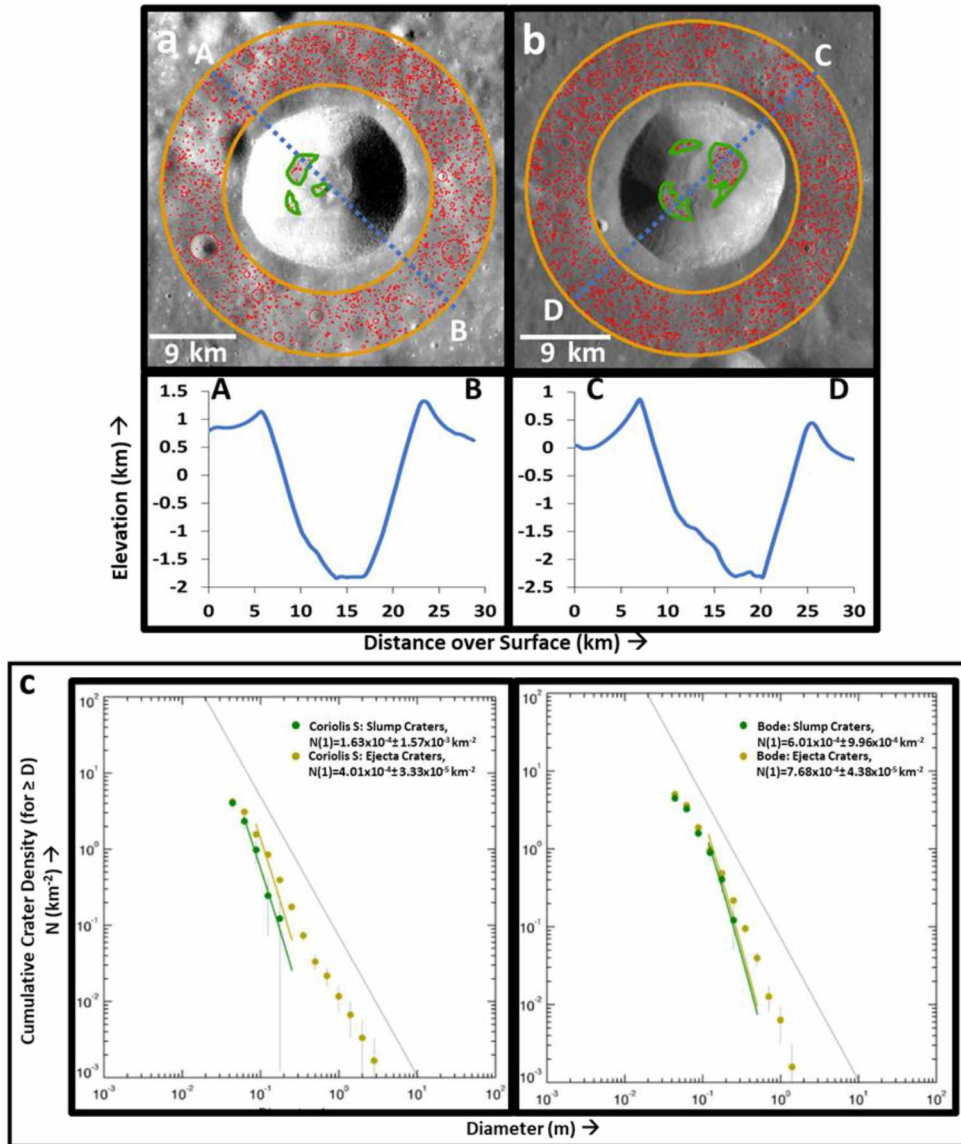


Figure A-2. Investigation of the timing of deposition of localized slumped material (green) relative to deposition of ejecta (orange) for craters (a) Coriolis S (0.1°N , 169.66°E) and (b) Bode (6.7°N , 357.54°E). To test whether our database consists of crater structures characteristic of both syn- and post-impact slumping, we performed crater counting on the ejecta and localized slumped material of few randomly selected craters to compare the relative ages of the slumped material with that of the ejecta. If the slumped material was deposited during crater formation, the slumped material must be as old as the ejecta. We first delineated the regions containing the unconsolidated material and the ejecta. We did not include very steep areas in case of both ejecta and slumped material because craters are more susceptible to erosion on slopes. Therefore, the steeper part of the rim was excluded and the region in between $1.25R$ and $2R$ from the crater center was selected as the ejecta area, where R refers to the crater radius. The red circles symbolize the craters that were outlined in these units using Kaguya Terrain Camera (TC) high resolution image data processed to 10 m/pixel (Haruyama et al., 2009). We digitized craters of size greater than or equal to 100 m because the standard isochrons provide the most accurate estimates of surface ages between 100 m and 100 km crater sizes (Neukum & Ivanov, 1994; Neukum et al., 2001). We then generated cumulative size-frequency distribution (CSFD) log-log plots (Figure A-2(c)) using square root of two binning for both surfaces, where the frequency refers to the cumulative density of the craters on a given surface (N) (number of craters per unit area \geq a given Diameter D) (Neukum, 1983; Neukum

et al., 1975a; Neukum et al., 1975b). We estimated the error bar on each data point to be equal to $\sqrt{\text{number of craters} \geq D_{\text{data point}}/\text{area}}$ (Arvidson et al., 1979). Next, we fit production functions to those parts of the CSFD plots that corresponded to the diameter ranges that were common between the ejecta and slump units. The production function fitting helped in obtaining cumulative crater densities at 1 km diameter. In cases of change in slope along the CSFD plots relative to crater saturation line (Hartmann, 1984), larger crater diameter bins were preferred for the production function fit because smaller craters degrade faster over time. Therefore, the larger craters reflect ages that are closer to the time of formation of the surface unit. The cumulative crater densities at 1 km diameter ($N(1)$) for slumped material (green dots and green lines) and ejecta (orange dots and orange lines) are available in the legends of A-2(c). For Coriolis S (left in A-2(c)), the statistically different crater densities at 1 km diameter on the slumped material and the ejecta indicate that the fragmented material we see today may have been a result of slumping over time post crater formation. For Bode (right in A-2(c)), the statistically similar crater densities at 1 km diameter on both surfaces suggest that the slumping process occurred immediately post transient cavity formation.

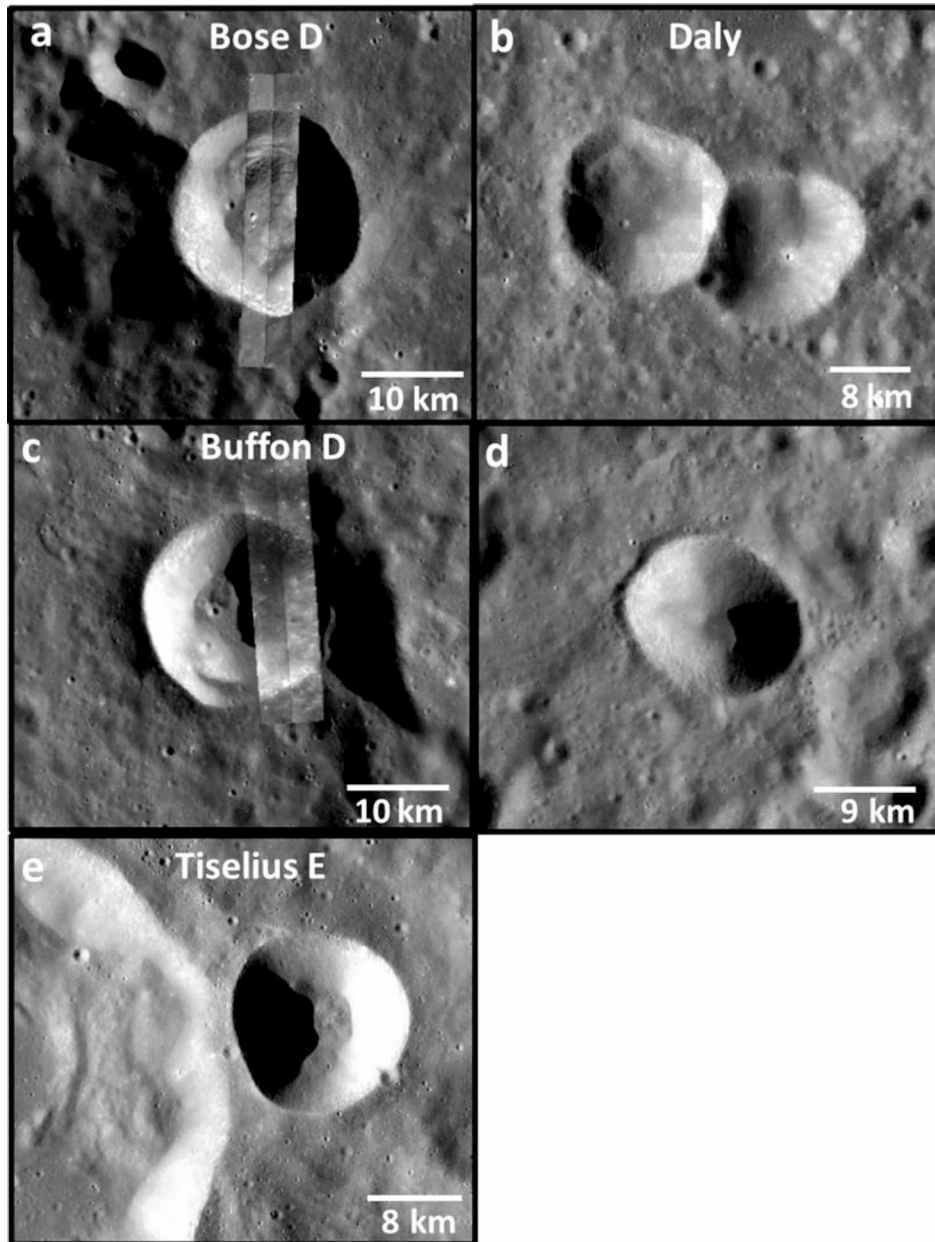


Figure A-3. WAC image illustrations of craters that were discarded from the close-proximity analysis. (a) Crater with localized slumps and terraces, that superposes the rim of a larger, pre-existing crater and is located at -53.13°N , 193.1°E ; (b) Crater with localized slumps (on the left, located at 5.74°N , 59.5°E), that truncates against another crater's rim; (c) Crater with localized slumps, that superposes a larger crater's terrace, and is located at -40.23°N , 227.81°E ; (d) Elliptical crater located at 32.18°N , 208.56°E and (e) Crater with localized slumps that superposes the elevated outer wall/ejecta of a larger crater on the west, and is located at 7.17°N , 177.83°E .

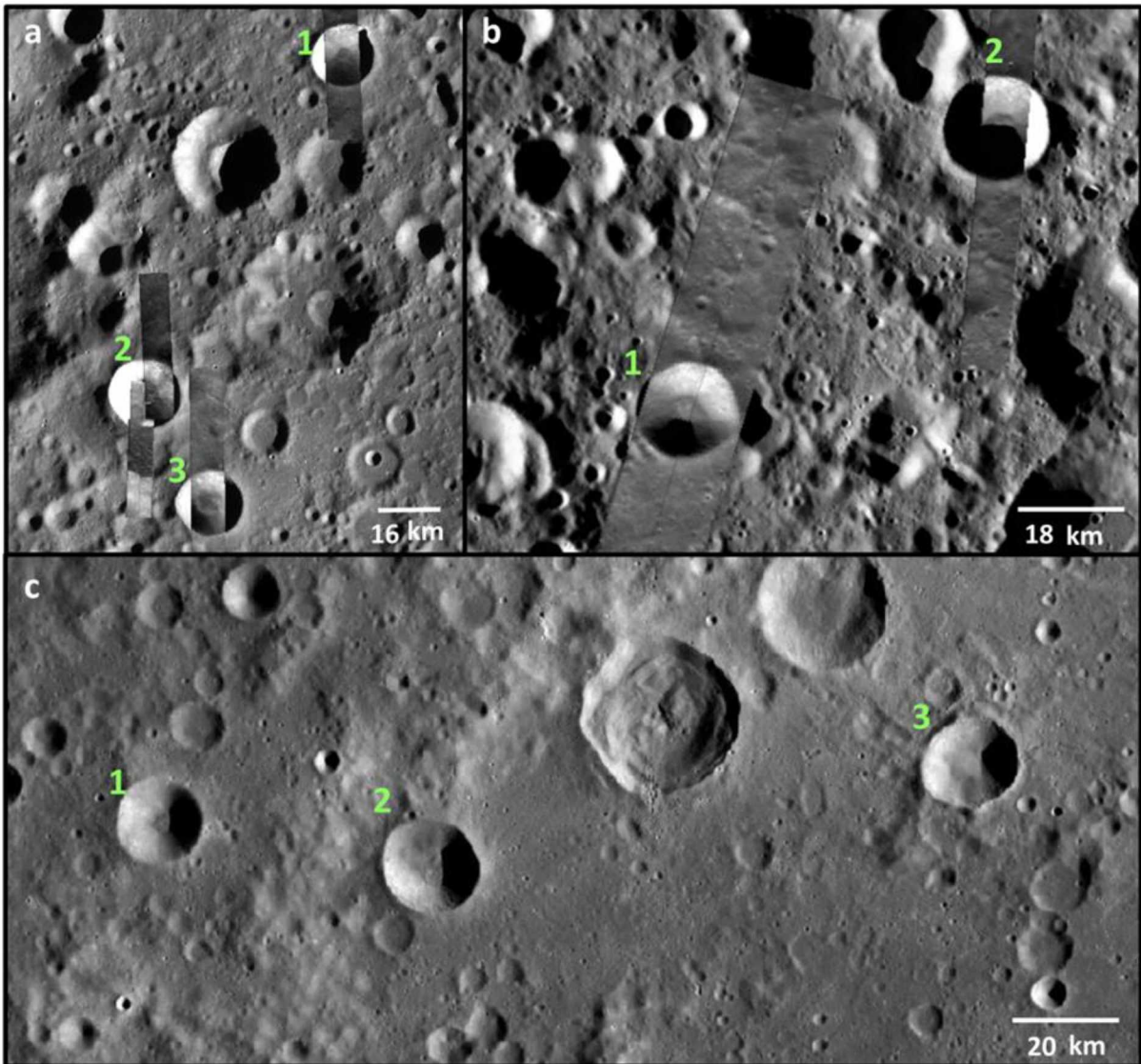


Figure A-4. WAC images of close proximity groups that were not shown in the article. (a) Group A; (b) Group H and (c) Group D. The details of the groups have been listed in Table A-3 of Appendix A. The numbers in each image are the serial numbers allotted to the craters in each group in Table A-3. The NAC strips that highlight the floor features where the WAC display of the floor is shadowed are: (a) M1102301746L (Crater 1), M107998899 pair & M1194166036L (Crater 2) and M1099958635R (Crater 3); (b) M1117773337 pair (Crater 1) and M1194228826L (Crater 2).

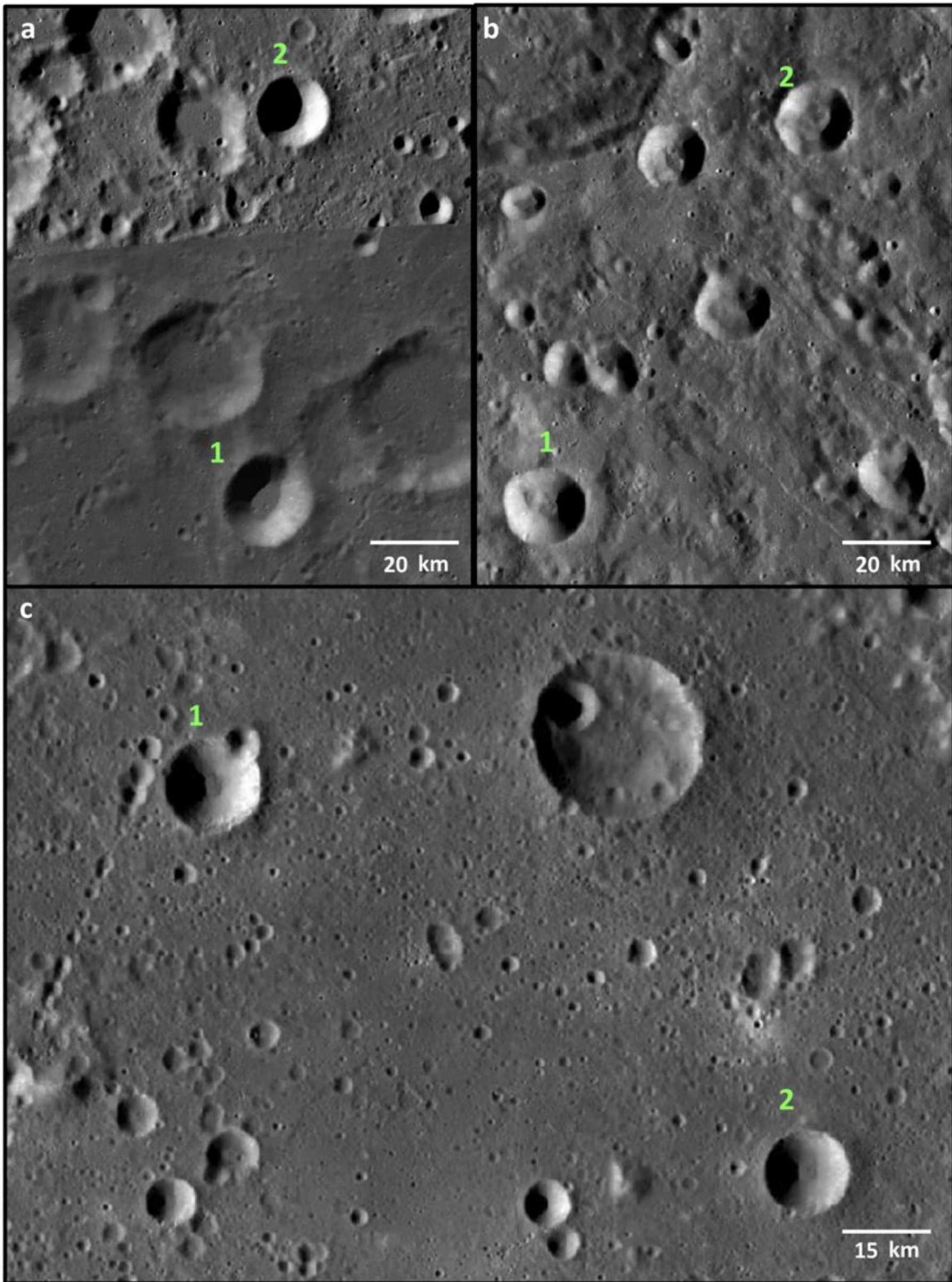


Figure A-5. WAC images of more close proximity groups that were not shown in the article. (a) Group I; (b) Group K and (c) Group L. The details of the groups have been listed in Table A-3 of Appendix A. The numbers in each image are the serial numbers allotted to the craters in each group in Table A-3.

Table A-1. List of the 244 well-preserved lunar impact craters in the 15-20 km diameter range, their geographic locations, morphologies and evaluated morphometric parameters.

Crater Name	Longitude (°E)	Latitude (°N)	Morphological class	Target	Diameter (D) (km)	Rim-to-floor Depth (d) (km)	Std. Dev. (Rim-to-floor Depth) (km)	d/D	Std. Dev. (d/D)	Central Uplift Height (m)
Abul Wafa A	116.86	1.39	Crater with localized slumps	Highlands	16.4	2.4	0.69	0.15	0.04	-
Agatharchides A	331.54	-23.27	Crater with localized slumps	Mare	16.4	2.8	0.21	0.17	0.01	-
Al Khwarizmi M	107.44	3.06	Crater with localized slumps	Highlands	17.0	2.8	0.28	0.17	0.02	-
Alden B	113.11	-20.59	Simple crater	Highlands	15.0	2.7	0.16	0.18	0.01	-
Alhazen A	74.3	16.16	Simple crater	Highlands	16.1	3.2	0.48	0.20	0.03	-
Arrhenius J	271.55	-57.51	Simple crater	Highlands	17.5	2.9	0.23	0.17	0.01	-
Bailly F	290.41	-67.46	Simple crater	Highlands	16.6	3.2	0.14	0.19	0.01	-
Baldet J	209.75	-54.77	Crater with localized slumps	Highlands	18.0	2.3	0.09	0.13	0.01	-
Barocius M	19.48	-42.45	Crater with localized slumps	Highlands	16.1	2.9	0.12	0.18	0.01	-
Bartels A	270.39	25.69	Simple crater	Highlands	18.0	3.3	0.39	0.18	0.02	-
Beaumont B	26.8	-18.71	Simple crater	Highlands	15.2	2.6	0.13	0.17	0.01	-
Bell E	264.06	22.06	Concentric crater	Highlands	15.5	1.2	0.10	0.08	0.01	-
Bell J	265.88	19.88	Crater with localized slumps	Highlands	20.0	2.8	0.47	0.14	0.02	-
Bell K	264.83	18.34	Crater with localized slumps	Highlands	19.5	3.0	0.22	0.16	0.01	-
Bellot	48.19	-12.47	Crater with localized slumps	Highlands	17.2	3.0	0.20	0.18	0.01	-
Bessel	17.92	21.73	Crater with localized slumps	Mare	15.2	1.6	0.11	0.11	0.01	-
Biela W	49.87	-55.31	Crater with localized slumps	Highlands	19.1	3.2	1.33	0.17	0.07	-
Birt	351.4	-22.36	Crater with localized slumps	Mare	16.0	3.6	0.22	0.23	0.01	-
Black	80.39	-9.19	Simple crater	Highlands	19.3	3.0	0.18	0.16	0.01	-
Bode	357.54	6.7	Crater with localized slumps	Highlands	18.2	2.9	0.31	0.16	0.02	-
Bose D	193.1	-53.13	Crater with localized slumps and terraces	Highlands	19.4	2.8	0.15	0.14	0.01	-
Boussingault T	43.06	-63.01	Simple crater	Highlands	18.8	2.8	0.26	0.15	0.01	-
Bouvard C	282.52	-37.05	Simple crater	Highlands	15.0	3.0	0.30	0.20	0.02	-
Brunner N	90.71	-11.38	Simple crater	Highlands	18.0	3.4	0.15	0.19	0.01	-
Buffon D	227.81	-40.23	Crater with localized slumps	Highlands	19.5	3.0	0.35	0.15	0.02	-
Bunsen C	270.18	44.2	Simple crater	Highlands	18.9	3.8	0.32	0.20	0.02	-
Campbell E	158.88	46.33	Simple crater	Highlands	15.8	2.4	0.51	0.15	0.03	-
Carmichael	40.36	19.53	Crater with localized slumps	Mare	19.7	3.6	0.10	0.19	0.01	-
Carrel	26.68	10.66	Crater with localized slumps and terraces	Mare	16.3	2.1	0.11	0.13	0.01	-
Cassegrain K	113.88	-54.45	Simple crater	Highlands	16.8	3.2	0.18	0.19	0.01	-
Cassini A	4.77	40.51	Crater with localized slumps	Mare	16.4	2.6	0.21	0.16	0.01	-
Catalan U	269.34	-45	Simple crater	Highlands	19.0	3.8	0.11	0.20	0.01	-
Chaffee S	202.5	-39.76	Crater with localized slumps and central uplift	Highlands	19.8	3.1	0.14	0.16	0.01	202
Chaplygin K	151.35	-7.68	Crater with localized slumps	Highlands	20.0	3.3	0.39	0.17	0.02	-
Clavius G	345.99	-52.02	Simple crater	Highlands	17.1	2.8	0.14	0.16	0.01	-
Cleostratus J	276.34	61.39	Crater with localized slumps and terraces	Highlands	19.3	2.4	0.18	0.13	0.01	-
Compton W	96.59	58.58	Crater with localized slumps	Highlands	15.8	2.6	0.25	0.16	0.02	-
Congreve G	196.12	-0.89	Simple crater	Highlands	17.6	3.1	0.40	0.18	0.02	-
Cooper G	178.76	52.42	Simple crater	Highlands	19.2	2.8	0.15	0.14	0.01	-

Table A-1 contd.

Crater Name	Longitude (°E)	Latitude (°N)	Morphological class	Target	Diameter (D) (km)	Rim-to- floor Depth (d) (km)	Std. Dev. (Rim-to- floor Depth) (km)	d/D	Std. Dev. (d/D)	Central Uplift Height (m)
Coriolis G	174.54	-0.03	Simple crater	Highlands	17.6	2.9	0.21	0.17	0.01	-
Coriolis S	169.66	0.1	Crater with localized slumps	Highlands	17.7	3.2	0.18	0.18	0.01	-
D. Brown	212.86	-41.68	Crater with localized slumps	Highlands	15.8	2.7	0.38	0.17	0.02	-
d'Alembert G	167.36	50.7	Simple crater	Highlands	18.2	3.3	0.17	0.18	0.01	-
Daly	59.5	5.74	Crater with localized slumps	Highlands	17.2	2.5	0.36	0.15	0.02	-
Dante S	177.66	25.09	Simple crater	Highlands	17.9	3.4	0.30	0.19	0.02	-
Darney	336.43	-14.6	Simple crater	Highlands	15.2	2.8	0.13	0.18	0.01	-
Dawes	26.34	17.21	Crater with localized slumps	Mare	17.5	2.4	0.13	0.14	0.01	-
Dionysius	17.29	2.77	Crater with localized slumps	Mare	18.0	2.9	0.11	0.16	0.01	-
Diophantus	325.7	27.62	Crater with localized slumps and central uplift	Mare	17.8	2.8	0.14	0.16	0.01	145
Donner N	97.19	-33.17	Simple crater	Highlands	20.0	3.4	0.49	0.17	0.02	-
Donner Q	95.63	-34.29	Crater with localized slumps	Boundary	15.1	2.5	0.08	0.17	0.01	-
Donner R	92.28	-34.34	Crater with localized slumps	Boundary	15.8	2.7	0.19	0.17	0.01	-
Donner V	95.58	-30.56	Crater with localized slumps	Highlands	19.5	2.9	0.38	0.15	0.02	-
Doppler W	197.86	-10.99	Simple crater	Highlands	15.2	2.9	0.11	0.19	0.01	-
Dreyer R	94.47	8.49	Crater with localized slumps	Highlands	19.9	2.6	0.13	0.13	0.01	-
Dunthorne	328.29	-30.12	Simple crater	Highlands	15.9	2.9	0.43	0.18	0.03	-
Emden F	188.89	62.98	Simple crater	Highlands	19.5	4.1	0.40	0.21	0.02	-
Endymion E	66.24	53.59	Simple crater	Highlands	17.6	2.9	0.35	0.17	0.02	-
Epimenides A	329.82	-43.26	Simple crater	Highlands	15.0	2.9	0.18	0.19	0.01	-
Franklin C	44.25	35.68	Crater with localized slumps	Highlands	15.0	2.4	0.27	0.16	0.02	-
Fryxell	258.34	-21.25	Crater with localized slumps	Highlands	17.6	3.4	0.36	0.19	0.02	-
G. Bond	36.32	32.38	Crater with localized slumps	Highlands	19.8	2.7	0.52	0.13	0.03	-
Galilaei	297.16	10.48	Crater with localized slumps and terraces	Mare	15.7	2.0	0.16	0.13	0.01	-
Gardner	33.81	17.74	Simple crater	Highlands	17.6	3.0	0.20	0.17	0.01	-
Gauss A	82.76	36.54	Crater with localized slumps	Highlands	18.9	3.0	0.50	0.16	0.03	-
Gauss J	72.65	40.57	Crater with localized slumps	Highlands	15.9	2.8	0.52	0.17	0.03	-
Geissler	76.5	-2.59	Crater with localized slumps	Highlands	17.2	3.1	0.11	0.18	0.01	-
Geminus D	47.29	30.57	Simple crater	Highlands	15.6	2.9	0.22	0.18	0.01	-
Glaisher	49.34	13.18	Simple crater	Highlands	16.0	3.0	0.37	0.19	0.02	-
Glauber	142.66	11.31	Simple crater	Highlands	15.3	2.5	0.22	0.16	0.01	-
Golitsyn J	256.79	-27.68	Simple crater	Highlands	19.4	3.7	0.35	0.19	0.02	-
Gruithuisen	320.22	32.88	Crater with localized slumps	Mare	15.8	1.7	0.15	0.11	0.01	-
Guillaume J	189.48	43.56	Simple crater	Highlands	16.6	3.1	0.16	0.18	0.01	-
Gullstrand C	232.9	46.57	Simple crater	Highlands	15.5	3.0	0.26	0.20	0.02	-
Gutenberg A	39.91	-9.03	Simple crater	Highlands	15.0	2.9	0.39	0.20	0.03	-
Hagen Q	133.29	-50.33	Crater with localized slumps	Highlands	15.9	2.5	0.41	0.15	0.03	-
Hahn A	69.72	29.66	Crater with localized slumps	Highlands	18.7	3.2	0.09	0.17	0.01	-
Hahn B	76.97	31.37	Crater with localized slumps	Highlands	16.7	2.7	0.22	0.16	0.01	-
Harden	143.54	5.46	Simple crater	Highlands	15.1	2.7	0.11	0.18	0.01	-
Harkhebi T	95.31	40.04	Crater with localized slumps	Highlands	18.4	3.0	0.25	0.16	0.01	-
Hatanaka Q	235.34	25.99	Crater with localized slumps	Highlands	19.1	2.9	0.28	0.15	0.01	-
Heinsius A	342.38	-39.77	Crater with localized slumps	Highlands	19.5	3.2	0.18	0.17	0.01	-

Table A-1 contd.

Crater Name	Longitude (°E)	Latitude (°N)	Morphological class	Target	Diameter (D) (km)	Rim-to-floor Depth (d) (km)	Std. Dev. (Rim-to-floor Depth) (km)	d/D	Std. Dev. (d/D)	Central Uplift Height (m)
Hendrix	200.06	-46.86	Crater with localized slumps and terraces	Highlands	16.5	1.9	0.17	0.11	0.01	-
Herigonius	326.03	-13.35	Crater with localized slumps	Mare	15.4	1.9	0.22	0.12	0.01	-
Hermann	302.53	-0.87	Crater with localized slumps, terraces and central uplift	Mare	16.2	1.6	0.11	0.10	0.01	116
Heyrovsky	264.57	-39.55	Simple crater	Highlands	16.4	3.3	0.39	0.20	0.02	-
Hill	40.81	20.91	Simple crater	Highlands	15.7	3.3	0.19	0.21	0.01	-
Hipparchus C	8.21	-7.41	Simple crater	Highlands	16.6	3.4	0.34	0.21	0.02	-
Hommel J	27.87	-53.53	Crater with localized slumps	Highlands	17.5	2.8	0.15	0.16	0.01	-
Hooke D	55.8	40.69	Crater with localized slumps	Highlands	18.8	2.5	0.14	0.13	0.01	-
Hypatia A	22.21	-4.9	Crater with localized slumps	Highlands	15.2	2.5	0.69	0.17	0.05	-
Inghirami C	285.41	-44.07	Simple crater	Highlands	17.5	3.5	0.45	0.20	0.03	-
Isidorus D	34.07	-4.27	Simple crater	Highlands	15.2	3.1	0.09	0.20	0.01	-
Jacobi J	10.27	-57.96	Simple crater	Highlands	18.8	2.8	0.52	0.15	0.03	-
Janssen K	42.31	-46.19	Simple crater	Highlands	15.5	2.9	0.14	0.19	0.01	-
Joule K	218.15	25.64	Simple crater	Highlands	16.0	3.1	0.49	0.20	0.03	-
Kekule M	221.97	12.05	Crater with localized slumps	Highlands	19.4	3.5	0.36	0.18	0.02	-
Kies A	337.23	-28.36	Crater with localized slumps	Mare	16.2	3.1	0.20	0.19	0.01	-
Kircher E	309.64	-69.05	Crater with localized slumps	Highlands	17.2	3.0	0.18	0.17	0.01	-
Kirkwood T	194.73	68.98	Simple crater	Highlands	18.4	3.3	0.71	0.18	0.04	-
Korolev V	197.94	-1.21	Crater with localized slumps	Highlands	19.6	3.4	0.14	0.17	0.01	-
Korolev Y	201.53	-0.5	Crater with localized slumps	Highlands	19.1	3.8	0.27	0.20	0.01	-
Kurchatov X	140.07	41.18	Simple crater	Highlands	16.8	3.0	0.35	0.18	0.02	-
la Condamine A	329.8	54.43	Crater with localized slumps	Highlands	18.2	3.2	0.13	0.18	0.01	-
la Condamine B	328.33	58.87	Crater with localized slumps	Mare	16.7	2.6	0.08	0.15	0.01	-
Lallemand	275.79	-14.4	Crater with localized slumps	Highlands	16.7	3.2	0.21	0.19	0.01	-
Langrenus M	66.41	-9.81	Simple crater	Highlands	18.0	3.8	0.25	0.21	0.01	-
Lehmann C	309.83	-35.57	Simple crater	Highlands	15.1	3.2	0.32	0.21	0.02	-
Lents J	262.62	-3.63	Simple crater	Highlands	16.1	3.2	0.17	0.20	0.01	-
Leucippus K	244.49	27.27	Crater with localized slumps	Highlands	15.6	2.6	0.28	0.17	0.02	-
Leuschner Z	250.43	5.24	Crater with localized slumps	Highlands	16.7	2.6	0.43	0.16	0.03	-
Lichtenberg	292.28	31.85	Crater with localized slumps	Mare	19.8	2.5	0.14	0.13	0.01	-
Liouville	73.56	2.72	Simple crater	Highlands	16.6	2.9	0.10	0.18	0.01	-
Lippmann J	253.68	-58.74	Simple crater	Highlands	17.8	3.5	0.41	0.20	0.02	-
Lowell W	252.79	-10.16	Simple crater	Highlands	17.4	3.0	0.56	0.17	0.03	-
Lyot D	82.53	-51.69	Crater with localized slumps	Highlands	16.8	2.0	0.19	0.12	0.01	-
Mairan A	321.21	38.63	Crater with localized slumps	Highlands	15.9	2.6	0.19	0.16	0.01	-
Manners	19.99	4.57	Floor-fractured crater	Mare	15.0	1.7	0.13	0.11	0.01	-
Manzinus E	25.15	-68.98	Simple crater	Highlands	18.4	2.9	0.48	0.16	0.03	-
Marius A	313.95	12.59	Crater with localized slumps	Mare	15.3	2.7	0.09	0.17	0.01	-
Mauder A	269.38	-3.28	Simple crater	Highlands	15.2	2.9	0.23	0.19	0.01	-
Maury	39.69	37.11	Simple crater	Highlands	16.9	3.3	0.07	0.19	0.01	-
Mendel B	252.33	-46.52	Crater with localized slumps	Highlands	16.4	2.8	0.60	0.17	0.04	-
Mersenius S	312.93	-19.22	Crater with localized slumps	Highlands	15.3	2.5	0.17	0.16	0.01	-

Table A-1 contd.

Crater Name	Longitude (°E)	Latitude (°N)	Morphological class	Target	Diameter (D) (km)	Rim-to-floor Depth (d) (km)	Std. Dev. (Rim-to-floor Depth) (km)	d/D	Std. Dev. (d/D)	Central Uplift Height (m)
Messala B	59.8	37.37	Crater with localized slumps	Highlands	16.5	2.7	0.64	0.16	0.04	-
Minnaert C	183.78	-64.36	Crater with localized slumps	Highlands	19.6	2.9	0.25	0.15	0.01	-
Moigno A	29.71	64.81	Crater with localized slumps	Highlands	15.7	2.6	0.25	0.16	0.02	-
Mutus L	24.81	-61.84	Simple crater	Highlands	19.6	2.8	0.32	0.14	0.02	-
Mutus P	25.55	-59.16	Simple crater	Highlands	15.5	2.4	0.11	0.16	0.01	-
Nicollet	347.5	-21.95	Crater with localized slumps	Mare	15.0	1.7	0.19	0.12	0.01	-
Nikolaev J	155.42	31.59	Simple crater	Highlands	19.0	3.5	0.32	0.19	0.02	-
Noggerath J	311.98	-48.47	Crater with localized slumps	Highlands	17.0	2.7	0.18	0.16	0.01	-
Olbers B	285.79	6.84	Crater with localized slumps	Highlands	16.3	3.0	0.21	0.19	0.01	-
Parenago Z	250.71	28.96	Crater with localized slumps	Highlands	17.3	2.6	0.36	0.15	0.02	-
Peirce	53.35	18.26	Crater with localized slumps, terraces and central uplift	Mare	18.5	1.8	0.13	0.10	0.01	106
Piccolomini D	32.26	-26.95	Crater with localized slumps	Highlands	16.3	3.0	0.19	0.18	0.01	-
Pickering	6.99	-2.87	Simple crater	Highlands	15.7	2.9	0.29	0.19	0.02	-
Pingre J	291.03	-59.05	Crater with localized slumps	Highlands	16.5	2.5	0.16	0.15	0.01	-
Planck W	131.27	-55.44	Simple crater	Highlands	17.1	3.1	0.15	0.18	0.01	-
Poincare C	168.7	-54.59	Crater with localized slumps	Highlands	19.2	2.8	0.14	0.15	0.01	-
Poincare X	161.18	-53.91	Crater with localized slumps	Highlands	19.7	2.8	0.17	0.14	0.01	-
Polybius A	27.97	-23.04	Simple crater	Highlands	16.6	4.1	0.09	0.25	0.01	-
Pontecouant A	62.79	-57.68	Simple crater	Highlands	18.8	3.0	0.24	0.16	0.01	-
Posidonius P	27.58	33.62	Crater with localized slumps and terraces	Mare	15.2	2.5	0.14	0.17	0.01	-
Pytheas	339.4	20.56	Crater with localized slumps	Mare	19.7	2.5	0.23	0.13	0.01	-
Ramon	211.78	-41.27	Crater with localized slumps	Highlands	16.6	2.5	0.47	0.15	0.03	-
Rayleigh B	88.5	29.05	Crater with localized slumps	Highlands	15.8	2.8	0.12	0.18	0.01	-
Riccioli H	284.96	1.11	Simple crater	Highlands	18.0	3.6	0.21	0.20	0.01	-
Richards	140.09	7.7	Simple crater	Highlands	17.1	3.3	0.32	0.19	0.02	-
Roberts Q	177.65	68.38	Crater with localized slumps	Highlands	19.1	2.6	0.62	0.14	0.03	-
Ryder	143.29	-43.87	Crater with localized slumps	Highlands	15.6	2.6	0.75	0.17	0.05	-
Saenger C	104.35	6.25	Simple crater	Highlands	18.7	3.3	0.58	0.18	0.03	-

Table A-1 contd.

Crater Name	Longitude (°E)	Latitude (°N)	Morphological class	Target	Diameter (D) (km)	Rim-to- floor Depth (d) (km)	Std. Dev. (Rim-to- floor Depth) (km)	d/D	Std. Dev. (d/D)	Central Uplift Height (m)
Saenger X	102.17	6.39	Crater with localized slumps	Highlands	18.0	3.0	0.32	0.17	0.02	-
Safarik H	178.54	9.53	Simple crater	Highlands	15.5	2.8	0.26	0.18	0.02	-
Sanford C	222.61	33.8	Simple crater	Highlands	18.9	3.0	0.12	0.16	0.01	-
Santbech B	41.57	-24.73	Simple crater	Highlands	15.7	3.1	0.33	0.20	0.02	-
Schickard H	297.66	-43.52	Simple crater	Highlands	16.2	3.0	0.11	0.19	0.01	-
Schliemann G	156.7	-2.23	Crater with localized slumps	Highlands	18.1	3.4	0.32	0.19	0.02	-
Schliemann W	152.35	0.26	Simple crater	Highlands	17.5	3.1	0.60	0.18	0.03	-
Schwarzschild Q	108.83	66.24	Crater with localized slumps	Highlands	17.6	2.7	0.43	0.15	0.02	-
Schwarzschild T	107.63	69.82	Simple crater	Highlands	16.2	3.2	0.36	0.20	0.02	-
Seneca F	81.93	29.63	Crater with localized slumps	Highlands	16.2	2.7	0.16	0.17	0.01	-
Sharp A	317.32	47.63	Crater with localized slumps	Highlands	16.9	3.2	0.10	0.19	0.01	-
Sherrington	118	-11.13	Crater with localized slumps	Highlands	18.1	2.8	0.62	0.16	0.03	-
Sisakyan C	111.03	41.98	Simple crater	Highlands	17.2	3.5	0.15	0.20	0.01	-
Spencer Jones H	168.12	11.93	Simple crater	Highlands	15.1	3.1	0.28	0.21	0.02	-
Steinheil G	49.98	-45.69	Crater with localized slumps	Highlands	18.9	2.6	0.12	0.14	0.01	-
Stetson N	239.57	-43.2	Crater with localized slumps	Highlands	17.6	3.1	0.31	0.18	0.02	-
Sumner G	110.41	37.42	Simple crater	Highlands	17.4	3.1	0.24	0.18	0.01	-
Sundman V	266.44	11.96	Simple crater	Highlands	18.3	3.5	0.19	0.19	0.01	-
Swann C	114.28	52.9	Crater with localized slumps	Highlands	19.9	2.9	0.37	0.15	0.02	-
Thebit A	355.07	-21.58	Crater with localized slumps	Highlands	20.0	3.0	0.38	0.15	0.02	-
Theon Junior	15.79	-2.41	Crater with localized slumps	Highlands	17.7	3.0	0.23	0.17	0.01	-
Theon Senior	15.42	-0.81	Crater with localized slumps	Highlands	17.6	3.4	0.17	0.19	0.01	-
Tiling G	231.29	-52.85	Crater with localized slumps	Highlands	15.3	2.2	0.23	0.15	0.02	-
Tiselius E	177.83	7.17	Crater with localized slumps	Highlands	15.4	2.7	0.09	0.18	0.01	-
Tralles A	47.03	27.42	Simple crater	Highlands	17.4	3.3	0.09	0.19	0.01	-
Unnamed10	140.87	25.78	Crater with localized slumps	Highlands	17.5	3.0	0.59	0.17	0.03	-
Unnamed11	149.17	-60.59	Crater with localized slumps	Highlands	18.9	2.7	0.60	0.15	0.03	-
Unnamed12	152.25	56.68	Simple crater	Highlands	16.5	3.3	0.66	0.20	0.04	-
Unnamed13	167.22	-46.84	Simple crater	Highlands	17.5	2.9	0.36	0.17	0.02	-
Unnamed14	172.54	64.4	Simple crater	Highlands	17.1	3.0	0.27	0.18	0.02	-
Unnamed15	175.66	66.32	Simple crater	Highlands	18.0	3.2	0.35	0.18	0.02	-
Unnamed16	176.71	34.92	Crater with localized slumps	Highlands	17.2	3.0	0.50	0.18	0.03	-
Unnamed17	181.38	53.45	Simple crater	Highlands	17.2	2.9	0.41	0.17	0.02	-
Unnamed18	181.85	8.79	Simple crater	Highlands	16.2	3.0	0.48	0.19	0.03	-
Unnamed19	183.76	-57.33	Crater with localized slumps	Highlands	16.5	2.3	0.17	0.14	0.01	-
Unnamed2	90.33	-56.32	Crater with localized slumps	Highlands	18.2	2.7	0.75	0.15	0.04	-
Unnamed20	188.7	44.43	Simple crater	Highlands	17.9	3.6	0.24	0.20	0.01	-
Unnamed21	189.65	36.54	Simple crater	Highlands	16.3	3.1	0.16	0.19	0.01	-
Unnamed22	190.16	-48.7	Crater with localized slumps	Highlands	16.0	2.4	0.35	0.15	0.02	-
Unnamed23	190.87	52.21	Simple crater	Highlands	15.5	3.0	0.29	0.19	0.02	-
Unnamed24	191.06	47.24	Simple crater	Highlands	15.6	3.3	0.14	0.21	0.01	-
Unnamed25	192.21	-31.99	Crater with localized slumps	Highlands	19.0	2.2	0.25	0.12	0.01	-
Unnamed26	192.81	-60.35	Simple crater	Highlands	16.5	2.6	0.35	0.16	0.02	-
Unnamed28	203.12	29.1	Simple crater	Highlands	16.2	3.3	0.28	0.21	0.02	-
Unnamed29	207.7	-45.6	Simple crater	Highlands	17.1	3.3	0.37	0.19	0.02	-

Table A-1 contd.

Crater Name	Longitude (°E)	Latitude (°N)	Morphological class	Target	Diameter (D) (km)	Rim-to- floor Depth (d) (km)	Std. Dev. (Rim-to- floor Depth) (km)	d/D	Std. Dev. (d/D)	Central Uplift Height (m)
Unnamed3	114.29	29.73	Crater with localized slumps	Highlands	15.8	3.0	0.29	0.19	0.02	-
Unnamed30	208.56	32.18	Simple crater	Highlands	15.6	2.7	0.14	0.17	0.01	-
Unnamed31	218.59	18.32	Simple crater	Highlands	15.9	3.5	0.14	0.22	0.01	-
Unnamed32	223.52	-36.9	Simple crater	Highlands	17.4	3.0	0.51	0.17	0.03	-
Unnamed33	224.18	15.15	Crater with localized slumps	Highlands	18.4	2.9	0.37	0.16	0.02	-
Unnamed34	224.35	-46.16	Crater with localized slumps	Highlands	16.9	2.9	0.26	0.17	0.02	-
Unnamed35	224.98	-1.9	Simple crater	Highlands	15.8	3.4	0.21	0.21	0.01	-
Unnamed36	225.13	-44.87	Crater with localized slumps	Highlands	16.0	2.8	0.25	0.18	0.02	-
Unnamed37	227.2	-2.74	Crater with localized slumps	Highlands	15.6	2.9	0.28	0.18	0.02	-
Unnamed38	234.89	-38.55	Crater with localized slumps	Highlands	18.9	3.4	0.17	0.18	0.01	-
Unnamed39	235.66	-1.36	Simple crater	Highlands	15.8	3.4	0.14	0.21	0.01	-
Unnamed4	127.2	62.73	Simple crater	Highlands	16.7	3.1	0.22	0.19	0.01	-
Unnamed40	237.77	-65.74	Simple crater	Highlands	17.8	2.5	0.56	0.14	0.03	-
Unnamed42	238.73	-67.84	Crater with localized slumps	Highlands	18.0	2.9	0.35	0.16	0.02	-
Unnamed43	241.4	-20.96	Simple crater	Highlands	16.2	2.9	0.30	0.18	0.02	-
Unnamed44	247.29	-57.76	Simple crater	Highlands	16.2	2.6	0.58	0.16	0.04	-
Unnamed45	249.27	32.93	Crater with localized slumps	Highlands	15.1	2.3	0.63	0.15	0.04	-
Unnamed46	253.65	71.2	Simple crater	Highlands	16.3	3.0	0.42	0.18	0.03	-
Unnamed47	254.34	41.01	Simple crater	Highlands	15.6	3.3	0.36	0.21	0.02	-
Unnamed48	262.34	64.8	Simple crater	Highlands	15.9	3.1	0.21	0.20	0.01	-
Unnamed49	264.16	29.45	Crater with localized slumps	Highlands	18.1	2.9	0.27	0.16	0.01	-
Unnamed5	127.57	-56.22	Simple crater	Highlands	15.1	3.0	0.22	0.20	0.01	-
Unnamed50	268.41	37.16	Simple crater	Highlands	15.8	2.9	0.19	0.19	0.01	-
Unnamed6	132.1	62.15	Simple crater	Highlands	15.4	2.8	0.16	0.18	0.01	-
Unnamed7	134.77	44.88	Crater with localized slumps	Highlands	19.4	3.1	0.31	0.16	0.02	-
Unnamed8	137.65	23.62	Simple crater	Highlands	17.7	4.4	0.34	0.25	0.02	-
Unnamed9	139.37	44.52	Simple crater	Highlands	15.3	3.0	0.26	0.19	0.02	-
Van de Graaff C	172.81	-26.43	Crater with localized slumps	Highlands	18.1	3.4	0.13	0.19	0.01	-
Van de Graaff F	174.71	-26.77	Crater with localized slumps	Highlands	19.0	2.7	0.15	0.14	0.01	-
Van de Graaff Q	171.36	-27.62	Crater with localized slumps	Highlands	15.0	2.4	0.19	0.16	0.01	-
van den Bergh M	200.75	30.35	Crater with localized slumps	Highlands	15.2	2.1	0.72	0.14	0.05	-
van den Bergh P	199.81	29.2	Simple crater	Highlands	15.0	2.2	0.29	0.15	0.02	-
Ventris B	158.08	-2.22	Simple crater	Highlands	17.4	3.6	0.50	0.21	0.03	-
Ventris M	157.89	-5.68	Crater with localized slumps	Highlands	17.0	2.8	0.93	0.17	0.05	-
Vestine A	94.57	36.01	Simple crater	Highlands	17.9	3.2	0.54	0.18	0.03	-
Vetchinkin P	130.56	7.06	Simple crater	Highlands	16.3	2.6	0.25	0.16	0.02	-
Virchow	83.76	9.88	Crater with localized slumps and terraces	Mare	19.4	1.7	0.19	0.09	0.01	-
Viviani N	116.5	3.49	Simple crater	Highlands	15.2	2.4	0.10	0.16	0.01	-
Vlacq A	39	-51.28	Simple crater	Highlands	16.7	2.8	0.50	0.17	0.03	-
von Bekesy F	137.04	52.8	Simple crater	Highlands	19.5	3.8	0.27	0.20	0.01	-
von der Pahlen V	223.98	-23.78	Crater with localized slumps	Highlands	18.2	3.2	0.46	0.18	0.03	-
W. Bond B	7.51	65.03	Simple crater	Highlands	15.2	3.3	0.09	0.22	0.01	-
Wargentín D	294.7	-51.03	Simple crater	Highlands	15.7	3.0	0.14	0.19	0.01	-
Wilhelm A	337.88	-44.69	Crater with localized slumps	Highlands	19.6	3.1	0.44	0.16	0.02	-
Wurzelbauer A	344.58	-35.74	Simple crater	Highlands	16.5	2.6	0.17	0.15	0.01	-
Zeno K	66.73	42.83	Crater with localized slumps	Highlands	19.4	2.5	0.34	0.13	0.02	-

Table A-2. Data on layering, floor melt, elevation variation of pre-impact terrains of highlands craters, and crater selection for close-proximity analyses for the 244 well-preserved lunar craters within the simple-to-complex transition.

Symbology Definitions:

[1] Layering on walls of craters (Y/N):

Y: Layering is present

N: Layering is absent

[2] Visible melt on floor of simple crater (Y/N):

Y: Melt is visible

N: Melt is not visible

[3] Transitional craters formed on sharp Topographic Breaks (Y/N):

Y: Topographic breaks are present

N: Topographic breaks are absent

[4] Excluded from Close-Proximity Analysis (Y/N):

Y: Crater was excluded from close proximity analysis

N: Crater was selected for close proximity analysis

Name	Longitude (°E)	Latitude (°N)	Morphological class	Target	Layering on walls of craters (Y/N)	Visible Melt on floor of Simple crater (Y/N)	Elevation variation of Highlands terrain surrounding Simple craters and Craters with localized slumps (km)	Std. Dev. of Elevation variation of Highlands terrain surrounding Simple craters and Craters with localized slumps (km)	Transitional craters formed on sharp Topographic Breaks (Y/N)?	Excluded from Close Proximity Analyses (Y/N)?	Reason for exclusion from Close Proximity Analyses
Abul Wafa A	116.86	1.39	Crater with localized slumps	Highlands	N	-	2.25	0.61	Y	Y	Superposition on a crater's terrace
Agatharchides A	331.54	-23.27	Crater with localized slumps	Mare	Y	-	-	-	N	N	-
Al Khwarizmi M	107.44	3.06	Crater with localized slumps	Highlands	N	-	0.58	0.61	Y	Y	Superposition on a crater's rim
Alden B	113.11	-20.59	Simple crater	Highlands	N	N	0.9	0.5	-	Y	Superposition on a crater's rim
Alhazen A	74.3	16.16	Simple crater	Highlands	N	N	1.1	0.3	-	Y	Superposition on a crater's rim
Arrhenius J	271.55	-57.51	Simple crater	Highlands	N	N	0.4	0.2	-	N	-
Bailly F	290.41	-67.46	Simple crater	Highlands	Y	N	0.3	0.3	-	N	-
Baldet J	209.75	-54.77	Crater with localized slumps	Highlands	Y	-	0.19	0.17	Y	Y	Superposition on a crater's rim
Barocius M	19.48	-42.45	Crater with localized slumps	Highlands	N	-	0.36	0	N	Y	Superposition on a crater's rim
Bartels A	270.39	25.69	Simple crater	Highlands	N	N	0.84	0	Y	Y	Truncation against a crater's rim
Beaumont B	26.8	-18.71	Simple crater	Highlands	N	N	0.3	0.4	-	Y	Superposition on a crater's rim
Bell E	264.06	22.06	Concentric crater	Highlands	N	-	-	-	-	N	-

Table A-2 contd.

Name	Longitude (°E)	Latitude (°N)	Morphological class	Target	Layering on walls of craters (Y/N)	Visible Melt on floor of Simple crater (Y/N)	Elevation variation of Highlands terrain surrounding Simple craters and Craters with localized slumps (km)	Std. Dev. of Elevation variation of Highlands terrain surrounding Simple craters and Craters with localized slumps (km)	Transitional craters formed on sharp Topographic Breaks (Y/N)?	Excluded from Close Proximity Analyses (Y/N)?	Reason for exclusion from Close Proximity Analyses
Bell J	265.88	19.88	Crater with localized slumps	Highlands	N	-	0.75	0.44	N	Y	Superposition on a crater's rim
Bell K	264.83	18.34	Crater with localized slumps	Highlands	N	-	0.71	0.59	Y	Y	Superposition on a crater's rim
Bellot	48.19	-12.47	Crater with localized slumps	Highlands	Y	-	0.35	0.19	Y	Y	Superposition on a crater's rim
Bessel	17.92	21.73	Crater with localized slumps	Mare	Y	-	-	-	N	N	-
Biela W	49.87	-55.31	Crater with localized slumps	Highlands	N	-	2.99	1.36	Y	Y	Superposition on a crater's terrace
Birt	351.4	-22.36	Crater with localized slumps	Mare	Y	-	-	-	Y	Y	Truncation against a crater's rim
Black Bode	80.39 357.54	-9.19 6.7	Simple crater Crater with localized slumps	Highlands Highlands	N Y	N -	0.4 0.8	0.3 0.32	- N	N N	- -
Bose D	193.1	-53.13	Crater with localized slumps and terraces	Highlands	Y	-	-	-	Y	Y	Superposition on a crater's rim
Boussingault T	43.06	-63.01	Simple crater	Highlands	N	N	0.5	0.6	-	N	-
Bouvard C	282.52	-37.05	Simple crater	Highlands	N	N	0.86	0.23	-	N	-
Brunner N	90.71	-11.38	Simple crater	Highlands	N	N	0.51	0.27	-	N	-
Buffon D	227.81	-40.23	Crater with localized slumps	Highlands	N	-	1.68	1.19	Y	Y	Superposition on a crater's terrace
Bunsen C	270.18	44.2	Simple crater	Highlands	Y	N	1.1	0.5	-	Y	Truncation against a crater's rim
Campbell E	158.88	46.33	Simple crater	Highlands	N	N	0.9	0.7	-	N	-
Carmichael	40.36	19.53	Crater with localized slumps	Mare	Y	-	-	-	N	N	-
Carrel	26.68	10.66	Crater with localized slumps and terraces	Mare	Y	-	-	-	N	N	-
Cassegrain K	113.88	-54.45	Simple crater	Highlands	Y	Y	0.2	0.2	-	Y	Superposition on a crater's rim
Cassini A	4.77	40.51	Crater with localized slumps	Mare	Y	-	-	-	N	N	-
Catalan U	269.34	-45	Simple crater	Highlands	Y	N	0.23	0.03	-	N	-
Chaffee S	202.5	-39.76	Crater with localized slumps and central uplift	Highlands	Y	-	-	-	-	N	-
Chaplygin K	151.35	-7.68	Crater with localized slumps	Highlands	N	-	1.6	0.62	Y	Y	Superposition on a crater's rim
Clavius G	345.99	-52.02	Simple crater	Highlands	N	N	0.33	0	-	N	-
Cleostratus J	276.34	61.39	Crater with localized slumps and terraces	Highlands	Y	-	-	-	N	N	-
Compton W	96.59	58.58	Crater with localized slumps	Highlands	N	-	0.31	0.14	Y	N	-
Congreve G	196.12	-0.89	Simple crater	Highlands	N	N	0.6	0.4	-	N	-
Cooper G	178.76	52.42	Simple crater	Highlands	N	Y	0.2	0.1	-	N	-
Coriolis G	174.54	-0.03	Simple crater	Highlands	N	N	1	0.7	-	Y	Superposition on a crater's rim
Coriolis S	169.66	0.1	Crater with localized slumps	Highlands	N	-	0	0	N	N	-
D. Brown	212.86	-41.68	Crater with localized slumps	Highlands	N	-	0.9	0.46	Y	Y	Superposition on a crater's terrace
d'Alembert G	167.36	50.7	Simple crater	Highlands	Y	N	0.1	0.1	-	N	-
Daly	59.5	5.74	Crater with localized slumps	Highlands	N	-	0.54	0.19	Y	Y	Truncation against a crater's rim
Dante S	177.66	25.09	Simple crater	Highlands	N	N	0.3	0.1	-	N	-
Darney	336.43	-14.6	Simple crater	Highlands	Y	Y	0.26	0.13	-	N	-
Dawes	26.34	17.21	Crater with localized slumps	Mare	Y	-	-	-	N	N	-

Table A-2 contd.

Name	Longitude (°E)	Latitude (°N)	Morphological class	Target	Layering on walls of craters (Y/N)	Visible Melt on floor of Simple crater (Y/N)	Elevation variation of Highlands surrounding Simple craters and Craters with localized slumps (km)	Std. Dev. of Elevation variation of Highlands terrain surrounding Simple craters and Craters with localized slumps (km)	Transitional craters formed on sharp Topographic Breaks (Y/N)?	Excluded from Close Proximity Analyses (Y/N)?	Reason for exclusion from Close Proximity Analyses
Dionysius	17.29	2.77	Crater with localized slumps	Mare	Y	-	-	-	N	N	-
Diophantus	325.7	27.62	Crater with localized slumps and central uplift	Mare	Y	-	-	-	-	N	-
Donner N	97.19	-33.17	Simple crater	Highlands	N	Y	0.83	0	Y	Y	Superposition on a crater's rim
Donner Q	95.63	-34.29	Crater with localized slumps	Boundary	Y	-	0.34	0.39	Y	Y	Superposition on a crater's rim
Donner R	92.28	-34.34	Crater with localized slumps	Boundary	N	-	0.23	0.22	Y	Y	Superposition on a crater's rim
Donner V	95.58	-30.56	Crater with localized slumps	Highlands	N	-	0.89	0.82	Y	Y	Superposition on a crater's rim
Doppler W	197.86	-10.99	Simple crater	Highlands	Y	N	0.2	0.2	-	N	-
Dreyer R	94.47	8.49	Crater with localized slumps	Highlands	N	-	0.25	0.21	N	N	-
Dunthorne	328.29	-30.12	Simple crater	Highlands	Y	N	0.83	0.51	-	N	-
Erden F	188.89	62.98	Simple crater	Highlands	Y	N	1.89	0	-	Y	Superposition on a crater's rim
Endymion E	66.24	53.59	Simple crater	Highlands	N	N	0.7	0.4	-	N	-
Epimenides A	329.82	-43.26	Simple crater	Highlands	N	N	0.3	0.04	-	N	-
Franklin C	44.25	35.68	Crater with localized slumps	Highlands	Y	-	0.63	0.42	Y	Y	Superposition on a crater's rim
Fryxell	258.34	-21.25	Crater with localized slumps	Highlands	Y	-	0.86	0.24	N	N	-
G. Bond	36.32	32.38	Crater with localized slumps	Highlands	Y	-	0.73	0.39	Y	Y	Superposition on a crater's rim
Galilaei	297.16	10.48	Crater with localized slumps and terraces	Mare	Y	-	-	-	N	N	-
Gardner	33.81	17.74	Simple crater	Highlands	Y	N	0.64	0	-	N	-
Gauss A	82.76	36.54	Crater with localized slumps	Highlands	N	-	0.73	0.43	Y	Y	Truncation against a crater's rim
Gauss J	72.65	40.57	Crater with localized slumps	Highlands	Y	-	0.55	0.26	Y	Y	Superposition on a crater's rim
Geissler	76.5	-2.59	Crater with localized slumps	Highlands	Y	-	0.21	0.15	N	N	-
Geminus D	47.29	30.57	Simple crater	Highlands	N	Y	0.3	0.2	-	Y	Superposition on a crater's rim
Glaisher	49.34	13.18	Simple crater	Highlands	N	N	0.7	0.5	-	N	-
Glauber	142.66	11.31	Simple crater	Highlands	Y	N	0.6	0.4	-	Y	Superposition on a crater's rim
Golitsyn J	256.79	-27.68	Simple crater	Highlands	Y	N	0.36	0	-	Y	Superposition on a crater's rim
Gruithuisen	320.22	32.88	Crater with localized slumps	Mare	Y	-	-	-	N	N	-
Guillaume J	189.48	43.56	Simple crater	Highlands	Y	N	0.1	0.1	-	N	-
Gullstrand C	232.9	46.57	Simple crater	Highlands	N	N	0.38	0.25	-	N	-
Gutenberg A	39.91	-9.03	Simple crater	Highlands	N	Y	0.9	0.2	-	Y	Superposition on a crater's rim
Hagen Q	133.29	-50.33	Crater with localized slumps	Highlands	N	-	0.75	0.35	N	N	-
Hahn A	69.72	29.66	Crater with localized slumps	Highlands	Y	-	0.35	0.31	N	N	-
Hahn B	76.97	31.37	Crater with localized slumps	Highlands	N	-	0.69	0.14	N	N	-
Harden	143.54	5.46	Simple crater	Highlands	N	N	0.2	0.1	-	N	-
Harkhebi T	95.31	40.04	Crater with localized slumps	Highlands	N	-	0.53	0.1	N	N	-
Hatanaka Q	235.34	25.99	Crater with localized slumps	Highlands	N	-	0.79	0.53	N	N	-
Heinsius A	342.38	-39.77	Crater with localized slumps	Highlands	Y	-	0.58	0.12	Y	Y	Superposition on a crater's terrace

Table A-2 contd.

Name	Longitude (°E)	Latitude (°N)	Morphological class	Target	Layering on walls of craters (Y/N)	Visible Melt on floor of Simple crater (Y/N)	Elevation variation of Highlands terrain surrounding Simple craters and Craters with localized slumps (km)	Std. Dev. of Elevation variation of Highlands terrain surrounding Simple craters and Craters with localized slumps (km)	Transitional craters formed on sharp Topographic Breaks (Y/N)?	Excluded from Close Proximity Analyses (Y/N)?	Reason for exclusion from Close Proximity Analyses
Hendrix	200.06	-46.86	Crater with localized slumps and terraces	Highlands	Y	-	-	-	N	N	-
Herigonius	326.03	-13.35	Crater with localized slumps	Mare	Y	-	-	-	N	N	-
Hermann	302.53	-0.87	Crater with localized slumps, terraces and central uplift	Mare	Y	-	-	-	-	N	-
Heyrovsky Hill	264.57	-39.55	Simple crater	Highlands	N	N	0.9	0.45	-	N	-
Hipparchus C	40.81	20.91	Simple crater	Highlands	Y	Y	0.28	0.28	-	N	-
Hommel J	8.21	-7.41	Simple crater	Highlands	N	Y	0.88	0.5	-	N	-
	27.87	-53.53	Crater with localized slumps	Highlands	N	-	0.4	0.15	N	N	-
Hooke D	55.8	40.69	Crater with localized slumps	Highlands	Y	-	0.7	0.27	Y	Y	Superposition on a crater's rim
Hypatia A	22.21	-4.9	Crater with localized slumps	Highlands	N	-	1.16	0.77	Y	Y	Superposition on a crater's rim
Inghirami C	285.41	-44.07	Simple crater	Highlands	N	Y	0.44	0.4	-	N	-
Isidorus D	34.07	-4.27	Simple crater	Highlands	Y	N	0.13	0.09	-	N	-
Jacobi J	10.27	-57.96	Simple crater	Highlands	N	Y	0.54	0.54	-	Y	Truncation against a crater's rim
Janssen K	42.31	-46.19	Simple crater	Highlands	Y	Y	0.34	0.07	-	N	-
Joule K	218.15	25.64	Simple crater	Highlands	N	N	0.44	0.24	-	Y	Truncation against a crater's rim
Kekule M	221.97	12.05	Crater with localized slumps	Highlands	N	-	0.98	0.41	N	N	-
Kies A	337.23	-28.36	Crater with localized slumps	Mare	Y	-	-	-	N	N	-
Kircher E	309.64	-69.05	Crater with localized slumps	Highlands	N	-	0.4	0.24	Y	Y	Truncation against a crater's rim
Kirkwood T	194.73	68.98	Simple crater	Highlands	N	Partially shadowed floor in NACs	0.99	0.95	-	Y	Superposition on a crater's rim
Korolev V	197.94	-1.21	Crater with localized slumps	Highlands	Y	-	0.73	0.29	N	N	-
Korolev Y	201.53	-0.5	Crater with localized slumps	Highlands	Y	-	0.35	0.28	N	N	-
Kurchatov X	140.07	41.18	Simple crater	Highlands	N	Y	0.79	0.45	-	N	-
la Condamine A	329.8	54.43	Crater with localized slumps	Highlands	Y	-	0.3	0.28	N	N	-
la Condamine B	328.33	58.87	Crater with localized slumps	Mare	Y	-	-	-	N	N	-
Lallemand	275.79	-14.4	Crater with localized slumps	Highlands	Y	-	0.46	0.46	Y	Y	Superposition on a crater's rim
Langrenus M	66.41	-9.81	Simple crater	Highlands	N	Y	0.58	0.22	-	N	-
Lehmann C	309.83	-35.57	Simple crater	Highlands	Y	N	1.05	0.64	-	N	-
Lents J	262.62	-3.63	Simple crater	Highlands	Y	Y	0.58	0.33	-	N	-
Leucippus K	244.49	27.27	Crater with localized slumps	Highlands	Y	-	0.54	0.22	N	N	-
Leuschner Z	250.43	5.24	Crater with localized slumps	Highlands	Y	-	1.41	0.65	N	N	-
Lichtenberg	292.28	31.85	Crater with localized slumps	Mare	Y	-	-	-	Y	Y	Superposition on a crater's rim
Liouville	73.56	2.72	Simple crater	Highlands	Y	N	0.38	0.18	-	Y	Superposition on a crater's rim
Lippmann J	253.68	-58.74	Simple crater	Highlands	Y	Partially shadowed floor in NACs	0.91	0.83	-	N	-
Lowell W	252.79	-10.16	Simple crater	Highlands	N	N	1.15	1	-	Y	Truncation against a crater's rim
Lyot D	82.53	-51.69	Crater with localized slumps	Highlands	Y	-	0.73	0.25	Y	Y	Superposition on a crater's terrace

Table A-2 contd.

Name	Longitude (°E)	Latitude (°N)	Morphological class	Target	Layering on walls of craters (Y/N)	Visible Melt on floor of Simple crater (Y/N)	Elevation variation of Highlands terrain surrounding Simple craters and Craters with localized slumps (km)	Std. Dev. of Elevation variation of Highlands terrain surrounding Simple craters and Craters with localized slumps (km)	Transitional craters formed on sharp Topographic Breaks (Y/N)	Excluded from Close Proximity Analyses (Y/N)	Reason for exclusion from Close Proximity Analyses
Mairan A	321.21	38.63	Crater with localized slumps	Highlands	Y	-	0.15	0.12	N	N	-
Manners	19.99	4.57	Floor-fractured crater	Mare	Y	-	-	-	-	N	-
Manzinus E	25.15	-68.98	Simple crater	Highlands	N	N	1.65	0.9	-	Y	Superposition on a crater's rim
Marius A	313.95	12.59	Crater with localized slumps	Mare	Y	-	-	-	N	N	-
Maunder A	269.38	-3.28	Simple crater	Highlands	Y	N	0.33	0.16	-	N	-
Maury	39.69	37.11	Simple crater	Highlands	Y	Y	0.41	0.13	-	Y	Superposition on a crater's rim
Mendel B	252.33	-46.52	Crater with localized slumps	Highlands	Y	-	0.95	0.53	Y	Y	Superposition on a crater's rim
Mersenius S	312.93	-19.22	Crater with localized slumps	Highlands	N	-	0.46	0.26	Y	Y	Superposition on a crater's rim
Messala B	59.8	37.37	Crater with localized slumps	Highlands	N	-	1.28	0.37	Y	Y	Superposition on a crater's rim
Minnaert C	183.78	-64.36	Crater with localized slumps	Highlands	N	-	1.29	1.41	Y	Y	Superposition on a crater's rim
Moigno A	29.71	64.81	Crater with localized slumps	Highlands	Y	-	0.19	0.06	Y	Y	Superposition on a crater's rim
Mutus L	24.81	-61.84	Simple crater	Highlands	N	N	0.29	0.36	-	N	-
Mutus P	25.55	-59.16	Simple crater	Highlands	N	N	0.2	0.18	-	N	-
Nicollet	347.5	-21.95	Crater with localized slumps	Mare	Y	-	-	-	N	N	-
Nikolaev J	155.42	31.59	Simple crater	Highlands	N	Y	0.61	0.36	-	N	-
Noggerath J	311.98	-48.47	Crater with localized slumps	Highlands	Y	-	0.24	0.09	Y	Y	Superposition on a crater's rim
Olbers B	285.79	6.84	Crater with localized slumps	Highlands	N	-	0.55	0.34	N	N	-
Parenago Z	250.71	28.96	Crater with localized slumps	Highlands	N	-	0.41	0.4	N	N	-
Peirce	53.35	18.26	Crater with localized slumps, terraces and central uplift	Mare	Y	-	-	-	-	N	-
Piccolomini D	32.26	-26.95	Crater with localized slumps	Highlands	Y	-	0.34	0.24	Y	Y	Superposition on a crater's terrace
Pickering	6.99	-2.87	Simple crater	Highlands	Y	Y	0.33	0.17	-	N	-
Pingre J	291.03	-59.05	Crater with localized slumps	Highlands	N	-	0.36	0.06	Y	Y	Superposition on a crater's rim
Planck W	131.27	-55.44	Simple crater	Highlands	N	N	0.05	0.06	-	Y	Superposition on a crater's rim
Poincare C	168.7	-54.59	Crater with localized slumps	Highlands	Y	-	0.25	0.17	N	N	-
Poincare X	161.18	-53.91	Crater with localized slumps	Highlands	N	-	0.6	0.32	Y	Y	Superposition on a crater's rim
Polybius A	27.97	-23.04	Simple crater	Highlands	N	N	0.35	0.12	-	N	-
Pontecoulant A	62.79	-57.68	Simple crater	Highlands	N	Partially shadowed floor in NACs	0.49	0.14	-	N	-
Posidonius P	27.58	33.62	Crater with localized slumps and terraces	Mare	Y	-	-	-	N	N	-
Pytheas	339.4	20.56	Crater with localized slumps	Mare	Y	-	-	-	N	N	-
Ramon	211.78	-41.27	Crater with localized slumps	Highlands	N	-	0.88	0.83	Y	Y	Superposition on a crater's rim
Rayleigh B	88.5	29.05	Crater with localized slumps	Highlands	Y	-	0.41	0.14	N	N	-
Riccioli H	284.96	1.11	Simple crater	Highlands	Y	Y	0.3	0.2	-	N	-
Richards	140.09	7.7	Simple crater	Highlands	N	N	0.13	0.05	-	N	-
Roberts Q	177.65	68.38	Crater with localized slumps	Highlands	N	-	1.61	0.83	Y	Y	Superposition on a crater's rim

Table A-2 contd.

Name	Longitude (°E)	Latitude (°N)	Morphological class	Target	Layering on walls of craters (Y/N)	Visible Melt on floor of Simple crater (Y/N)	Elevation variation of Highlands terrain surrounding Simple craters and Craters with localized slumps (km)	Std. Dev. of Elevation variation of Highlands terrain surrounding Simple craters and Craters with localized slumps (km)	Transitional craters formed on sharp Topographic Breaks (Y/N)	Excluded from Close Proximity Analyses (Y/N)	Reason for exclusion from Close Proximity Analyses
Ryder	143.29	-43.87	Crater with localized slumps	Highlands	Y	-	2.18	1	Y	Y	Superposition on a crater's rim
Saenger C	104.35	6.25	Simple crater	Highlands	N	N	1.5	1.08	-	Y	Truncation against a crater's rim
Saenger X	102.17	6.39	Crater with localized slumps	Highlands	N	-	0.85	0.51	Y	Y	Superposition on a crater's rim
Safarik H	178.54	9.53	Simple crater	Highlands	N	N	0.69	0.55	-	N	-
Sanford C	222.61	33.8	Simple crater	Highlands	N	N	0.2	0.22	-	N	-
Santbech B	41.57	-24.73	Simple crater	Highlands	N	N	0.79	0.43	-	N	-
Schickard H	297.66	-43.52	Simple crater	Highlands	Y	N	0.2	0	-	N	-
Schliemann G	156.7	-2.23	Crater with localized slumps	Highlands	N	-	0.33	0.46	Y	Y	Superposition on a crater's rim
Schliemann W	152.35	0.26	Simple crater	Highlands	N	N	0.41	0.35	-	Y	Superposition on a crater's rim
Schwarzschild Q	108.83	66.24	Crater with localized slumps	Highlands	N	-	0.73	0	N	N	-
Schwarzschild T	107.63	69.82	Simple crater	Highlands	N	N	0.56	0.47	-	N	-
Seneca F	81.93	29.63	Crater with localized slumps	Highlands	N	-	0.69	0.45	Y	Y	Superposition on a crater's rim
Sharp A	317.32	47.63	Crater with localized slumps	Highlands	N	-	0.31	0.08	N	N	-
Sherrington	118	-11.13	Crater with localized slumps	Highlands	N	-	2.5	1.74	Y	Y	Superposition on a crater's rim
Sisakyan C	111.03	41.98	Simple crater	Highlands	Y	Y	0.48	0.29	-	Y	Superposition on a crater's rim
Spencer Jones H	168.12	11.93	Simple crater	Highlands	Y	Y	0.3	0.14	-	N	-
Steinheil G	49.98	-45.69	Crater with localized slumps	Highlands	N	-	0.29	0	Y	Y	Superposition on a crater's rim
Stetson N	239.57	-43.2	Crater with localized slumps	Highlands	Y	-	0.7	0.38	N	N	-
Sumner G	110.41	37.42	Simple crater	Highlands	Y	N	0.43	0.15	-	N	-
Sundman V	266.44	11.96	Simple crater	Highlands	Y	Y	0.26	0.28	-	N	-
Swann C	114.28	52.9	Crater with localized slumps	Highlands	N	-	0.18	0.05	N	N	-
Thebit A	355.07	-21.58	Crater with localized slumps	Highlands	Y	-	0.65	0.12	Y	Y	Superposition on a crater's rim
Theon Junior	15.79	-2.41	Crater with localized slumps	Highlands	N	-	0.35	0.31	N	N	-
Theon Senior	15.42	-0.81	Crater with localized slumps	Highlands	N	-	0.36	0.36	N	N	-
Tiling G	231.29	-52.85	Crater with localized slumps	Highlands	N	-	1.06	0.83	Y	Y	Superposition on a crater's rim
Tiselius E	177.83	7.17	Crater with localized slumps	Highlands	N	-	0.73	0.86	Y	Y	Superposition on crater's outer wall
Tralles A	47.03	27.42	Simple crater	Highlands	Y	Y	0.2	0.1	-	N	-
Unnamed10	140.87	25.78	Crater with localized slumps	Highlands	N	-	1.23	0.83	Y	Y	Superposition on a crater's rim
Unnamed11	149.17	-60.59	Crater with localized slumps	Highlands	N	-	0.79	0.48	Y	Y	Superposition on a crater's rim
Unnamed12	152.25	56.68	Simple crater	Highlands	N	Y	0.99	0.73	-	Y	Superposition on a crater's rim
Unnamed13	167.22	-46.84	Simple crater	Highlands	N	Y	0.43	0.16	-	N	-
Unnamed14	172.54	64.4	Simple crater	Highlands	N	N	0.61	0.26	-	N	-
Unnamed15	175.66	66.32	Simple crater	Highlands	Y	N	0.6	0.4	-	N	-
Unnamed16	176.71	34.92	Crater with localized slumps	Highlands	N	-	0.85	0.64	N	N	-
Unnamed17	181.38	53.45	Simple crater	Highlands	N	N	1.28	0.66	-	N	-
Unnamed18	181.85	8.79	Simple crater	Highlands	N	N	0.94	0.65	-	Y	Superposition on a crater's rim
Unnamed19	183.76	-57.33	Crater with localized slumps	Highlands	N	-	0.23	0.22	Y	Y	Superposition on a crater's rim
Unnamed2	90.33	-56.32	Crater with localized slumps	Highlands	Y	-	1.93	0.15	Y	Y	Superposition on a crater's terrace
Unnamed20	188.7	44.43	Simple crater	Highlands	Y	Y	0.39	0.21	-	N	-
Unnamed21	189.65	36.54	Simple crater	Highlands	N	N	0.89	0.99	-	N	-

Table A-2 contd.

Name	Longitude (°E)	Latitude (°N)	Morphological class	Target	Layering on walls (Y/N)	Visible Melt on floor of Simple crater (Y/N)	Elevation variation of Highlands terrain surrounding Simple craters and Craters with localized slumps (km)	Std. Dev. of Elevation variation of Highlands terrain surrounding Simple craters and Craters with localized slumps (km)	Transitional craters formed on sharp Topographic Breaks (Y/N)	Excluded from Close Proximity Analyses (Y/N)	Reason for exclusion from Close Proximity Analyses
Unnamed22	190.16	-48.7	Crater with localized slumps	Highlands	N	-	0.66	0.35	Y	Y	Superposition on a crater's rim
Unnamed23	190.87	52.21	Simple crater	Highlands	N	Y	0.73	0.4	-	N	-
Unnamed24	191.06	47.24	Simple crater	Highlands	Y	Y	0.21	0.09	-	N	-
Unnamed25	192.21	-31.99	Crater with localized slumps	Highlands	N	-	1.43	0.51	Y	Y	Superposition on a crater's rim
Unnamed26	192.81	-60.35	Simple crater	Highlands	N	Partially shadowed floor in NACs	0.75	0.2	-	Y	Superposition on a crater's rim
Unnamed27	193.63	14.04	Simple crater	Highlands	N	Y	0.58	0.43	-	N	-
Unnamed28	203.12	29.1	Simple crater	Highlands	N	N	0.94	0.24	-	N	-
Unnamed29	207.7	-45.6	Simple crater	Highlands	Y	Y	0.48	0.36	-	Y	Superposition on a crater's rim
Unnamed3	114.29	29.73	Crater with localized slumps	Highlands	Y	-	0.78	0.56	Y	Y	Superposition on a crater's rim
Unnamed30	208.56	32.18	Simple crater	Highlands	N	N	0.41	0.37	-	Y	Elliptical crater
Unnamed31	218.59	18.32	Simple crater	Highlands	N	Y	0.56	0.27	-	N	-
Unnamed32	223.52	-36.9	Simple crater	Highlands	N	N	1.39	0	-	Y	Superposition on crater's outer wall
Unnamed33	224.18	15.15	Crater with localized slumps	Highlands	N	-	0.75	0.26	N	N	-
Unnamed34	224.35	-46.16	Crater with localized slumps	Highlands	Y	-	0.89	0.51	Y	Y	Superposition on a crater's rim
Unnamed35	224.98	-1.9	Simple crater	Highlands	Y	Y	0.25	0.17	-	N	-
Unnamed36	225.13	-44.87	Crater with localized slumps	Highlands	N	-	0.53	0	N	N	-
Unnamed37	227.2	-2.74	Crater with localized slumps	Highlands	Y	-	0.49	0.54	Y	Y	Superposition on a crater's rim
Unnamed38	234.89	-38.55	Crater with localized slumps	Highlands	N	-	0.61	0.43	Y	Y	Superposition on a crater's rim
Unnamed39	235.66	-1.36	Simple crater	Highlands	N	N	0.8	0.42	-	N	-
Unnamed40	127.2	62.73	Simple crater	Highlands	N	N	0.25	0.21	-	N	-
Unnamed40	237.77	-65.74	Simple crater	Highlands	N	Partially shadowed floor in NACs	1.05	0	-	Y	Superposition on a crater's rim
Unnamed42	238.73	-67.84	Crater with localized slumps	Highlands	Y	-	0.91	0.57	Y	Y	Superposition on a crater's terrace
Unnamed43	241.4	-20.96	Simple crater	Highlands	Y	N	0.7	0.4	-	Y	Superposition on a crater's terrace
Unnamed44	247.29	-57.76	Simple crater	Highlands	N	Partially shadowed floor in NACs	0.96	0.72	-	Y	Superposition on a crater's terrace
Unnamed45	249.27	32.93	Crater with localized slumps	Highlands	N	-	1.29	1.1	Y	Y	Superposition on a crater's terrace
Unnamed46	253.65	71.2	Simple crater	Highlands	N	Partially shadowed floor in NACs	1	0.4	-	Y	Superposition on a crater's terrace
Unnamed47	254.34	41.01	Simple crater	Highlands	N	N	0.53	0.29	-	N	-
Unnamed48	262.34	64.8	Simple crater	Highlands	N	N	0.33	0.18	-	N	-
Unnamed49	264.16	29.45	Crater with localized slumps	Highlands	N	-	0.66	0.36	Y	Y	Superposition on a crater's rim
Unnamed5	127.57	-56.22	Simple crater	Highlands	N	N	0.73	0.66	-	Y	Superposition on a crater's terrace
Unnamed50	268.41	37.16	Simple crater	Highlands	N	N	0.5	0.2	-	N	-
Unnamed6	132.1	62.15	Simple crater	Highlands	N	N	0.38	0.1	-	Y	Superposition on a crater's rim
Unnamed7	134.77	44.88	Crater with localized slumps	Highlands	N	-	0.98	0.36	N	N	-
Unnamed8	137.65	23.62	Simple crater	Highlands	N	N	0.35	0.44	-	N	-
Unnamed9	139.37	44.52	Simple crater	Highlands	N	N	0.63	0.45	-	N	-
Van de Graaff C	172.81	-26.43	Crater with localized slumps	Highlands	Y	-	0.15	0.12	N	N	-
Van de Graaff F	174.71	-26.77	Crater with localized slumps	Highlands	Y	-	0.36	0.15	Y	Y	Superposition on a crater's terrace
Van de Graaff Q	171.36	-27.62	Crater with localized slumps	Highlands	Y	-	0.31	0.21	Y	Y	Truncation against a crater's rim

Table A-2 contd.

Name	Longitude (°E)	Latitude (°N)	Morphological class	Target	Layering on walls of craters (Y/N)	Visible Melt on floor of Simple crater (Y/N)	Elevation variation of Highlands terrain surrounding Simple craters and Craters with localized slumps (km)	Std. Dev. of Elevation variation of Highlands terrain surrounding Simple craters and Craters with localized slumps (km)	Transitional craters formed on sharp Topographic Breaks (Y/N)	Excluded from Close Proximity Analyses (Y/N)	Reason for exclusion from Close Proximity Analyses
van den Bergh M	200.75	30.35	Crater with localized slumps	Highlands	N	-	1.26	0.64	Y	Y	Superposition on a crater's rim
van den Bergh P	199.81	29.2	Simple crater	Highlands	N	N	0.45	0.51	-	Y	Superposition on a crater's rim
Ventris B	158.08	-2.22	Simple crater	Highlands	N	N	0.73	0.41	-	Y	Superposition on a crater's rim
Ventris M	157.89	-5.68	Crater with localized slumps	Highlands	Y	-	1.83	1.16	Y	Y	Superposition on a crater's rim
Vestine A	94.57	36.01	Simple crater	Highlands	N	N	0.78	0.53	-	Y	Superposition on a crater's rim
Vetchinkin P	130.56	7.06	Simple crater	Highlands	N	N	0.78	0.21	-	Y	Superposition on a crater's rim
Virchow	83.76	9.88	Crater with localized slumps and terraces	Mare	Y	-	-	-	Y	Y	Superposition on a crater's terrace
Viviani N	116.5	3.49	Simple crater	Highlands	N	N	0.15	0.13	-	N	-
Vlacq A	39	-51.28	Simple crater	Highlands	N	N	1.19	0.55	-	Y	Superposition on a crater's rim
von Bekesy F	137.04	52.8	Simple crater	Highlands	N	Y	0.55	0.53	-	Y	Superposition on a crater's rim
von der Pahlen V	223.98	-23.78	Crater with localized slumps	Highlands	N	-	1.15	0.72	Y	Y	Superposition on a crater's rim
W. Bond B	7.51	65.03	Simple crater	Highlands	Y	Partially shadowed floor in NACs	0.03	0.05	-	N	-
Wargentín D	294.7	-51.03	Simple crater	Highlands	Y	N	0.2	0.1	-	N	-
Wilhelm A	337.88	-44.69	Crater with localized slumps	Highlands	Y	-	0.59	0.71	Y	Y	Superposition on a crater's rim
Wurzelbauer A	344.58	-35.74	Simple crater	Highlands	N	N	0.63	0.57	-	N	-
Zeno K	66.73	42.83	Crater with localized slumps	Highlands	N	-	0.43	0.32	Y	Y	Superposition on a crater's rim

Table A-3. List of the groups of close proximity craters. This table also includes the locations, diameters, d/D s of the craters and discussion of observed similarities or differences in the morphologies and geologic settings of the craters in each group.

Group	Crater number	Crater Name	Latitude (°N)	Longitude (°E)	Diameter (km)	Nearest neighbour distance (km)	Morphology	Target	d/D	Std. Dev. (d/D)	Similarity (S)/Difference (D) in morphologies?	Similarity (S)/Difference (D) in d/D s if S in morphologies?	Terrain signatures
A	1	Unnamed24	47.24	191.1	15.6		Simple crater	Highlands	0.21	0.01			Gradually sloping or flat highland terrains
	2	Unnamed20	44.43	188.7	17.9	1-2: 98, 2-3: 33	Simple crater	Highlands	0.20	0.01	S	S	
	3	Guillaume J	43.56	189.5	16.6		Simple crater	Highlands	0.18	0.01			
B	1	Unnamed7	44.88	134.8	19.4		Crater with localized slumps	Highlands	0.16	0.02			Crater 1 could form on optically unrecognized topographic break or could have undergone post-crater modification or undergo slumping by influence of some impactor property. Crater 2 and Crater 3 are
	2	Unnamed9	44.52	139.4	15.3	1-2: 100, 2-3: 102	Simple crater	Highlands	0.19	0.02	D	-	
	3	Kurchatov X	41.18	140.1	16.8		Simple crater	Highlands	0.18	0.02			
C	1	Theon Senior	-0.81	15.42	17.6		Crater with localized slumps	Highlands	0.19	0.01			Slumping influenced by a sharp topographic break obscured by ejecta of nearby crater and/or strength degradation of target by basin
	2	Theon Junior	-2.41	15.79	17.7	1-2: 51	Crater with localized slumps	Highlands	0.17	0.01	S	D	
D	1	Congreve G	-0.89	196.1	17.6		Simple crater	Highlands	0.18	0.02			Crater 1 occurs on smooth ejecta blanket, crater 2 on the terrace and crater 3 on the subdued peak ring of buried crater
	2	Korolev V	-1.21	197.9	19.6	1-2: 56, 2-3: 111	Crater with localized slumps	Highlands	0.17	0.01	D	-	
	3	Korolev Y	-0.5	201.5	19.1		Crater with localized slumps	Highlands	0.20	0.01			
E	1	Hill	20.91	40.81	15.7		Simple crater	Highlands	0.21	0.01			Carmichael exhibits more extensive layering of mare basalts on its walls
	2	Carmichael	19.53	40.36	19.7	1-2: 45	Crater with localized slumps	Mare	0.19	0.01	D	-	
F	1	Dionysius	2.77	17.29	18.0		Crater with localized slumps	Mare	0.16	0.01			Rayed Dionysius occurs in the mare adjacent to the lithologic boundary and has layering on its walls, non-rayed Manners is surrounded by arcuate rilles which indicates that tectonic processes shaped its floor
	2	Manners	4.57	19.99	15.0	1-2: 98	Floor-fractured crater	Mare	0.11	0.01	D	-	
G	1	Cooper G	52.42	178.8	19.2		Simple crater	Highlands	0.14	0.01			Gradually sloping or flat highland terrains
	2	Unnamed17	53.45	181.4	17.2	1-2: 57	Simple crater	Highlands	0.17	0.02	S	S	

Group	Crater number	Crater Name	Latitude (°N)	Longitude (°E)	Diameter (km)	Nearest neighbour distance (km)	Morphology	Target	d/D	Std. Dev. (d/D)	Similarity (S)/Difference (D) in morphologies?	Similarity (S)/Difference (D) in d/Ds if S in morphologies?	Terrain signatures
H	1	Unnamed14	64.4	172.5	17.1	1-2: 57	Simple crater	Highlands	0.18	0.02	S	S	Gradually sloping or flat highland terrains
	2	Unnamed15	66.32	175.7	18.0		Simple crater	Highlands	0.18	0.02			
I	1	Mutus L	-61.8	24.81	19.6	1-2: 81	Simple crater	Highlands	0.14	0.02	S	S	Gradually sloping or flat highland terrains
	2	Mutus P	-59.2	25.55	15.5		Simple crater	Highlands	0.16	0.01			
J	1	Schwarzschild T	69.82	107.6	16.2	1-2: 109	Simple crater	Highlands	0.20	0.02	D	-	Slumping in Crater 2 influenced by a sharp topographic break obscured by ejecta of nearby crater, or by impactor properties
	2	Schwarzschild Q	66.24	108.8	17.6		Crater with localized slumps	Highlands	0.15	0.02			
K	1	Kekule M	12.05	222	19.4	1-2: 114	Crater with localized slumps	Highlands	0.18	0.02	S	S	Slumping influenced by a sharp topographic break obscured by ejecta of Orientale and/or strength degradation of target by basin ejecta, or by impactor properties
	2	Unnamed33	15.15	224.2	18.4		Crater with localized slumps	Highlands	0.16	0.02			
L	1	Richards	7.7	140.1	17.1	1-2: 124	Simple crater	Highlands	0.18	0.01	S	S	Both craters occur on a topographically smooth floor of a pre-existing, larger crater
	2	Harden	5.46	143.5	15.1		Simple crater	Highlands	0.19	0.02			

References

- Arvidson, R., et al. (1979), Standard techniques for presentation and analysis of crater size-frequency data, *Icarus*, 37(2), 467-474, doi: [https://doi.org/10.1016/0019-1035\(79\)90009-5](https://doi.org/10.1016/0019-1035(79)90009-5).
- Hartmann, W. (1984), Does "saturation" cratering exist in the solar system? Paper presented at Lunar and Planetary Science Conference, Houston, TX.
- Haruyama, J., Ohtake, M., Matsunaga, T., Morota, T., Honda, C., Yokota, Y., Ogawa, Y., and Group, L. W. (2009), Selene (Kaguya) terrain camera observation results of nominal mission period. Paper presented at 40th Lunar and Planetary Science Conference, Houston, TX.
- Neukum, G. (1983), Meteoritenbombardement und datierung planetarer oberflächen, Ludwig Maximilianis Univ., Munich, Germany.
- Neukum, G., and Ivanov, B. A. (1994), Crater size distributions and impact probabilities on Earth from lunar, terrestrial-planet, and asteroid cratering data. In *Hazards due to Comets and Asteroids*, edited by T. Gehrels, pp. 359-416, University of Arizona Press, Tucson, AZ.
- Neukum, G., Ivanov, B. A., and Hartmann, W. K. (2001), Cratering records in the inner solar system in relation to the lunar reference system, *Space Science Reviews*, 96, 55-86, doi: <https://doi.org/10.1023/A:1011989004263>.
- Neukum, G., König, B., and Arkani-Hamed, J. (1975a), A study of lunar impact crater size-distributions, *The Moon*, 12(2), 201-229, doi: <https://doi.org/10.1007/BF00577878>.
- Neukum, G., König, B., Fechtig, H., and Storzer, D. (1975b), Cratering in the Earth-Moon system-Consequences for age determination by crater counting. Paper presented at 6th Lunar and Planetary Science Conference Proceedings, Houston, TX.

CHAPTER 3 GEOLOGIC INVESTIGATION OF DEEP SIMPLE CRATERS IN THE LUNAR SIMPLE-TO-COMPLEX TRANSITION

Abstract

From a group of well-preserved lunar simple craters in the 15-20 km diameter range, and with the help of Lunar Orbiter Laser Altimeter (LOLA) topography data, we identified a subset of eight deep craters (depth/diameter ratio > 0.20). These craters are in the regions around the mare-highlands boundaries, which are characterized as having the highest porosity on the lunar surface. To understand the cratering mechanics behind the formation of these craters, a geologic investigation of the terrains of these craters was performed. We evaluated the depth/diameter ratios of smaller simple craters surrounding several 15-20 km diameter craters, analyzed the morphometry of the craters, and visually examined the cavities using multiple data sets. We conclude that deep transient cavities were formed from compaction of porous target material. The result was a deeper than normal simple crater without an identifiable increase in the volume of excavated material, as inferred from the craters' rim heights and shapes. While all of these craters formed in areas of high porosity, not all craters in high-porosity regions are deep. It may be that some unusual impactor property is also required to produce a deep crater, such as a high velocity impact, a near-vertical impact or a dense impactor that yielded a large penetration depth.

Chandnani, M., Herrick, R. R., & Kramer, G. Y. (2019). Geologic Investigation of Deep Simple Craters in the Lunar Simple-to-Complex Transition. *Journal of Geophysical Research: Planets*, doi: <https://doi.org/10.1029/2018JE005903>.

3.1 Introduction

3.1.1 Deep Simple Craters

Planetary impact crater formation can be considered conceptually as occurring in three stages (Melosh, 1989d; Melosh & Ivanov, 1999). In the contact and compression stage, a projectile impacts a target at high velocity (many km/s) and transfers a large portion of its kinetic energy to the target in the form of shock waves. These waves propagate through the substrate, fracturing and compressing it. The remaining kinetic energy is converted into internal energy which heats the target and projectile. The pressure release after the shock wave passes through the target, combined with the surface-directed pressure gradients, result in a radial outward and upward motion of the target material. This excavation stage causes the formation of a bowl-shaped cavity, the transient cavity (Dence, 1968). The growth of the cavity is determined primarily by target strength and surface gravity. For smaller craters, the target strength exceeds the lithostatic stresses at the cavity depth, which defines the strength regime of cratering. Above a certain crater size, the lithostatic stresses due to gravity surpass the target strength, thus transitioning the cratering process to the gravity regime (Holsapple, 1993b; Holsapple & Schmidt, 1982; Melosh, 1989f). Therefore, the cavity continues to widen until the kinetic energy of the target is too low to resist the strength of the material in the strength regime and the gravitational force in the gravity regime of impact cratering. Field studies and nuclear explosion experiments have revealed that the raised rim is a consequence of the structural uplift of the target rocks and the thickness of the ejecta blanket formed by the excavated material during the excavation stage (Roddy et al., 1977; Shoemaker, 1959; Shoemaker & Chao, 1961). Recent observational studies on lunar (Sharpton, 2014) and Martian craters (Sturm et al., 2016) have inferred structural uplift to be the primary contributor (>80%) of the elevated rim. The third stage, the modification stage, differentiates a simple crater from a complex crater. For impacts that produce craters of sizes less than the simple-to-complex transition diameter, minor

slumping stabilizes the cavity and forms a breccia lens on the floor in combination with some fallback ejecta and/or melt deposits. In this process, the bowl shape is largely retained and the resultant morphology is referred to as a simple crater (Melosh, 1989b). As the energy of the impact increases beyond the simple-to-complex transition threshold, the cavity enlarges and steepens until it is unable to sustain its shape; the crater center rebounds in the form of a central peak, and discrete blocks slump to form terraces (Collins, 2014), thus producing a complex crater (Hargitai & Öhman, 2014; Kenkmann et al., 2012; Melosh, 1989b; Pike, 1980a, b; Quaide et al., 1965).

The crater volume and depth in the gravity regime are primarily a function of the impact velocity, impactor size, impactor density, target density and target gravity (Holsapple, 1993a; Holsapple & Schmidt, 1982; Schmidt & Housen, 1987), with some potential influence of target friction, porosity and cohesion (Housen & Holsapple, 2011; Wünnemann et al., 2011). A typical simple crater has been modelled and measured to form with a depth/diameter (d/D) ratio of ~ 0.2 (Kenkmann et al., 2012; Melosh, 1989b; Melosh & Ivanov, 1999; Pike, 1976, 1980a) with the wall slope approaching the angle of repose of the substrate material. However, published results from experimental studies (Housen & Holsapple, 1999, 2003; Housen et al., 1999; Love et al., 1993) and numerical simulations (Collins et al., 2011; Wünnemann et al., 2006; Wünnemann et al., 2008) of hypervelocity impacts into porous materials have revealed that a certain amount (increases with porosity) of the impact energy is utilized in crushing of the pore space and compaction of the target material (Zel'dovich & Raizer, 1966). Increased impact melt may also occur with an increase in porosity (Kieffer, 1975; Wünnemann et al., 2008; Wünnemann et al., 2011). Shock waves generated by the remaining energy attenuate rapidly (Pierazzo et al., 1997; Zel'dovich & Raizer, 1966), leading to decreased values of ejection velocity and lower amounts of excavated material (Housen & Holsapple, 2003, 2011). The compaction of the pores leaves behind a permanent volume and therefore enhances the

depth of the cavity that is growing by excavation (Love et al., 1993). In case of very low-density targets such as rubble pile asteroids (~50% porosity (Britt et al., 2003; Veverka et al., 1999)) the large-sized craters located close to each other show no signs of ejecta filling from later adjacent impacts, possibly because the craters might have been created out of compaction of the pore space, with negligible excavation, a process termed “compaction-dominated” cratering (Housen & Holsapple, 2011, 2012; Housen et al., 1999; Prieur et al., 2017).

The effective strength that accounts for the weakening of the transient cavity and its collapse has been determined to be much lower than the cohesion of intact rocks (Güldemeister et al., 2015; Kenkmann et al., 2012; Melosh, 1977, 1989b). Consequently, if the target strength increases to cross a certain threshold, the target can resist collapse. Several simple craters that are deeper than fresh craters in the northern lowlands of Mars were discovered in the southwestern Utopia Planitia and Isidis Planitia regions of Mars (Boyce et al., 2005a; Boyce et al., 2005b; Boyce et al., 2006; Garvin et al., 2000; Pike, 1980a). With the help of high-resolution thermal infrared, optical and topography data, Boyce et al. (2006), in agreement with Pike (1980a), suggested that strong targets stabilized the transient cavities and prevented rim collapse, thus resulting in larger-than-normal depths.

The transition from simple to complex crater morphology on the Moon takes place over a range of diameters that varies geographically. Several values for the transition diameter on the Moon have been estimated that vary with the criteria and data sets used for defining them (Croft, 1985; Pike, 1977b, 1980a, b, 1988). The coherent but layered nature of younger (Hiesinger et al., 2000; Shoemaker & Hackman, 1962) mare may aid in uniform cavity collapse in the form of terraces (Cintala et al., 1977; Cooper, 1977; Pike, 1980b; Quaide & Oberbeck, 1968; Roddy, 1977; Smith & Hartnell, 1978), hence a smaller transition size (Krüger et al., 2018; Pike, 1980a, b), as opposed to non-pervasive slumping of material in craters formed on the older, regolith-dominated highlands (Soderblom et al., 2015). Globally for the Moon, a

transition size range of 15-20 km overlaps with the published values. For a fixed target, impact velocity, impact angle, impactor size, and impactor composition, the volume of the transient crater cavity scales with impact energy to the power 0.78 (Holsapple, 1993b; Holsapple & Schmidt, 1982; Melosh, 1989e; Schmidt & Housen, 1987). Consequently, a crater diameter range of 15-20 km corresponds to a factor of ~ 3 in the magnitude of impact energy, although considerably larger impactor energy differences could be present in this size range.

The 15-20 km diameter range spans a diversity of crater morphologies on the Moon. The morphological differences in similar-sized craters can be governed by variations in target properties and/or impactor parameters. To determine the factors behind these morphological differences, Chandnani et al. (2019) performed a geologic investigation of 244 well-preserved lunar craters in the 15-20 km size range. Craters with sharp rims, distinctly visible features and no apparent post-impact degradation (class 1 craters defined by Arthur et al., 1964) were selected. Using high resolution Lunar Reconnaissance Orbiter Camera (Robinson et al., 2010) Wide Angle Camera (LROC WAC), LROC Narrow Angle Camera (NAC) images and Lunar Orbiter Laser Altimeter (LOLA) (Smith et al., 2011) gridded topography (Gridded Data Records (GDR)) data, Chandnani et al. (2019) classified craters based on cavity shape and its components (for example, presence of localized slumped material terraces central uplift, floor fractures) into 7 morphologies:

[1] Simple crater;

[2] Crater with localized slumps;

[3] Crater with localized slumps and terraces;

[4] Crater with localized slumps and central uplift;

[5] Crater with localized slumps, terraces and central uplift;

[6] Concentric crater and

[7] Floor-fractured crater.

From the group of 244 craters, Chandnani et al. (2019) identified 117 simple craters based on uniform wall slopes and roughly bowl-shaped cavities, and observed that they are confined to flat or gradually sloping surfaces of the highlands and complex craters (the ones with central uplift) are more abundant in the mare. The study suggested that formation of simple craters is favored by a substrate whose attributes (strength, lithology, topography) are spatially and vertically homogeneous (weaker but non-layered highlands), whereas heterogeneity in terrain properties (layering in mare) facilitates cavity collapse, hence formation of shallower, complex craters (also previously reported by Cintala et al., 1977; Cooper, 1977; Dence, 1972; Osinski et al., 2018; Pike, 1980a; Quaide & Oberbeck, 1968; Roddy, 1977; Senft & Stewart, 2008; Smith & Hartnell, 1978; Stewart & Valiant, 2006). Simple craters have been observed, experimented and modeled to form with a d/D of ~ 0.2 on targets that have bulk properties such that they can be considered cohesionless, largely homogeneous and not unusually porous (Kenkmann et al., 2012; Melosh, 1989b; Melosh & Ivanov, 1999; Pike, 1974, 1977a, 1980a; Salamunićcar et al., 2012; Wood & Anderson, 1978). A recent study from Krüger et al. (2018) of lunar fresh craters with $D > \sim 3$ km shows that for highland craters there is a broad distribution in d/D from 0.1 to 0.25. The mean is 0.191 with a standard deviation of 0.023; about 35% of highland simple craters have a d/D ratio larger than 0.2. Based on the historical citations of 0.2 as a solar-system wide mean for fresh craters, and the recent work of Krüger et al. (2018), we set the threshold for a "deep" crater as one with a d/D that exceeds 0.200 by more than the standard deviation in the d/D value; six of the 117 simple craters in Chandnani et al. (2019) met this criterion. These craters occur in the highlands in proximity to the mare-highlands boundaries or within the ejecta blanket of the mare basins. The WAC images and orthogonal cross-sectional profiles of three such craters are shown in Figure 3.1. These six craters are thus both remarkably deep and of large diameter for lunar simple craters. In this

work we explore these craters and their surroundings to evaluate potential causes for their unusual shapes.

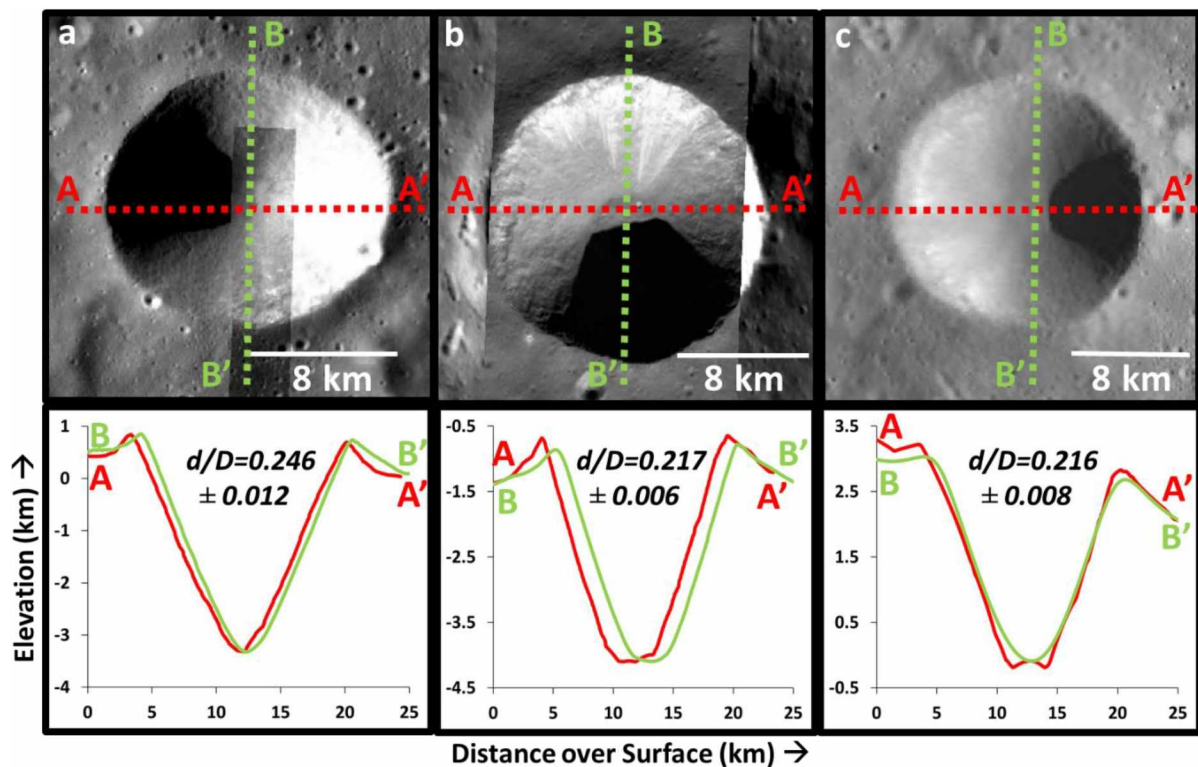


Figure 3.1. WAC images and orthogonal cross-sectional profiles of deep simple craters that were identified using LOLA gridded topography data. Their locations on the lunar surface are labelled in Figure 3.4. Their d/D s are listed in Table 3.1. The geographic coordinates of their centers are: a) Polybius A: -23.04°N , 27.97°E , b) W. Bond B: 65.03°N , 7.51°E and c) Unnamed39: -1.36°N , 235.66°E . For enhancing the visibility of the cavities, a) M1113978438L and b) NAC M188208338L and NAC M188201190R and have been used. North is up in all images.

3.1.2 Objectives

The deep craters show a correlation with target setting: proximity to mare-highlands contact. Therefore, our focus is on target properties as a plausible explanation for the larger-than-normal depths. We investigate the following two hypotheses for the origin of these deep craters:

3.1.2.1 Greater compaction of target with increase in porosity results in larger crater depths

The mare margins are characterized with the highest porosity (17-20%) on the Moon as shown by the red-orange shaded region in the surface porosity distribution map of Besserer et al. (2014) in Figure 3.4. The high porosity is most likely due to fracturing by impact-

generated shock waves and deposition of mare basin ejecta (Wieczorek et al., 2012). While the results of experiments and observations on impacts into porous targets have revealed that creation of crater volume (and hence crater depth) by compaction becomes more significant for porosity values above 35%, and compaction dominates the cratering process for highly porous targets (<50%) (Housen & Holsapple, 1999, 2003, 2011, 2012), compaction of a target can still occur in much lower but non-zero proportion relative to excavation as long as the target has porosity (Prieur et al., 2017). Therefore, we are suggesting a role for porosity in deepening and modestly altering the crater shape. The strong association of these deep craters in the most porous lunar geologic settings drives our thought that the contribution of porosity in influencing the cratering mechanics is non-negligible.

3.1.2.2 The highlands are more coherent in these locations and more resistant to minor slumping of the transient cavity

Intrusion into the highlands and crustal heating around the mare margins (Gong et al., 2016; Kiefer, 2013) fills in the cracks and pores in the highlands crust, leading to a more consolidated and cohesive highland substrate. In granular materials, friction coefficient plays an important role in determining the angle of repose (Melosh, 1977). The filling of pores in the highlands crust results in increased inter-particle locking and hence a higher friction coefficient that implies higher target strength, higher angle of repose and hence larger wall slope. The transient cavities created on these terrains are stabilized by the enhanced strength of the target material, thereby preserving the large depths of the cavities. This theory is similar to the one proposed by Boyce et al. (2006) for discerning the reasons for formation of deep craters in a region of the northern Martian lowlands. The mare terrain is more coherent and stronger than the more porous regolith-dominated highlands (Kiefer et al., 2012; Soderblom et al., 2015; Wieczorek et al., 2012) and therefore is expected to be more resistant to cavity collapse thereby supporting deeper craters. The mare themselves, are composed of laterally extensive layers of

basalt flows, likely interleaved with regolith layers (Head, 1975; Hiesinger et al., 2000; Philpotts & Schnetzler, 1970; Shoemaker & Hackman, 1962; Smith et al., 1970; Taylor, 1989), and this layering produces strength heterogeneities with depth that results in slumping/terracing in this diameter range (Chandnani et al., 2019; Cooper, 1977; Kalynn et al., 2013; Osinski et al., 2018; Pike, 1980a; Quaide & Oberbeck, 1968; Roddy, 1977; Smith & Hartnell, 1978). So, the second hypothesis may not work for the mare. The highlands crust being non-layered, filling of pores by mafic intrusions can homogenize and enhance the target strength thereby driving the formation of deeper, simple craters. Additionally, we are not investigating mare craters in this study because the simple craters in our survey are confined to the highlands.

In this study, we test the two hypotheses to uncover the cratering dynamics behind the deep simple lunar craters that fall in the 15-20 km diameter range. All tests were conducted on the set of 117 simple craters or subsets within this group.

3.2 Methods and Data Sets

3.2.1 Crater Depths from SLDEM and LOLA tracks

The initial evaluation of crater depths was made using gridded LOLA altimetry (LOLA GDRs). The GDRs are products of interpolation of the elevation data from LOLA altimetry tracks or Reduced Data Records (RDRs). Although LOLA RDRs have the highest geodetic precision of ~10 cm and vertical accuracy of 1 m (Mazarico et al., 2013), gaps of 2-4 km exist between the tracks, especially around the equator, a large distance relative to the floors of our study craters that could lead to depth errors. To confirm that our craters are deep, we re-evaluated the d/D_s of the simple craters using SLDEM, an improved lunar digital elevation model (DEM) that covers latitudes between 60°N and 60°S (Barker et al., 2016). The SLDEM was created by co-registering the globally extensive stereo-derived Kaguya Terrain Camera (TC) DEMs (Haruyama et al., 2008) with the LOLA RDRs. The co-registration resulted in a

DEM that provides a continuous coverage of surface elevations with a vertical accuracy of 3-4 m and precision of less than 1 m, without the need for surface interpolation. In case of craters occurring beyond 60° latitudes, d/D s were calculated with the help of LOLA RDR data. To calculate the crater depth, we first obtained rim and floor elevations. We averaged the elevation measurements along the rim to obtain the rim elevation. To get the floor elevation, we measured the minimum value in case of narrower floors (maximum diameters of ~ 500 m), and averaged the values included within the floor area in case of more areally extensive floors. The crater depth was calculated by subtraction of floor elevation from rim elevation. The source of the standard deviation was contributed by rim variability if a minimum value for floor elevation was selected. Otherwise, both the floor and rim variability were included to evaluate the uncertainty associated with the crater depth. We used the diameters that we had determined using the 'Circle by Points' method of the CraterTools in ArcGIS (Kneissl et al., 2010). A maximum diameter was measured for each crater by creating circular outlines that accommodated the maximum area enclosed by the rim crest. So, direct measurement of one diameter value for each crater did not require an error estimate. Because our objective was to probe craters with larger-than-normal depths, we started our d/D evaluation with the deepest crater and continued it until we started encountering craters that exhibit d/D s of ~ 0.200 or less. The craters that turned out to have d/D values greater than 0.2 in the RDR data were finalized as deep craters for the remaining analyses.

3.2.2 Depths of Proximity Craters

If the large crater depths are a function of a terrain attribute, surrounding craters may also have similar d/D s. Using the high resolution (10m/pixel) Kaguya Terrain Camera (TC) (Haruyama et al., 2008) ortho image data, we identified smaller well-preserved simple craters occurring within a 100 km radius from the centers of 28 simple craters with $15 < D < 20$ km that span a wide range of d/D s, porosities and geographic locations (listed in Table 3.2).

SLDEM data (Barker et al., 2016) was used for calculation of the crater d/D s with the help of the method described in section 3.2.1 because the diameters of most of the proximity craters are smaller than 2 km and therefore many of them may not have a single LOLA track passing through their cavities. We limited our crater selection to locations within 60°N and 60°S due to the limited coverage of SLDEM. Craters well-distributed across the lunar surface and representative of the various target porosities within $\pm 60^\circ$ latitudes were adequately selected. For these smaller craters we measured the minimum elevation of the floor in determining the rim-floor depth. The rest of the procedure for rim crest elevation measurements and d/D calculation is similar to the techniques adopted for the depth re-evaluation of the deep craters (section 3.2.1). The lower limit of crater diameter was set at 500 m to ensure that we had adequate sampling to reliably determine the minimum elevation of the floor. Small lunar craters form on the uppermost crustal layers that are mostly composed of regolith. So, they may initially form with sharp rims and hollow cavity but collapse at a faster rate and are likely to have softer rims than larger simple craters that penetrate the deeper and more consolidated layers of the crust (Basilevsky et al., 2014; Mahanti et al., 2018). We noticed such morphologies for craters of sizes smaller than 800 m. Therefore, we relaxed our selection criteria for the small craters and picked the ones that have raised rims with interiors close to bowl-shape, and/or are rayed craters. Figure 3.2.2 illustrates the morphologies of simple craters of varying sizes that surround the deep craters.

3.2.3 Trends in Crater Morphometry

Final crater cavity shape can provide important insights into the crater excavation and modification processes. We analyzed the cavities of all 117 simple craters with $15 < D < 20$ km in greater detail by evaluating the following morphometric parameters: rim height/diameter ratio (h/D), wall slope (θ) and floor diameter/crater diameter ratio (f/D). For the purpose of

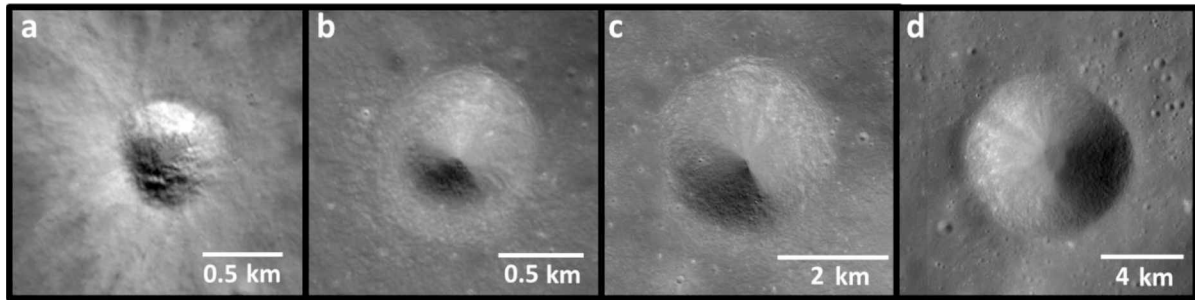


Figure 3.2. WAC images of simple craters surrounding the 15-20 km-sized deep simple craters, in order of increasing diameter. Their diameters and geographic coordinates of centers are: a) 603 m and 55.74°N, 147.12°E; b) 956 m and 58.29°N, 156.93°E; c) 3.2 km and 57.03°N, 155.34°E; d) 7.1 km and 11.44°N, 167.19°E. The ejecta rays of the crater in (a) reflect its Copernican age, although its quick collapse post formation on a more unconsolidated target caused the rim to soften and floor to widen. Gradual sharpening of rims can be observed with increase in crater size from (a) to (d) because the target material gets denser and more cohesive with depth thereby enabling more resistance of the crater to modification for a longer period. North is up in all images.

analyzing the morphometry trends of all 117 craters, we used LOLA GDR data because despite the errors due to cross-track spacing, LOLA GDR DEMs have the highest vertical accuracy and precision (Mazarico et al., 2013) and also provide a global coverage of the lunar surface (Smith et al., 2011).

For calculation of the rim height, six transects passing through the center of each crater and extending to one crater radius (1R) beyond the rim on each end (to include the surrounding pre-impact terrain) were generated at azimuthal intervals of 30°. Six elevation profiles were extracted along these transects. Because the topography of the heavily cratered highlands terrain can vary within meter-scale distances, the elevation of the surrounding terrain from the topographic profile was estimated at the nearest position where the ejecta profile levels out, that is, 1.5R from the center. We obtained two sets of rim crest and terrain elevation values for each profile (see example in Figure 3.3). We subtracted the terrain elevation from the rim crest elevation of the corresponding sets (h_A and h_B for one profile in Figure 3.3) to obtain a total of twelve rim height values whose average resulted in the final rim height of a crater. The standard deviation in this case is contributed by both rim and terrain variability.

Measurement of slope angle requires the presence of a straight line. From our observations of various simple crater profiles, the region of the crater wall in between $0.5R$ and $0.7R$ from the center qualified as a straight-line segment (segments 1 and 2 in Figure 3.3) on walls of all 117 craters. Slope maps of each crater were generated from 512 ppd LOLA Digital Elevation Models (DEMs). From every slope map, the mean of the slope angle values that were confined to the area of the walls bounded by $0.5R$ and $0.7R$ resulted in the final θ .

We obtained the crater floor diameter by identifying the floor area through LOLA DEMs and by fitting a circle to it with the help of the ‘Circle by Points’ method of the CraterTools in ArcGIS (Kneissl et al., 2010), ensuring that the circle covered the maximum possible area of the floor.

If there is no bulking of ejecta, then the volume of the rim/ejecta above the pre-existing terrain level would be the same as the volume of the cavity below. If significant compaction accompanies excavation in transient cavity formation, then we might expect the cavity volume to increase relative to the ejecta volume. Therefore, comparing the ejecta volume and cavity volume below the pre-impact terrain can be useful in testing the first hypothesis. Except for rayed craters on flat terrain, it is challenging to identify the ejecta boundary of lunar craters. Continuous ejecta blankets extend $\sim 2R$ to $3R$ from the center of well-preserved craters (Melosh, 1989c). The ejecta is thickest at the rim and reduces in thickness with increasing distance from the rim until its elevation profile starts flattening to merge with the elevation of the surrounding surface. With the help of LOLA DEM-derived elevation profiles, we noted that this portion of ejecta (red region in Figure 3.3) extends to $\sim 1.5R$ from the crater center. We used this region to determine the volume of near-rim ejecta above the pre-impact reference elevation at $1.5R$ (solid black line across the cavity profile in Figure 3.3). The volume of the region of the cavity below the same reference elevation (green area in Figure 3.3) was also calculated. The 117 simple craters are located in the highlands. Unlike the mare, the topography

of the terrain immediately surrounding a crater can be extremely variable because of greater abundance of impact craters. Consequently, it is challenging to generate a pre-impact surface of a constant elevation. First, we selected only those craters whose average pre-impact terrain slope at a radius of $1.5R$ varied from 0° to 7° , that is, relatively flat terrain. The uncertainties in slope are a measure of its variability that could be sourced from meter-scale craters (that can be neglected) and/or a sharp change in elevation. We observed that the standard deviation in elevation of a pre-impact surface marked by a major break in elevation exceeds the mean elevation of the surface. So, we eliminated craters associated with these terrains from the list of flat-terrain craters. A total of 53 craters qualified for the volume analysis. Next, we evaluated the near-rim ejecta volume-cavity volume ratios (E/C) for these craters. The variability in the pre-impact reference elevation sourced the uncertainties in the volume ratios. If we were able to include all ejecta and no compaction has taken place, E/C would be ≥ 1 . Because we have cut off measuring ejecta thickness at $1.5R$, we likely miss a good portion of the ejecta, but even at this distance our ejecta volume is quite sensitive to where we set the elevation of the pre-impact terrain. Nevertheless, we may have some ability to compare the E/C for our craters, and E/C should be lower for those craters in which cavity compaction due to high porosity occurs.

The four morphometric parameters were plotted against the crater d/Ds to look for trends in cavity shape, especially differences between the deep craters and other simple craters. The data points in the scatter plots were also classified by porosity for observing morphometric patterns with change in porosity. However, the classification based on porosity is accompanied by the caveat that only seven simple craters from our survey are in the 10-12% porosity regions, which is a small number as compared to the much larger sample size corresponding to the higher porosity regions (32 for 12-15%, 26 for 15-17% and 52 for 17-20%). So, emphasis was given to correlations of the morphometric parameters with d/Ds unless a prominent variation in a

parameter based on porosity was noticed. The values of all parameters for each simple crater are listed in Table B-1 of Appendix B.

3.2.4 Impact Melt Deposits

Theoretical models and geologic studies of impact structures have helped in understanding the general process of impact melt formation (Cintala & Grieve, 1998; Dence, 1971; Dence et al., 1977; Grieve, 1978; Grieve & Cintala, 1992; Grieve & Floran, 1978). Shock wave compression generates heat in the target that raises the target temperatures to far above the melting point of the target rocks. After the shock wave has passed, the release of pressure is followed by melting of the target rocks. The pressure release also accelerates the melted material to become a part of the flow field that forms the transient cavity during the excavation stage. The melt that remains inside the cavity may stick to the walls or form ponds among the breccia lens on the floor of the cavity whereas the ejected melt, after landing on the surface outside the cavity, could flow for some distance until it decelerates completely and gets ponded. Wünnemann et al. (2008) generated numerical models of craters formed by impacts on dry targets with porosities up to 50% and observed a significant increase in the volume of melt with increase in porosity. This is because the compaction of pores raises the heat that is stored in the target due to shock wave compression, and therefore reduces the critical pressure required for melting, which enhances melt production.

From the 117 simple craters analyzed in this study, we identified visible impact melt deposits on the floors of 32 simple craters with LROC NAC images (Chandnani et al., 2019). Their locations are symbolized by grey outlines in Figure 3.4. We additionally looked for the presence melt flows around the craters to determine if a correlation exists between the melt distribution (flows and floor melts) and porosity. Because the craters selected for the assessment of proximity crater depths are well-distributed across the lunar surface, we used the same group of 28 craters (listed in Table 3.2) for melt flow identification. High resolution (10

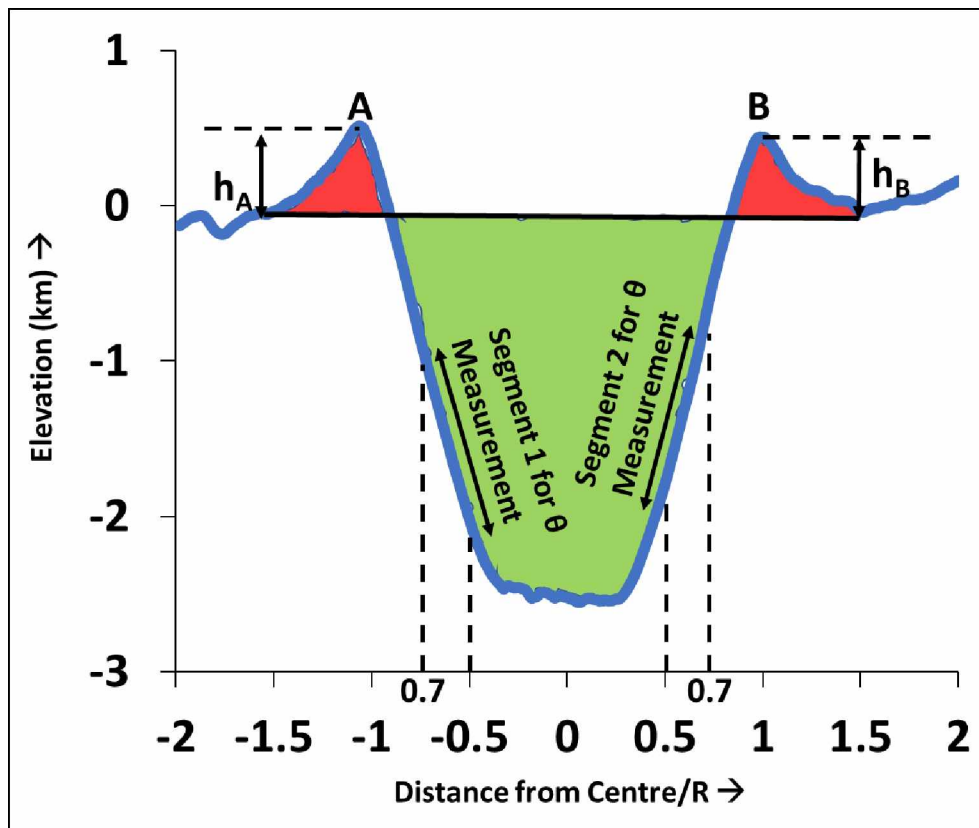


Figure 3.3. Illustration of rim height, slope measurement and volume calculation methods for a simple crater. The solid blue line refers to an example of a simple crater's cross-sectional profile. Rim height (h_A at end A and h_B at end B) is the vertical distance between the rim crest and the surrounding terrain (where ejecta profile flattens out). Rim height values measured from six such profiles were averaged to result in the final rim height of one simple crater. The region of the walls bounded by distances $0.5R$ and $0.7R$ from the center, exemplified by line segments 1 and 2, satisfies the criteria for slope angle measurement along straight line. Slope angle values from slope map were extracted from this region and averaged to result in the final wall slope (θ) for one simple crater. The solid black line represents the elevation of the pre-impact surface. The red region refers to the detectable ejecta that was used to derived ejecta volume. The area shaded in green is the portion of the cavity below the pre-impact surface whose volume was determined to evaluate the ejecta-cavity volume ratio (E/C).

m/pixel) Kaguya TC ortho images were used to identify melt flows within a radius of $3R$ from the crater center. These images provide views of the lunar surface at moderate sun-angles. Also, the sun-angle variation is minimized across large distances because each image is ~ 50 kilometers across. This helps in the detection of features on surfaces that are larger than crater floors. The melt flows were identified based on their generic diagnostic characteristics such as flow textures, smoother surfaces and lower albedo relative to surrounding terrain, and sharp contacts with elevated structures (Fink et al., 1982; Greeley et al., 1980; Howard & Wilshire, 1973; Plescia & Cintala, 2012).

3.2.5 Visual Examinations of Crater Cavities

Any visual similarities or differences between the cavities of the two crater groups (deep craters and normal-depth craters) that could potentially explain the observed morphometric trends were assessed for all 117 craters using LROC NAC images, Kaguya Optical Maturity (OMAT) maps (Lemelin et al., 2016), LRO Diviner rock abundance maps (Bandfield et al., 2011), and Kaguya FeO wt% maps (Lemelin et al., 2016). The 1 m resolution NAC data can provide a highly magnified view of the crater features. We looked for components that were unique for the deep or the normal-depth craters. Minor slumping along the walls during crater formation can be distinguished from the younger, less mature, higher-albedo flows with higher OMAT values. Thus, we looked for presence or absence of later modification, the source of the younger dry granular wall flows and if the floor material was sourced by the granular flows. The Diviner rock abundance maps (Bandfield et al., 2011) helped us in identifying rocky and unconsolidated material in the cavities and their relationship with the floor material, granular wall flows, layering if any, boulders and so on. All simple craters identified by us in the 15-20 km size range are in the highlands. FeO content > 10 wt% is a direct measure of the presence of mafic lithologies around the mare-highlands boundaries (French et al., 1991). We used the Kaguya FeO abundance maps in identifying any mafic lithologies among the anorthosites exposed by the crater and their connection with the other crater features diagnosed with the help of optical and thermal infra-red data.

3.3 Results

3.3.1 Crater Depths from SLDEM and LOLA Tracks

Table 3.1 lists the 18 craters that were tested for their depths using SLDEM and LOLA RDR data. The table indicates that the data confirmed eight craters as deep. These craters include the six craters that were also implied as deep by the LOLA GDR data (Figure 3.1) and

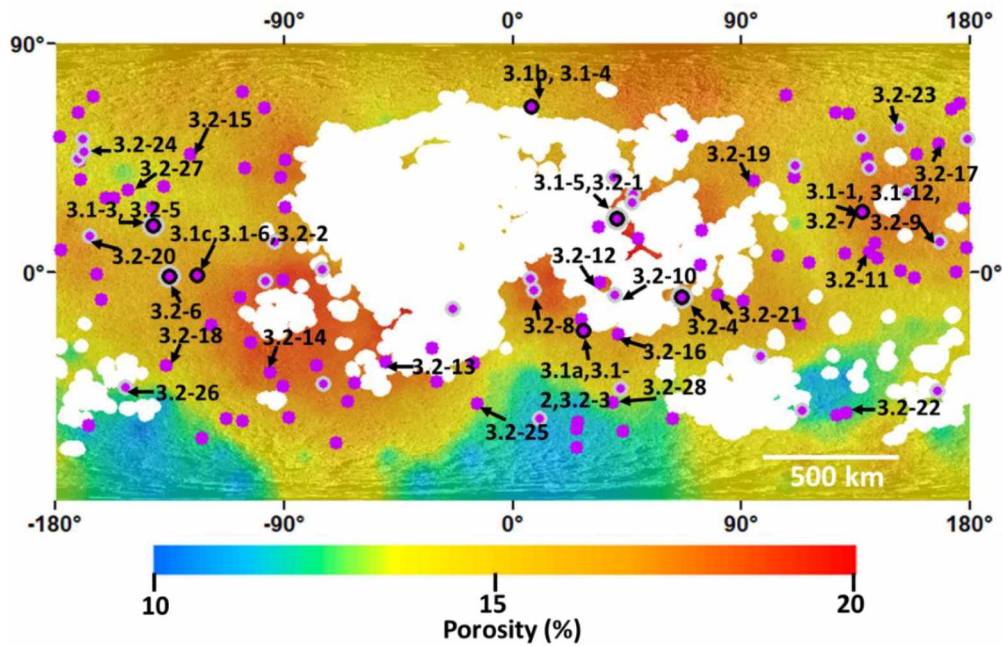


Figure 3.4. Mapped distribution of well-preserved 15-20 km-sized simple craters (purple circles) that are superposed on the lunar highlands porosity map from Besserer et al. (2014). The porosity map was generated from the Bouguer Anomaly data derived from Gravity Recovery and Interior Laboratory (GRAIL) gravity data (Zuber et al., 2013). All mare regions and the highland terrains around the mare-highlands boundaries were covered with a white mask because the porosity model is only valid for the non-layered highlands crust. The purple circles outlined in black refer to the LOLA RDR-confirmed deep craters (see crater details in Table 3.1). Craters with visible melt lined floors (Chandnani et al., 2019) are symbolized by purple circles outlined in grey. The deep craters with visible melt-lined floors are outlined in an inner layer of black and outer layer of grey. The alpha-numeric labels refer to craters shown in Figure 3.1. All the confirmed deep craters are marked by labels beginning with “3.1-“ that are serial numbers in Table 3.1. The craters that were selected for evaluation of d/D s of simple craters within 100 km around them are represented by labels starting with “3.2-“ and the proximity d/D statistics are listed in Table 3.2. Labels separated by commas refer to the same crater. The labels and corresponding symbols have been connected by arrows. North is up.

two craters (Unnamed35 and Langrenus M) that show up to be of normal depth in the GDR data. The larger depths of craters Unnamed35 and Langrenus M from SLDEM are attributable to errors from lack of floor elevation data along ~ 1.5 km cross-track spacing. The floor area of crater Unnamed39 (located near the equator) suffers from the limited coverage of LOLA tracks. But the floor of Unnamed39 is uniformly covered with slumped unconsolidated debris unlike Unnamed35 and Langrenus M whose floors are topographically more variable because of being overlain by a mix of unconsolidated material, breccia boulders and impact melt. Therefore, the SLDEM data is more consistent with the LOLA data in case of Unnamed39. For the remaining

analyses, we used the SLDEM- and RDR-derived d/D s of the confirmed deep craters. The geographic locations of the eight craters are mapped in Figure 3.4. Throughout the remaining text, we refer to the other 109 craters as normal-depth craters.

3.3.2 Depths of Proximity Craters

The locations of the 28 craters selected for this analysis have been mapped in Figure 3.4. The serial numbers in Table 3.2 are the respective labels for these craters in Figure 3.4. The number of identified well-preserved smaller craters surrounding each of the 28 craters is listed in the sixth column of Table 3.2. From the derived d/D values of smaller simple craters near the selected 28 simple craters in the 15-20 km-size range, we observed that the deep smaller craters had $D > 900$ m, even though our minimum crater size was $D > 500$ m. This could reflect differences in mechanical properties in the upper few hundred meters of target that the smaller craters form entirely within, or that the smaller craters more rapidly degrade to lower d/D (Basilevsky et al., 2014; Mahanti et al., 2018).

Table 3.1. List of 15-20 km-sized simple craters, whose d/D s were re-evaluated using SLDEM (and LOLA RDRs in case of craters located beyond 60° latitudes). They occur in decreasing order of LOLA GDR-derived d/D s. We stopped obtaining d/D s when we began encountering craters whose d/D s less standard deviations measure 0.200 or smaller values. Figure numbers of some craters have been mentioned for reference. The records of the confirmed deep craters, which means the craters whose d/D s exceed the sum of their standard deviations and 0.200 in the RDR data, are highlighted in bold. The minimum d/D s obtained by subtracting the standard deviations (eighth column) from the mean d/D s (seventh column) are listed in the ninth column.

Number	Crater Name	Figure	Latitude (°N)	Longitude (°E)	Diameter (km)	d/D LOLA GDR	d/D SLDEM	1σ min d/D - SLDEM	d/D LOLA RDR
3.1-1	Unnamed8	-	23.62	137.65	17.7	0.250±0.019	0.250±0.020	0.230	-
3.1-2	Polybius A	3.1a	-23.04	27.97	16.6	0.246±0.005	0.246±0.005	0.241	-
3.1-3	Unnamed31	-	18.32	218.59	15.9	0.217±0.009	0.223±0.008	0.215	-
3.1-4	W. Bond B	3.1b	65.03	7.51	15.2	0.215±0.006	-	0.211 (LOLA)	0.217±0.006
3.1-5	Hill	-	20.91	40.81	15.7	0.214±0.012	0.218±0.012	0.206	-
3.1-6	Unnamed39	3.1c	-1.36	235.66	15.8	0.212±0.009	0.213±0.009	0.204	-
3.1-7	Unnamed35	-	-1.9	224.98	15.8	0.212±0.013	0.215±0.013	0.202	-
3.1-8	Unnamed47	-	41.01	254.34	15.6	0.211±0.023	0.216±0.023	0.193	-
3.1-9	Unnamed24	-	47.24	191.06	15.6	0.211±0.012	0.213±0.013	0.200	-
3.1-10	Ventris B	-	-2.22	158.08	17.4	0.209±0.029	0.211±0.029	0.182	-
3.1-11	Lehmann C	-	-35.57	309.83	15.1	0.209±0.021	0.210±0.022	0.188	-
3.1-12	Spencer Jones H	-	11.93	168.12	15.1	0.209±0.018	0.212±0.018	0.194	-
3.1-13	Langrenus M	-	-9.81	66.41	18.0	0.208±0.014	0.213±0.012	0.201	-
3.1-14	Emden F	-	62.98	188.89	19.5	0.207±0.020	-	0.182 (LOLA)	0.209±0.027
3.1-15	Hipparchus C	-	-7.41	8.21	16.6	0.207±0.021	0.209±0.020	0.189	-
3.1-16	Unnamed28	-	29.1	203.12	16.2	0.205±0.017	0.208±0.017	0.191	-
3.1-17	Riccioli H	-	1.11	284.96	18.0	0.203±0.012	0.206±0.011	0.195	-
3.1-18	Bunsen C	-	44.2	270.18	18.9	0.202±0.017	0.205±0.016	0.189	-

Table 3.2. The list of percentages of smaller deep simple craters ($d/D > 0.2$ after subtracting d/D uncertainty) surrounding (within 100 km from crater center) each of the selected 28 simple craters in the 15-20 km size range.

Serial Number	Crater Name	Latitude (°N)	Longitude (°E)	d/D	No. of surrounding well-preserved simple craters	% of surrounding deep craters
Deep Craters (17-20% porosity)						
3.2-1	Hill	20.91	40.81	0.218±0.012	16	35
3.2-2	Unnamed39	-1.36	235.66	0.213±0.009	40	20
3.2-3	Polybius A	-23.04	27.97	0.246±0.005	30	15
3.2-4	Langrenus M	-9.81	66.41	0.213±0.012	22	11
3.2-5	Unnamed31	18.32	218.59	0.223±0.008	27	9
3.2-6	Unnamed35	-1.9	224.98	0.215±0.013	54	3
3.2-7	Unnamed8	23.62	137.65	0.250±0.020	52	0
Normal-depth Craters (17-20% porosity)						
3.2-8	Hipparchus C	-7.41	8.21	0.207±0.021	29	30
3.2-9	Spencer Jones H	11.93	168.12	0.209±0.018	30	24
3.2-10	Riccioli H	1.11	284.96	0.203±0.012	38	20
3.2-11	Richards	7.7	140.01	0.194±0.019	40	17
3.2-12	Isidorus D	-4.27	34.07	0.202±0.006	28	10
3.2-13	Lehmann C	-35.57	309.83	0.209±0.021	25	5
3.2-14	Heyrovsky	-39.55	264.57	0.201±0.024	34	0
Normal-depth Craters (15-17% porosity)						
3.2-15	Gullstrand C	46.57	232.9	0.196±0.017	35	10
3.2-16	Santbech B	-24.73	41.57	0.197±0.021	44	7
3.2-17	d'Alembert G	50.7	167.36	0.181±0.009	29	4
3.2-18	Unnamed32	-36.9	223.52	0.171±0.030	31	2
3.2-19	Vestine A	36.01	94.57	0.180±0.030	26	2
3.2-20	Unnamed27	14.04	193.63	0.193±0.015	33	0
3.2-21	Black	-9.19	80.39	0.157±0.009	30	0
Normal-depth Craters (10-15% porosity)						
3.2-22	Planck W	-55.44	131.27	0.183±0.009	30	3
3.2-23	Unnamed12	56.68	152.25	0.197±0.040	39	3
3.2-24	Unnamed24	47.24	191.06	0.211±0.009	39	2
3.2-25	Clavius G	-52.02	345.99	0.162±0.008	34	1
3.2-26	Unnamed29	-45.6	207.7	0.192±0.022	27	0
3.2-27	Unnamed30	32.18	208.56	0.173±0.009	33	0
3.2-28	Vlacq A	-51.28	39	0.166±0.030	29	0

We noted that in most cases except for Hill, Hipparchus C and Spencer Jones H, less than 20% of craters surrounding the selected simple craters are deep (Table 3.2). In some cases (3.2-20, 3.2-21, 3.2-26, 3.2-27, 3.2-28 in Table 3.2), we did not encounter any crater with a

larger-than-normal depth. However, even with such small numbers, Table 3.2 shows that the ranges of percentage of deep surrounding craters can be observed to decline with decrease in porosity. In the terrains characterized with the highest porosity (17-20%), excluding the case of Unnamed8, 3-35% of surrounding craters are deep. We excluded the deep crater W. Bond B (Figure 3.1b) in this analysis because it is located above 60°N latitude and craters in such high latitudes are partially or completely in shadow in the Kaguya TC images. The shadowed regions are accompanied by noise and NoData in the SLDEM data. For the craters analyzed in the 15-17% porosity terrain, only 2-10% proximity craters showed up as deep and two craters are not surrounded by any deep simple crater. We could not find any deep close-proximity craters for three selected craters and not more than 3% deep craters for four other craters in the lowest porosity target surfaces. These positive depth-porosity correlations for proximity craters suggest that porosity as a target property could be an influencing factor in the formation of the deep simple craters.

3.3.3 Trends in Crater Morphometry

3.3.3.1 Association of Crater Depth with Porosity

We initially noted that the deep craters were formed in the highland regions that were characterized by the highest porosity (17-20%). In order to determine if a relation exists between the depths of the normal-depth simple craters and porosity, we formed ranges from porosity and d/D s and plotted them in a stacked bar chart. Each bar in the chart (Figure 3.5) represents a porosity range and each stacked region of the bar refers to the percentage of total number of craters belonging to that porosity range that fall in a specific d/D range. Unlike the evaluated d/D values, a porosity value was not assigned to each crater because the porosity data points in Besserer et al. (2014)'s map are separated by at least a few hundred kilometers. Therefore, there is a possibility that the local porosity around a crater can differ from the nearest regional porosity value. So, we preferred to use porosity ranges for all tests corresponding to

the first hypothesis. Figure 3.5 shows that the frequency of the shallowest craters ($0.14 \leq d/D < 0.16$) declines with increase in porosity such that the highest porosity (17-20%) regions are devoid of these craters. The deepest craters in the normal-depth category ($0.18 \leq d/D < 0.20$) have a similar abundance of ~50% in the 10-15% and 15-17% porosity regions, which displays a sharp increase to 84% in the highest porosity (17-20%) terrains.

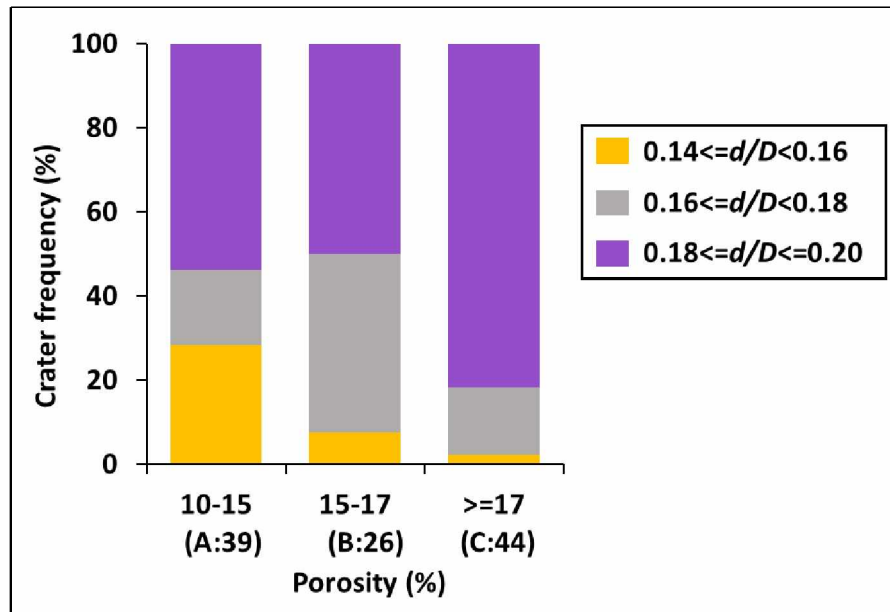


Figure 3.5. Stacked bar chart that depicts the % distribution of crater d/D ranges corresponding to each porosity range (or each bar). The values in parenthesis that are adjacent to the porosity range labels on the X-axis contain the group name (letter) and total number of craters (number) belonging to that porosity range. Deep craters were excluded from this plot.

To understand if the means of d/D s in the porosity groups are statistically different, a one-way ANOVA (Analysis of Variance) test (St & Wold, 1989) was performed on the d/D s belonging to three porosity groups: 10-15% (Group A), 15-17% (Group B) and 17-20% (Group C). The results show that the p-value is lower than 0.05 (Table B-2 of Appendix B). Therefore, the null hypothesis that states that the means across the groups are not statistically different can be rejected. This means that d/D s of one or more groups are significantly different. The ANOVA test was followed by the Tukey-Kramer Honestly Significant Difference (HSD) test (Tukey & Cleveland, 1984) that provided us with the statistically different groups. For each of the three pairs formed by the three groups, the Q-statistic and its corresponding p-value was evaluated. The results are listed in Table B-3 of Appendix B. The p-values for pair A vs C and

pair B vs C (bold font in Table B-3) were observed to be lower than 0.05 which indicates statistically significant differences between the d/D s in the highest porosity group (A) and the d/D s in the lower porosity groups (A and B). Therefore, it can be deduced that majority of craters formed in the lower porosity terrains have significantly lower depths relative to the craters occurring in the highest porosity regions.

3.3.3.2 Rim height

The rim heights scaled to crater diameter (h/D) were plotted against the d/D s for all 117 simple craters (Figure 3.6). We also classified the scatter plot by porosity values and symbolized the data points of the deep craters with red markers outlined in black (see legend in Figure 3.6). We noticed that the plot does not show any positive or negative correlation of h/D with d/D for either the group of 117 craters or groups classified by porosity. The deep craters also do not show up as outliers of any kind. It can be observed that the h/D values overlap significantly. This result indicates that all craters, including the deep craters, are characterized with similar rim heights regardless of the differences in their depths.

3.3.3.3 Wall Slope

Overall, the scatter plot of crater wall slope (θ) vs crater d/D in Figure 3.7 indicates a slight positive correlation of slope with crater d/D . This correlation can also be seen within the groups classified by porosity. For the verification of our interpretation, a correlation coefficient (r) for the relation between θ and d/D was determined. The formula used for the correlation coefficient (r) is as follows:

$$r = \text{covar} / (\text{std}_{\theta} * \text{std}_{d/D})$$

where covar = covariance between θ and d/D

std_{θ} = standard deviation of θ s

$\text{std}_{d/D}$ = standard deviation of d/D s

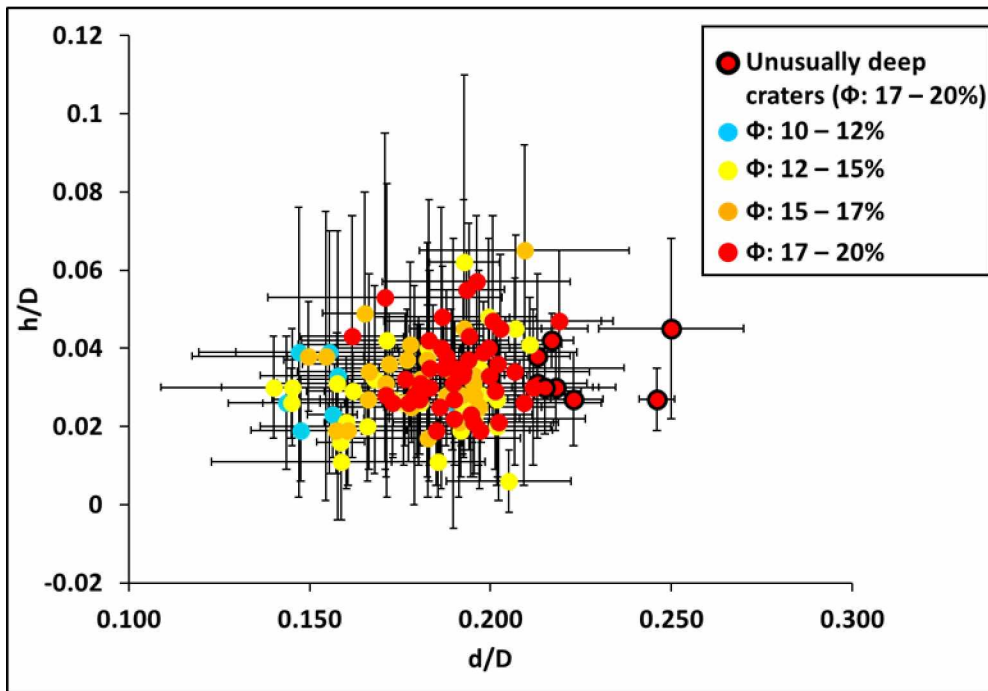


Figure 3.6. Scatter plot of rim height scaled to crater diameter (h/D) against depth/diameter (d/D) ratio for 117 well-preserved 15-20 km-sized simple craters. The markers representing the deep craters are red circles that are outlined in black. The remaining data points have been classified by porosity values (ϕ) that are enlisted in the legend on the right.

A value of 0.268 was obtained for r which confirms our observation that the crater wall slopes display a mild increase with rise in crater d/D . Similar to the d/D pattern observed with relation to porosity, majority of wall slopes with the highest values are characterized by craters (both deep and normal-depth) occurring in 17-20% porosity terrains. The wall slopes of craters in the lowest porosity (10-12%) terrains are mostly confined to the lower end of the slope range. However, the wall slopes of the deep craters are not significantly higher than the other craters, but their values are scattered around the θ values for craters with d/D s at the high end ($d/D \sim 0.20$). For a better understanding of the θ variations with respect to porosity, we divided the θ measurements (including the θ values of the deep craters) into the three porosity groups that were also used for classification of d/D measurements in item 1 of the current section (3.3.3). A one-way ANOVA was conducted on the three groups. The p-value from this test turned out to be lower than 0.05 ($3.894e-05$), indicating that one or more groups are significantly different. The ANOVA was followed by Tukey-Kramer HSD test whose results

showed that the p-values for two groups, A vs C and B vs C, were lower than 0.05. This result corroborates our observation that the wall slopes of most craters in the 17-20% porosity regions are significantly higher relative to the wall slopes of craters belonging to the lower porosity terrains. The numeric details of the statistical test results are listed in Tables B-4 (ANOVA) and B-5 (Tukey-Kramer HSD) of Appendix B.

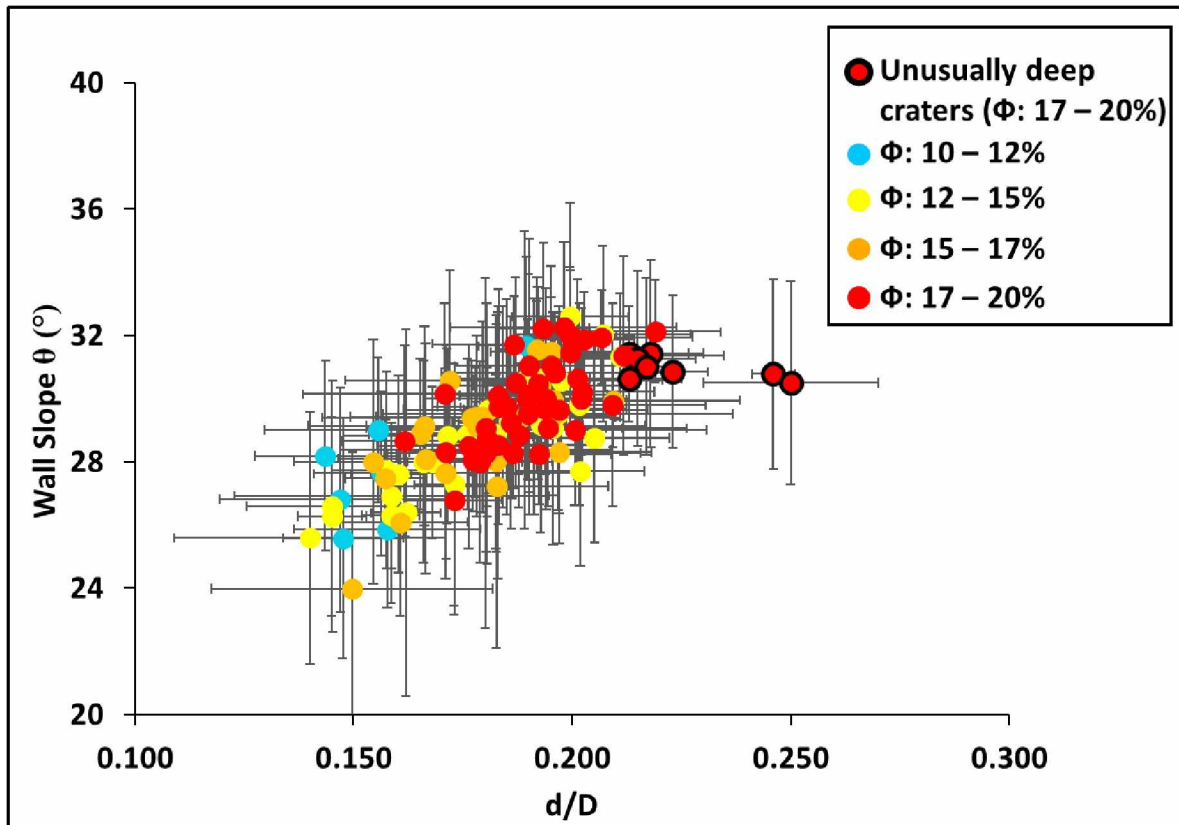


Figure 3.7. Scatter plot of wall slopes (θ) against depth/diameter (d/D) ratio for 117 well-preserved 15-20 km-sized simple craters. The markers representing the deep craters are red circles that are outlined in black. The remaining data points have been classified by porosity values (ϕ). The legend on the right can be used to access the ϕ values associated with the different marker shades.

3.3.3.4 Floor Size

We generated scatter plots of crater d/D (Figure 3.8) and θ (Figure 3.9) against floor diameter scaled to crater diameter (f/D). We also classified the data points by porosity values and symbolized the deep craters in the same manner as the plots in Figures 3.6 and 3.7. In Figure 3.8, the scatter plot does not give a clear visual indication of the trends that the d/D s follow in relation to f/D s. Visually, it appears to be either an independent or, from the smallest

floor sizes associated with the two deepest craters, a weak negative correlation. We verified the relationship by calculation of correlation coefficient (r) from the covariance between d/D and f/D for all 117 craters and obtained r as -0.451 . The minus sign reflects a negative correlation between d/D and f/D . The value suggests that an increase in floor size can weakly correlate with a drop in crater depth. However, the deeper craters, especially in the 17-20% porosity regions, are not clustered around the smallest floor sizes but span a wide f/D range (0.06-0.4) such that their floor sizes overlap with that of the shallower craters.

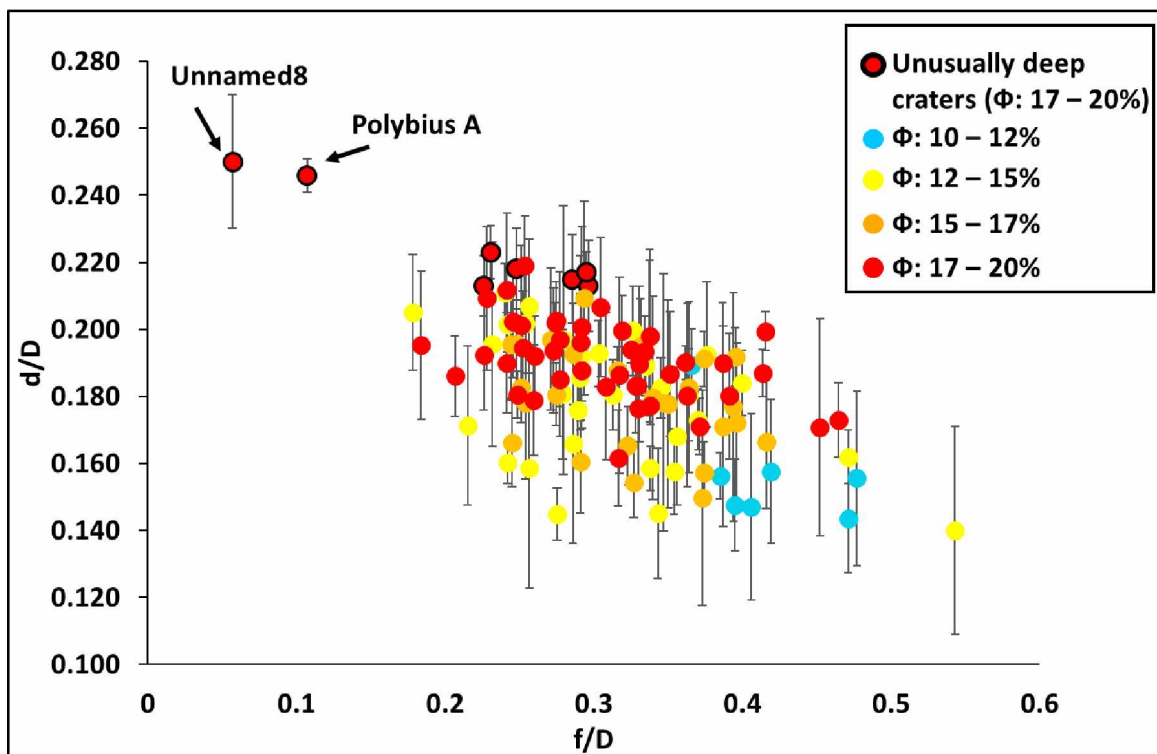


Figure 3.8. Scatter plot of crater d/D against floor diameter scaled to crater diameter (f/D) for 117 well-preserved 15-20 km-sized simple craters. The deep craters are symbolized as red circles outlined in black. The deepest craters have the smallest floors and are labelled with their respective names. The remaining markers have been classified by porosity values (ϕ). The legend on the right lists the ϕ values associated with the different marker shades.

From the large coverage of the error bars in the scatter plots of wall slope vs floor diameter (Figure 3.9), the wall slopes of all craters show a significant overlap regardless of porosity or floor diameter, suggesting that irrespective of the terrain or other crater dimensions, the wall slopes of all 117 simple craters are independent of their floor sizes.

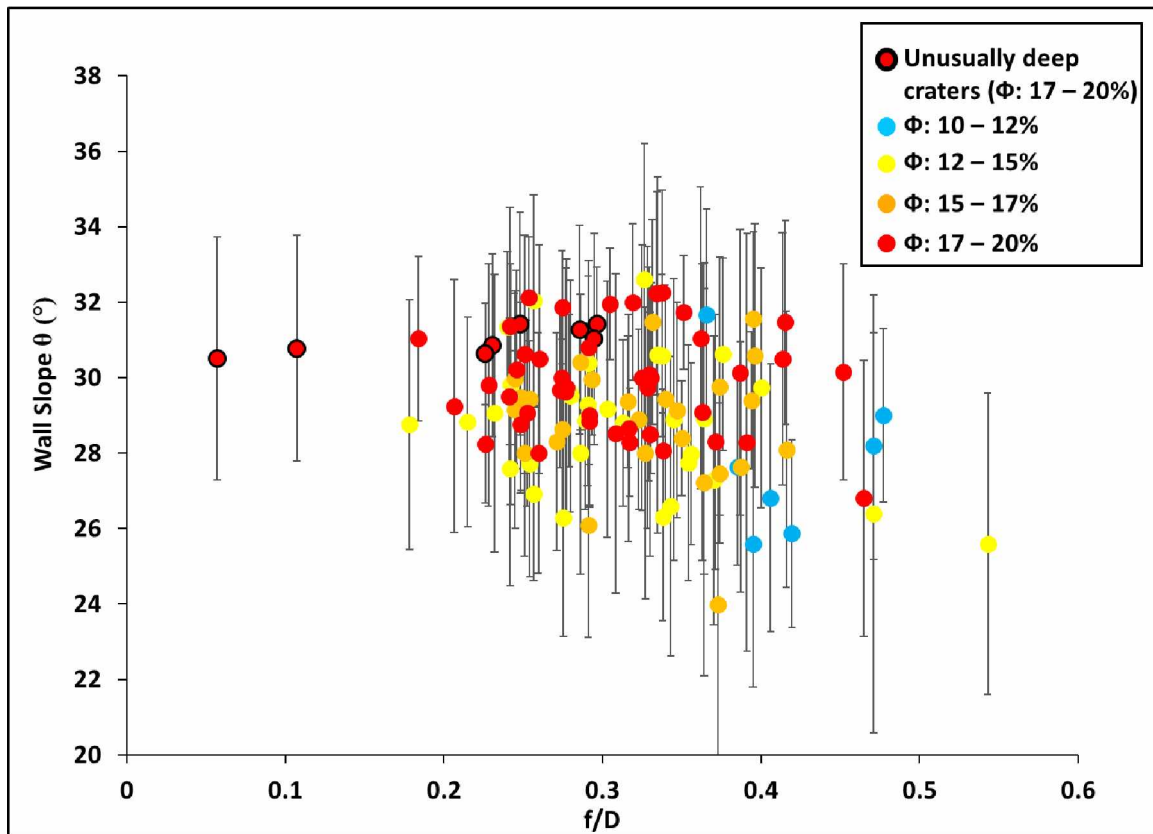


Figure 3.9. Scatter plot of crater wall slope (θ) against floor diameter scaled to crater diameter (f/D) for 117 well-preserved 15-20 km-sized simple craters. The red circles outlined in black refer to the deep craters. The remaining markers have been classified by porosity values (ϕ). The legend on the right lists the ϕ values associated with the different marker shades.

3.3.3.5 Cavity Profiles

The cavity shapes of the 117 simple craters in our 15-20 km diameter database support the observed trends in the morphometric parameters in items 2, 3 and 4 of the current section (3.3.3). Figure 3.10 demonstrates the cavity shapes of two deep and two normal-depth craters. The cavity profiles have been scaled to the respective crater sizes. Nearly all ejecta profiles at both ends A and B appear to be overlapping, thus indicating that the rim heights of these craters are approximately equal. The walls of the shallowest crater Congreve G ($d/D \sim 0.18$) are slightly less steep than the walls of the other craters. The walls of the second normal-depth crater Unnamed29 ($d/D \sim 0.2$) approach the same steepness as the walls of the deep crater Hill ($d/D \sim 0.22$) and Unnamed8 which is one of the two deepest craters ($d/D \sim 0.25$). We also noticed that the walls of crater Unnamed8 taper down to a significantly narrow floor in comparison to

the broader floors of the other three craters, as is also evident from the scatter plot in Figure 3.8.

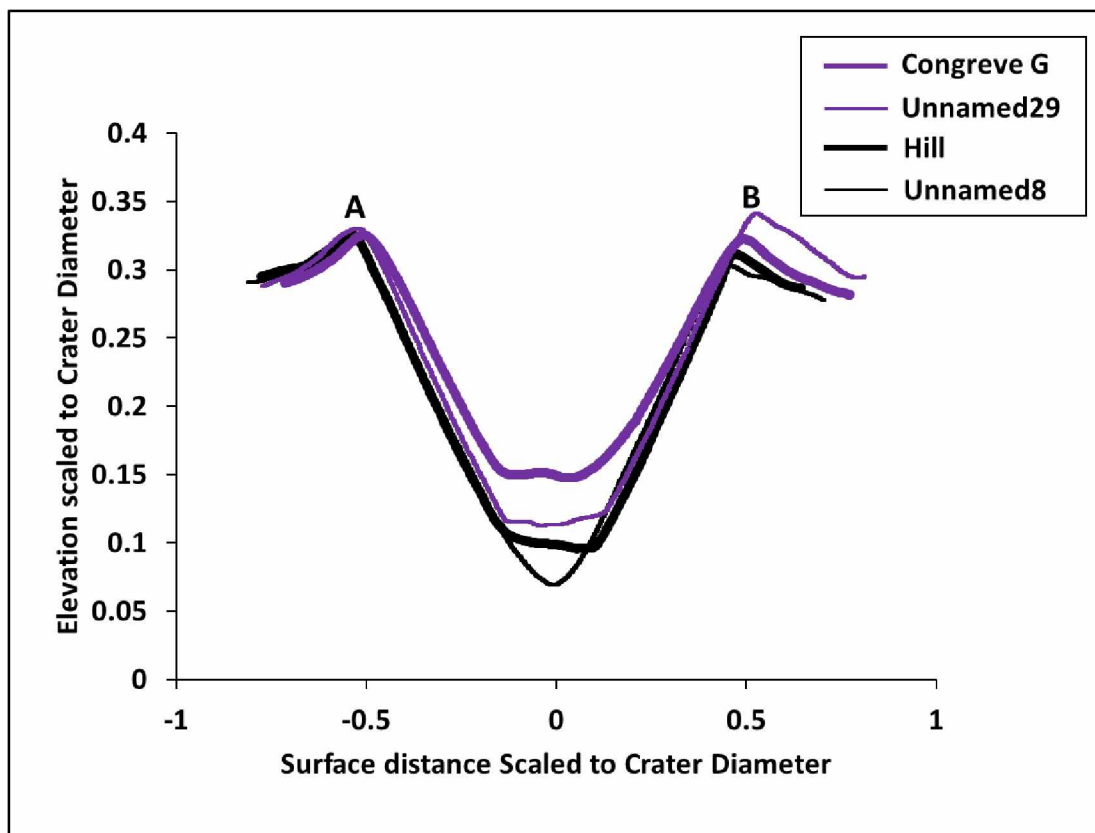


Figure 3.10. Cavity profiles of two normal-depth craters Congreve G ($d/D \sim 0.18$; -0.89°N , 196.12°E) and Unnamed29 ($d/D \sim 0.20$; -45.6°N , 207.7°E), and two deep craters Hill ($d/D \sim 0.22$; 20.91°N , 40.81°E) and Unnamed8 ($d/D \sim 0.25$; 23.62°N , 137.65°E). The legend on the right corner lists the crater names associated with the different shades and thicknesses of the lines in the plot. The ground distance and elevation have been scaled to the respective crater diameters. Please refer to section 3.3.2.4 for a description of the cavity shape comparison.

3.3.3.6 Ejecta-Cavity Volume Ratio (E/C)

The data points and error bars in the scatter plot of E/C against d/D in Figure 3.11 indicate a significant overlap of E/C s that is similar to the observation of rim heights in Figure 3.6. The value of the correlation coefficient r for E/C and d/D is -0.099 . This value suggests that E/C s and d/D s of the 53 sampled craters are nearly independent of each other or have an extremely weak negative correlation. The data points were also classified by porosity values. A random pattern of E/C with change in porosity can be observed. However, the deepest craters appear to have lower mean E/C values (~ 0.2) as compared to the shallowest craters (~ 0.5).

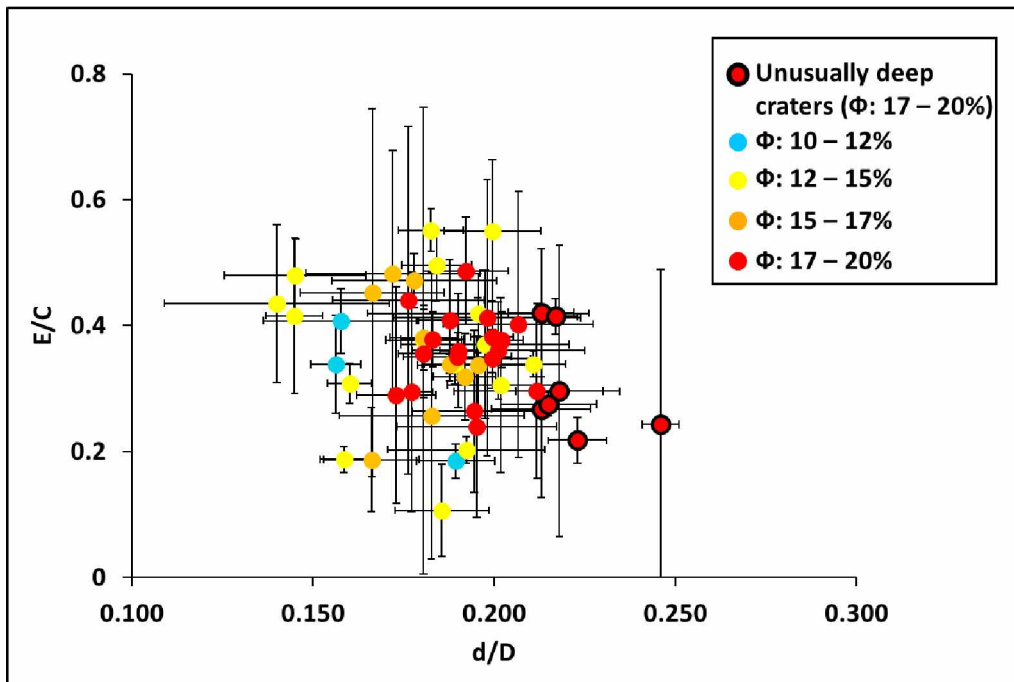


Figure 3.11. Scatter plot of crater ejecta-cavity volume ratio (E/C) against d/D for 53 well-preserved 15-20 km-sized simple craters. The red markers outlined in black refer to the deep craters. The remaining markers have been classified by porosity values (ϕ). The legend on the right lists the ϕ values associated with the different marker shades. Note that the deepest crater is characterized with one of the lowest mean E/C values.

3.3.4 Impact Melt Deposits

We could find impact melt flow deposits around nearly all 18 craters that we studied for this analysis. This group includes deep craters and normal-depth craters, with or without visible floor melt deposits. We did observe similar distribution of melt flows around each crater, but we cannot draw an inference on the differences in the volumes of the melts around craters with differing depths. Examples of the melt flows around a deep crater without signatures of melt-lined floor, and a normal-depth crater whose floor is overlain by visible impact melt are shown in Figure 3.12. Melt flows around craters that contain visible floor melt deposits are illustrated in Figure B-1 of Appendix B.

3.3.5 Visual Examinations of Crater Cavities

We studied the cavities of the deep and normal-depth simple craters in the 15-20 km diameter range with the help of imaging data in different wavelengths. Figures 3.13a, 3.13e,

3.13i, 3.13m (NAC images superposed on WAC data); 3.13b, 3.13f, 3.13j, 3.13n (magnified NACs); 3.13c, 3.13g, 3.13k, 3.13o (Diviner rock abundance maps) and 3.13d, 3.13h, 3.13l, 3.13p (Kaguya FeO abundance maps) summarize the visual examination results by demonstration of cavity morphologies of the four craters whose profiles are shown in Figure 3.10. Figures 3.13b, 3.13f, 3.13j and 3.13n include references to the optical maturity indices (OMAT) that were obtained from the global Kaguya Multiband Imager-derived and topographic shading-corrected OMAT map (Lemelin et al., 2016). The higher the OMAT

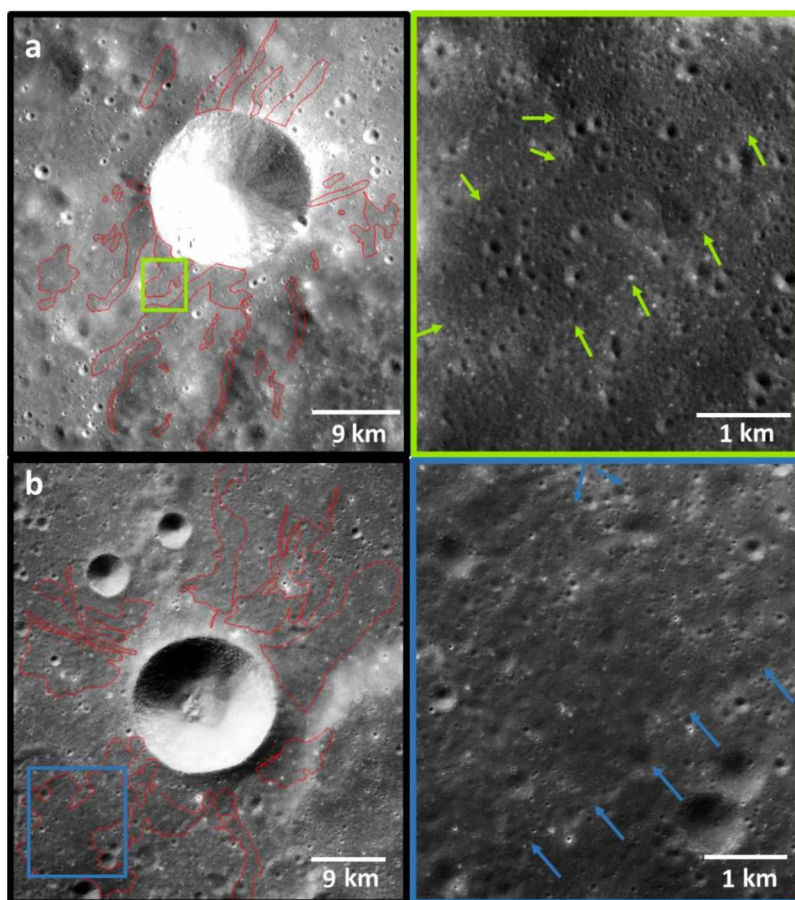


Figure 3.12. Impact melt flows outlined in red surrounding a) Deep crater Polybius A (-23.04°N, 27.97°E) and b) Normal-depth crater Planck W (-55.44°N, 131.27°E). The floors of both craters do not show visible melt deposits. The small boxes outlined in green and blue in the images on the left refer to the insets outlined in the respective shades, that represent magnified views of the melt flows included in the boxes. The arrows in the insets have been used to mark the edges of the flows. Kaguya TC ortho images have been used in the background. North is up in all images.

index, the more immature or younger the surface is (Lucey et al., 2000). In the Diviner rock abundance data, the shade of blue represents unconsolidated material. Rock fraction of five

percent and above is symbolized by shades of green-yellow-red and refers to consolidated material in the form of boulders or exposed bedrock layering (Bandfield et al., 2011). In the Kaguya FeO wt% abundance maps which have been corrected for topographic shading, a value of 10 wt% or higher indicates the presence of basaltic or mafic lithologies (yellow to orange) (Lemelin et al., 2016). The OMAT indices and FeO wt% values for craters located beyond latitudes of (+/-) 50° were not analyzed due to the difficulty of applying corrections for topographic shading in these regions.

As is evident from the superposed NAC images, the crater floors in Figures 3.13a, 3.13e, 3.13i and 3.13m vary in sizes and are covered with breccia lens (except for the floor of the deep crater in 3.13m). The floors of the normal-depth crater Unnamed29 (Figure 3.13e) and deep crater Hill (Figure 3.13i) are covered with melt as well. The walls of the cavities are characterized with granular sediment flows that appear in the form of bright and dark streaks and are most likely contributing to the floor debris.

Figures 3.13b, 3.13f, 3.13j and 3.13n refer to the magnified regions of the crater walls that are outlined in red in Figures 3.13a, 3.13e, 3.13i and 3.13p respectively. The numbers in the magnified regions of the walls are the OMAT indices of the younger (red font) and older (white font) granular flows (red font) and ejecta (green font). In Figure 3.13b that represents the normal-depth crater Congreve G, OMAT indices of the granular flows with higher albedo exceed those of the darker granular flows and ejecta, suggesting that they are a result of slumping that post-dates ejecta emplacement. These flows are composed of loose, fragmented (Figure 3.13c) anorthositic highland material (Figure 3.13d).

Younger granular flows can also be noticed on the walls of the normal-depth crater Unnamed29 in Figure 3.13f based on the higher OMAT indices in comparison to the darker, older flows. The higher albedo granular flows appear to have <10 wt% FeO (Figure 3.13h) which indicates anorthositic highland material. The walls on the east and west are primarily

lined with mafic material (orange shade in Figure 3.13h; 15-20 wt% FeO). The regional view of the widespread thin layer composed of mare basalts (~18 wt% FeO) around Unnamed29 in Figure 3.13h suggests that the mafic layer was most likely sourced from a thin layer of basaltic lava flows that might have overlain the highland surface after eruption. The more cohesive basaltic flows also show up in Figure 3.13g as more consolidated (shades of green) material as compared to the remaining lithologies lining up the cavity walls of this normal-depth crater.

The walls of the deep crater Hill display both high and low albedo granular flows (Figures 3.13i-j) that are primarily of anorthositic composition (<10 wt% FeO; blue shades in Figure 3.13l). Mafic lithologies (orange shade in Figure 3.13l) are present on the walls in the form of continuous, cohesive layering (shades of red in Figure 3.13k). This crater is in the highlands at the edges of Mare Tranquilitatis. The terrain immediately surrounding Hill is covered by its ejecta and is composed of feldspathic lithologies that are typical of the highlands crust (blue shade in Figure 3.13l). With increasing distance from the crater, the surface becomes more mafic (yellow shaded in Figure 3.13l) as it approaches the boundary between the highlands and the mare. Thus, the layered mafic material is most likely a thin layer of solidified basaltic lava flows that covered the highlands terrain around the mare margins. This layering is the source of the brighter coarse-grained sediment flows whose magnified views are shown in Figure 3.13j. Their higher OMAT index values as compared to the OMAT indices of the darker flows suggest their origin from modification post-crater formation. The granular flows begin with broad alcoves that taper down to narrow channels, or gullies. The gullies channelize the flows towards the floor. Similar flow morphology on lunar crater walls has also been observed by Kumar et al. (2013). We noticed such flow morphologies in 34 simple craters on those regions of the walls that are characterized with layering.

The cavity of one of the deepest craters Unnamed8 (Figure 3.13m) is composed of unconsolidated (Figure 3.13o) anorthositic highland material (Figure 3.13p). This material

streaks down the cavity walls in the form of bright and dark granular flows (Figures 3.13m-n). The OMAT indices in Figure 3.13n indicate that the high albedo granular flows are younger than the ejecta and were formed from slumping along the walls after ejecta emplacement and crater formation.

We observed youthful dry granular flows that appear to have occurred from wall collapse after crater formation and contributed to the floor material in nearly all 117 simple craters. Broader flows devoid of channels can be called landslides that originated from the slumping of loose, unconsolidated highland material. Granular flows occurring in the form of narrow gullies were observed to exist on the regions of the walls that are composed of layering of cohesive material. The mass wasting in the form of gullies and landslides after the formation of the craters could have been a consequence of rim collapse induced by seismic shaking from the formation of nearby younger craters (Kumar et al., 2013; Schultz & Gault, 1975). If mafic lithologies exist in the cavities, they occur in the form of cohesive layering or isolated boulders on the walls.

These mafic rock layers were generally observed on the walls of craters located around the mare margins and were surrounded by 15-20 wt% FeO abundance surfaces, and therefore were most likely sourced by thin layers of basaltic lava flows that had erupted to form the mare (Hiesinger et al., 2000; Osinski et al., 2018; Philpotts & Schnetzler, 1970; Smith et al., 1970; Taylor, 1989). The layering was observed to contribute to the youthful granular wall flows, thus adding to the slumped material.

3.4 Discussion

In Figure 3.11, a similarity in E/C_s across d/D_s was observed. But because the topographic variability of the highlands terrain magnifies the uncertainties in near-rim ejecta

and cavity volumes, we are not able to validate the accuracy of the observed E/C pattern. Thus, we refrain from basing our interpretations on this result.

Several observations indicate that target properties play a role in the creation of the deep, large-diameter (15-20 km) simple craters. These deep craters have a higher percentage of deep smaller simple craters surrounding them as compared to the normal-depth craters. Additionally, all the deep craters and most of the normal-depth craters with the largest depths preferentially occur in high porosity regions.

If only excavation is involved in producing the transient cavity, creating a deeper hole generally means excavating more material, and thus the deep craters are expected to have greater rim heights but similar ejecta-cavity volume ratios. Additionally, there would be observable differences between the rim heights associated with the shallowest (d/D of ~ 0.14) and the deepest craters (d/D of ~ 0.25). However, we found the rim heights of the deep craters to overlap with those of the normal-depth craters. A possible interpretation is that increased target compaction, rather than increased excavation, is creating the deeper craters.

There are multiple lines of evidence that argue against the explanation that the deep craters are simply the very youngest, least-degraded, simple craters in the 15-20 km diameter range. If this were the case, then we would expect the deep craters to be scattered throughout the highlands and not preferentially located in the high porosity regions within the coverage of the mare basin ejecta. We would also expect that the deep craters would have higher rim heights, steeper wall slopes, narrower floors and lower ejecta-cavity volume ratios than the normal-depth craters. Trends of depth versus rim height, wall slope, and floor width would be easily identifiable if crater degradation were the primary cause of depth differences among these craters (Bouley & Baratoux, 2011; Craddock & Howard, 2000; Fassett & Thomson, 2014; Kreslavsky et al., 2013; Soderblom, 1970). These trends would also be observable if the craters are of similar ages but the amount of cavity collapse at the time of crater formation was

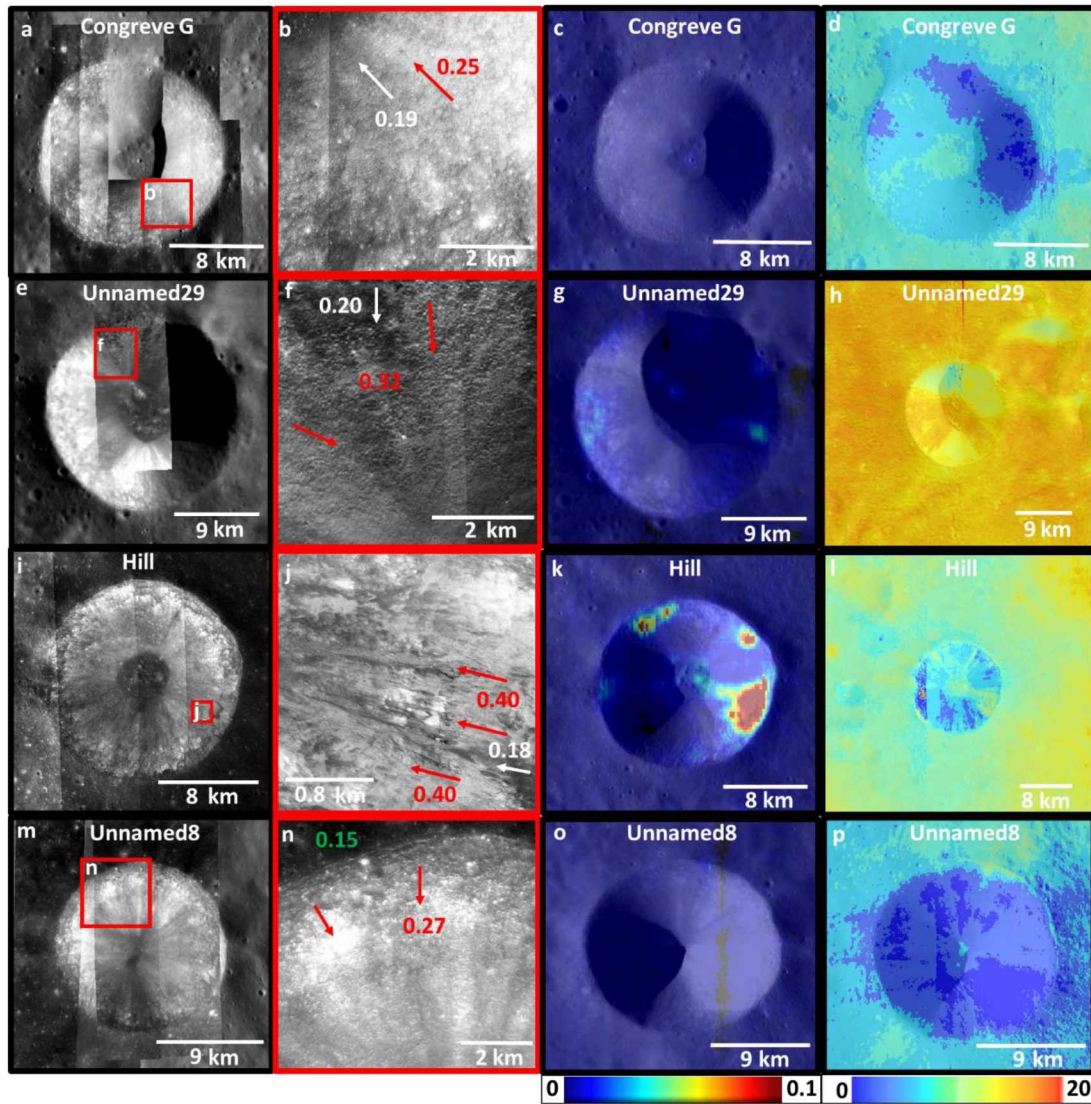


Figure 3.13. Illustration of cavity morphologies of the craters whose profiles have been displayed in Figure 3.10. The NAC images of the cavities superposed on their WAC images are shown in Figures 3.13a, 3.13e, 3.13i and 3.13m. Figures 3.13b, 3.13f, 3.13j and 3.13n are the magnified insets that are outlined in red in Figures 3.13a, 3.13e, 3.13i and 3.13m respectively. The NAC strips used in the insets are: (b) M184604311L & M184604311R; (f) M1132846453L & M1132846453R; (j) M1100938021L; (k) M1102659336R and (n) M1102659336R. In Figures 3.13b, 3.13f, 3.13j and 3.13n, the numbers in red, white and green font refer to the OMAT indices of the youthful dry granular flows, older granular flows and ejecta respectively. The young and old flows are indicated by red and white arrows respectively. Please refer to section 3.3.4 for the description of each image and inset. Figures 3.13c, 3.13g, 3.13k and 3.13o refer to Diviner rock abundance maps superposed on WAC images of the four craters. As denoted by the legend on the bottom of these figures, isolated boulders are marked in shades of green and consolidated layering is highlighted in shades of yellow to red. Kaguya FeO wt% maps superposed on WAC images of the four craters are displayed in Figures 3.13d, 3.13h, 3.13l and 3.13p. The legend for these figures is at the bottom of Figure 3.13p. An FeO abundance of 10 wt% and above indicates the presence of mafic lithologies. North is up in all figures. Please refer to section 3.3.5 for the description of each figure.

significant enough to cause the depth variations. The scatter plots show that wall slope increases with d/D for all craters, as expected. The dry granular flows that were observed on the walls of all craters and were generated syn-or post-crater formation might have contributed to floor material, and hence the observed small increase in floor size along with reduction in crater depth. However, the overlap of the floor sizes of the deeper and shallower craters suggests that modification is not the only process controlling the crater depth. Additionally, overlapping rim heights and independence of wall slopes with respect to floor size was observed. These results contradict the expected decrease in rim heights with decrease in crater depth and reduction in wall slope with increase in floor size if modification were the dominant process. At least differences in rim heights and floor sizes of the deepest craters and shallowest craters would be noticeable if the depths were attributable primarily to differences in amount of slumped material. These observations weaken the possibility that degree of modification due to age difference or other reasons is the only factor governing the differences in depths between the deep and the normal-depth simple craters.

We explore the two hypotheses proposed by us for the contribution of target properties around the mare-highlands boundaries:

3.4.1 Greater compaction of target with increase in porosity results in larger crater depths

All deep craters in the 15-20 km size range, and the highest number of similarly deep smaller craters surrounding the 15-20 km-sized simple craters, were formed in the most porous terrains (17-20% porosity). Wall slope is directly proportional to crater d/D as also indicated by the scatter plot in Figure 3.7. For similar-sized craters formed by excavation (and no compaction), the rim height should increase with crater depth because an increased amount of ejecta results in larger depths and also larger rim heights (Sharpton, 2014; Sturm et al., 2016). However, the overlap in rim heights of our deep and normal-depth craters can be explained by a modification in the cratering mechanics due to impact into a high porosity target. We propose

that a portion of the impact energy was consumed in crushing of pore space and hence compaction of the high porosity target material by the projectile, with the result of a larger, deeper transient cavity but amounts of rim uplift and excavated material that is similar to that of other simple craters (Collins et al., 2011; Housen & Holsapple, 2003, 2011, 2012; Housen et al., 1999; Love et al., 1993; Pierazzo et al., 1997; Wünnemann et al., 2006; Wünnemann et al., 2008; Zel'dovich & Raizer, 1966). Additionally, the rise in abundance of deeper craters with increase in porosity suggests compaction influenced the cratering process across all porosities. This further reflects that a deeper crater in a higher porosity region could have resulted from a higher degree of compaction as compared to a shallower crater in a lower porosity terrain such that the deeper crater developed a lower rim height relative to a similarly deep crater whose formation did not involve compaction. This lowering in rim height could have reduced the differences in rim height values between the shallower and deeper craters and is reflected by the scatter plots in Figures 3.6 and 3.11 that show similar h/D s across all d/D s. Further, the two deepest craters Polybius A and Unnamed8 have floor areas that are significantly smaller than the floors of the shallower craters (Figure 3.8). The walls of Unnamed8 in the profile in Figure 3.10 taper to a much narrower floor relative to the more areally extensive floors of the deep crater Hill and the shallower craters. From the images in Figures 3.13a, 3.13e and 3.13i, it can be observed that the slumped material and/or impact melt have ponded on the floors of the normal-depth craters and the deep crater Hill. However, in case of crater Unnamed8 (Figure 3.13m), the slumped material has lined up along the base of the crater walls and surrounded the floor rather than completely covering it. Such a case could reflect that the deeper transient crater of Unnamed8 with steeper walls was created by larger amount of compaction relative to other craters such that during cavity collapse, the finely crushed debris along the walls would be driven further into the crater and would collect in localized regions below the bottom of the crater floor. Therefore, less material would cover the

crater floor and result in the observed profile (Housen & Holsapple, 2003; Housen et al., 2018). The same concept applies to Polybius A. However, we are not ruling out the possibility of formation of the other deep craters by the influence of target compaction. We are suggesting that the signature of significantly increased target compaction in case of the two deepest craters is indicated by their floor geology.

Visible impact melt deposits overlying the crater floor were identified in the cavities of 32 craters from the group of 117 simple craters (Chandnani et al., 2019). Impact melt flows around the crater cavity were detected in case of normal-depth and deep craters regardless of the presence or absence of exposed impact melts on their floors. Because the presence of melt flows indicates that impact melt was generated at the bottom of the crater, it is possible that the slumped debris obscured the floor melt in craters where it was not visible. Neish et al. (2014) reported more frequent occurrences of exterior melt deposits around craters in the highlands as compared to mare craters and attributed them to the higher porosity of regolith-dominated highlands relative to the more consolidated and cohesive mare terrains (Kiefer et al., 2012; Wieczorek et al., 2012). However, the locations of all simple craters investigated in this study are confined to the highlands. The melt signatures in and around the cavities of craters across all porosities only reflect that the peak shock pressures reached the critical pressure required for even the least porous (10-12%) highlands target to melt. This information does not shed light on enhanced melt production with increase in porosity as deduced by the numerical modelling study of Wünnemann et al. (2008). Perhaps a future impact melt volume evaluation can help in determining the effect of the shallow lunar highlands crustal porosity variation on impact melt production.

We noticed an inconsistent pattern of deep craters in the high porosity regions. Although the mean depths of craters in the high porosity (17-20%) regions are statistically higher relative to the depths of craters formed in the lower porosity terrains, only 8 out of 61

craters in the high porosity regions are deep and 20% or less of the smaller well-preserved craters surrounding the craters in these regions are deep. Additionally, the regional surface porosity values (averaged across few hundreds of km) around the mare-highlands boundaries measure 17-20% (Besserer et al., 2014) such that it is possible that the local porosity may vary about the regional mean values. Therefore, other impact conditions being the same, the deep craters could have formed as a result of increased target compaction on the localized higher porosity patches. The positive correlation between porosity and degree of compaction has been determined experimentally (Housen & Holsapple, 1999, 2003; Housen et al., 1999; Love et al., 1993) and through numerical modelling (Collins et al., 2011; Wünnemann et al., 2006; Wünnemann et al., 2008).

Another explanation to formation of limited deep craters is the involvement of some particular set of impactor properties in enhancing the crater depths. Examples of impactor properties that may play a role are impact velocity, impactor density, and impact angle. When a projectile strikes a surface, the rise in peak shock pressures increases the amount of impact energy that is used up in the mobilization and deformation of the target, and hence increases the penetration depth. The shock pressures and the penetration depth are a function of ρv^2 where ρ and v refer to the smaller of target and projectile density and impactor velocity (Holsapple & Schmidt, 1982; Melosh & Ivanov, 1999; Schultz, 1997). Results from experimental impacts on low density, porous targets reveal that the penetration depth increases linearly with increase in projectile-to-target density ratio (Hörz et al., 1993; Love et al., 1993; Melosh, 1989a). From the results of impact cratering experiments, Hermalyn and Schultz (2011) noted that higher density projectiles can penetrate to a larger depth relative to less dense projectiles. Results from numerical modelling by Pierazzo and Melosh (2000) state that peak shock pressures and the volume of material experiencing those pressures are enhanced during vertical impacts because a higher magnitude of the vertical component of the impact velocity contributes to the vertically

directed stresses on the target. This results in higher levels of heating and disruption of the target particles and greater penetration depths. So, for the formation of the deep craters identified by us, it is possible that an impactor characteristic of high density, high velocity and/or impacting at a near-vertical angle enabled the generation of stresses that were sufficiently high for overcoming the crushing strength of the high porosity target grains thereby driving the process of minor compaction and hence the formation of deep cavities.

3.4.2 The highlands are more coherent in these locations and more resistant to minor slumping of the transient cavity

A higher strength (higher cohesion and higher friction coefficient) of the target material may inhibit rim/wall slumping of the transient cavity, potentially producing both a deep simple crater and increasing the simple-complex crater transition diameter. This idea was proposed by Boyce et al. (2006) to explain deep simple Martian craters whose sizes exceeded the global mean simple-to-complex transition diameter for Mars. In this hypothesis, on the Moon around the mare-highlands boundary, the basaltic lava flows intruded into the highlands and enhanced their cohesive strength (Gong et al., 2016; Kiefer, 2013). Only two deep craters were observed to expose mafic lithologies. These lithologies exist in the form of layering that contributed to granular flows along the walls from rim collapse. Such material exists in most craters around the mare-highlands contacts, but it appears to facilitate and not prevent modification. Also, if less transient crater modification were the explanation for the deep craters, then we might expect the deep craters to also have higher rim heights, which is not observed (Figure 3.6). Lastly, if the crater is formed primarily by excavation and negligible modification, the cavities of the deep craters must be stabilized at higher wall slopes and smaller floors as compared to the normal-depth craters due to the exceedingly greater depths. Figure 3.7 shows that the wall slopes of the deep craters ($\sim 30^\circ$ - 34°) are higher than the wall slopes of most craters. This could reflect a larger angle of repose caused by resistance to slumping due to higher friction

coefficient (Melosh, 1977). Figure 3.8 shows that the deepest craters have the smallest floor diameters, but the floor diameters of the remaining deep craters and the craters with d/D s close to 0.20 are not significantly smaller but overlap with the floor sizes of the shallower craters. This suggests that some minor modification of the transient cavity could have occurred in the cavities of the deep craters as well. The modification is also evidenced by the visual identification of dry granular flows that are representative of slumping of both highlands and cohesive (layered) mare material in both deep (Figures 3.13(g-l) and 3.13(c-d)) and normal-depth craters (Figures 3.13(a-f) and 3.13(a-b)). Also, in contrast to an expected increase in wall slope with reduction in floor depth, the two parameters appear to be independent of each other (Figure 3.9). All these results are contradictory to the expected outcome of crater formation according to the second hypothesis and convey that it is unlikely that highlands crust with high strength around the mare-highlands border exists that could enable the preservation of the deep transient cavities by the inhibition of minor slumping.

3.5 Conclusions

We identified eight deep lunar simple craters in the 15-20 km diameter range. They are located in the highlands near mare-highlands boundaries or within the ejecta coverage of the mare basins. These locations are characterized by the highest porosity (17-20%) on the lunar surface. After comparison with the 109 normal-depth simple craters in the same size range, we conclude that compaction in a high-porosity target is a likely the cause of the high crater depths. Because only a small fraction of the craters in the high-porosity terrains are deep, we suggest that increased compaction of the target due to impact on locally higher porosity patches and/or an unusual impactor property may also be required to result in a deep crater, such as a dense impactor and/or a projectile striking at near-vertical impact angle. We base our interpretation on the following observations:

[1] The deep craters ($d/D > 0.200$) and the normal-depth craters with d/D s close to 0.200 preferentially occur in the high porosity regions.

[2] The frequency of deep craters surrounding the simple craters in our survey reduces with decrease in porosity.

[3] The crater morphometry pattern is characterized by an increase of wall slope with increase in crater depths across all 117 craters. The crater depths display a weak negative correlation with floor diameters. But the rim heights of the deep craters overlap significantly with those of the normal-depth craters. The wall slopes appear to be independent of the floor diameters. The latter two observations argue against the hypotheses that the depth variations originate from differences in the amount of slumping in the cavities either syn- or post-crater formation, or from strong target material-driven resistance to collapse of the deep crater cavities.

[4] Old and young dry granular flows, contributed by both highlands and rocky or layered mare material, were observed on the walls of all craters, thus also weakening the hypothesis that an unusually strong target was formed by the filling of cracks in the highlands by basaltic lava flows, which thus inhibited modification of the deep transient cavities.

3.6 Acknowledgements

This work was funded by a grant to RRH from the NASA Lunar Advanced Science and Exploration Research (LASER) Program. We are thankful to Dr. Jonathan Besserer of l'Université de Nantes for providing us with the data required to reproduce the lunar porosity map. We are also grateful to Dr. Prasun Mahanti from Arizona State University for providing valuable suggestions pertaining to morphometric analyses of the deep craters. We express our thanks to Dr. Franz Meyer of the University of Alaska Fairbanks for guiding us with the statistical tests. We thank reviewers Catherine Neish, Jason Soderblom, and Associate Editor Gareth Collins for their insightful comments which greatly improved the manuscript.

3.7 References

- Arthur, D., Agnieray, A. P., Horvath, R. A., Wood, C., and Chapman, C. (1964), The system of lunar craters, quadrant I, *Communications of the Lunar and Planetary Laboratory*, 2, 71-78.
- Bandfield, J. L., Ghent, R. R., Vasavada, A. R., Paige, D. A., Lawrence, S. J., and Robinson, M. S. (2011), Lunar surface rock abundance and regolith fines temperatures derived from LRO Diviner Radiometer data, *Journal of Geophysical Research: Planets*, 116(E12), doi:<https://doi.org/10.1029/2011JE003866>.
- Barker, M. K., Mazarico, E., Neumann, G. A., Zuber, M. T., Haruyama, J., and Smith, D. E. (2016), A new lunar digital elevation model from the Lunar Orbiter Laser Altimeter and SELENE Terrain Camera, *Icarus*, 273, 346-355, doi: <https://doi.org/10.1016/j.icarus.2015.07.039>.
- Basilevsky, A., Kreslavsky, M., Karachevtseva, I., and Guskova, E. (2014), Morphometry of small impact craters in the Lunokhod-1 and Lunokhod-2 study areas, *Planetary and Space Science*, 92, 77-87, doi: <https://doi.org/10.1016/j.pss.2013.12.016>.
- Besserer, J., Nimmo, F., Wieczorek, M. A., Weber, R. C., Kiefer, W. S., McGovern, P. J., Andrews-Hanna, J. C., Smith, D. E., and Zuber, M. T. (2014), GRAIL gravity constraints on the vertical and lateral density structure of the lunar crust, *Geophysical Research Letters*, 41(16), 5771-5777, doi: <https://doi.org/10.1002/2014GL060240>.
- Bouley, S., and Baratoux, D. (2011), Variation of small crater degradation on the Moon. Paper presented at 42nd Lunar and Planetary Science Conference, Houston, TX.
- Boyce, J. M., Mouginis-Mark, P. J., Garbeil, H., and Soderblom, L. A. (2005a), History of major degradational events in the highlands of Mars: Preliminary results from crater

- depth/diameter measurements. Paper presented at 36th Annual Lunar and Planetary Science Conference, Houston, TX.
- Boyce, J. M., Mouginis-Mark, P. J., and Garbeil, H. (2005b), Ancient oceans in the northern lowlands of Mars: Evidence from impact crater depth/diameter relationships, *Journal of Geophysical Research: Planets*, 110(E3), doi: <https://doi.org/10.1029/2004JE002328>.
- Boyce, J. M., Mouginis-Mark, P. J., Garbeil, H., and Tornabene, L. L. (2006), Deep impact craters in the Isidis and southwestern Utopia Planitia regions of Mars: High target material strength as a possible cause, *Geophysical Research Letters*, 33(6), doi: <https://doi.org/10.1029/2005GL024462>.
- Britt, D. T., Yeomans, D., Housen, K., and Consolmagno, G. (2003), Asteroid density, porosity, and structure. In *Asteroids III*, edited by W. F. Bottke, University of Arizona Press.
- Chandnani, M., Herrick, R. R., and Kramer, G. Y. (2019), Geologic Analyses of Causes for Morphological Variations in Lunar Craters within the Simple-to-Complex Transition, *Journal of Geophysical Research: Planets*, 1238-1265, doi: <https://doi.org/10.1029/2018JE005729>.
- Cintala, M., Wood, C., and Head, J. (1977), The effects of target characteristics on fresh crater morphology-Preliminary results for the moon and Mercury. Paper presented at 8th Lunar and Planetary Science Conference Proceedings, Houston, TX.
- Cintala, M. J., and Grieve, R. A. (1998), Scaling impact melting and crater dimensions: Implications for the lunar cratering record, *Meteoritics & Planetary Science*, 33(4), 889-912, doi: <https://doi.org/10.1111/j.1945-5100.1998.tb01695.x>.
- Collins, G., Melosh, H., and Wünnemann, K. (2011), Improvements to the ϵ - α porous compaction model for simulating impacts into high-porosity solar system objects,

- International Journal of Impact Engineering, 38(6), 434-439, doi: <https://doi.org/10.1016/j.ijimpeng.2010.10.013>.
- Collins, G. S. (2014), Terraced Crater Wall (Mass Wasting). In Encyclopedia of Planetary Landforms, edited, pp. 1-6, Springer, New York, NY, doi: https://doi.org/10.1007/978-1-4614-9213-9_361-1.
- Cooper, H. (1977), A summary of explosion cratering phenomena relevant to meteor impact events. In Impact and Explosion Cratering, edited by D. J. Roddy, R. O. Pepin and R. B. Merrill, pp. 11-44, Pergamon Press, New York.
- Craddock, R. A., and Howard, A. D. (2000), Simulated degradation of lunar impact craters and a new method for age dating farside mare deposits, Journal of Geophysical Research: Planets, 105(E8), 20387-20401, doi: <https://doi.org/10.1029/1999JE001099>.
- Croft, S. K. (1985), The scaling of complex craters, Journal of Geophysical Research: Solid Earth, 90(S02), doi: <https://doi.org/10.1029/JB090iS02p0C828>.
- Dence, A. F. (1972), The nature and significance of terrestrial impact structures. Paper presented at 24th International Geological Congress, Section 15, Montreal, Canada.
- Dence, M. R. (1968), Shock zoning at Canadian craters: Petrography and structural implications. In Contributions from the Dominion Astrophysical Observatory in Victoria, edited by B. M. French and N. M. Short, pp. 169-184, Baltimore, MD.
- Dence, M. R. (1971), Impact melts, Journal of Geophysical Research, 76(23), 5552-5565, doi: <https://doi.org/10.1029/JB076i023p05552>.
- Dence, M. R., Grieve, R. A. F., and Robertson, P. B. (1977), Terrestrial impact structures-Principal characteristics and energy considerations. In Impact and explosion cratering: Planetary and terrestrial implications, edited by D. J. Roddy, R. O. Pepin and R. B. Merrill, pp. 247-275, Pergamon Press, New York.

- Fassett, C. I., and Thomson, B. J. (2014), Crater degradation on the lunar maria: Topographic diffusion and the rate of erosion on the Moon, *Journal of Geophysical Research: Planets*, 119(10), 2255-2271, doi: <https://doi.org/10.1002/2014JE004698>.
- Fink, J., Greeley, R., and Gault, D. (1982), Impact cratering experiments in Bingham materials and the morphology of craters on Mars and Ganymede. Paper presented at 12th Lunar and Planetary Science Conference Proceedings, Houston, TX.
- French, B. M., Heiken, G., Vaniman, D., and Schmitt, J. (1991), *Lunar sourcebook: A user's guide to the Moon*, Cambridge University Press, New York.
- Garvin, J. B., Sakimoto, S. E., Frawley, J. J., and Schnetzler, C. (2000), North polar region craterforms on Mars: Geometric characteristics from the Mars Orbiter Laser Altimeter, *Icarus*, 144(2), 329-352, doi: <https://doi.org/10.1006/icar.1999.6298>.
- Gong, S., Wieczorek, M. A., Nimmo, F., Kiefer, W. S., Head, J. W., Huang, C., Smith, D. E., and Zuber, M. T. (2016), Thicknesses of mare basalts on the Moon from gravity and topography, *Journal of Geophysical Research: Planets*, 121(5), 854-870, doi: <https://doi.org/10.1002/2016JE005008>.
- Greeley, R., Fink, J., Snyder, D., Gault, D., Guest, J., and Schultz, P. (1980), Impact cratering in viscous targets-Laboratory experiments. Paper presented at 11th Lunar and Planetary Science Conference Proceedings, Houston, TX.
- Grieve, R. A. (1978), Meteoritic component and impact melt composition at the Lac a l'Eau Claire (Clearwater) impact structures, Quebec, *Geochimica et Cosmochimica Acta*, 42(4), 429-431, doi: [https://doi.org/10.1016/0016-7037\(78\)90275-2](https://doi.org/10.1016/0016-7037(78)90275-2).
- Grieve, R. A. F., and Cintala, M. J. (1992), An analysis of differential impact melt-crater scaling and implications for the terrestrial impact record, *Meteoritics*, 27(5), 526-538, doi: <https://doi.org/10.1111/j.1945-5100.1992.tb01074.x>.

- Grieve, R. A. F., and Floran, R. J. (1978), Manicouagan Impact Melt, Quebec 2. Chemical interrelations with basement and formational processes, *Journal of Geophysical Research: Solid Earth*, 83(B6), 2761-2771, doi: <https://doi.org/10.1029/JB083iB06p02761>.
- Güldemeister, N., Wünnemann, K., and Poelchau, M. (2015), Scaling impact crater dimensions in cohesive rock by numerical modeling and laboratory experiments, *Geological Society of America Special Papers*, 518, SPE518-SPE502, doi: [https://doi.org/10.1130/2015.2518\(02\)](https://doi.org/10.1130/2015.2518(02)).
- Hargitai, H., and Öhman, T. (2014), Complex Crater. In *Encyclopedia of Planetary Landforms*, edited, pp. 1-17, Springer, New York, NY, doi: https://doi.org/10.1007/978-1-4614-9213-9_429-2.
- Haruyama, J., Matsunaga, T., Ohtake, M., Morota, T., Honda, C., Yokota, Y., Torii, M., Ogawa, Y., and Group, L. W. (2008), Global lunar-surface mapping experiment using the Lunar Imager/Spectrometer on SELENE, *Earth, planets and space*, 60(4), 243-255.
- Head, J. (1975), Lunar mare deposits: Areas, volumes, sequence, and implication for melting in source areas. Paper presented at Conference on Origins of Mare Basalts and their Implications for Lunar Evolution, Lunar Science Institute, Houston, TX.
- Hermalyn, B., and Schultz, P. H. (2011), Time-resolved studies of hypervelocity vertical impacts into porous particulate targets: Effects of projectile density on early-time coupling and crater growth, *Icarus*, 216(1), 269-279.
- Hiesinger, H., Jaumann, R., Neukum, G., and Head, J. W. (2000), Ages of mare basalts on the lunar nearside, *Journal of Geophysical Research: Planets*, 105(E12), 29239-29275, doi: <https://doi.org/10.1029/2000JE001244>.
- Holsapple, K. (1993a), The scaling of impact processes in planetary sciences, *Annual review of earth and planetary sciences*, 21(1), 333-373.

- Holsapple, K. A. (1993b), The scaling of impact processes in planetary sciences, *Annual review of earth and planetary sciences*, 21(1), 333-373, doi: <https://doi.org/10.1146/annurev.ea.21.050193.002001>.
- Holsapple, K. A., and Schmidt, R. M. (1982), On the scaling of crater dimensions: 2. Impact processes, *Journal of Geophysical Research: Solid Earth*, 87(B3), 1849-1870, doi: <https://doi.org/10.1029/JB087iB03p01849>.
- Hörz, F., Cintala, M., and Zolensky, M. (1993), Hypervelocity penetration tracks in very low-density, porous targets. In *Hypervelocity impacts in space*, edited by J. A. M. McDonnell, pp. 19-23, University of Kent Canterbury, Canterbury, England.
- Housen, K. R., and Holsapple, K. A. (1999), Scale effects in strength-dominated collisions of rocky asteroids, *Icarus*, 142(1), 21-33, doi: <https://doi.org/10.1006/icar.1999.6206>.
- Housen, K. R., and Holsapple, K. A. (2003), Impact cratering on porous asteroids, *Icarus*, 163(1), 102-119, doi: [https://doi.org/10.1016/S0019-1035\(03\)00024-1](https://doi.org/10.1016/S0019-1035(03)00024-1).
- Housen, K. R., and Holsapple, K. A. (2011), Ejecta from impact craters, *Icarus*, 211(1), 856-875, doi: <https://doi.org/10.1016/j.icarus.2010.09.017>.
- Housen, K. R., and Holsapple, K. A. (2012), Craters without ejecta, *Icarus*, 219(1), 297-306, doi: <https://doi.org/10.1016/j.icarus.2012.02.030>.
- Housen, K. R., Holsapple, K. A., and Voss, M. E. (1999), Compaction as the origin of the unusual craters on the asteroid Mathilde, *Nature*, 402(6758), 155, doi: <https://doi.org/10.1038/45985>.
- Housen, K. R., Sweet, W. J., and Holsapple, K. A. (2018), Impacts into porous asteroids, *Icarus*, 300, 72-96, doi: <https://doi.org/10.1016/j.icarus.2017.08.019>.
- Howard, K. A., and Wilshire, H. G. (1973), Flows of impact melt at lunar craters. Paper presented at 4th Lunar and Planetary Science Conference, Houston, TX.

- Kalynn, J., Johnson, C. L., Osinski, G. R., and Barnouin, O. (2013), Topographic characterization of lunar complex craters, *Geophysical Research Letters*, 40(1), 38-42, doi: <https://doi.org/10.1029/2012GL053608>.
- Kenkmann, T., Collins, G. S., and Wünnemann, K. (2012), The modification stage of crater formation. In *Impact cratering: Processes and products*, edited by G. R. Osinski and E. Pierazzo, pp. 60-75, John Wiley & Sons, Oxford, U.K.
- Kiefer, W. S. (2013), Gravity constraints on the subsurface structure of the Marius Hills: The magmatic plumbing of the largest lunar volcanic dome complex, *Journal of Geophysical Research: Planets*, 118(4), 733-745, doi: <https://doi.org/10.1029/2012JE004111>.
- Kiefer, W. S., Macke, R. J., Britt, D. T., Irving, A. J., and Consolmagno, G. J. (2012), The density and porosity of lunar rocks, *Geophysical Research Letters*, 39(7), doi: <https://doi.org/10.1029/2012GL051319>.
- Kieffer, S. W. (1975), From regolith to rock by shock, *The Moon*, 13(1-3), 301-320, doi: <https://doi.org/10.1007/BF00567522>.
- Kneissl, T., van Gasselt, S., and Neukum, G. (2010), New software tool for map-projection-independent crater size-frequency determination in ArcGIS. Paper presented at 41st Lunar and Planetary Science Conference, Houston, TX.
- Kreslavsky, M. A., Head, J. W., Neumann, G. A., Rosenburg, M. A., Aharonson, O., Smith, D. E., and Zuber, M. T. (2013), Lunar topographic roughness maps from Lunar Orbiter Laser Altimeter (LOLA) data: Scale dependence and correlation with geologic features and units, *Icarus*, 226(1), 52-66, doi: <https://doi.org/10.1016/j.icarus.2013.04.027>.
- Krüger, T., Hergarten, S., and Kenkmann, T. (2018), Deriving morphometric parameters and the simple-to-complex transition diameter from a new, high resolution database of fresh lunar impact craters ≥ 3 km, *Journal of Geophysical Research: Planets*, 123(10), 2667-2690, doi: <https://doi.org/10.1029/2018JE005545>.

- Kumar, P. S., Keerthi, V., Kumar, A. S., Mustard, J., Gopala Krishna, B., Ostrach, L. R., Kring, D., Kiran Kumar, A., and Goswami, J. (2013), Gullies and landslides on the Moon: Evidence for dry-granular flows, *Journal of Geophysical Research: Planets*, 118(2), 206-223, doi: <https://doi.org/10.1002/jgre.20043>.
- Lemelin, M., Lucey, P., Gaddis, L., Hare, T., and Ohtake, M. (2016), Global Map Products from the Kaguya Multiband Imager at 512 pppd: Minerals, FeO, and OMAT. Paper presented at 47th Lunar and Planetary Science Conference, Houston, TX.
- Love, S. G., Hörz, F., and Brownlee, D. E. (1993), Target porosity effects in impact cratering and collisional disruption, *Icarus*, 105(1), 216-224, doi: <https://doi.org/10.1006/icar.1993.1119>.
- Lucey, P. G., Blewett, D. T., Taylor, G. J., and Hawke, B. (2000), Imaging of lunar surface maturity, *Journal of Geophysical Research: Planets*, 105(E8), 20377-20386, doi: <https://doi.org/10.1029/1999JE001110>.
- Mahanti, P., Robinson, M., Thompson, T., and Henriksen, M. (2018), Small lunar craters at the Apollo 16 and 17 landing sites-morphology and degradation, *Icarus*, 299, 475-501, doi: <https://doi.org/10.1016/j.icarus.2017.08.018>.
- Mazarico, E., Lemoine, F., Goossens, S., Sabaka, T., Nicholas, J., Rowlands, D., Neumann, G., Torrence, M., Smith, D., and Zuber, M. (2013), Improved precision orbit determination of lunar orbiters from the GRAIL-derived lunar gravity models. Paper presented at 23rd AAS/AIAA Space Flight Mechanics Meeting, Hawaii Kauai.
- Melosh, H. J. (1977), Crater modification by gravity-A mechanical analysis of slumping. Paper presented at Impact and Explosion Cratering: Planetary and Terrestrial Implications, Flagstaff, AZ.
- Melosh, H. J. (1989a), Cratering Mechanics: Contact and Compression Stage. In *Impact cratering: A geologic process*, edited, pp. 46-59, Oxford University Press, New York.

- Melosh, H. J. (1989b), Cratering Mechanics: Modification Stage. In *Impact cratering: A geologic process*, edited, pp. 126-161, Oxford University Press, New York.
- Melosh, H. J. (1989c), Ejecta Deposits. In *Impact cratering: A geologic process*, edited, pp. 60-86, Oxford University Press, New York.
- Melosh, H. J. (1989d), *Impact cratering: A geologic process*, Oxford University Press, New York.
- Melosh, H. J. (1989e), Scaling of Crater Dimensions. In *Impact cratering: A geologic process*, edited, pp. 112-125, Oxford University Press, New York.
- Melosh, H. J. (1989f), Scaling of Crater Dimensions. In *Impact cratering: A geologic process*, edited, Oxford University Press, New York.
- Melosh, H. J., and Ivanov, B. (1999), Impact crater collapse, *Annual Review of Earth and Planetary Sciences*, 27(1), 385-415, doi: <https://doi.org/10.1146/annurev.earth.27.1.385>.
- Neish, C. D., Madden, J., Carter, L. M., Hawke, B. R., Giguere, T., Bray, V. J., Osinski, G. R., and Cahill, J. T. S. (2014), Global distribution of lunar impact melt flows, *Icarus*, 239, 105-117, doi: <https://doi.org/10.1016/j.icarus.2014.05.049>.
- Osinski, G. R., Silber, E. A., Clayton, J., Grieve, R. A., Hansen, K., Johnson, C. L., Kalynn, J., and Tornabene, L. L. (2018), Transitional impact craters on the Moon: Insight into the effect of target lithology on the impact cratering process, *Meteoritics & Planetary Science*, doi: <https://doi.org/10.1111/maps.13226>.
- Philpotts, J. A., and Schnetzler, C. (1970), Potassium, rubidium, strontium, barium, and rare-earth concentrations in lunar rocks and separated phases, *Science*, 167(3918), 493-495, doi: <https://doi.org/10.1126/science.167.3918.493>.
- Pierazzo, E., and Melosh, H. (2000), Melt production in oblique impacts, *Icarus*, 145(1), 252-261, doi: <https://doi.org/10.1006/icar.1999.6332>.

- Pierazzo, E., Vickery, A., and Melosh, H. (1997), A reevaluation of impact melt production, *Icarus*, 127(2), 408-423, doi: <https://doi.org/10.1006/icar.1997.5713>.
- Pike, R. J. (1974), Depth/diameter relations of fresh lunar craters: Revision from spacecraft data, *Geophysical Research Letters*, 1(7), 291-294, doi: <https://doi.org/10.1029/GL001i007p00291>.
- Pike, R. J. (1976), Crater dimensions from Apollo data and supplemental sources, *The Moon*, 15(3-4), 463-477, doi: <https://doi.org/10.1007/BF00562253>.
- Pike, R. J. (1977a), Apparent depth/apparent diameter relation for lunar craters. Paper presented at 8th Lunar and planetary science conference proceedings, Houston, TX.
- Pike, R. J. (1977b), Size-dependence in the shape of fresh impact craters on the Moon. In *Impact and Explosion Cratering: Planetary and Terrestrial Implications*, edited by D. J. Roddy, R. Pepin and R. Merrill, pp. 489-509, Pergamon Press, New York.
- Pike, R. J. (1980a), Control of crater morphology by gravity and target type-Mars, Earth, Moon. Paper presented at 11th Lunar and Planetary Science Conference Proceedings, Houston, TX.
- Pike, R. J. (1980b), Geometric interpretation of lunar craters, USGS Professional Paper Rep. 1046-C, C1-C77 pp, US Govt. Print. Off., Washington.
- Pike, R. J. (1988), Geomorphology of impact craters on Mercury. In *Mercury*, edited by F. Vilas, C. Chapman and M. Matthews, pp. 165-273, University of Arizona Press, Tucson, AZ.
- Plescia, J. B., and Cintala, M. (2012), Impact melt in small lunar highland craters, *Journal of Geophysical Research: Planets*, 117(E12), doi: <https://doi.org/10.1029/2011JE003941>.
- Prieur, N., Rolf, T., Luther, R., Wünnemann, K., Xiao, Z., and Werner, S. (2017), The effect of target properties on transient crater scaling for simple craters, *Journal of Geophysical Research: Planets*, 122(8), doi: <https://doi.org/10.1002/2017JE005283>.

- Quaide, W. L., Gault, D. E., and Schmidt, R. A. (1965), Gravitative effects on lunar impact structures, *Annals of the New York Academy of Sciences*, 123(1), 563-572, doi: <https://doi.org/10.1111/j.1749-6632.1965.tb20388.x>.
- Quaide, W. L., and Oberbeck, V. R. (1968), Thickness determinations of the lunar surface layer from lunar impact craters, *Journal of Geophysical Research*, 73(16), 5247-5270, doi: <https://doi.org/10.1029/JB073i016p05247>.
- Robinson, M., Eliason, E., Hiesinger, H., Jolliff, B., McEwen, A., Malin, M., Ravine, M., Thomas, P., Turtle, E., and Bowman-Cisneros, E. (2010), Lunar reconnaissance orbiter camera: first results. Paper presented at European Planetary Science Congress 2010, Rome, Italy.
- Roddy, D. (1977), Tabular comparisons of the Flynn Creek impact crater, United States, Steinheim impact crater, Germany and Snowball explosion crater, Canada. Paper presented at *Impact and Explosion Cratering: Planetary and Terrestrial Implications*, Flagstaff, AZ.
- Roddy, D. J., Pepin, R. O., and Merrill, R. B. (1977). Paper presented at *Impact and Explosion Cratering: Planetary and Terrestrial Implications*, Pergamon Press, New York.
- Salamunićar, G., Lončarić, S., and Mazarico, E. (2012), LU60645GT and MA132843GT catalogues of Lunar and Martian impact craters developed using a Crater Shape-based interpolation crater detection algorithm for topography data, *Planetary and Space Science*, 60(1), 236-247, doi: <https://doi.org/10.1016/j.pss.2011.09.003>.
- Schmidt, R. M., and Housen, K. R. (1987), Some recent advances in the scaling of impact and explosion cratering, *International Journal of Impact Engineering*, 5(1-4), 543-560, doi: [https://doi.org/10.1016/0734-743X\(87\)90069-8](https://doi.org/10.1016/0734-743X(87)90069-8).
- Schultz, P. (1997), Forming the south-pole Aitken basin-The extreme games. Paper presented at 28th Lunar and Planetary Science Conference, Houston, TX.

- Schultz, P., and Gault, D. (1975), Seismically induced modification of lunar surface features. Paper presented at 6th Lunar and Planetary Science Conference Proceedings, Houston, TX.
- Senft, L. E., and Stewart, S. T. (2008), Impact crater formation in icy layered terrains on Mars, *Meteoritics & Planetary Science*, 43(12), 1993-2013, doi: <https://doi.org/10.1111/j.1945-5100.2008.tb00657.x>.
- Sharpton, V. L. (2014), Outcrops on lunar crater rims: Implications for rim construction mechanisms, ejecta volumes and excavation depths, *Journal of Geophysical Research: Planets*, 119(1), 154-168, doi: <https://doi.org/10.1002/2013JE004523>.
- Shoemaker, E. M. (1959), Impact mechanics at Meteor crater, ArizonaRep. 2331-1258, US Geological Survey.
- Shoemaker, E. M., and Chao, E. C. (1961), New evidence for the impact origin of the Ries Basin, Bavaria, Germany, *Journal of Geophysical Research*, 66(10), 3371-3378, doi: <https://doi.org/10.1029/JZ066i010p03371>.
- Shoemaker, E. M., and Hackman, R. J. (1962), Stratigraphic basis for a lunar time scale. In *The Moon*, edited by Z. Kopal and Z. Mikhailov, pp. 289-300, Academic Press, New York.
- Smith, D. E., Zuber, M. T., Neumann, G. A., Mazarico, E., Head, J., and Torrence, M. H. (2011), Results from the Lunar Orbiter Laser Altimeter (LOLA): global, high resolution topographic mapping of the Moon. Paper presented at 42nd Lunar and Planetary Science Conference, Houston, TX.
- Smith, E. I., and Hartnell, J. A. (1978), Crater size-shape profiles for the Moon and Mercury: terrain effects and interplanetary comparisons, *The moon and the planets*, 19(4), 479-511, doi: <https://doi.org/10.1007/BF00901976>.

- Smith, J., Anderson, A., Newton, R., Olsen, E., Crewe, A., Isaacson, M., Johnson, D., and Wyllie, P. (1970), Petrologic history of the moon inferred from petrography, mineralogy and petrogenesis of Apollo 11 rocks, *Geochimica et Cosmochimica Acta Supplement*, 1, 897-925.
- Soderblom, J. M., Evans, A. J., Johnson, B. C., Melosh, H. J., Miljković, K., Phillips, R. J., Andrews-Hanna, J. C., Bierson, C. J., Head, J. W., and Milbury, C. (2015), The fractured Moon: Production and saturation of porosity in the lunar highlands from impact cratering, *Geophysical Research Letters*, 42(17), 6939-6944, doi: <https://doi.org/10.1002/2015GL065022>.
- Soderblom, L. A. (1970), A model for small-impact erosion applied to the lunar surface, *Journal of Geophysical Research*, 75(14), 2655-2661, doi: <https://doi.org/10.1029/JB075i014p02655>.
- Sthle, L., and Wold, S. (1989), Analysis of variance (ANOVA), *Chemometrics and intelligent laboratory systems*, 6(4), 259-272, doi: [https://doi.org/10.1016/0169-7439\(89\)80095-4](https://doi.org/10.1016/0169-7439(89)80095-4).
- Stewart, S. T., and Valiant, G. J. (2006), Martian subsurface properties and crater formation processes inferred from fresh impact crater geometries, *Meteoritics & Planetary Science*, 41(10), 1509-1537, doi: <https://doi.org/10.1111/j.1945-5100.2006.tb00433.x>.
- Sturm, S., Kenkmann, T., and Hergarten, S. (2016), Ejecta thickness and structural rim uplift measurements of Martian impact craters: Implications for the rim formation of complex impact craters, *Journal of Geophysical Research: Planets*, 121(6), 1026-1053, doi: <https://doi.org/10.1002/2015JE004959>.
- Taylor, S. R. (1989), Growth of planetary crusts, *Tectonophysics*, 161(3-4), 147-156, doi: [https://doi.org/10.1016/0040-1951\(89\)90151-0](https://doi.org/10.1016/0040-1951(89)90151-0).
- Tukey, J. W., and Cleveland, W. S. (1984), *The collected works of John W. Tukey*, Taylor & Francis.

- Veverka, J., Thomas, P., Harch, A., Clark, B., Bell III, J., Carcich, B., Joseph, J., Murchie, S., Izenberg, N., and Chapman, C. (1999), NEAR encounter with asteroid 253 Mathilde: overview, *Icarus*, 140(1), 3-16, doi: <https://doi.org/10.1006/icar.1999.6120>.
- Wieczorek, M. A., Neumann, G. A., Nimmo, F., Kiefer, W. S., Taylor, G. J., Melosh, H. J., Phillips, R. J., Solomon, S. C., Andrews-Hanna, J. C., and Asmar, S. W. (2012), The crust of the Moon as seen by GRAIL, *Science*, 1231530, doi: <https://doi.org/10.1126/science.1231530>.
- Wood, C., and Anderson, L. (1978), New morphometric data for fresh lunar craters. Paper presented at 9th Lunar and Planetary Science Conference Proceedings, Houston, TX.
- Wünnemann, K., Collins, G., and Melosh, H. (2006), A strain-based porosity model for use in hydrocode simulations of impacts and implications for transient crater growth in porous targets, *Icarus*, 180(2), 514-527, doi: <https://doi.org/10.1016/j.icarus.2005.10.013>.
- Wünnemann, K., Collins, G., and Osinski, G. (2008), Numerical modelling of impact melt production in porous rocks, *Earth and Planetary Science Letters*, 269(3-4), 530-539, doi: <https://doi.org/10.1016/j.epsl.2008.03.007>.
- Wünnemann, K., Nowka, D., Collins, G., Elbeshausen, D., and Bierhaus, M. (2011), Scaling of impact crater formation on planetary surfaces—Insights from numerical modeling. Paper presented at Proceedings of the 11th hypervelocity impact symposium, Freiburg, Germany.
- Zel'dovich, Y. B., and Raizer, Y. P. (1966), *Physics of Shock Waves and High Temperature Phenomena*, Academic Press, New York, doi: <https://doi.org/10.1016/B978-0-12-395672-9.X5001-2>.
- Zuber, M. T., Smith, D. E., Watkins, M. M., Asmar, S. W., Konopliv, A. S., Lemoine, F. G., Melosh, H. J., Neumann, G. A., Phillips, R. J., and Solomon, S. C. (2013), Gravity field

of the Moon from the Gravity Recovery and Interior Laboratory (GRAIL) mission,
Science, 339(6120), 668-671, doi: <https://doi.org/10.1126/science.1231507>.

APPENDIX B

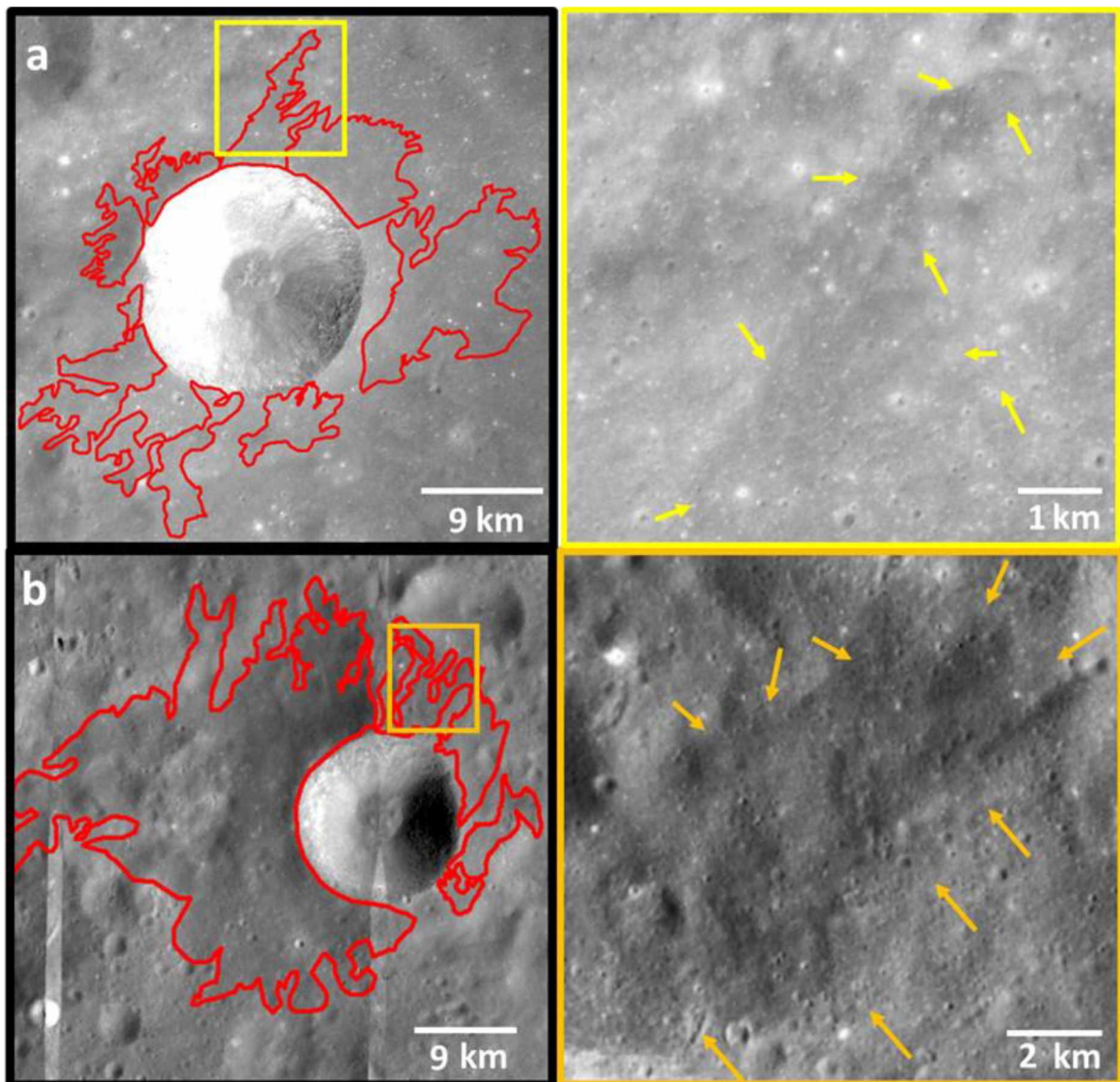






Figure B-1. Mapped distribution of impact melt flows (red outlines) around the rims of a) deep crater Hill (20.91°N, 40.81°E) and b) normal-depth crater Unnamed27 (14.04°N, 193.63°E). Visible impact melt deposits are present on the floors of both craters. The small boxes outlined in green and blue in the images on the left refer to the insets outlined in the respective shades on the right that represent magnified views of the melt flows included in the boxes. The arrows in the insets have been used to mark the edges of the flows. Kaguya TC ortho images have been used in the background. North is up in all images.

Table B-1. Data on the morphometric parameters of 15-20 km-sized 117 simple impact craters. Deep craters have been highlighted in bold font.

Color Legend:

	Porosity (%)
	10-12
	12-15
	15-17
	17-20

Symbology Definitions:

[1] d/D : Crater depth/Crater diameter ratio

[2] h/D : Rim height/Crater diameter ratio

[3] θ : Crater wall slope

[4] f/D : Floor diameter/Crater diameter ratio

[5] E/C : Ejecta volume/Cavity volume ratio

Name	Longitude (°E)	Latitude (°N)	Diameter (D) (km)	d/D	Std. Dev. (d/D)	h/D	Std. Dev. (h/D)	f/D	Wall Slope (θ)	Std. Dev. (θ)	Pre-impact terrain Elevation (km)	Std. Dev. (Pre-impact terrain Elevation) (km)	Pre-impct terrain Slope (°)	Std. Dev. (Pre-impct terrain Slope) (°)	EC	Std. Dev. (EC)
Boussingault T	43.06	-63	18.8	0.148	0.014	0.019	0.013	0.395	25.59	3.79	0.257	0.461	5.690	3.107	-	-
Cassegrain K	113.9	-54.5	16.8	0.189	0.011	0.026	0.012	0.366	31.67	2.80	-2.089	0.216	6.057	3.162	0.185	0.027
Jacobi J	10.27	-58	18.8	0.147	0.028	0.039	0.037	0.406	26.81	3.55	-0.508	0.677	9.970	6.544	-	-
Manzinus E	25.15	-69	18.4	0.156	0.026	0.039	0.031	0.477	29.01	2.30	0.805	0.862	9.923	5.260	-	-
Mutus L	24.81	-61.8	19.6	0.144	0.016	0.026	0.017	0.471	28.19	3.01	-0.165	0.307	4.300	2.570	-	-
Mutus P	25.55	-59.2	15.5	0.156	0.007	0.023	0.011	0.385	27.63	2.60	-0.896	0.146	4.756	1.888	0.338	0.078
Unnamed26	192.8	-60.4	16.5	0.158	0.021	0.033	0.037	0.419	25.87	2.49	-5.467	0.491	6.768	2.340	0.407	0.052
Clavius G	346	-52	17.1	0.162	0.008	0.029	0.010	0.471	26.39	5.80	0.037	0.183	4.337	2.246	-	-
Cooper G	178.8	52.42	19.2	0.145	0.008	0.026	0.009	0.275	26.28	3.14	1.042	0.219	6.163	4.113	0.416	0.123
Emden F	188.9	62.98	19.5	0.207	0.020	0.045	0.024	0.257	32.05	2.78	1.213	0.656	9.661	7.819	-	-
Guillaume J	189.5	43.56	16.6	0.184	0.010	0.040	0.011	0.400	29.73	3.18	2.477	0.201	5.563	2.936	0.496	0.057
Janssen K	42.31	-46.2	15.5	0.189	0.009	0.034	0.016	0.335	30.60	4.72	-2.697	0.175	4.849	2.797	0.338	0.031
Joule K	218.2	25.64	16.0	0.196	0.031	0.022	0.014	0.232	29.06	3.68	4.748	0.504	6.352	5.555	0.419	0.063
Lippmann J	253.7	-58.7	17.8	0.197	0.023	0.028	0.012	0.337	30.58	2.15	2.680	0.602	5.503	2.617	0.370	0.117
Planck W	131.3	-55.4	17.1	0.183	0.009	0.040	0.011	0.345	28.89	3.74	-1.977	0.085	3.523	1.318	0.551	0.034
Pontecoulant A	62.79	-57.7	18.8	0.158	0.013	0.031	0.013	0.354	27.74	3.13	-0.036	0.344	5.053	2.237	-	-
Sanford C	222.6	33.8	18.9	0.160	0.006	0.021	0.017	0.242	27.60	3.12	3.445	0.250	6.818	5.072	0.309	0.032
Sisakyan C	111	41.98	17.2	0.202	0.008	0.027	0.022	0.242	29.82	3.19	-1.532	0.351	7.560	3.347	-	-
Sumner G	110.4	37.42	17.4	0.181	0.014	0.031	0.011	0.364	28.91	4.12	-0.186	0.259	5.953	3.143	-	-
Unnamed12	152.3	56.68	16.5	0.197	0.040	0.035	0.025	0.280	29.52	3.07	0.558	0.573	8.686	4.685	-	-
Unnamed13	167.2	-46.8	17.5	0.168	0.020	0.032	0.024	0.356	27.98	2.40	-3.241	0.274	7.767	3.912	-	-
Unnamed14	172.5	64.4	17.1	0.176	0.016	0.026	0.016	0.289	28.88	2.38	0.472	0.369	5.720	4.525	-	-
Unnamed15	175.7	66.32	18.0	0.181	0.019	0.031	0.015	0.279	29.65	2.02	0.088	0.416	4.949	3.233	-	-
Unnamed17	181.4	53.45	17.2	0.171	0.024	0.042	0.040	0.215	28.83	2.77	1.407	0.728	10.338	5.717	-	-
Unnamed20	188.7	44.43	17.9	0.200	0.013	0.048	0.020	0.327	32.60	3.60	2.480	0.359	6.130	2.866	0.550	0.113
Unnamed21	189.7	36.54	16.3	0.193	0.010	0.062	0.048	0.303	29.17	3.40	3.834	0.366	11.222	5.454	-	-

Name	Longitude (°E)	Latitude (°N)	Diameter (D) (km)	d/D	Std. Dev. (d/D)	h/D	Std. Dev. (h/D)	f/D	Wall Slope (θ)	Std. Dev. (θ)	Pre-impact terrain Elevation (km)	Std. Dev. (Pre-impact terrain Elevation) (km)	Pre-impct terrain Slope (°)	Std. Dev. (Pre-impct terrain Slope) (°)	E/C	Std. Dev. (E/C)
Unnamed23	190.9	52.21	15.5	0.192	0.019	0.019	0.012	0.291	30.40	2.70	2.720	0.279	9.185	6.331	-	-
Unnamed24	191.1	47.24	15.6	0.211	0.009	0.041	0.012	0.240	31.34	2.01	2.160	0.092	5.684	3.568	0.339	0.020
Unnamed28	203.1	29.1	16.2	0.205	0.017	0.006	0.008	0.178	28.76	3.31	4.097	0.713	10.111	4.670	-	-
Unnamed29	207.7	-45.6	17.1	0.192	0.022	0.025	0.013	0.376	30.62	2.55	-3.830	0.284	7.188	4.014	0.203	0.021
Unnamed30	208.6	32.18	15.6	0.173	0.009	0.027	0.015	0.370	27.28	3.83	4.865	0.290	5.492	2.847	-	-
Unnamed4	127.2	62.73	16.7	0.186	0.013	0.011	0.009	0.291	29.29	2.16	-0.511	0.251	6.041	3.772	0.106	0.074
Unnamed40	237.8	-65.7	17.8	0.140	0.031	0.030	0.013	0.543	25.60	3.99	-3.464	0.707	4.864	2.759	0.435	0.126
Unnamed44	247.3	-57.8	16.2	0.159	0.036	0.011	0.015	0.257	26.92	2.30	-0.540	0.858	9.213	4.667	-	-
Unnamed5	127.6	-56.2	15.1	0.202	0.015	0.020	0.013	0.254	27.71	2.98	-1.728	0.556	5.435	4.549	0.305	0.139
Unnamed6	132.1	62.15	15.4	0.181	0.010	0.026	0.011	0.313	28.80	2.20	0.391	0.272	6.223	3.814	0.376	0.371
van den Bergh P	199.8	29.2	15.0	0.145	0.019	0.030	0.015	0.343	26.59	3.98	4.829	0.414	6.006	3.978	0.480	0.058
Viviani N	116.5	3.49	15.2	0.159	0.007	0.016	0.004	0.338	26.31	2.76	1.664	0.129	4.498	2.159	0.187	0.021
Vlacq A	39	-51.3	16.7	0.166	0.030	0.020	0.014	0.286	28.00	3.20	-0.661	0.602	6.309	3.043	-	-
Alden B	113.1	-20.6	15.0	0.183	0.010	0.037	0.030	0.251	28.01	2.74	1.376	0.345	7.922	4.848	-	-
Arrhenius J	271.6	-57.5	17.5	0.166	0.013	0.027	0.010	0.245	29.15	3.15	0.883	0.277	5.735	3.444	0.187	0.083
Bailly F	290.4	-67.5	16.6	0.192	0.009	0.028	0.013	0.395	31.56	2.30	-1.208	0.185	5.183	3.631	0.319	0.069
Black	80.39	-9.19	19.3	0.157	0.009	0.019	0.011	0.374	27.47	1.85	0.090	0.347	5.609	2.572	-	-
Brunner N	90.71	-11.4	18.0	0.191	0.008	0.021	0.019	0.374	29.77	3.42	0.188	0.324	6.609	3.999	-	-
Campbell E	158.9	46.33	15.8	0.150	0.032	0.038	0.014	0.373	23.98	4.33	3.390	0.509	7.495	3.250	-	-
Congreve G	196.1	-0.89	17.6	0.178	0.023	0.025	0.008	0.254	29.43	1.54	6.739	0.430	5.310	2.324	0.471	0.043
Coriolis G	174.5	-0.03	17.6	0.165	0.012	0.049	0.031	0.323	28.89	2.39	1.453	0.441	9.962	4.520	-	-
d'Alembert G	167.4	50.7	18.2	0.181	0.009	0.032	0.010	0.274	28.64	2.38	-1.078	0.102	4.353	2.350	0.381	0.051
Donner N	97.19	-33.2	20.0	0.172	0.024	0.036	0.013	0.396	30.58	3.49	-1.815	0.518	6.206	3.029	0.483	0.195
Doppler W	197.9	-11	15.2	0.188	0.007	0.028	0.013	0.316	29.36	1.75	6.812	0.219	6.143	4.224	0.339	0.015
Endymion E	66.24	53.59	17.6	0.166	0.020	0.034	0.025	0.416	28.10	3.65	-1.160	0.531	7.348	3.523	0.452	0.292
Gullstrand C	232.9	46.57	15.5	0.196	0.017	0.028	0.011	0.245	29.97	2.26	1.167	0.261	4.156	2.109	0.337	0.107

Table B-1 contd.

Name	Longitude (°E)	Latitude (°N)	Diameter (D) (km)	d/D	Std. Dev. (d/D)	h/D	Std. Dev. (h/D)	f/D	Wall Slope (°)	Std. Dev. (°)	Pre-impact terrain Elevation (km)	Std. Dev. (Pre-impact terrain Elevation) (km)	Pre-impct terrain Slope (°)	Std. Dev. (Pre-impct terrain Slope) (°)	E/C	Std. Dev. (E/C)
Kirkwood T	194.7	68.98	18.4	0.178	0.039	0.027	0.011	0.347	29.14	2.86	0.119	0.730	4.345	2.273	-	-
Saenger C	104.3	6.25	18.7	0.178	0.031	0.041	0.021	0.350	28.39	1.52	0.008	0.830	8.788	4.758	-	-
Santbech B	41.57	-24.7	15.7	0.197	0.021	0.025	0.021	0.271	28.31	2.88	0.468	0.511	8.495	4.081	-	-
Schliemann W	152.3	0.26	17.5	0.177	0.034	0.037	0.013	0.394	29.40	1.81	2.346	0.580	8.595	4.253	-	-
Unnamed27	193.6	14.04	16.3	0.193	0.015	0.045	0.033	0.286	30.41	1.81	6.159	0.470	8.755	3.710	-	-
Unnamed32	223.5	-36.9	17.4	0.171	0.030	0.031	0.022	0.387	27.63	3.32	0.244	0.741	6.639	4.726	-	-
Unnamed46	253.7	71.2	16.3	0.183	0.025	0.017	0.015	0.364	27.23	5.13	-1.145	0.716	5.864	4.465	0.257	0.227
Unnamed48	262.3	64.8	15.9	0.196	0.013	0.033	0.009	0.248	29.47	2.52	-0.314	0.249	3.862	1.945	-	-
Ventris B	158.1	-2.22	17.4	0.209	0.029	0.065	0.027	0.293	29.95	1.47	3.147	0.539	11.130	4.219	-	-
Vestine A	94.57	36.01	17.9	0.180	0.030	0.029	0.017	0.340	29.43	3.03	0.697	0.559	6.983	3.869	-	-
Vetchinkin P	130.6	7.06	16.3	0.161	0.015	0.019	0.014	0.291	26.09	2.98	3.054	0.375	9.177	4.716	-	-
von Bekesy F	137	52.8	19.5	0.195	0.014	0.031	0.015	0.332	31.48	2.71	0.172	0.337	6.228	3.775	-	-
Wurzelbauer A	344.6	-35.7	16.5	0.154	0.011	0.038	0.037	0.327	28.00	3.87	-0.355	0.348	8.450	5.038	-	-
Alhazen A	74.3	16.16	16.1	0.201	0.030	0.047	0.027	0.292	29.01	2.40	1.590	0.710	9.105	4.576	-	-
Bartels A	270.4	25.69	18.0	0.183	0.022	0.042	0.036	0.308	28.52	4.23	-0.065	0.451	10.065	9.188	-	-
Beaumont B	26.8	-18.7	15.2	0.171	0.008	0.028	0.021	0.371	28.30	3.37	0.124	0.267	8.032	5.004	-	-
Bouvard C	282.5	-37	15.0	0.197	0.020	0.019	0.013	0.277	29.64	3.27	-0.346	0.402	8.604	4.978	-	-
Bunsen C	270.2	44.2	18.9	0.202	0.017	0.021	0.020	0.246	30.22	2.63	-1.645	0.789	9.173	5.785	-	-
Catalan U	269.3	-45	19.0	0.199	0.006	0.040	0.013	0.415	31.47	2.70	1.171	0.124	5.521	2.023	0.382	0.057
Dante S	177.7	25.09	17.9	0.192	0.016	0.034	0.021	0.226	28.24	1.57	0.453	0.375	7.519	3.923	-	-
Darney	336.4	-14.6	15.2	0.183	0.009	0.030	0.009	0.329	30.09	2.83	-1.840	0.150	4.961	2.616	0.378	0.044
Dunthorne	328.3	-30.1	15.9	0.180	0.027	0.027	0.014	0.363	29.08	3.93	-0.514	0.636	8.959	4.655	-	-
Epimenides A	329.8	-43.3	15.0	0.192	0.012	0.033	0.009	0.260	30.49	3.03	-1.353	0.168	4.416	2.289	0.487	0.085
Gardner	33.81	17.74	17.6	0.173	0.011	0.026	0.013	0.465	26.80	3.65	-0.634	0.265	4.798	2.000	0.289	0.171
Geminus D	47.29	30.57	15.6	0.183	0.014	0.035	0.025	0.328	29.74	3.73	-0.372	0.416	7.976	2.932	-	-
Glaisher	49.34	13.18	16.0	0.190	0.023	0.031	0.037	0.330	29.99	2.53	0.229	0.477	9.232	7.127	-	-

Table B-1 contd.

Name	Longitude (°E)	Latitude (°N)	Diameter (D) (km)	d/D	Std. Dev. (d/D)	h/D	Std. Dev. (h/D)	f/D	Wall Slope (θ)	Std. Dev. (θ)	Pre-impact terrain Elevation (km)	Std. Dev. (Pre-impact terrain Elevation) (km)	Pre-impct terrain Slope (°)	Std. Dev. (Pre-impct terrain Slope) (°)	E/C	Std. Dev. (E/C)
Glauber	142.7	11.31	15.3	0.162	0.014	0.043	0.031	0.316	28.66	3.01	3.813	0.329	9.772	5.476	-	-
Golitsyn J	256.8	-27.7	19.4	0.190	0.018	0.022	0.012	0.387	30.14	3.79	1.159	0.436	7.665	5.008	-	-
Gutenberg A	39.91	-9.03	15.0	0.196	0.026	0.057	0.017	0.291	30.81	1.89	-0.791	0.466	11.299	3.703	-	-
Harden	143.5	5.46	15.1	0.181	0.007	0.031	0.004	0.249	28.76	1.75	-0.818	0.114	4.926	2.880	0.355	0.070
Heyrovsky	264.6	-39.5	16.4	0.201	0.024	0.029	0.020	0.251	30.62	3.16	3.396	0.511	6.161	2.733	0.360	0.077
Hipparchus C	8.21	-7.41	16.6	0.207	0.021	0.034	0.024	0.305	31.95	1.47	1.403	0.521	7.372	3.305	0.402	0.211
Inghirami C	285.4	-44.1	17.5	0.198	0.026	0.039	0.013	0.338	32.26	2.70	0.983	0.369	7.265	2.809	0.412	0.219
Isidorus D	34.07	-4.27	15.2	0.202	0.006	0.036	0.006	0.274	30.01	1.79	-1.281	0.106	4.941	2.300	0.377	0.044
Kurchatov X	140.1	41.18	16.8	0.176	0.021	0.032	0.017	0.330	28.50	3.23	0.988	0.438	6.320	4.337	0.440	0.276
Lehmann C	309.8	-35.6	15.1	0.209	0.021	0.026	0.021	0.228	29.80	3.21	0.229	0.665	6.056	2.989	-	-
Lents J	262.6	-3.63	16.1	0.200	0.011	0.033	0.014	0.319	32.00	2.07	3.310	0.314	5.391	2.343	0.347	0.047
Liouville	73.56	2.72	16.6	0.177	0.006	0.026	0.015	0.338	28.06	1.63	-0.658	0.301	5.654	3.286	0.294	0.190
Lowell W	252.8	-10.2	17.4	0.171	0.032	0.053	0.042	0.452	30.15	2.87	4.870	0.805	12.675	8.630	-	-
Maunder A	269.4	-3.28	15.2	0.190	0.015	0.027	0.011	0.241	29.51	2.08	2.433	0.183	5.968	3.786	0.351	0.037
Maury	39.69	37.11	16.9	0.194	0.004	0.043	0.029	0.325	30.00	3.51	-0.165	0.260	7.601	4.185	-	-
Nikolaev J	155.4	31.59	19.0	0.185	0.017	0.019	0.014	0.277	29.75	3.40	1.307	0.319	6.854	3.403	-	-
Pickering	6.99	-2.87	15.7	0.187	0.019	0.048	0.013	0.351	31.73	1.51	0.458	0.247	6.830	3.620	-	-
Riccioli H	285	1.11	18.0	0.203	0.012	0.045	0.019	0.275	31.86	1.50	0.337	0.310	6.916	2.550	-	-
Richards	140.1	7.7	17.1	0.194	0.019	0.037	0.008	0.273	29.67	2.06	-1.021	0.182	8.498	5.951	-	-
Safarik H	178.5	9.53	15.5	0.179	0.017	0.028	0.028	0.260	28.00	3.19	3.698	0.576	8.383	3.548	-	-
Schickard H	297.7	-43.5	16.2	0.187	0.007	0.035	0.011	0.414	30.50	3.34	-0.018	0.210	5.722	2.917	-	-
Schwarzschild T	107.6	69.82	16.2	0.195	0.022	0.021	0.014	0.184	31.04	2.18	-1.223	0.520	5.355	2.557	0.239	0.144
Spencer Jones H	168.1	11.93	15.1	0.219	0.015	0.047	0.018	0.254	32.12	1.62	1.523	0.364	9.527	3.789	-	-
Sundman V	266.4	11.96	18.3	0.193	0.010	0.055	0.010	0.334	32.24	2.69	1.813	0.253	6.064	2.295	-	-
Tralles A	47.03	27.42	17.4	0.190	0.005	0.035	0.012	0.362	31.05	4.00	-1.010	0.180	4.922	1.907	0.360	0.091
Unnamed18	181.8	8.79	16.2	0.186	0.029	0.040	0.036	0.317	28.28	1.43	4.277	0.657	10.618	5.757	-	-

Table B-1 contd.

Name	Longitude (°E)	Latitude (°N)	Diameter (D) (km)	d/D	Std. Dev. (d/D)	h/D	Std. Dev. (h/D)	f/D	Wall Slope (°)	Std. Dev. (°)	Pre-impact terrain Elevation (km)	Std. Dev. (Pre-impact terrain Elevation) (km)	Pre-impct terrain Slope (°)	Std. Dev. (Pre-impct terrain Slope) (°)	E/C	Std. Dev. (E/C)
Unnamed43	241.4	-21	16.2	0.180	0.019	0.029	0.019	0.391	28.28	5.54	3.135	0.527	7.856	3.738	-	-
Unnamed47	254.3	41.01	15.6	0.212	0.023	0.030	0.020	0.242	31.37	3.14	1.015	0.338	5.960	3.049	0.296	0.139
Unnamed50	268.4	37.16	15.8	0.186	0.012	0.025	0.012	0.207	29.25	3.36	0.057	0.357	6.426	5.262	-	-
Unnamed9	139.4	44.52	15.3	0.195	0.017	0.023	0.016	0.252	29.06	2.46	1.172	0.405	5.549	2.013	0.264	0.129
Wargentín D	294.7	-51	15.7	0.188	0.009	0.038	0.017	0.292	28.84	2.28	0.877	0.147	6.578	3.902	0.408	0.097
Hill	40.81	20.91	15.7	0.222	0.012	0.030	0.011	0.248	31.43	2.96	-0.443	0.245	5.192	2.271	0.296	0.232
Langrenus M	66.41	-9.81	18.0	0.208	0.014	0.031	0.014	0.296	31.43	1.51	-1.058	0.392	5.864	2.265	0.267	0.140
Polybius A	27.97	-23	16.6	0.246	0.012	0.027	0.008	0.107	30.78	3.00	0.311	0.223	6.897	3.174	0.243	0.246
Unnamed31	218.6	18.32	15.9	0.221	0.019	0.027	0.012	0.231	30.85	2.42	2.706	0.323	5.397	3.641	0.218	0.037
Unnamed35	225	-1.9	15.8	0.212	0.013	0.030	0.012	0.286	31.27	2.77	3.218	0.156	6.900	5.031	0.275	0.019
Unnamed39	235.7	-1.36	15.8	0.216	0.008	0.038	0.021	0.226	30.63	1.35	2.581	0.441	7.404	2.980	0.420	0.102
Unnamed8	137.7	23.62	17.7	0.248	0.015	0.045	0.023	0.057	30.51	3.22	4.934	0.422	7.974	3.415	-	-
W. Bond B	7.51	65.03	15.2	0.217	0.006	0.042	0.007	0.295	31.02	2.80	-1.324	0.065	4.099	1.278	0.415	0.029

Table B-1 contd.

Table B-2. Results from one-way ANOVA of the three d/D groups classified by porosity ranges: A (17-20%), B (15-17%), C (10-15%). Deep craters were excluded from this test. A p-value of less than 0.05 indicates that the d/D s of craters in one or more groups are significantly different.

Source of Variation	Sum of Squares (SS)	Degrees of Freedom (df)	Mean Square Error (MSE)	F-statistic	p-value
Between Groups	0.005	2	0.0024	9.144	0.0002
Within Groups	0.028	106	0.0003		
Total	0.033	108			

Table B-3. Results from Tukey Kramer HSD test that are indicative of the pairs among the d/D groups (classified by porosity) that are significantly different from each other. The various groups have been labelled as: A (10-15%), B (15-17%), C (17-20%). The statistically significant pairs ($p < 0.05$) are highlighted in bold font. The critical value of the Q-statistic for $\alpha = 0.05$, $k = 3$ groups and $\nu = 106$ degrees of freedom is 3.362.

Pair	Q-statistic	p-value	Inference
A vs B	1.121	0.692	Insignificant
A vs C	5.792	0.001	p < 0.05
B vs C	4.002	0.015	P < 0.05

Table B-4. Results from one-way ANOVA of the three crater wall slope groups classified by porosity ranges: A (17-20%), B (15-17%), C (10-15%). A p-value of less than 0.05 indicates that the wall slopes of craters in one or more groups are significantly different.

Source of Variation	Sum of Squares (SS)	Degrees of Freedom (df)	Mean Square Error (MSE)	F-statistic	p-value
Between Groups	53.881	2	26.940	11.114	3.894e-05
Within Groups	276.336	114	2.424		
Total	330.216	116			

Table B-5. Results from Tukey Kramer HSD test that are indicative of the pairs among the crater wall slope groups (classified by porosity) that are significantly different from each other. The various groups have been labelled as: A (10-15%), B (15-17%), C (17-20%). The statistically significant pairs ($p < 0.05$) are highlighted in bold font. The critical value of the Q-statistic for $\alpha = 0.05$, $k = 3$ groups and $\nu = 114$ degrees of freedom is 3.359.

Pair	Q-statistic	p-value	Inference
A vs B	0.744	0.844	Insignificant
A vs C	6.175	0.001	p < 0.05
B vs C	4.662	0.004	P < 0.05

CHAPTER 4 INFLUENCE OF TARGET PROPERTIES ON WALL SLUMPING IN LUNAR CRATERS WITHIN THE SIMPLE-TO-COMPLEX TRANSITION

Abstract

The narrow 15-20 km crater diameter range on the Moon covers a diverse group of impact crater morphologies from simple to transitional to complex craters. Simple craters in this range are confined to the highlands. Transitional craters that contain localized slumps are scattered all over the lunar surface. Most craters with localized slumps on the highlands surface superpose sharp topographic breaks and the pre-existing topography may have caused conditions favorable for post-excavation internal slumping. However, some of these craters formed on terrains with topographic variation similar to the settings of simple craters: flat or gradually sloping surface, or degraded structures of older craters such as rims and terraces. To resolve the conundrum of two morphologies on one type of terrain, we performed detailed investigations of the local geology and topography of the pre-impact terrains. We evaluated if the localized slumping in the craters happened post-crater formation, looked for spatial variations in the strength of the highlands crust, detected topographic breaks (through elevation data) that were unnoticeable in the optical data, and examined rim circularity. Our findings corroborate the influence of pre-existing slopes on mass wasting along crater walls. The majority of the craters with localized slumps have walls superposing topographic breaks that slope in the same direction as the walls. These walls are located near the uphill sector of the rims which initiated localized slumping. Most simple craters were found to have formed on surfaces with topographic breaks/slopes that face away from the adjoining crater walls, so that any immediate mass wasting would likely be outside the crater cavity.

4.1 Introduction

4.1.1 Wall Slumping

The size-dependent simple-to-complex morphologic progression in impact craters on the Moon has been studied for over 40 years (Melosh, 1989; Pike, 1977, 1980a, 1980b). After formation of a transient parabolic cavity, crater features developed in the modification stage form the basis of a “simple” or “complex” crater morphology. For smaller craters, the walls undergo gravity-induced collapse and material slumps off the walls, thereby forming a breccia lens on the crater floor and giving the final crater a roughly parabolic profile (Melosh, 1989; Melosh & Ivanov, 1999). For lunar crater sizes greater than ~15 km (Croft, 1985; Krüger et al., 2018; Melosh & Ivanov, 1999; Pike, 1977, 1980a, 1980b, 1988), in addition to unconsolidated material from wall slumping, the onset of floor features such as terraces (sliding of discrete blocks along normal faults) and central peaks occurs, which are the diagnostic features of a complex crater morphology (Kenkmann et al., 2012; Melosh, 1989; Pike, 1980a, 1980b; Quaide et al., 1965). While complex craters on the Moon begin to form at sizes greater than ~15 km, the simple-to-complex transition occurs over a diameter range. The transition zone constitutes simple, complex and transitional craters. Transitional craters have floors that are broader than that of simple craters, contain localized or spread out unconsolidated slumped material and/or terraces while lacking a well-defined central peak (Cintala et al., 1977; Cintala & Grieve, 1998; Howard, 1974; Kalynn et al., 2013; Pike, 1974; Plescia, 2015; Robbins & Hynek, 2012; Smith & Sanchez, 1973). Chandnani et al. (2019) identified slumped debris based on gradual decrease in wall slope at the contact of the debris and wall, and terraces on the basis of a step-like pattern in topographic profiles.

Regardless of the morphology, transient cavity collapse is driven by gravity and extreme strength degradation of impacted target rocks (Melosh, 1977, 1989; Quaide et al., 1965). For the

transient cavity to weaken and rock to mobilize, the effective strength of the impacted rocks has been determined to be much lower than the cohesion of intact rocks (Güldemeister et al., 2015; Kenkmann et al., 2012; Melosh, 1977, 1989), and the effective coefficient of friction is much lower than that of typical granular targets (McKinnon, 1978). Melosh (1977) hypothesized that the dimensionless ratio $\rho gh/c$ (ρ is target density, g is acceleration of gravity, h is crater depth, c is transient yield strength) governs the stability of a crater. When $\rho gh/c$ is less than 5, the cavity is stable. For values of $\rho gh/c$ between 5 and 10, wall failures occur resulting in slumping and/or terracing. If $\rho gh/c$ exceeds 15, floor failure begins and rocks get uplifted to form central structures in addition to wall failure features.

While the mechanisms driving the transient strength degradation of target rocks are still debated, several target properties can assist in lowering of rock strength. Target heterogeneities such as interlayering of different lithologies or unconsolidated sediments with cohesive substrate can create strength variations in the target and trigger cavity collapse, thereby forming slump features and/or terraces and/or central peaks. This is why a smaller diameter has been observed for the onset of transitional and complex craters in layered targets (Chandnani et al., 2019; Cintala et al., 1977; Cooper, 1977; Dence, 1972; Osinski et al., 2018; Pike, 1980a; Quaide & Oberbeck, 1968; Roddy, 1977; Senft & Stewart, 2008; Smith & Hartnell, 1978; Stewart & Valiant, 2006). Impact on a target characterized by spatial variations in strength can also lead to cavity collapse features. Several experimental (Aschauer & Kenkmann, 2017) and observational studies on impact craters on slopes on the Moon (Plescia, 2012; Plescia et al., 2019), and asteroids Vesta (Krohn et al., 2014) and Lutetia (Elbeshausen et al., 2012), have reported that when a hypervelocity impactor hits a sloping surface, the transient cavity grows in a direction perpendicular to the slope of the surface. The cavity wall in the uphill sector of the rim (the wall sloping in the direction of the

surface slope) can get over-steepened, which initiates slumping in the form of landslides even for surface slope angles as low as 5° from horizontal. With increasing slope angles, the deepest point of the crater shifts downhill from crater-center and the depth-diameter ratio (d/D) decreases due to the mass movements. The crater shape also loses its symmetry and elongates in the downhill direction. If slope angles approach the angle of repose of the target material, the landslides can overshoot the downhill crater rim. However, no cases of craters with central peaks were observed in these studies. Other than the process of slumping during crater formation, seismic shaking from nearby younger impacts can trigger mass wasting along crater walls post-crater formation (Kumar et al., 2013; Schultz & Gault, 1975).

The narrow 15-20 km diameter range, which is a subset of the lunar simple-to-complex transition zone, constitutes a diverse group of morphologies spanning a variety of geologic settings. In order to elucidate the reasons behind these morphological variations, Chandnani et al. (2019) created a database of 244 well-preserved 15-20 km-sized lunar craters and characterized their morphologies based on their features in Lunar Reconnaissance Orbiter Camera (Robinson et al., 2010) Wide Angle Camera (LROC WAC) images, LROC Narrow Angle Camera (NAC) images and their LROC Lunar Orbiter Laser Altimeter (LOLA) (Smith et al., 2011) topographic profiles. The craters were not categorized as simple, transitional or complex, but classified according to the presence of crater units like slumped material, terraces, central uplifts, floor fractures and so on. Chandnani et al. (2019) created seven morphologic groups:

[1] Simple crater

[2] Crater with localized slumps

[3] Crater with localized slumps and terraces

[4] Crater with localized slumps and central uplift

[5] Crater with localized slumps, terraces and central uplift

[6] Concentric crater

[7] Floor-fractured crater

The cavities of the simple craters are characterized with uniform wall slopes and roughly parabolic profiles. The localized slumps refer to the unconsolidated slumped material that is confined to certain parts of the floor such that their position is marked by a gradual decrease in wall slope. Morphologies [2] and [3] are types of transitional craters while [4] and [5] can also be called complex craters due to the presence of a central uplift. The major morphologies that occupy the lunar highlands are the simple craters and the craters with localized slumps (see Figure 4 in Chandnani et al., 2019). On studying the geology of the terrains bearing these craters, Chandnani et al. (2019) noticed that the 117 simple craters occur on flat or gradually sloping surfaces or superpose degraded rims or terraces of pre-existing craters. The majority of the craters with localized slumps were formed on sharp topographic breaks such as well-developed rims, terraces or ejecta of older craters, and therefore the slumped debris could have resulted from oversteepening of a crater wall sloping in the direction of the topographic break (Aschauer & Kenkmann, 2017; Elbeshausen et al., 2012; Krohn et al., 2014; Plescia, 2012; Plescia et al., 2019). However, the topographic variation of the terrains comprising 35 of the 97 craters with localized slumps was observed to be similar (no sharp topographic breaks) to that of the terrains bearing the simple craters. Chandnani et al. (2019) also noted that the depth ranges of the simple craters and craters with localized slumps show a significant overlap. A preliminary examination of the geology of the two terrains indicated that no other differences in the target properties were visible that could justify the presence of localized slumps in the 35 craters and their absence in the simple craters. Figure 4.1 shows examples of the kind of topographic trends followed by pre-impact terrains of

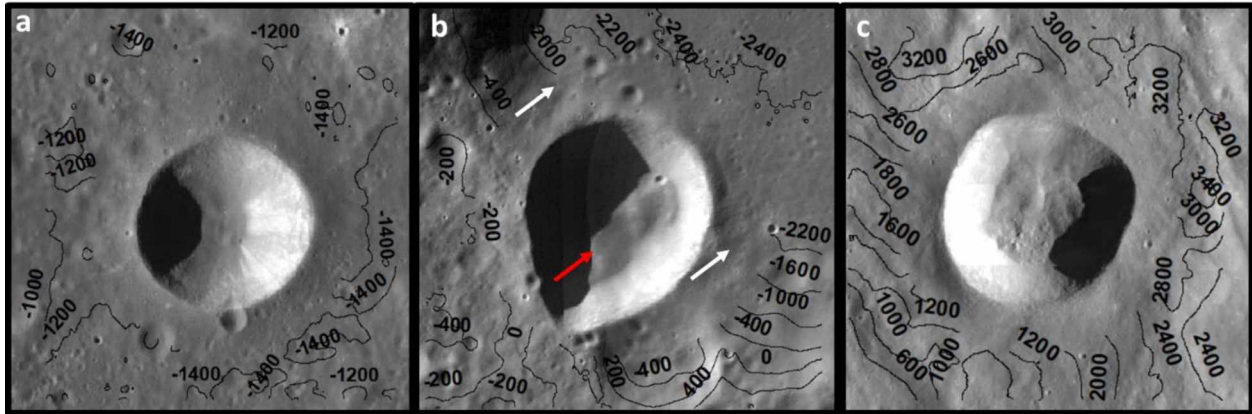


Figure 4.1. LOLA elevation contours superposed on WAC images of 15-20 km-sized simple craters and craters with localized slumps on highlands terrains. a) Simple crater Isidorus D (-4.27°N, 34.07°E) located on a flat highlands surface; b) Crater Unnamed2 (-56.32°N, 90.33°E) with localized slumps that superposes the terrace of a pre-existing larger crater; c) Crater Leuschner Z (5.24°N, 250.43°E) with localized slumps located on a highlands terrain that gradually slopes from north to south. The contours represent the pre-impact terrain elevation acquired from LOLA DEMs and begin at 1.5 radii from the crater center to avoid the ejecta. The elevation values are in meters. In (b) the terrace is the slope on which the crater was formed. The red arrow in (b) refers to the wall that slopes in the direction of the terrace slope (white arrows) and therefore experienced mass wasting from oversteepening, which is also evidenced by the uphill extension of that part of the rim. All images are 30 km wide. North is up in all images.

simple craters and craters with localized slumps. The elevation contours highlight the topographic variations.

4.1.2 Objectives

We aim to track down the factors responsible for variations in slumping, and hence morphological variations (simple craters and craters with localized slumping) in 15-20 km-sized craters on similar target terrains, that is terrains devoid of sharp topographic breaks. We propose and investigate three working hypotheses:

4.1.2.1 *Localized slumping occurred post-crater formation*

It is possible that the 35 craters with localized slumps formed with simple crater morphologies, and slumping occurs later due to seismic shaking caused by nearby younger impacts (Kumar et al., 2013; Schultz & Gault, 1975).

4.1.2.2 Localized slumping occurred on weaker target

As described earlier, wall collapse is caused by target strength degradation and gravitational force (Güldemeister et al., 2015; Kenkmann et al., 2012; Melosh, 1977, 1989; Quaide et al., 1965). The greater the strength, the less intense is the collapse. Ever since the formation of the highlands crust, it has been battered by impacts. The shock waves from these impacts have resulted in fractured and fragmented crust in the form of crater ejecta (Heiken et al., 1991), crater modification features, 10 km-deep fractured bed rock called megaregolith (Hartmann, 1973) and meter thick fine-grained surface regolith (Bart et al., 2011; Papike et al., 1982). Continuous impacts and fragmentation could have led to spatial heterogeneities in the highlands crustal strength. Therefore, we hypothesize that localized slumping occurred on the highlands terrains whose strength is lower than that of the terrains that bear simple craters in the same size regime.

4.1.2.3 Impact cratering on a slope causes the localized slumping

In the case of the remaining 62 highlands craters with localized slumps, the superposition of crater walls on topographic breaks was visible. So, the craters qualified for localized wall slumping along the uphill rim sector due to impact cratering on slopes (Aschauer & Kenkmann, 2017; Elbeshausen et al., 2012; Krohn et al., 2014; Plescia, 2012; Plescia et al., 2019). Similarly, there could be subtle topographic heterogeneities in the pre-impact terrains of the 35 craters with localized slumps that have been obscured by younger impact craters and their ejecta and therefore are not noticeable in the LROC WAC and NAC images. These heterogeneities may have served as slopes for the transient cavity walls that were superposing them and sloping in the same direction, and caused them to oversteepen and collapse, thereby resulting in localized slumped material.

4.2 Methods and Data Sets

4.2.1 Testing hypothesis 1: Comparison of crater densities on slumps and ejecta units of craters with localized slumps

If the localized slumped material accumulated post-crater formation, it is younger than the crater's ejecta. On airless bodies like the moon, new surfaces immediately begin collecting craters. An older surface would contain more craters per unit area than a younger surface, all else being equal. Counting of craters above a specified size on a given surface gives a crater-size frequency distribution (CSFD). Combined with an estimate of the rate of production of craters, the CSFD can be used to estimate the age of a surface (Neukum et al., 1975a; Neukum et al., 1975b; Neukum, 1983). For each of the 35 craters with localized slumps, we used 512 ppd LOLA DEMs to delineate regions of the slumped material and ejecta that are nearly flat (slope angles of 0° - 7°) to discard the influence of surface relief on a CSFD. The slumped material is positioned along the crater wall and can therefore have less flat and more steep surfaces. Craters whose slumped material did not have flat surfaces were excluded from the crater counting analysis. The area of ejecta beyond 1.25 crater radii (R) from the crater center showed up as nearly flat. So, we created an annulus from 1.25 R to 1.5 R for the crater counts on the ejecta surface. The upper limit of 1.5 R was selected because the ejecta profile starts levelling out at this distance and begins transitioning into the pre-impact terrain topography. Figure 4.2 illustrates the selected flat regions of the two units in a crater with localized slumps. Next, we used 10m/pixel Kaguya Terrain Camera (TC) images (Haruyama et al., 2008) to outline rims of craters on the delineated regions of the slumps and ejecta of each crater starting at 100 m diameter. A Kaguya TC image provides views of the lunar surface at moderate sun angles that allow for easier detection of surface features, and larger coverage (width of ~50 km) as compared to the higher resolution NAC image data, which minimizes sun-angle

variation across the area of coverage. On fitting circular outlines to the crater rims with the help of the CraterTools in ArcGIS (Kneissl et al., 2010), we obtained their diameters as well. For each crater belonging to the group of 35 craters, the cumulative crater densities (N) corresponding to the localized slumps and ejecta units were obtained by dividing the number of craters (with diameters up to a value) belonging to each unit by the area of the unit. The cumulative crater densities were used to generate separate log-log CSFD plots for the slumps and ejecta of each crater. The crater diameters were binned at 18 equally spaced intervals per 10 km, which is called pseudo-log binning (Neukum, 1983). The error bars on each data point were calculated by dividing the square root of the respective cumulative frequency by the surface area of the unit (Arvidson et al., 1979). Using the Craterstats program developed by Michael and Neukum (2010), we fit crater production functions updated by Neukum et al. (2001) to each CSFD. A production function is a polynomial curve that provides an estimate of the number and size of craters expected on a surface of a given age, and curves for different surface ages can be compared to a CSFD to provide an estimate of the cumulative crater density at diameter (D) of 1 km ($N(1)$) for that CSFD (Neukum, 1983; Neukum & Ivanov, 1994; Neukum et al., 2001). The values of $N(1)$ has been inferred to be a measure of the age of the respective surface unit (Neukum, 1983; Neukum & Ivanov, 1994; Neukum et al., 2001). Therefore, if the $N(1)$ values corresponding to the slump and ejecta units fall within each other's error bars (square root of cumulative crater frequency at D of 1 km divided by surface area of the unit), it means that localized slumping possibly occurred around the time of ejecta deposition, that is syn-crater formation. If the $N(1)$ values fall outside the error bars, the slumped material accumulated post-crater formation and therefore it is possible that such craters were initially formed as simple craters. The CSFD bins along or parallel to the Hartmann (1984) saturation line were excluded from the production function fit because crater densities along this

line imply that the number of craters created is equal to the number of craters destroyed. This applied to parallel bins as well because craters belonging to these bins may not reach the crater density that would coincide with the saturation line because of faster obliteration on rough highlands terrains, but have the same characteristics as bins along the saturation line. Chandnani et al. (2019) (see Figure S4 of that paper) performed crater counting on a few craters with localized slumps and found that crater densities on ejecta and slump units of one of the three craters statistically differed from each other. This preliminary result is our motivation to expand the crater counting task to the 35 craters with localized slumps and eliminate the deduced simple craters from the list.

Crater degradation through time involves certain changes in the crater geometry. A widely accepted model that explains the evolution of crater topography through time is the topographic diffusion model (Bouley & Baratoux, 2011; Craddock & Howard, 2000; Fassett & Thomson, 2014; Kreslavsky et al., 2013). According to this model, rim and wall collapse and consequent slumping can continue post-crater formation primarily due to seismic shaking from late impacts (Kumar et al., 2013; Schultz & Gault, 1975), which results in progressive lowering of rim height, reduction in wall slopes and shallowing and broadening of the crater floor. Topographic profiles of the craters inferred as simple from the crater counting procedure were compared with the profiles of inferred craters with localized slumps to verify the accumulation of slumped material in the simple craters as a result of crater degradation through topographic diffusion.

4.2.2 Testing hypothesis 2: Frequencies of proximal simple craters and craters with localized slumps

If there are major spatial variations in the strength of the highlands crust, then a greater number of simple craters should be formed in the stronger geologic settings whereas the weaker

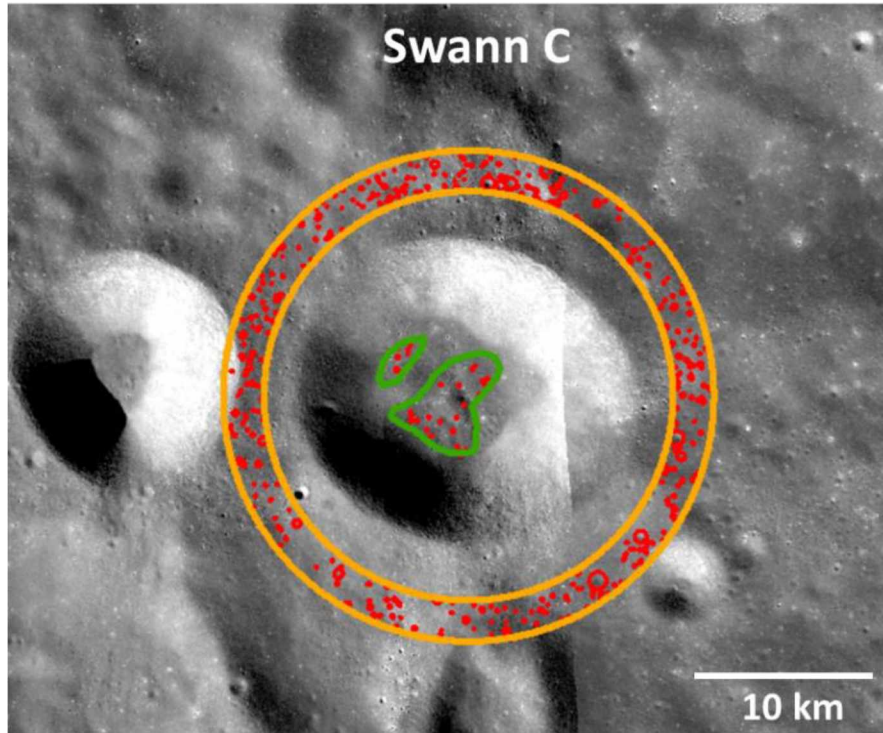


Figure 4.2. Slump and ejecta units mapped on the Kaguya TC image of crater Swann C that has localized slumped material. It is located at 52.9°N, 114.28°E. The annulus outlined in orange refers to the ejecta unit and the area outlined in green is the area of the localized slumps selected for crater counting based on flat surface criteria (slope angles of 0°-7°). The craters detected in both units are marked with red circular outlines. North is up.

terrains should contain more craters with localized slumps. Therefore, using LROC WAC images, we looked for and counted simple craters and craters with localized slumps in the simple-to-complex transition zone starting at a D of 15 km within a radius of 100 km from the center of all 117 simple craters and the 35 craters with localized slumps. We extended the crater diameter range for the proximity craters to beyond 20 km and set the upper limit to 40 km because recent studies have found transitional craters that measure up to ~40 km in size (Osinski et al., 2018). Only those craters were included that occur on flat surfaces, gradually sloping surfaces or superpose degraded craters, that is, the type of terrains on which the 15-20 km-sized simple craters and 35 craters with localized slumps were formed. Maps of the relative percentages of the proximal craters with localized slumps were generated. Maps of the relative percentages of the proximal craters with localized slumps with respect to the percentages of the proximal simple craters were generated for

each 15-20 km-sized crater. The maps would indicate if the 35 craters with localized slumps are surrounded by most craters with the same type of morphology (and hence weaker terrains) or if there are clusters of higher percentages of simple craters or craters with localized slumps in particular geologic settings surrounding both crater morphologies.

4.2.3 Testing hypothesis 3: Topographic variation in pre-impact terrains of the simple craters and craters with localized slumps along with rim circularity

The region located between a distance of 1.5 R (where the ejecta profile levels out) and 2 R from crater center was selected for the study of pre-impact terrain topography. For all 117 simple craters and 35 craters with localized slumps, with the help of LOLA DEMs, we created aspect-slope maps of the pre-impact region that would indicate if there are slopes reflecting sharp breaks in elevation that went unnoticed in the optical images and simultaneously display the aspect (slope direction) associated with each slope value. All aspect values were measured as azimuthal directions, that is, clockwise from North (0°). Similar maps were generated for the crater interior whose circular boundary was set at a distance of 1 R from the crater center. Presence of pre-impact terrain slope whose aspect is similar to adjoining crater walls would reflect the possibility of impact cratering on slopes.

The rim of a simple crater is roughly circular in outline, but the rim outline of a transitional or a complex crater has been observed to show deviations from circularity because of more intense and non-uniform collapse of different sectors of the rim and crater wall (Pike, 1977, 1980b; Pike, 1981). Localized slumping will also lead to an asymmetric crater shape and a non-circular rim outline. We used the Polsby-Popper Score (PP) (Cox, 1927) to determine the degree of circularity of the rims of the simple craters and craters with localized slumps. The formula for PP is as follows:

$$PP = 4\pi A/P^2;$$

A = Area of the polygon encompassing the crater interior and whose boundary is the rim outline

P = Perimeter of the polygon encompassing the crater interior and whose boundary is the rim outline

PP always ranges from 0 to 1. A value of 0 refers to a completely non-circular rim (an infinite perimeter) and 1 means a perfectly circular rim. For craters on flat surfaces with/without layering, terrains with topographic breaks whose sloping directions are opposite to that of adjoining crater walls with/without layering and terrains with breaks that slope in the same direction as the superposing crater walls with/without layering, box plots of PP scores were generated to obtain the ranges and the distribution of the score values that would indicate how different types of heterogeneities in the crust have contributed to the final crater morphology. A scatter plot of PP scores against crater floor diameters for simple craters was also constructed with the same terrain classification that was used for the box plots. This is because minor localized slumping, though not visible in the profiles of simple craters, can aid in broadening of the crater floor (Bouley & Baratoux, 2011; Craddock & Howard, 2000; Fassett & Thomson, 2014; Kreslavsky et al., 2013), causing deviation from rim circularity and hence a reduction in the PP score. So, the scatter plot would signal if the variations in the PP scores with spatial variations in topography, or layering is a consequence of variations in slumping. The floor diameters measured for the morphometry plots in Section 2.3.3 of Chapter 2 were used in this study.

4.3 Results

4.3.1 Comparison of crater densities on slumps and ejecta units of craters with localized slumps

Only 20 of the 35 craters with localized slumps were selected for the crater counting task because we did not find flat areas (slope angles in the range 0° - 7°) on the surfaces of the localized slumped material in 13 craters and the Kaguya TC images of two craters located beyond latitudes of 50° (Poincare C at -54.59° N, 168.7° E and Schwarzschild Q at 66.24° N, 108.83° E) appeared to be partially shadowed. Of the 20 craters, 5 craters could possibly be simple craters in which material slumped locally post crater formation because the $N(1)$ corresponding to the ejecta units was statistically different and greater than that of the slump units. In case of the remaining 15 craters, the $N(1)$ s of the ejecta and slump units were observed to be statistically similar which suggests that they formed as craters with localized slumps. In Figure 4.3, log-log CSFD plots and their production function fits for the ejecta and slump units of 2 of the 5 inferred simple craters and 2 of the 15 inferred craters with localized slumps have been displayed. The remaining plots are available in Figure C-1 of Appendix C. The $N(1)$ s with their error bar values are listed in Table 4.1 and in the legends of Figure 4.3 and Figure C-1. The Figures also show that the CSFD plots of the ejecta and slump units are aligned with each other for statistically similar $N(1)$ s and are separated in case of statistically different $N(1)$ s.

Figure 4.4 shows the topographic profiles of the four craters whose CSFD plots are displayed in Figure 4.3. The elevation and surface distance have been scaled to the crater diameters. The profiles of craters Barocius M and Swann C, in which $N(1)$ of slump units are statistically lower compared. A similarity in wall slopes is observed. A variation in rim heights on ends A, C, E and G was visible. This is probably because the localized slumped material in all

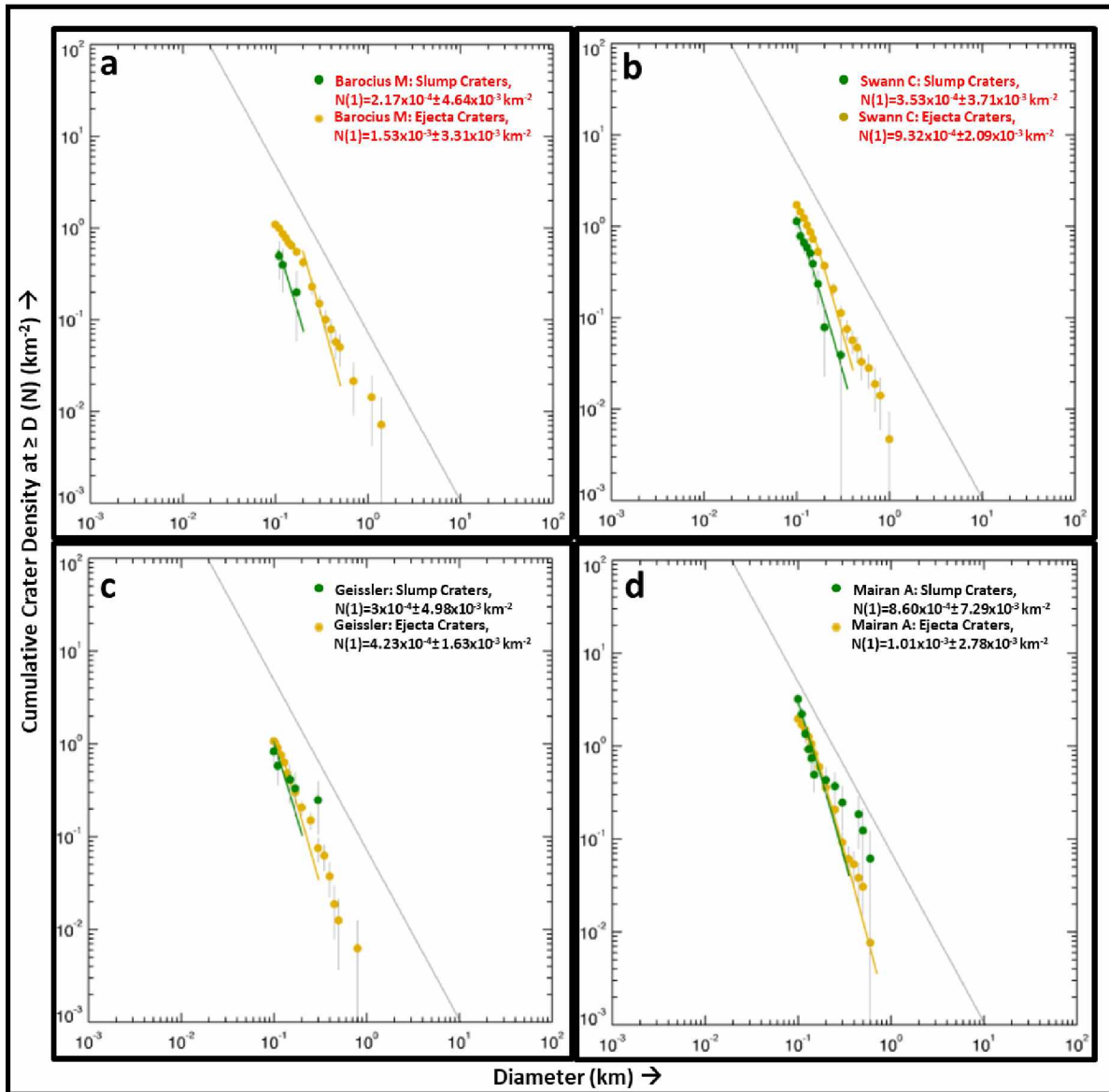


Figure 4.3. Log-log CSFD plots corresponding to ejecta and slump units of four craters with localized slumps. From the production function fits, a) Barocius M (-42.45°N , 19.48°E) and b) Swann C (52.9°N , 114.28°E) appear to be simple craters whose walls collapsed after crater formation (represented by $N(1)$ values in red font) while c) Geissler (-2.59°N , 76.5°E) and d) Mairan A (38.63°N , 321.21°E) appear to have slump blocks that formed synchronously with the crater. The green and orange dots represent the crater bins of slumps and ejecta respectively. The green and orange lines are the best fit production functions for the CSFDs of slump and ejecta units respectively. The grey sloping line is the Hartmann (1984) crater saturation line. The $N(1)$ values are given in the legends on the top right area of each plot.

Craters is positioned along the walls on this end. So the rim heights vary depending upon the amount of slumping. On ends B, D, F and H the rim heights show a significant overlap. We Observed similar morphometric trends from the profiles of the remaining craters. These results

Table 4.1. List of cumulative crater densities at D of 1 km (N(1)) along with error bar values for the slump and ejecta units of the selected 20 craters with localized slumps in the 15-20 km diameter range. The rows highlighted in bold refer to the craters whose localized slumped material possibly accumulated after crater formation.

Crater Name	Latitude (°N)	Longitude (°E)	Diameter (km)	N(1) of slump unit (km ⁻²)	N(1) of ejecta unit (km ⁻²)
Barocius M	-42.45	19.48	16.09	2.17x10⁻⁴ ± 4.64x10⁻³	3.53x10⁻⁴ ± 3.71x10⁻³
Bell J	19.88	265.88	20.03	6.16x10 ⁻⁴ ± 4.58x10 ⁻³	7.42x10 ⁻⁴ ± 1.85x10 ⁻³
Bode	6.7	357.54	18.17	7.02x10 ⁻⁴ ± 6.20x10 ⁻³	9.16x10 ⁻⁴ ± 2.27x10 ⁻³
Coriolis S	0.1	169.66	17.7	3.81x10 ⁻⁴ ± 8.42x10 ⁻³	5.88x10 ⁻⁴ ± 1.87x10 ⁻³
Dreyer R	8.49	94.47	19.9	4.12x10⁻⁴ ± 3.40x10⁻³	2.41x10⁻³ ± 3.36x10⁻³
Fryxell	-21.25	258.34	17.57	9.96x10 ⁻⁴ ± 7.52x10 ⁻³	1.26x10 ⁻³ ± 2.75x10 ⁻³
Geissler	-2.59	76.5	17.21	3x10 ⁻⁴ ± 4.98x10 ⁻³	4.23x10 ⁻⁴ ± 1.63x10 ⁻³
Hahn A	29.66	69.72	18.74	1.99x10⁻⁴ ± 6.04x10⁻³	7.12x10⁻⁴ ± 1.94x10⁻³
Hahn B	31.37	76.97	16.74	8.20x10 ⁻⁴ ± 6.48x10 ⁻³	8.89x10 ⁻⁴ ± 2.42x10 ⁻³
Harkhebi T	40.04	95.31	18.4	2.83x10 ⁻⁴ ± 6.74x10 ⁻³	4.92x10 ⁻⁴ ± 1.58x10 ⁻³
Hatanaka Q	25.99	235.34	19.05	3.71x10 ⁻⁴ ± 5.56x10 ⁻³	4.57x10 ⁻⁴ ± 1.53x10 ⁻³
Hommel J	-53.53	27.87	17.51	2.24x10⁻⁴ ± 3.18x10⁻³	2.04x10⁻³ ± 3.51x10⁻³
la Condamine A	54.43	329.8	18.25	5.47x10 ⁻⁴ ± 1.16x10 ⁻²	6.29x10 ⁻⁴ ± 1.87x10 ⁻³
Leucippus K	27.27	244.49	15.55	6.89x10 ⁻⁴ ± 1.46x10 ⁻²	6.92x10 ⁻⁴ ± 2.30x10 ⁻³
Mairan A	38.63	321.21	15.9	8.60x10 ⁻⁴ ± 7.29x10 ⁻³	1.01x10 ⁻³ ± 2.78x10 ⁻³
Swann C	52.9	114.28	19.87	3.53x10⁻⁴ ± 3.71x10⁻³	9.32x10⁻⁴ ± 2.09x10⁻³
Unnamed16	34.92	176.71	17.24	8.00x10 ⁻⁴ ± 1.05x10 ⁻²	8.18x10 ⁻⁴ ± 2.26x10 ⁻³
Unnamed33	15.15	224.18	18.36	5.22x10 ⁻⁴ ± 5.77x10 ⁻³	5.55x10 ⁻⁴ ± 1.75x10 ⁻³
Unnamed36	-44.87	225.13	16	3.29x10 ⁻⁴ ± 6.83x10 ⁻³	4.13x10 ⁻⁴ ± 1.73x10 ⁻³
Van de Graaff C	-26.43	172.81	18.15	4.49x10 ⁻⁴ ± 5.60x10 ⁻³	4.86x10 ⁻⁴ ± 1.65x10 ⁻³

contradict the expected geometry trends interpreted from the CSFDs that the craters whose localized slumped material was deposited post-ejecta deposition (or crater formation) should have lower rim heights, smaller slopes and lower depths if they experienced topographic diffusion through time (Bouley & Baratoux, 2011; Craddock & Howard, 2000; Fassett & Thomson, 2014; Kreslavsky et al., 2013).

There could be errors in the CSFDs of the five inferred simple craters stemming from inaccurate representation of the slump and ejecta units by the counted craters. This is because the crater density on the highlands is high enough that newly formed craters can overlap with or superpose older craters. So, ejecta from nearby craters may mask the craters superposing the slump and ejecta units thereby reducing the crater densities. Figure 4.2 illustrates the masking of a part

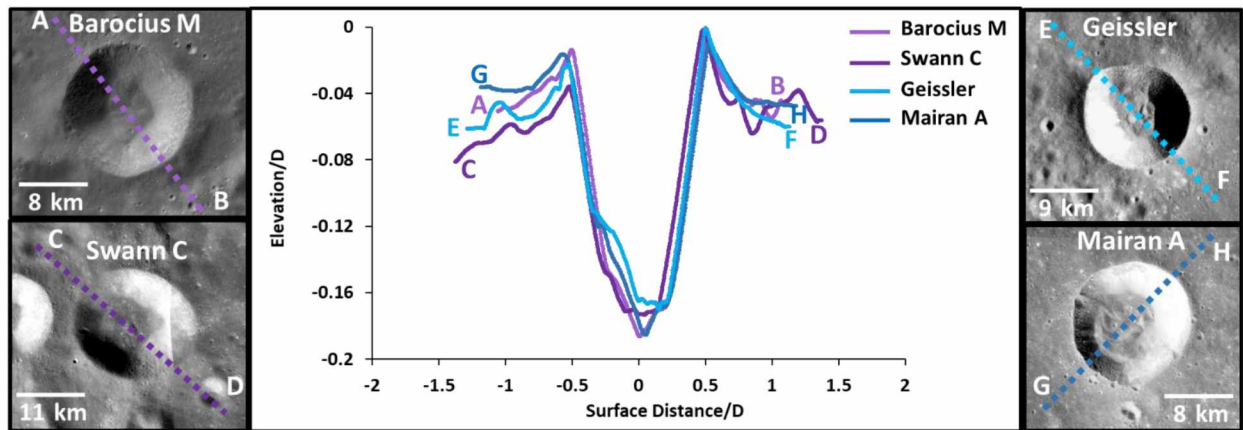


Figure 4.4. LOLA topographic profiles (center) of craters whose CSFD plots are shown in Figure 4.3. The profiles are accompanied by Kaguya TC images of craters Barocius M and Swann C (N(1)s of slump units are statistically lower than that of ejecta units) on the left and craters Geissler and Mairan A (N(1)s of slump and ejecta units are statistically similar). In the profiles, the surface distance and elevation are scaled to the respective crater diameters. North is up in all images.

of slumped material by a nearby crater's ejecta (north-west of Swann C). Small slumps along the crater wall throughout the crater's life in the form of dry granular flows (Kumar et al., 2013) may also fill the craters on some parts of pre-existing slump units and therefore result in lower-than-expected crater densities, so for the craters with apparently young slump blocks it may be that only a thin uppermost layer is younger. Owing to the discrepancies between the interpretations from CSFDs and crater profiles, we did not classify these five craters as simple craters, and continued acknowledging them as craters with localized slumps. For the investigation of the other two working hypotheses, the 35 craters with localized slumps and 117 simple craters were probed.

4.3.2 Frequencies of proximal simple craters and craters with localized slumps

We were able to detect well-preserved proximal simple craters and transitional craters for 83 simple craters and 24 craters with localized slumps. The transitional craters included craters with localized slumps and craters with broader, flatter floors. The flat-floored craters started appearing at diameters greater than 25 km. Each crater was surrounded by a maximum of six well-preserved craters in the simple-to-complex transition zone. The distribution of percentages of surrounding transitional craters relative to that of simple craters have been mapped in Figure 4.5

for simple craters and Figure 4.6 for craters with localized slumps. The graduated sizes of the circles refer to the classes of the total number of proximal craters. The shades of circles represent the relative percentages where magenta shades reflect that the simple craters outnumber the transitional craters (negative values). The pre-dominant presence of purple shades (0-60%) and blue (60-100%) circles in both Figures indicates that the distributions of proximal craters skewed towards transitional crater morphology. Proximal transitional craters outnumbered proximal simple craters in the case of 80% simple craters and 75% of craters with localized slumps. In 67% of cases for both morphologies, only proximal transitional craters were detected. The craters surrounded by higher relative percentages of proximal simple craters exist in patches across the lunar surface in both Figures. The percentages are available in Table C-1 of Appendix C.

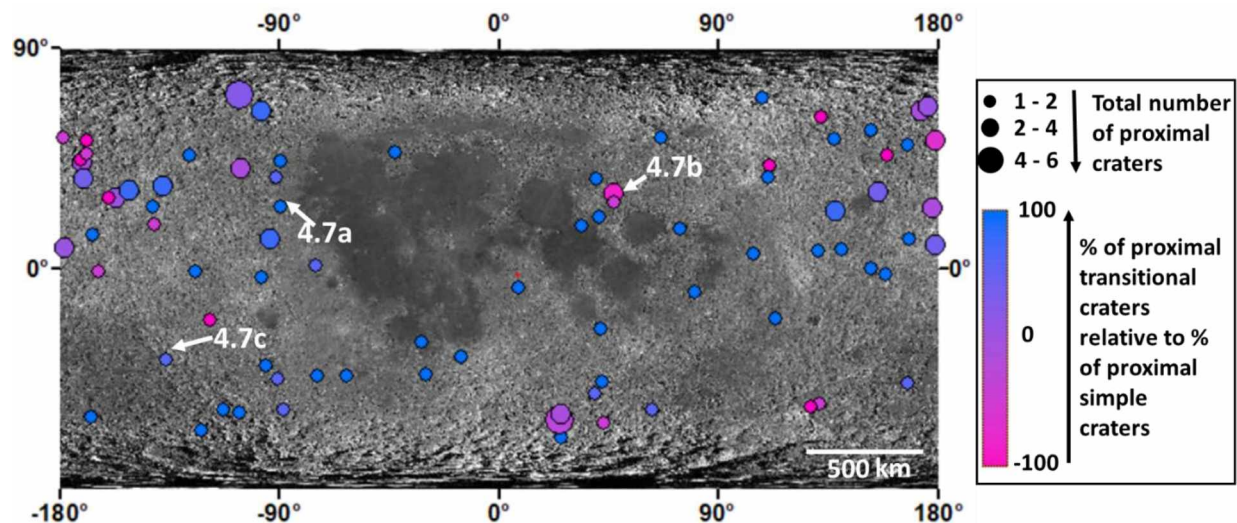


Figure 4.5. Mapped distribution of percentages of transitional craters relative to simple craters in the proximity of 83 15-20 km diameter simple craters. The graduated sizes of the circles are in increasing order of total number of proximal craters. The shades of the circles represent the percentages. The legend is available on the right. The LROC WAC mosaic has been used in the background. The alphanumeric labels refer to the locations of the craters displayed in Figure 4.7. The dominance of purple and blue shades is evident which means that most simple craters are surrounded by greater number of transitional craters. North is up.

4.3.3 Topographic variation in pre-impact terrains of the simple craters and craters with localized slumps along with rim circularity

The aspect-slope maps of crater cavities and pre-impact terrains reveal that 64% of simple craters are located on flat or gradually sloping surfaces or superpose topographic breaks that slope in a direction opposite to the adjoining crater walls. Around 60% of craters with localized slumps have walls that slope in the same direction as the superposed topographic breaks. The breaks are rims or terraces of pre-existing craters and are more noticeable in the aspect-slope maps than in the optical images. Figures 4.7 (simple craters) and 4.8 (craters with localized slumps) illustrate pre-impact terrains that are gradually sloping and have topographic breaks that are sloping in or opposite to the direction of slopes of adjoining crater walls. In cases of craters with localized slumps, we did not encounter surfaces that are completely flat, unlike the case of simple craters where 50% of surfaces sloping at angles of 0-7° appeared to slope gradually. The color wheel in the legend symbolizes the aspect values in the aspect-slope maps. The three rings of the wheel denote different classes of slopes. The saturation values of the colors reduce with decrease in slope angles. Slope values ranging from 0-7 are symbolized by grey regardless of the aspect to represent flat or gradually sloping surfaces. The relevant slopes of the walls and topographic breaks are marked by arrows. The LOLA elevation contours superposed on WAC images above the aspect-slope maps highlight the topographic variation of the pre-impact terrains. We obtained similar values of topographic break slopes for both morphologies, ranging from 8-15°. Details of the slopes and locations of topographic breaks are listed in Table C-2 of Appendix C.

Figure 4.9 shows the box plots of PP scores of simple craters (Figure 4.9a) and craters with localized slumps (Figure 4.9b) for different types of pre-impact heterogeneities. While the pre-impact terrains in case of simple craters have also been classified by presence and absence of

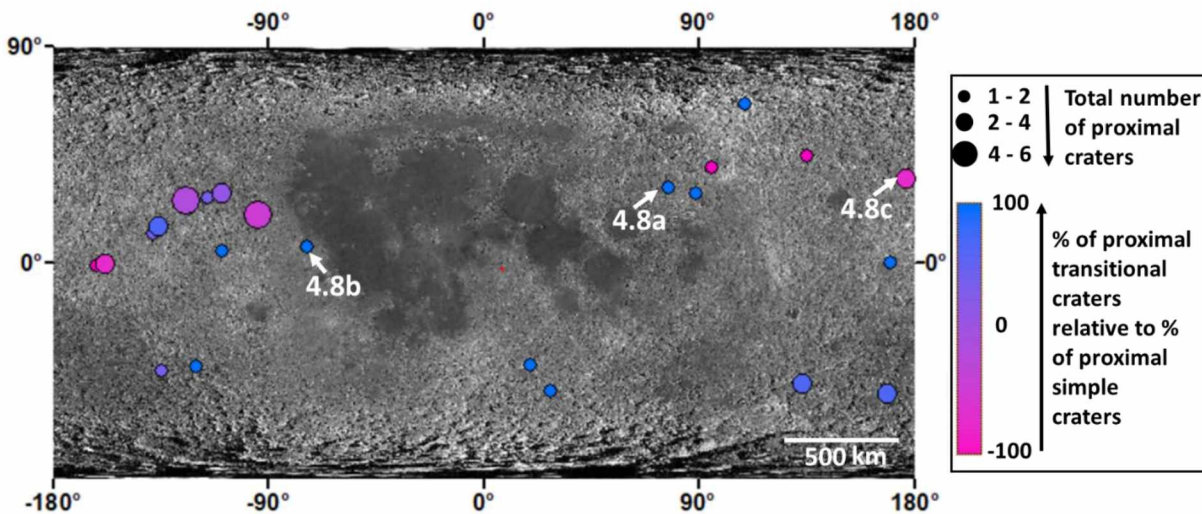


Figure 4.6. Mapped distribution of percentages of transitional craters relative to simple craters in the proximity of 24 15-20 km diameter craters with localized slumps. The graduated sizes of the circles are in increasing order of total number of proximal craters. The shades of the circles represent the percentages. The legend is available on the right. The LROC WAC mosaic has been used in the background. The alphanumeric labels refer to the locations of the craters displayed in Figure 4.8. Similar to Figure 4.7, the dominance of purple and blue shades, that is, the outnumbering of proximal simple craters by proximal transitional craters is evident from this Figure as well. North is up.

layering, this classification has been merged with the classes by topographic variation for craters with localized slumps due to their smaller sample sizes. It can be observed that the bulk of PP scores in all classes of simple craters range from 0.98 to 0.995 (boxes) which indicates a nearly circular rim. The median values are also clustered around 0.99. But with the onset of layering and presence of topographic breaks sloping in similar/opposite direction to the crater walls, the bottom whiskers that could also include outliers show a drop in minimum PP scores to 0.95-0.96 as compared to the lower bounds of bottom whiskers in flat/gradually sloping surfaces. The bulk distributions (boxes) for craters with localized slumps exhibit a similar pattern of overlapping ranges of PP scores from 0.975 to 0.987 that are lower than those for simple craters. Some outlier craters also exist in case of topographic breaks that slope in the same direction as the crater walls, whose minimum PP scores (lower bounds of bottom whiskers) are slightly smaller (0.955) but not

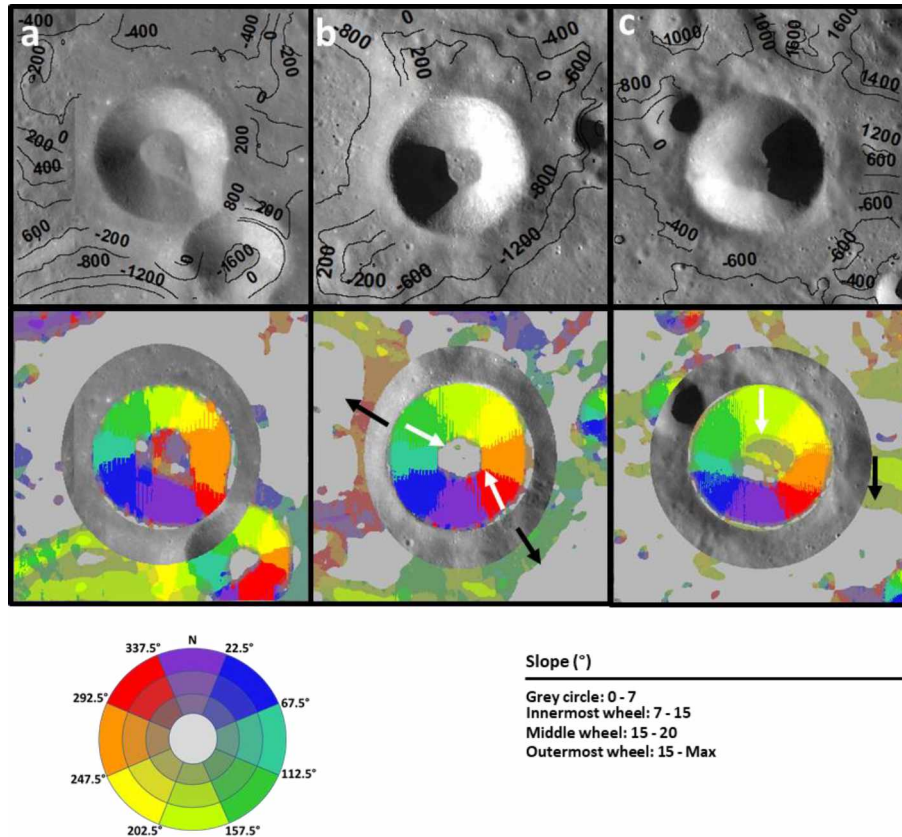


Figure 4.7. LOLA elevation contours (meters) superposed over WAC images of simple craters (top) and aspect-slope maps of their pre-impact terrains and crater cavities (bottom). The color wheel in the legend explains the aspect values oriented clockwise from North. The circle and the rings represent different classes of slopes that are shown on the right of the legend. a) Crater Bartels A (25.69°N, 270.3°E) on a gradually sloping surface (S-N). The crater on its south-east formed later, so it's not counted as a topographic break. b) Crater Geminus D (30.57°N, 47.29°E) superposing rims of older craters whose walls slope in opposite direction that of its walls. The grey region around the older craters shows that their ejecta are too degraded to be counted as topographic breaks. c) Crater Unnamed32 (-36.9°N, 223.5°E) whose crater wall superposes a part of an outer wall of an older crater that slopes in the same direction as the wall. The smaller crater on the north-west is not counted because it formed later than Unnamed32. All images are 33 km wide. North is up in all images.

significantly different from the minimum scores of the 'No Break' outlier craters (0.965). The PP score distribution for the topographic breaks that slope in opposite directions to the crater walls display smaller ranges with the largest minimum value (0.975) and lower bounds of the box (0.985). This observation accompanies the caveat that the sample size is too small (four) to draw any inference from this result.

The scatter plots of PP score vs simple crater floor diameter in Figure 4.10 convey that

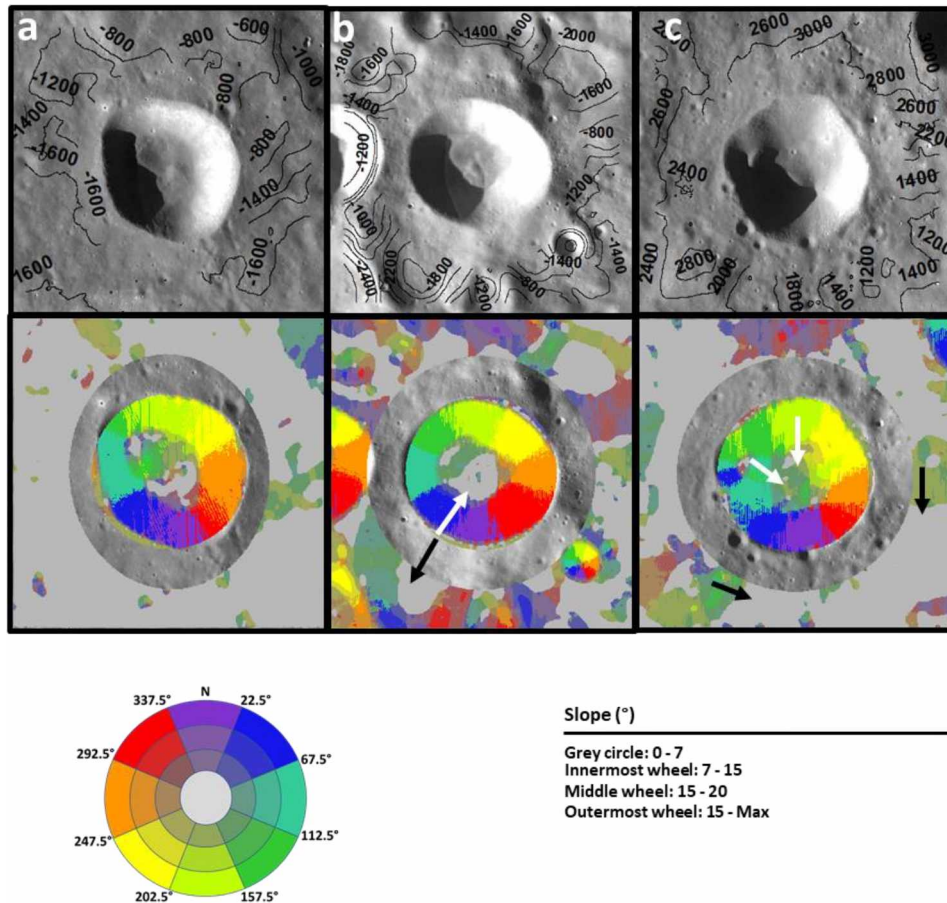


Figure 4.8. LOLA elevation contours (meters) superposed over WAC images of craters with localized slumps (top) and aspect-slope maps of their pre-impact terrains and crater cavities (bottom). The color wheel in the legend explains the aspect values oriented clockwise from North. The circle and the rings represent different classes of slopes that are shown on the right of the legend. a) Crater Hahn B (31.37°N , 76.97°E) on a gradually sloping surface (NE-SW). b) Crater Swann C (52.9°N , 114.28°E) superposing the rim of an older crater whose walls slope in opposite direction to that of its walls. The remaining topographic breaks around it can be ignored because they do not adjoin the walls. c) Crater Unnamed16 (34.92°N , 176.7°E) whose crater walls superpose the inner walls of a larger, older crater that slope in the same direction as Unnamed16's walls. The localized slumps are also positioned along these inner walls. All images are 33 km wide. North is up in all images.

most of the floor diameters are confined to a range of 0.2 to 0.4 corresponding to the PP score cluster between 0.98 and 0.995. For pre-impact terrains without topographic breaks, the floor diameters are exclusively restricted to the range of 0.2 – 0.4. With the onset of topographic breaks irrespective of their orientation with respect to crater walls, in addition to the clustering mentioned above, the floor diameters show an expansion in the range by an increase in the upper bounds to

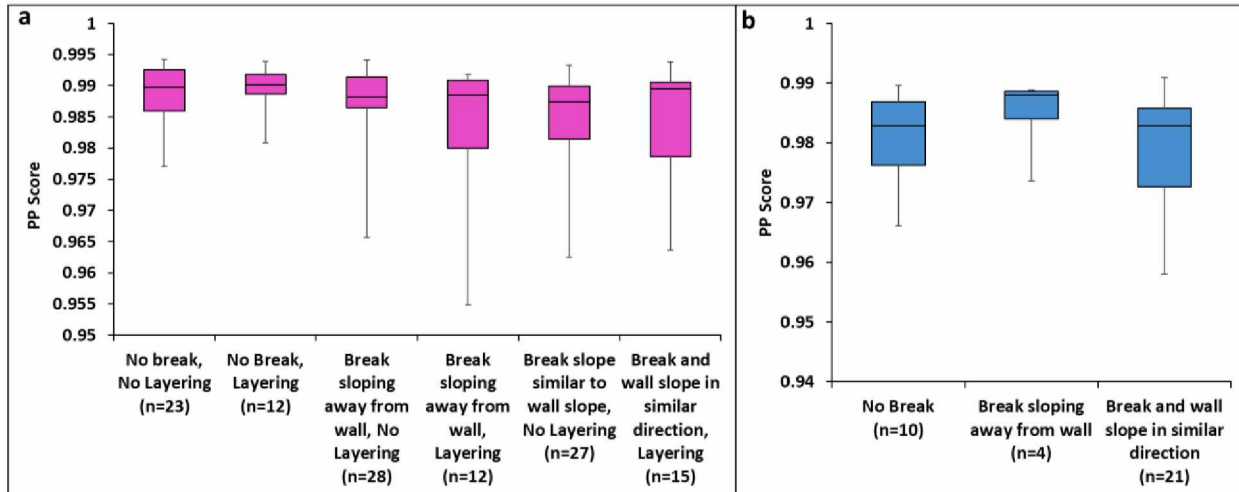


Figure 4.9. Box plots of PP scores of a) simple craters and b) craters with localized slumps. The distributions have been classified by the types of topographic heterogeneities in the pre-impact terrains. The classifications have been subdivided by presence/absence of layering in case of simple craters. The letter ‘n’ in parentheses below the x-axis labels refers to the sample sizes associated with the types of heterogeneities.

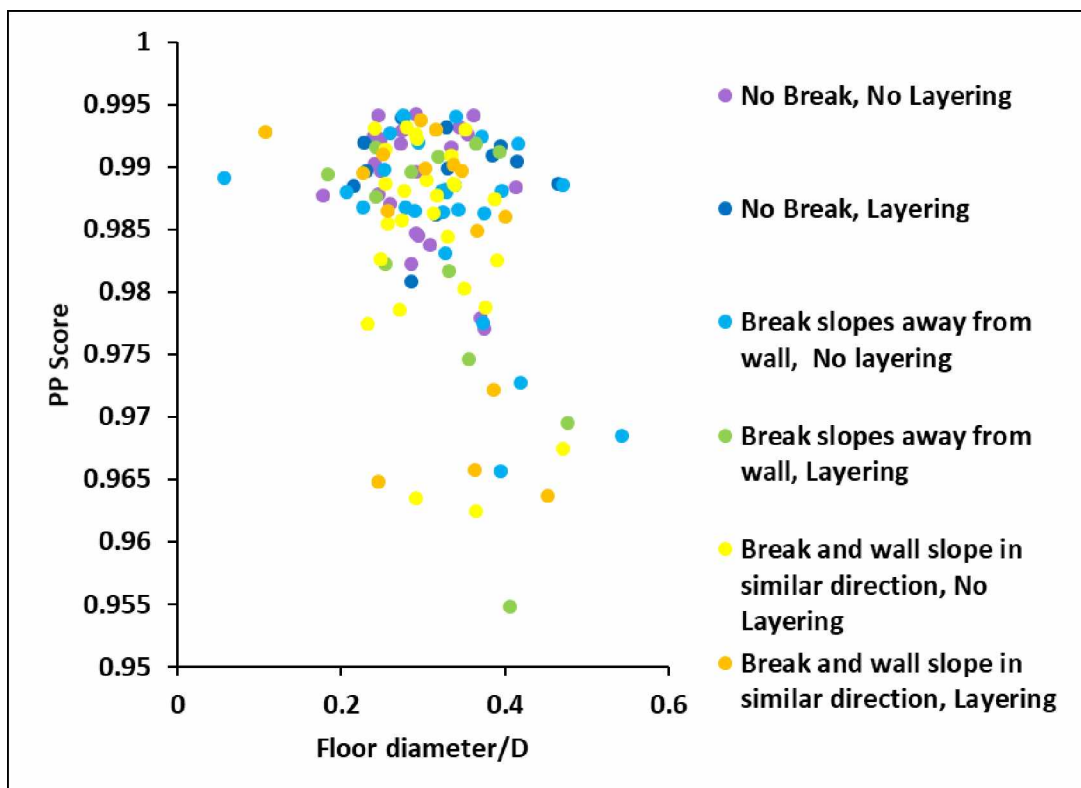


Figure 4.10. Scatter plots of PP score vs simple crater floor diameter scaled to crater diameter for various topographic heterogeneities and presence/absence of layering in the pre-impact terrains. The colors symbolize the heterogeneities.

values as high as 0.55 similar to the shift of the lower limits of the PP score range to smaller values. The role of layering is not clear because the maximum values of floor diameters for all cases of terrains with topographic breaks with/without layering appear to be similar.

4.4 Discussion

We did not find clear evidence that any of the 35 craters with localized slumps formed as simple craters and later experienced slumping. This is because although the CSFD plots of five craters indicate simple crater morphologies, the crater profiles suggest that they formed as craters with localized slumps. Thin layers of debris from slumping post-crater formation possibly overlie the bulk of the slumped material and consequently produce errors in the CSFD plots. So, the hypothesis stating that craters with localized slumps that are located on terrains with similar topographic variation as simple craters accumulated slumped material post-crater formation can be rejected.

While looking for craters surrounding the simple craters and craters with localized slumps, we observed that transitional crater morphologies are predominant not only around the craters with localized slumps (75% of the cases) but also around simple craters (80% of the cases). So there is very low probability of strength contrasts in the highlands. These results contradict the second hypothesis that states that the craters with localized slumps were formed on terrains that are weaker relative to simple crater locations. The only indication it gives about the strength of the highlands crust is that for crater sizes spanning the simple-to-complex transition, large strength degradation happens uniformly across the crustal terrain that causes the highlands to be more susceptible to the formation of transitional craters. Because we expanded the diameter range to 40 km, the size-dependent morphologic progression from simple-to-transitional craters (Kenkmann et al., 2012;

Melosh, 1989; Pike, 1980a, 1980b; Quaide et al., 1965) is also justified by the preponderance of the transitional craters. Additionally, well-preserved proximal crater morphologies in the simple-to-complex transition could be found only for 83 of 117 simple craters and 24 of 35 craters with localized slumps. The incomplete set of results serves as another limitation to the testing of the second hypothesis.

From the results of investigation of the third hypothesis that describes the role of impact cratering on slopes in producing craters with localized slumps, we conclude that it offers the most plausible explanation. First, it was possible to test this hypothesis for every simple crater and crater with localized slumps thereby making the results more robust than the findings from the investigation of the other two hypotheses. Second, the detection of topographic breaks sloping in similar directions as the superposing crater wall for 60% of the craters with localized slumps and breaks sloping in opposite directions to that of adjoining walls for 64% of the simple craters further strengthens the hypothesis. This is because on a slope, the cavity wall near the uphill rim sector is likely to get oversteepened and consequently collapse as compared to the wall near the downhill sector of the rim (Aschauer & Kenkmann, 2017; Elbeshausen et al., 2012; Krohn et al., 2014; Plescia, 2012; Plescia et al., 2019). The formation of transient cavity and the resulting orientations of its walls on a slope is demonstrated in Figure 4.11. In Figure 4.12, the 3D illustrations of simple craters on breaks sloping away from the walls and craters with localized slumps on slopes facing the walls help in interpreting the observed association of the two crater morphologies with the two types of topographic variations in pre-impact terrains. We also found that the terrains associated with the 10 craters with localized slumps that were devoid of topographic breaks were not flat but characterized with minor slopes with maximum values of 7° . Aschauer and Kenkmann (2017) reported that mass wasting along walls can occur for slope angles as low as 5° , and therefore these

minor slopes could have triggered the localized slumping as well. Thirdly, the broader ranges of the PP scores due to smaller values of lower bounds for both crater morphologies on terrains containing topographic breaks suggests that the presence of a slope caused the decrease in symmetry of the crater rim and hence the existence of lower PP scores. The mass wasting along the wall in the uphill sector of the rim results in the asymmetry of the rim. But for topographic breaks sloping away from crater walls, the mass wasting is initiated outside the downhill sector rim from the emplacement of ejecta along the slope of the topographic break which also causes deviations from rim circularity. The extremely high values of PP scores and low values of floor diameters in the majority of simple craters is understandable because minor slumping (as compared to more intense localized slumping) during crater formation is less likely to change the shape of the rim or the floor size. However, on terrains with topographic breaks, the occurrence of several simple craters with larger floor sizes and lower PP scores indicates that the slopes triggered mass wasting in simple craters as well, but on a much smaller scale.

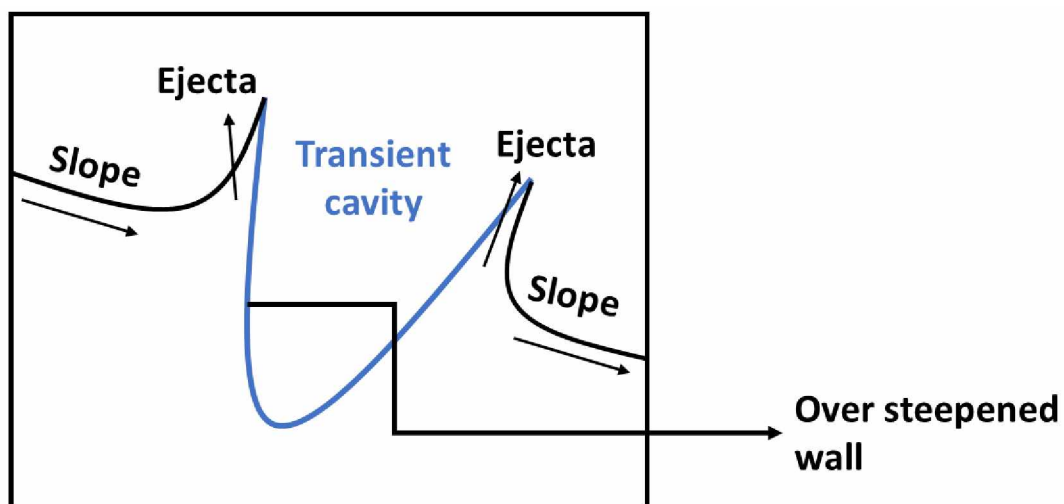


Figure 4.11. Demonstration of transient cavity formation on a slope. Post excavation stage, the over steepening of cavity wall near the uphill rim sector drives slumping along the wall (Aschauer & Kenkmann, 2017). The ejecta desposited along the slope initiates mass wasting around the downhill rim sector but along the outer cavity wall. Both mass wasting processes may produce deviations from rim circularity.

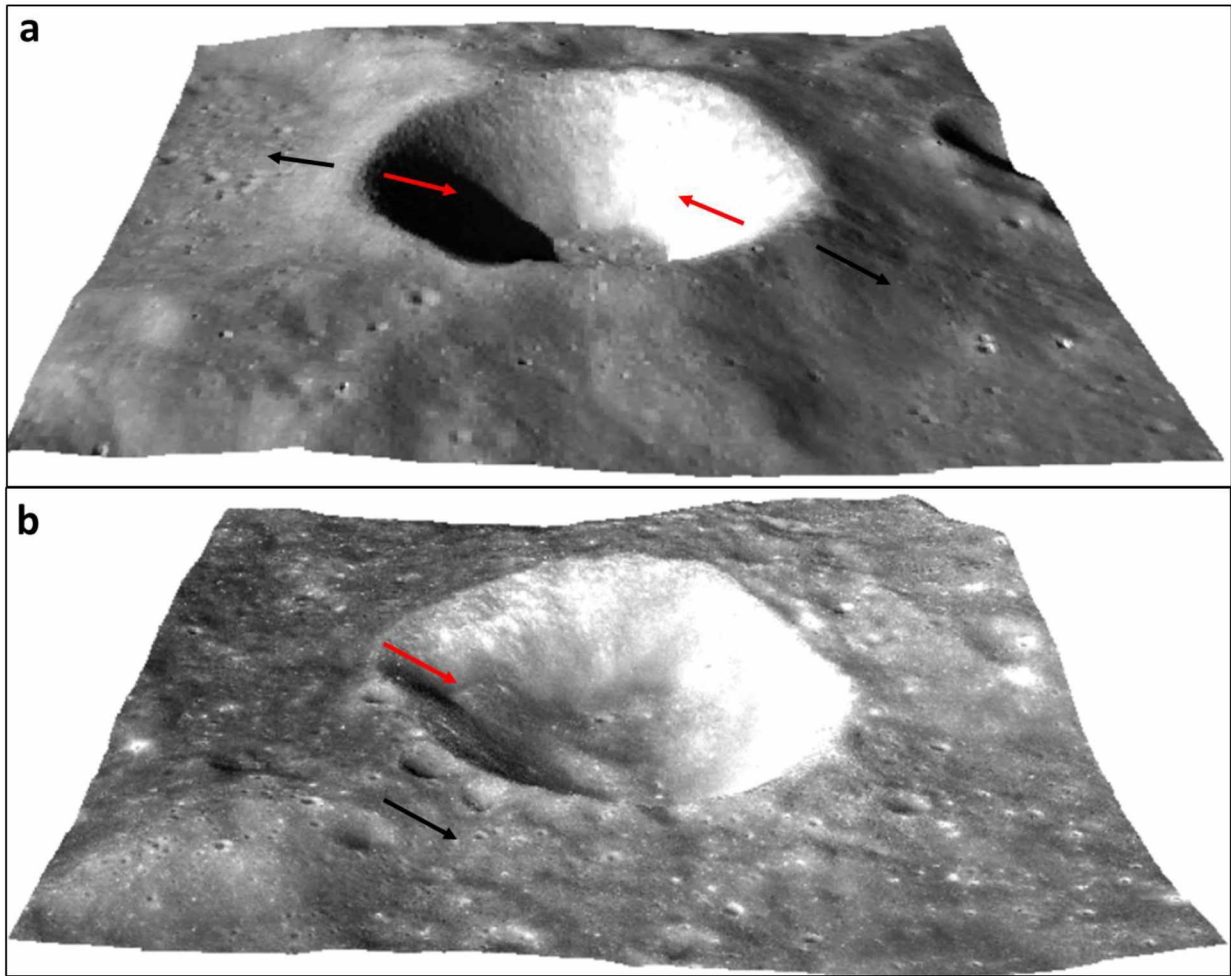


Figure 4.12. 3D illustrations of crater morphologies on pre-existing slopes. a) 3D WAC view of simple crater Geminus D (30.57°N, 47.29°E) superposing pre-existing crater walls that slope away from Geminus D's walls. B) 3D Kaguya TC view of Crater with localized slumps Unnamed16 (34.92°N, 176.7°E) superposed on a pre-existing crater wall that slopes in the same direction as Unnamed16's walls. The red and black arrows refer to the sloping directions of the craters' walls and the pre-existing topographic breaks, respectively. North is up.

We encountered four craters with localized slumps that are located on terrains characterized with topographic breaks sloping away from crater walls. Slumping along a wall near the downhill rim sector has lower probability of being as intense as slumping along the uphill sector wall. However, endless impacts on the highlands surface have produced several fractures, fragmented debris and structurally weak zones (Bart et al., 2011; Hartmann, 1973; Heiken et al., 1991; Papike et al., 1982; Soderblom et al., 2015) that, although not visible in the current high

resolution image data, could be contributing to subtle heterogeneities in the highlands crust and therefore trigger strength degradation and consequent slumping.

4.5 Conclusions

Within the 15-20 km crater diameter range, we identified two types of lunar crater morphologies (simple craters and craters with localized slumps) in the highlands with similar depths. Their pre-impact topography also appeared similar from optical imagery, that is, surfaces that appeared flat or gradually sloping or consisted of degraded rims and terraces of craters. We performed a detailed geologic and topographic investigation of the craters and their pre-impact terrains using high resolution Kaguya TC images and 512 ppd LOLA DEMs. We came to the conclusion that topographic breaks that were not noticeable in the optical images but prominent in the aspect-slope maps served as sloping surfaces that triggered localized slumping along the walls that were sloping in the same direction as the topographic break. We reached the following conclusions:

[1] No crater with localized slumps could be confidently inferred to be forming as a simple crater and then incurring later significant slumping. This is because only 20 craters with localized slumps qualified for comparison of crater densities on slump and ejecta units through the unit CSFDs. Additionally, five craters with localized slumps could be inferred as simple craters from their CSFD plots. However, their cavity profiles did not reflect the geometric trends due to topographic degradation from slumping post crater formation.

[2] The morphologies that are pre-dominantly in close proximity to most craters with localized slumps as well as simple craters are transitional crater morphologies. This finding weakens the possibility that spatial variations in strength of the highlands terrains was the primary reason

behind the two morphologies.

[3] The walls of 60% of craters with localized slumps were observed to be sloping in the same direction as the superposed topographic breaks. Around 64% of the simple craters superpose topographic breaks that slope away from the craters' walls.

[4] The presence of topographic breaks on pre-impact terrains of both crater morphologies exhibits a positive correlation with low PP scores or high asymmetry in rims (and broader floors in case of simple craters). These results show the influence of pre-existing slope on mass wasting along inner and outer crater walls near the uphill and downhill rim sectors respectively.

The four craters with localized slumps that superpose topographic breaks sloping away from the adjoining craters walls could be a consequence of unseen subsurface heterogeneities generated by several billion years of impacts on the highlands terrain.

4.6 Acknowledgments

This work was funded by a grant to RRH from the NASA Lunar Advanced Science and Exploration Research (LASER) Program. We are thankful to Dr. Harold Heisinger and his research group for guiding us with production function fits to Crater Size Frequency Distributions (CSFD).

4.7 References

- Arvidson, R., Boyce, J., Chapman, C., Cintala, M., Fulchignoni, M., Moore, H. et al. (1979). Standard techniques for presentation and analysis of crater size-frequency data. *Icarus*, 37(2), 467-474. doi:[https://doi.org/10.1016/0019-1035\(79\)90009-5](https://doi.org/10.1016/0019-1035(79)90009-5).
- Aschauer, J., and Kenkmann, T. (2017). Impact cratering on slopes. *Icarus*, 290, 89-95. doi:<https://doi.org/10.1016/j.icarus.2017.02.021>.

- Bart, G. D., Nickerson, R. D., Lawder, M. T., and Melosh, H. J. (2011). Global survey of lunar regolith depths from LROC images. *Icarus*, 215(2), 485-490. doi:<https://doi.org/10.1016/j.icarus.2011.07.017>.
- Bouley, S., and Baratoux, D. (2011). *Variation of small crater degradation on the Moon*. Paper presented at 42nd Lunar and Planetary Science Conference, Houston, TX.
- Chandnani, M., Herrick, R. R., and Kramer, G. Y. (2019). Geologic Analyses of Causes for Morphological Variations in Lunar Craters within the Simple-to-Complex Transition. *Journal of Geophysical Research: Planets*, 1238-1265. doi:<https://doi.org/10.1029/2018JE005729>.
- Cintala, M., Wood, C., and Head, J. (1977). *The effects of target characteristics on fresh crater morphology-Preliminary results for the moon and Mercury*. Paper presented at 8th Lunar and Planetary Science Conference Proceedings, Houston, TX.
- Cintala, M. J., and Grieve, R. A. (1998). Scaling impact melting and crater dimensions: Implications for the lunar cratering record. *Meteoritics & Planetary Science*, 33(4), 889-912. doi:<https://doi.org/10.1111/j.1945-5100.1998.tb01695.x>.
- Cooper, H. (1977), A summary of explosion cratering phenomena relevant to meteor impact events In D.J. Roddy et al. (Eds.), *Impact and Explosion Cratering*, pp. 11-44, Pergamon Press, New York.
- Cox, E. (1927). A method of assigning numerical and percentage values to the degree of roundness of sand grains. *Journal of Paleontology*, 1(3), 179-183. doi:<http://www.jstor.org/stable/1298056>.

- Craddock, R. A., and Howard, A. D. (2000). Simulated degradation of lunar impact craters and a new method for age dating farside mare deposits. *Journal of Geophysical Research: Planets*, 105(E8), 20387-20401. doi:<https://doi.org/10.1029/1999JE001099>.
- Croft, S. K. (1985). The scaling of complex craters. *Journal of Geophysical Research: Solid Earth*, 90(S02). doi:<https://doi.org/10.1029/JB090iS02p0C828>.
- Dence, A. (1972). *The nature and significance of terrestrial impact structures*. Paper presented at 24th International Geological Congress, Section 15, Montreal, Canada.
- Elbeshhausen, D., Wünnemann, K., Sierks, H., Vincent, J., and Ockay, N. (2012). *The effect of topography on the impact cratering process on Lutetia*. Paper presented at 43rd Lunar and Planetary Science Conference, Houston, TX.
- Fassett, C. I., and Thomson, B. J. (2014). Crater degradation on the lunar maria: Topographic diffusion and the rate of erosion on the Moon. *Journal of Geophysical Research: Planets*, 119(10), 2255-2271. doi:<https://doi.org/10.1002/2014JE004698>.
- Güldemeister, N., Wünnemann, K., and Poelchau, M. (2015). Scaling impact crater dimensions in cohesive rock by numerical modeling and laboratory experiments. *Geological Society of America Special Papers*, 518, SPE518-SPE502. doi:[https://doi.org/10.1130/2015.2518\(02\)](https://doi.org/10.1130/2015.2518(02)).
- Hartmann, W. K. (1973). Ancient lunar mega-regolith and subsurface structure. *Icarus*, 18(4), 634-636. doi:[https://doi.org/10.1016/0019-1035\(73\)90066-3](https://doi.org/10.1016/0019-1035(73)90066-3).
- Hartmann, W. K. (1984). Does crater “saturation equilibrium” occur in the solar system? *Icarus*, 60(1), 56-74. doi:[https://doi.org/10.1016/0019-1035\(84\)90138-6](https://doi.org/10.1016/0019-1035(84)90138-6).

- Haruyama, J., Matsunaga, T., Ohtake, M., Morota, T., Honda, C., Yokota, Y. et al. (2008). Global lunar-surface mapping experiment using the Lunar Imager/Spectrometer on SELENE. *Earth, planets and space*, 60(4), 243-255.
- Heiken, G. H., Vaniman, D. T., and French, B. M. (Eds.) (1991). *Lunar sourcebook-A user's guide to the moon*, Cambridge, England; New York: Cambridge University Press.
- Howard, K. A. (1974). *Fresh lunar impact craters-Review of variations with size*. Paper presented at 2nd Lunar and Planetary Science Conference Proceedings, Houston, TX.
- Kalynn, J., Johnson, C. L., Osinski, G. R., and Barnouin, O. (2013). Topographic characterization of lunar complex craters. *Geophysical Research Letters*, 40(1), 38-42. doi:<https://doi.org/10.1029/2012GL053608>
- Kenkmann, T., Collins, G. S., and Wünnemann, K. (2012), The modification stage of crater formation, In Gordon R Osinski et al. (Eds.), *Impact cratering: Processes and products*, pp. 60-75, John Wiley & Sons, Oxford, U.K.
- Kneissl, T., van Gasselt, S., and Neukum, G. (2010). *New software tool for map-projection-independent crater size-frequency determination in ArcGIS*. Paper presented at 41st Lunar and Planetary Science Conference, Houston, TX.
- Kreslavsky, M. A., Head, J. W., Neumann, G. A., Rosenburg, M. A., Aharonson, O., Smith, D. E., and Zuber, M. T. (2013). Lunar topographic roughness maps from Lunar Orbiter Laser Altimeter (LOLA) data: Scale dependence and correlation with geologic features and units. *Icarus*, 226(1), 52-66. doi:<https://doi.org/10.1016/j.icarus.2013.04.027>.
- Krohn, K., Jaumann, R., Elbeshausen, D., Kneissl, T., Schmedemann, N., Wagner, R. et al. (2014). Asymmetric craters on Vesta: Impact on sloping surfaces. *Planetary and Space Science*, 103, 36-56. doi:<https://doi.org/10.1016/j.pss.2014.04.011>.

- Krüger, T., Hergarten, S., and Kenkmann, T. (2018). Deriving morphometric parameters and the simple-to-complex transition diameter from a new, high resolution database of fresh lunar impact craters ≥ 3 km. *Journal of Geophysical Research: Planets*, 123(10), 2667-2690. doi:<https://doi.org/10.1029/2018JE005545>.
- Kumar, P. S., Keerthi, V., Kumar, A. S., Mustard, J., Gopala Krishna, B., Ostrach, L. R. et al. (2013). Gullies and landslides on the Moon: Evidence for dry-granular flows. *Journal of Geophysical Research: Planets*, 118(2), 206-223. doi:<https://doi.org/10.1002/jgre.20043>.
- McKinnon, W. B. (1978). *An investigation into the role of plastic failure in crater modification*. Paper presented at 9th Lunar and Planetary Science Conference Proceedings, Houston, TX.
- Melosh, H. J. (1977). *Crater modification by gravity-A mechanical analysis of slumping*. Paper presented at Impact and Explosion Cratering: Planetary and Terrestrial Implications, Flagstaff, AZ.
- Melosh, H. J. (1989), Cratering Mechanics: Modification Stage, In *Impact cratering: A geologic process*, pp. 126-161, Oxford University Press, New York.
- Melosh, H. J., and Ivanov, B. (1999). Impact crater collapse. *Annual Review of Earth and Planetary Sciences*, 27(1), 385-415. doi:<https://doi.org/10.1146/annurev.earth.27.1.385>.
- Michael, G. G., and Neukum, G. (2010). Planetary surface dating from crater size–frequency distribution measurements: Partial resurfacing events and statistical age uncertainty. *Earth and Planetary Science Letters*, 294(3-4), 223-229.
- Neukum, G. (1983), *Meteoritenbombardement und datierung planetarer oberflächen*, Ludwig Maximilianis Univ., Munich, Germany.

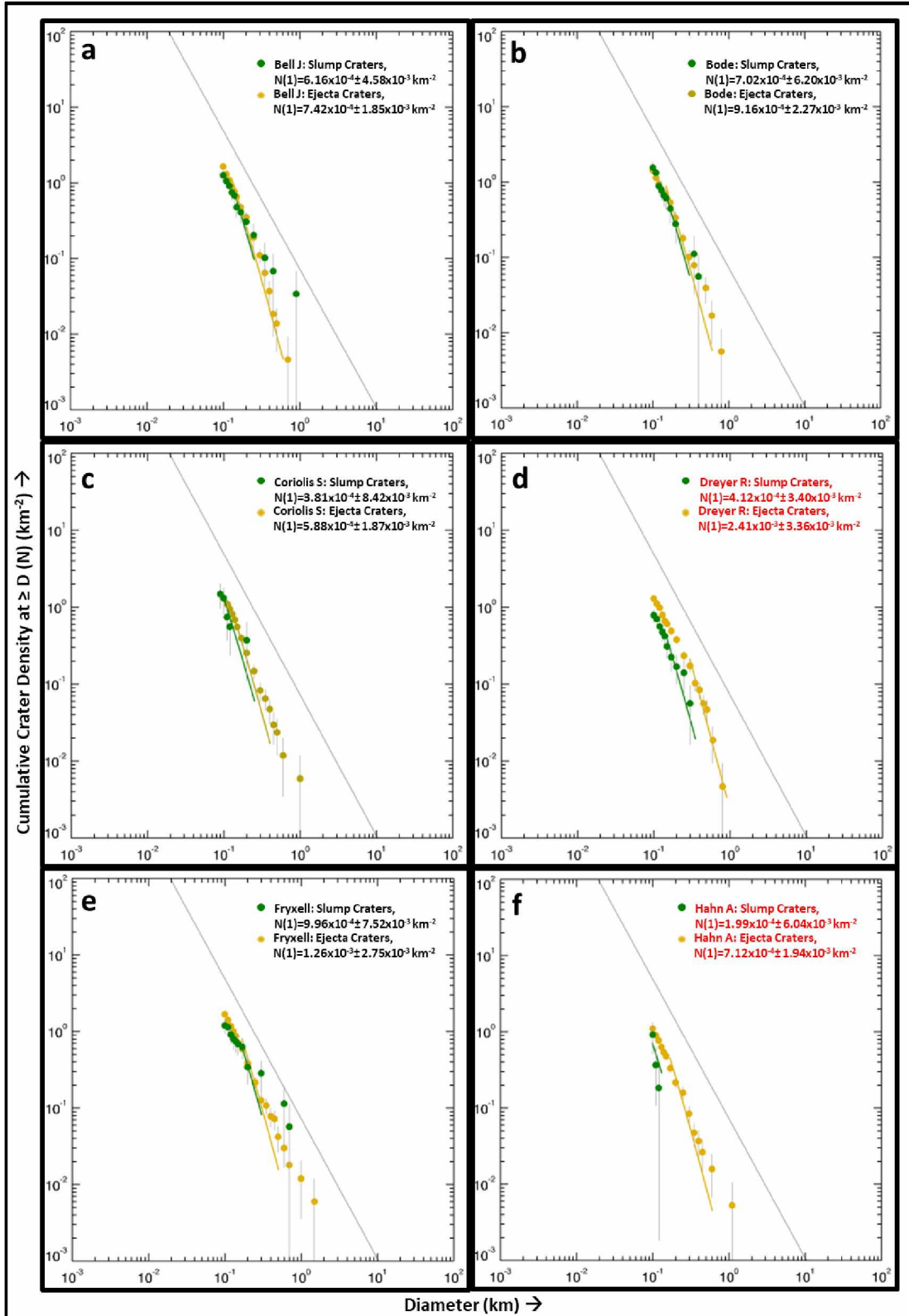
- Neukum, G., and Ivanov, B. (1994), Crater size distributions and impact probabilities on Earth from lunar, terrestrial-planet, and asteroid cratering data, In T Gehrels et al. (Eds.), *Hazards due to Comets and Asteroids*, pp. 359-416.
- Neukum, G., Ivanov, B. A., and Hartmann, W. K. (2001), Cratering records in the inner solar system in relation to the lunar reference system, In *Chronology and evolution of Mars*, pp. 55-86, Springer, doi:https://doi.org/10.1007/978-94-017-1035-0_3.
- Neukum, G., König, B., and Arkani-Hamed, J. (1975a). A study of lunar impact crater size-distributions. *The Moon*, 12(2), 201-229. doi:<https://doi.org/10.1007/BF00577878>.
- Neukum, G., König, B., Fechtig, H., and Storzer, D. (1975b). *Cratering in the Earth-Moon system- Consequences for age determination by crater counting*. Paper presented at 6th Lunar and Planetary Science Conference Proceedings, Houston, TX.
- Osinski, G. R., Silber, E. A., Clayton, J., Grieve, R. A., Hansen, K., Johnson, C. L. et al. (2018). Transitional impact craters on the Moon: Insight into the effect of target lithology on the impact cratering process. *Meteoritics & Planetary Science*. doi:<https://doi.org/10.1111/maps.13226>.
- Papike, J. J., Simon, S. B., and Laul, J. C. (1982). The lunar regolith: Chemistry, mineralogy, and petrology. *Reviews of Geophysics*, 20(4), 761-826. doi:<https://doi.org/10.1029/RG020i004p00761>.
- Pike, R. (1981). *Meteorite craters: Rim height, circularity, and gravity anomalies*. Paper presented at Lunar and Planetary Science Conference.
- Pike, R. J. (1974). Depth/diameter relations of fresh lunar craters: Revision from spacecraft data. *Geophysical Research Letters*, 1(7), 291-294. doi:<https://doi.org/10.1029/GL001i007p00291>.

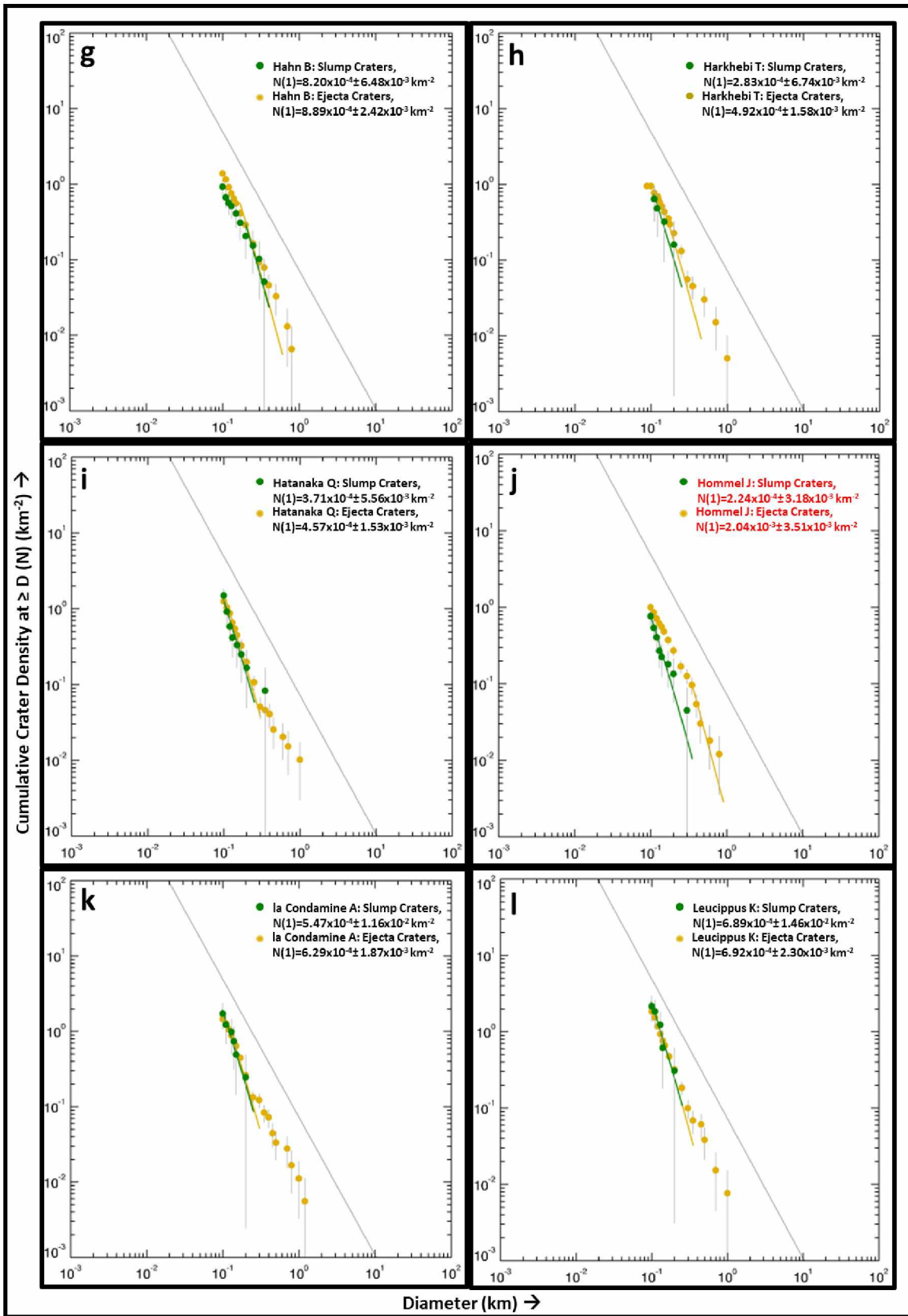
- Pike, R. J. (1977), Size-dependence in the shape of fresh impact craters on the Moon, In D.J. Roddy et al. (Eds.), *Impact and Explosion Cratering: Planetary and Terrestrial Implications*, pp. 489-509, Pergamon Press, New York.
- Pike, R. J. (1980a). *Control of crater morphology by gravity and target type-Mars, Earth, Moon*. Paper presented at 11th Lunar and Planetary Science Conference Proceedings, Houston, TX.
- Pike, R. J. (1980b), Geometric interpretation of lunar craters. *USGS Professional Paper*, Rep. 1046-C, C1-C77, Washington: US Govt. Print. Off.
- Pike, R. J. (1988), Geomorphology of impact craters on Mercury, In F Vilas et al. (Eds.), *Mercury*, pp. 165-273, University of Arizona Press, Tucson, AZ.
- Plescia, J. (2012). Impacts on sloping surfaces: Lunar examples. *Meteoritics and Planetary Science Supplement*, 75.
- Plescia, J. B. (2015), Transitional Crater (Simple/Complex), in *Encyclopedia of Planetary Landforms*, edited, pp. 1-5, Springer, New York, NY, doi:https://doi.org/10.1007/978-1-4614-9213-9_407-2.
- Plescia, J. B., Barnouin, O., Anderson, J. L. B., and Cintala, M. J. (2019). *Morphometry and Morphology of Lunar Craters on Slopes*. Paper presented at 50th Lunar and Planetary Science Conference, Houston, TX.
- Quaide, W. L., Gault, D. E., and Schmidt, R. A. (1965). Gravitational effects on lunar impact structures. *Annals of the New York Academy of Sciences*, 123(1), 563-572. doi:<https://doi.org/10.1111/j.1749-6632.1965.tb20388.x>.

- Quaide, W. L., and Oberbeck, V. R. (1968). Thickness determinations of the lunar surface layer from lunar impact craters. *Journal of Geophysical Research*, 73(16), 5247-5270. doi:<https://doi.org/10.1029/JB073i016p05247>
- Robbins, S. J., and Hynek, B. M. (2012). A new global database of Mars impact craters ≥ 1 km: 2. Global crater properties and regional variations of the simple-to-complex transition diameter. *Journal of Geophysical Research: Planets*, 117(E6). doi:<https://doi.org/10.1029/2011JE003967>.
- Robinson, M., Eliason, E., Hiesinger, H., Jolliff, B., McEwen, A., Malin, M. et al. (2010). *Lunar reconnaissance orbiter camera: first results*. Paper presented at European Planetary Science Congress 2010, Rome, Italy.
- Roddy, D. (1977). *Tabular comparisons of the Flynn Creek impact crater, United States, Steinheim impact crater, Germany and Snowball explosion crater, Canada*. Paper presented at Impact and Explosion Cratering: Planetary and Terrestrial Implications, Flagstaff, AZ.
- Schultz, P., and Gault, D. (1975). *Seismically induced modification of lunar surface features*. Paper presented at 6th Lunar and Planetary Science Conference Proceedings, Houston, TX.
- Senft, L. E., and Stewart, S. T. (2008). Impact crater formation in icy layered terrains on Mars. *Meteoritics & Planetary Science*, 43(12), 1993-2013. doi:<https://doi.org/10.1111/j.1945-5100.2008.tb00657.x>
- Smith, D. E., Zuber, M. T., Neumann, G. A., Mazarico, E., Head, J., and Torrence, M. H. (2011). *Results from the Lunar Orbiter Laser Altimeter (LOLA): global, high resolution topographic mapping of the Moon*. Paper presented at 42nd Lunar and Planetary Science Conference, Houston, TX.

- Smith, E. I., and Hartnell, J. A. (1978). Crater size-shape profiles for the Moon and Mercury: terrain effects and interplanetary comparisons. *The moon and the planets*, 19(4), 479-511. doi:<https://doi.org/10.1007/BF00901976>.
- Smith, E. I., and Sanchez, A. G. (1973). Fresh lunar craters: Morphology as a function of diameter, a possible criterion for crater origin. *Modern Geology*, 4, 51-59.
- Soderblom, J. M., Evans, A. J., Johnson, B. C., Melosh, H. J., Miljković, K., Phillips, R. J. et al. (2015). The fractured Moon: Production and saturation of porosity in the lunar highlands from impact cratering. *Geophysical Research Letters*, 42(17), 6939-6944. doi:<https://doi.org/10.1002/2015GL065022>
- Stewart, S. T., and Valiant, G. J. (2006). Martian subsurface properties and crater formation processes inferred from fresh impact crater geometries. *Meteoritics & Planetary Science*, 41(10), 1509-1537. doi:<https://doi.org/10.1111/j.1945-5100.2006.tb00433.x>

APPENDIX C





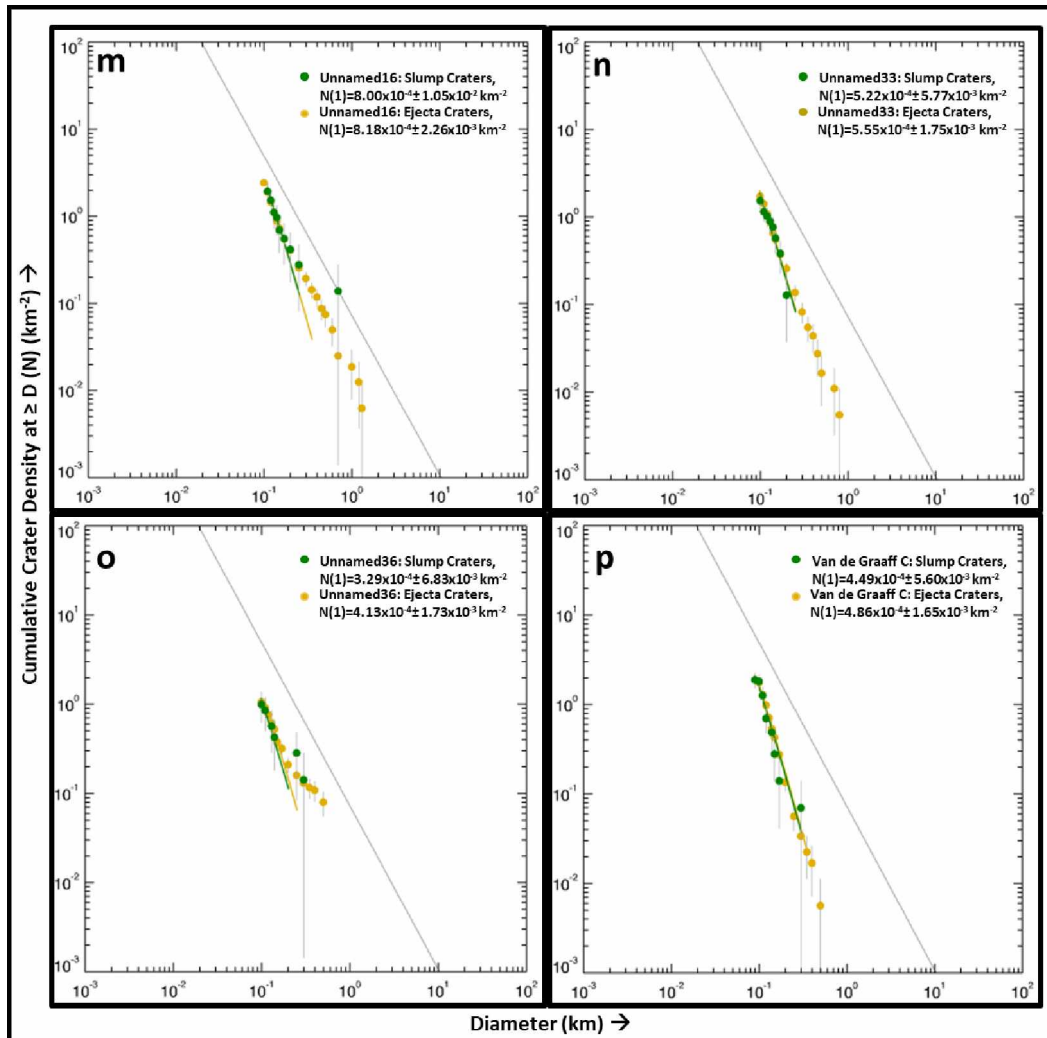


Figure C-1. Log-log CSFD plots corresponding to ejecta and slump units of remaining 16 craters with localized slumps. The geographic coordinates of the craters are listed in Table 4.1. The green and orange dots represent the crater bins of slumps and ejecta respectively. The green and orange lines are the best fit production functions for the CSFDs of slump and ejecta units respectively. The grey sloping line is the Hartmann (1984) crater saturation line. The $N(1)$ values are given in the legends on the top right area of each plot. According to the production function fits, the $N(1)$ values in red font represent the craters that appear to have formed as simple craters while the $N(1)$ values in black font correspond to the craters whose localized slumped material accumulated during crater formation.

Table C-1. Tabulated statistics of proximal well-preserved transitional craters relative to well-preserved simple craters for each of the 15-20 km-sized simple craters and craters with localized slumps. The pre-impact terrains of the proximal craters are characterized with similar topographic variations as the terrains of the 15-20 km diameter craters.

Crater Name	Morphology	Latitude (°N)	Longitude (°E)	Number of Pristine Proximal Simple craters (PSC)	Number of Pristine Proximal Transitional Craters (PTC)	Total Pristine Proximal Craters on Smooth Surface	% PTC relative to PSC
Alden B	Simple crater	-20.59	113.11	0	1	1	100
Alhazen A	Simple crater	16.16	74.3	0	1	1	100
Arrhenius J	Simple crater	-57.51	271.55	0	2	2	100
Bailly F	Simple crater	-67.46	290.41	0	0	0	-
Barocius M	Crater with localized slumps	-42.45	19.48	0	1	1	100
Bartels A	Simple crater	25.69	270.39	0	1	1	100
Beaumont B	Simple crater	-18.71	26.8	0	0	0	-
Bell J	Crater with localized slumps	19.88	265.88	2	4	6	33
Black	Simple crater	-9.19	80.39	0	1	1	100
Bode	Crater with localized slumps	6.7	357.54	0	0	0	-
Boussingault T	Simple crater	-63.01	43.06	1	1	2	0
Bouvard C	Simple crater	-37.05	282.52	0	0	0	-
Brunner N	Simple crater	-11.38	90.71	0	0	0	-
Bunsen C	Simple crater	44.2	270.18	0	1	1	100
Campbell E	Simple crater	46.33	158.88	1	0	1	-100
Cassegrain K	Simple crater	-54.45	113.88	0	0	0	-
Catalan U	Simple crater	-45	269.34	0	2	2	100
Clavius G	Simple crater	-52.02	345.99	0	0	0	-
Congreve G	Simple crater	-0.89	196.12	1	1	2	0
Cooper G	Simple crater	52.42	178.76	2	1	3	-33
Coriolis G	Simple crater	-0.03	174.54	0	0	0	-
Coriolis S	Crater with localized slumps	0.1	169.66	0	1	1	100
d'Alembert G	Simple crater	50.7	167.36	0	1	1	100
Dante S	Simple crater	25.09	177.66	1	2	3	33
Darney	Simple crater	-14.6	336.43	0	0	0	-
Donner N	Simple crater	-33.17	97.19	0	0	0	-
Doppler W	Simple crater	-10.99	197.86	0	0	0	-
Dreyer R	Crater with localized slumps	8.49	94.47	0	0	0	-
Dunthorne	Simple crater	-30.12	328.29	0	1	1	100

Table C-1 contd.

Crater Name	Morphology	Latitude (°N)	Longitude (°E)	Number of Pristine Proximal Simple craters (PSC)	Number of Pristine Proximal Transitional Craters (PTC)	Total Pristine Proximal Craters on Smooth Surface	% PTC relative to PSC
Emden F	Simple crater	62.98	188.89	0	0	0	-
Endymion E	Simple crater	53.59	66.24	0	1	1	100
Epimenides A	Simple crater	-43.26	329.82	0	1	1	100
Fryxell	Crater with localized slumps	-21.25	258.34	0	0	0	-
Gardner	Simple crater	17.74	33.81	0	1	1	100
Geissler	Crater with localized slumps	-2.59	76.5	0	0	0	-
Geminus D	Simple crater	30.57	47.29	3	0	3	-100
Glaisher	Simple crater	13.18	49.34	0	0	0	-
Glauber	Simple crater	11.31	142.66	0	0	0	-
Golitsyn J	Simple crater	-27.68	256.79	0	0	0	-
Guillaume J	Simple crater	43.56	189.48	1	2	3	33
Gullstrand C	Simple crater	46.57	232.9	0	1	1	100
Gutenberg A	Simple crater	-9.03	39.91	0	0	0	-
Hagen Q	Crater with localized slumps	-50.33	133.29	0	3	3	100
Hahn A	Crater with localized slumps	29.66	69.72	0	0	0	-
Hahn B	Crater with localized slumps	31.37	76.97	0	1	1	100
Harden	Simple crater	5.46	143.54	0	0	0	-
Harkhebi T	Crater with localized slumps	40.04	95.31	1	0	1	-100
Hatanaka Q	Crater with localized slumps	25.99	235.34	1	5	6	67
Heyrovsky	Simple crater	-39.55	264.57	0	1	1	100
Hill	Simple crater	20.91	40.81	0	1	1	100
Hipparchus C	Simple crater	-7.41	8.21	0	1	1	100
Hommel J	Crater with localized slumps	-53.53	27.87	0	1	1	100
Inghirami C	Simple crater	-44.07	285.41	0	1	1	100
Isidorus D	Simple crater	-4.27	34.07	0	0	0	-
Jacobi J	Simple crater	-57.96	10.27	0	0	0	-
Janssen K	Simple crater	-46.19	42.31	0	1	1	100
Joule K	Simple crater	25.64	218.15	0	1	1	100
Kekule M	Crater with localized slumps	12.05	221.97	0	2	2	100
Kirkwood T	Simple crater	68.98	194.73	0	0	0	-
Korolev V	Crater with localized slumps	-1.21	197.94	1	0	1	-100
Korolev Y	Crater with localized slumps	-0.5	201.53	2	1	3	-33
Kurchatov X	Simple crater	41.18	140.07	0	0	0	-

Table C-1 contd.

Crater Name	Morphology	Latitude (°N)	Longitude (°E)	Number of Pristine Proximal Simple craters (PSC)	Number of Pristine Proximal Transitional Craters (PTC)	Total Pristine Proximal Craters on Smooth Surface	% PTC relative to PSC
la Condamine A	Crater with localized slumps	54.43	329.8	0	0	0	-
Langrenus M	Simple crater	-9.81	66.41	0	0	0	-
Lehmann C	Simple crater	-35.57	309.83	0	0	0	-
Lents J	Simple crater	-3.63	262.62	0	1	1	100
Leucippus K	Crater with localized slumps	27.27	244.49	0	2	2	100
Leuschner Z	Crater with localized slumps	5.24	250.43	0	1	1	100
Liouville	Simple crater	2.72	73.56	0	0	0	-
Lippmann J	Simple crater	-58.74	253.68	0	1	1	100
Lowell W	Simple crater	-10.16	252.79	0	0	0	-
Mairan A	Crater with localized slumps	38.63	321.21	0	0	0	-
Manzinus E	Simple crater	-68.98	25.15	0	1	1	100
Maunder A	Simple crater	-3.28	269.38	0	0	0	-
Maury	Simple crater	37.11	39.69	0	1	1	100
Mutus L	Simple crater	-61.84	24.81	2	4	6	33
Mutus P	Simple crater	-59.16	25.55	1	2	3	33
Nikolaev J	Simple crater	31.59	155.42	0	4	4	100
Olbers B	Crater with localized slumps	6.84	285.79	0	1	1	100
Parenago Z	Crater with localized slumps	28.96	250.71	0	4	4	100
Pickering	Simple crater	-2.87	6.99	0	0	0	-
Planck W	Simple crater	-55.44	131.27	1	1	2	0
Poincare C	Crater with localized slumps	-54.59	168.7	0	3	3	100
Polybius A	Simple crater	-23.04	27.97	0	0	0	-
Pontecoulant A	Simple crater	-57.68	62.79	0	2	2	100
Rayleigh B	Crater with localized slumps	29.05	88.5	0	1	1	100
Riccioli H	Simple crater	1.11	284.96	0	2	2	100
Richards	Simple crater	7.7	140.09	0	1	1	100
Saenger C	Simple crater	6.25	104.35	0	1	1	100
Safarik H	Simple crater	9.53	178.54	0	4	4	100
Sanford C	Simple crater	33.8	222.61	0	3	3	100
Santbech B	Simple crater	-24.73	41.57	0	1	1	100
Schickard H	Simple crater	-43.52	297.66	0	1	1	100
Schliemann W	Simple crater	0.26	152.35	0	1	1	100
Schwarzschild Q	Crater with localized slumps	66.24	108.83	0	1	1	100

Table C-1 contd.

Crater Name	Morphology	Latitude (°N)	Longitude (°E)	Number of Pristine Proximal Simple craters (PSC)	Number of Pristine Proximal Transitional Craters (PTC)	Total Pristine Proximal Craters on Smooth Surface	% PTC relative to PSC
Schwarzschild T	Simple crater	69.82	107.63	0	1	1	100
Sharp A	Crater with localized slumps	47.63	317.32	0	1	1	100
Sisakyan C	Simple crater	41.98	111.03	1	0	1	-100
Spencer Jones H	Simple crater	11.93	168.12	0	1	1	100
Stetson N	Crater with localized slumps	-43.2	239.57	0	1	1	100
Sumner G	Simple crater	37.42	110.41	0	1	1	100
Sundman V	Simple crater	11.96	266.44	0	3	3	100
Swann C	Crater with localized slumps	52.9	114.28	0	1	1	100
Theon Junior	Crater with localized slumps	-2.41	15.79	0	0	0	-
Theon Senior	Crater with localized slumps	-0.81	15.42	0	0	0	-
Tralles A	Simple crater	27.42	47.03	1	1	2	0
Unnamed12	Simple crater	56.68	152.25	0	1	1	100
Unnamed13	Simple crater	-46.84	167.22	0	2	2	100
Unnamed14	Simple crater	64.4	172.54	1	2	3	33
Unnamed15	Simple crater	66.32	175.66	1	3	4	50
Unnamed16	Crater with localized slumps	34.92	176.71	2	1	3	-33
Unnamed17	Simple crater	53.45	181.38	1	1	2	0
Unnamed18	Simple crater	8.79	181.85	1	3	4	50
Unnamed20	Simple crater	44.43	188.7	1	0	1	-100
Unnamed21	Simple crater	36.54	189.65	0	4	4	100
Unnamed23	Simple crater	52.21	190.87	1	0	1	-100
Unnamed24	Simple crater	47.24	191.06	1	1	2	0
Unnamed26	Simple crater	-60.35	192.81	0	1	1	100
Unnamed27	Simple crater	14.04	193.63	0	1	1	100
Unnamed28	Simple crater	29.1	203.12	1	3	4	50
Unnamed29	Simple crater	-45.6	207.7	0	0	0	-
Unnamed30	Simple crater	32.18	208.56	0	3	3	100
Unnamed31	Simple crater	18.32	218.59	1	1	2	0
Unnamed32	Simple crater	-36.9	223.52	0	2	2	100
Unnamed33	Crater with localized slumps	15.15	224.18	0	3	3	100
Unnamed35	Simple crater	-1.9	224.98	0	0	0	-
Unnamed36	Crater with localized slumps	-44.87	225.13	0	2	2	100
Unnamed39	Simple crater	-1.36	235.66	0	1	1	100

Table C-1 contd.

Crater Name	Morphology	Latitude (°N)	Longitude (°E)	Number of Pristine Proximal Simple craters (PSC)	Number of Pristine Proximal Transitional Craters (PTC)	Total Pristine Proximal Craters on Smooth Surface	% PTC relative to PSC
Unnamed4	Simple crater	62.73	127.2	0	0	0	-
Unnamed40	Simple crater	-65.74	237.77	0	1	1	100
Unnamed43	Simple crater	-20.96	241.4	1	0	1	-100
Unnamed44	Simple crater	-57.76	247.29	0	1	1	100
Unnamed46	Simple crater	71.2	253.65	1	4	5	60
Unnamed47	Simple crater	41.01	254.34	1	2	3	33
Unnamed48	Simple crater	64.8	262.34	0	3	3	100
Unnamed5	Simple crater	-56.22	127.57	1	0	1	-100
Unnamed50	Simple crater	37.16	268.41	0	2	2	100
Unnamed6	Simple crater	62.15	132.1	1	0	1	-100
Unnamed7	Crater with localized slumps	44.88	134.77	1	0	1	-100
Unnamed8	Simple crater	23.62	137.65	0	3	3	100
Unnamed9	Simple crater	44.52	139.37	0	0	0	-
Van de Graaff C	Crater with localized slumps	-26.43	172.81	0	0	0	-
van den Bergh P	Simple crater	29.2	199.81	1	0	1	-100
Ventris B	Simple crater	-2.22	158.08	0	1	1	100
Vestine A	Simple crater	36.01	94.57	0	0	0	-
Vetchinkin P	Simple crater	7.06	130.56	0	1	1	100
Viviani N	Simple crater	3.49	116.5	0	0	0	-
Vlacq A	Simple crater	-51.28	39	0	2	2	100
von Bekesy F	Simple crater	52.8	137.04	0	1	1	100
W. Bond B	Simple crater	65.03	7.51	0	0	0	-
Wargentín D	Simple crater	-51.03	294.7	0	0	0	-
Wurzelbauer A	Simple crater	-35.74	344.58	0	1	1	100

Table C-2. List of slopes and respective sloping directions (relative to sloping directions of adjacent craters' walls) of topographic breaks adjoining the walls of the 15-20 km diameter simple craters and craters with localized slumps. The last column provides information on presence/absence of layering. The direction of terrain slope was estimated for pre-impact terrains devoid of topographic breaks. Majority of the craters were found to be superposing more than one topographic break. Therefore, individual geographic coordinates and slope values corresponding to each break have been listed. The geographic coordinates of the breaks refer to the latitude/longitude values of the portion of breaks adjoining the craters' walls.

Symbol Definitions:

[1] Terrain Slope Direction:

E-W: East-West (W-E: West-East)

N-S: North-South (S-N: South-North)

NE-SW: Northeast-Southwest (SE-NW: Southeast-Northwest)

[2] Topographic Break (SA/ST/N):

SA: Sloping away from adjoining crater's walls

ST: Sloping in the direction of adjoining crater wall slope

N: Absence of topographic break

[3] STD: Standard deviation associated with slope of topographic break

[4] Layering (Y/N):

Y: Layering is present, N: Layering is absent

Simple Craters

Crater Name	Latitude (°N)	Longitude (°E)	Terrain Slope Direction	Topographic break (SA/ST/N)	Break 1				Break 2				Break 3				Layering (Y/N)
					Latitude (°E)	Longitude (°E)	Slope (°)	STD (°)	Latitude (°E)	Longitude (°E)	Slope (°)	STD (°)	Latitude (°E)	Longitude (°E)	Slope (°)	STD (°)	
Alden B	-20.59	113.11	-	SA	-20.48	112.89	-	-	-20.59	113.36	-	-	-	-	-	-	N
Alhazen A	16.16	74.3	-	ST	15.89	74.3	10.43	2.66	16.35	74.48	12.04	1.58	-	-	-	-	N
Arrhenius J	-57.51	271.55	E-W	N	-	-	-	-	-	-	-	-	-	-	-	-	N
Bailly F	-67.46	290.41	Flat	N	-	-	-	-	-	-	-	-	-	-	-	-	Y
Bartels A	25.69	270.39	-	N	-	-	-	-	-	-	-	-	-	-	-	-	N
Beaumont B	-18.71	26.8	-	SA	-18.5	26.69	-	-	-18.79	26.81	-	-	-	-	-	-	N
Black	-9.19	80.39	N-S	N	-	-	-	-	-	-	-	-	-	-	-	-	N
Boussingault T	-63.01	43.06	-	SA	-63.75	43.24	-	-	-63.26	43.49	-	-	-	-	-	-	N
Bouvard C	-37.05	282.52	-	ST	-37.01	282.22	12.12	1.6	-36.92	282.76	10.56	1.35	-	-	-	-	N
Brunner N	-11.38	90.71	-	SA	-11.67	90.82	-	-	-	-	-	-	-	-	-	-	N
Bunsen C	44.2	270.18	-	ST	44.48	269.99	10.82	1.52	44.2	270.56	8.1	0.37	-	-	-	-	Y
Campbell E	46.33	158.88	-	SA	46.47	159.19	-	-	46.32	158.51	-	-	-	-	-	-	N
Cassegrain K	-54.45	113.88	-	ST	-54.72	113.6	6.39	2.23	-	-	-	-	-	-	-	-	Y
Catalan U	-45	269.34	Flat	N	-	-	-	-	-	-	-	-	-	-	-	-	Y
Clavius G	-52.02	345.99	-	ST	-52.26	345.68	9.52	1.05	-	-	-	-	-	-	-	-	N
Congreve G	-0.89	196.12	-	ST	-0.61	196.13	12.79	1.45	-	-	-	-	-	-	-	-	N
Cooper G	52.42	178.76	-	SA	52.11	178.6	-	-	-	-	-	-	-	-	-	-	N
Coriolis G	-0.03	174.54	-	SA	0.08	174.3	-	-	0.05	174.82	-	-	-0.32	174.57	-	-	N
d'Alembert G	50.7	167.36	Flat	N	-	-	-	-	-	-	-	-	-	-	-	-	Y
Dante S	25.09	177.66	-	SA	25.22	177.37	-	-	25.06	177.98	-	-	24.86	177.89	-	-	N
Damey	-14.6	336.43	W-E	N	-	-	-	-	-	-	-	-	-	-	-	-	Y
Donner N	-33.17	97.19	-	SA	-33.37	96.89	-	-	-33.15	97.59	-	-	-	-	-	-	N
Doppler W	-10.99	197.86	-	ST	-11.26	197.89	9.19	0.73	-	-	-	-	-	-	-	-	Y
Dunthorne	-30.12	328.29	-	ST	-30.33	328.08	18.99	4.28	-	-	-	-	-	-	-	-	Y
Emden F	62.98	188.89	-	ST	63.36	189	10.87	3.57	62.92	188.23	13.03	0.97	62.67	188.99	12.42	1.16	Y

Simple Craters

Crater Name	Latitude (°N)	Longitude (°E)	Terrain Slope Direction	Topographic break (SA/ST/N)	Break 1				Break 2				Break 3				Layering (Y/N)	
					Latitude (°E)	Longitude (°E)	Slope (°)	STD (°)	Latitude (°E)	Longitude (°E)	Slope (°)	STD (°)	Latitude (°E)	Longitude (°E)	Slope (°)	STD (°)		
Endymion E	53.59	66.24	-	SA	53.72	66.65	-	-	-	-	-	-	-	-	-	-	-	N
Epimenides A	-43.26	329.82	Flat	N	-	-	-	-	-	-	-	-	-	-	-	-	-	N
Gardner	17.74	33.81	SW-NE	N	-	-	-	-	-	-	-	-	-	-	-	-	-	Y
Geminus D	30.57	47.29	-	SA	30.63	47	-	-	30.37	47.45	-	-	-	-	-	-	-	N
Glaisher	13.18	49.34	-	ST	12.93	49.27	9.32	1.18	-	-	-	-	-	-	-	-	-	N
Glauber	11.31	142.66	Flat	N	-	-	-	-	-	-	-	-	-	-	-	-	-	Y
Golitsyn J	-27.68	256.79	-	ST	-27.48	256.52	23.1	3.3	-	-	-	-	-	-	-	-	-	Y
Guillaume J	43.56	189.48	-	ST	43.52	189.1	-	-	43.29	189.41	-	-	-	-	-	-	-	Y
Gullstrand C	46.57	232.9	SW-NE	N	-	-	-	-	-	-	-	-	-	-	-	-	-	N
Gutenberg A	-9.03	39.91	-	ST	-9	40.16	13.17	1.96	-	-	-	-	-	-	-	-	-	N
Harden	5.46	143.54	Flat	N	-	-	-	-	-	-	-	-	-	-	-	-	-	N
Heyrovsky	-39.55	264.57	-	ST	-39.31	264.68	11.52	0.91	-	-	-	-	-	-	-	-	-	Y
Hill	20.91	40.81	Flat	N	-	-	-	-	-	-	-	-	-	-	-	-	-	N
Hipparchus C	-7.41	8.21	-	ST	-7.65	8.3	10.14	1.44	-	-	-	-	-	-	-	-	-	N
Inghirami C	-44.07	285.41	-	ST	-44.17	285.76	12.42	1.33	-	-	-	-	-	-	-	-	-	Y
Isidorus D	-4.27	34.07	Flat	N	-	-	-	-	-	-	-	-	-	-	-	-	-	N
Jacobi J	-57.96	10.27	-	SA	-57.74	10.5	11.97	2.14	-58.2	10.69	-	-	-58.22	9.99	-	-	-	Y
Janssen K	-46.19	42.31	Flat	N	-	-	-	-	-	-	-	-	-	-	-	-	-	N
Joule K	25.64	218.15	-	ST	25.45	218.02	8.7	0.82	-	-	-	-	-	-	-	-	-	N
Kirkwood T	68.98	194.73	-	ST, SA	69.28 (ST)	194.77 (ST)	8.99	0.92	69.1 (SA)	193.93 (SA)	-	-	68.71 (SA)	195.15 (SA)	-	-	-	Y
Kurchatov X	41.18	140.07	S-N	N	-	-	-	-	-	-	-	-	-	-	-	-	-	Y
Langrenus M	-9.81	66.41	-	ST	-9.68	66.13	10.87	1.46	-	-	-	-	-	-	-	-	-	Y
Lehmann C	-35.57	309.83	SE-NW	N	-	-	-	-	-	-	-	-	-	-	-	-	-	Y
Lents J	-3.63	262.62	-	SA	-3.69	262.38	-	-	-	-	-	-	-	-	-	-	-	Y
Liouville	2.72	73.56	-	ST	2.76	73.31	10.95	1.47	-	-	-	-	-	-	-	-	-	N

Simple Craters

Crater Name	Latitude (°N)	Longitude (°E)	Terrain Slope Direction	Topographic break (SA/ST/N)	Break 1				Break 2				Break 3				Layering (Y/N)
					Latitude (°E)	Longitude (°E)	Slope (°)	STD (°)	Latitude (°E)	Longitude (°E)	Slope (°)	STD (°)	Latitude (°E)	Longitude (°E)	Slope (°)	STD (°)	
Lippmann J	-58.74	253.68	-	ST	-58.54	254.06	9.91	1.33	-	-	-	-	-	-	-	-	N
Lowell W	-10.16	252.79	-	ST	-10.41	252.96	21.1	3.63	-	-	-	-	-	-	-	-	Y
Manzinus E	-68.98	25.15	-	SA	-68.7	25.44	-	-	-69.21	24.67	-	-	-	-	-	-	Y
Maunder A	-3.28	269.38	W-E	N	-	-	-	-	-	-	-	-	-	-	-	-	N
Maury	37.11	39.69	-	SA	36.83	39.7	-	-	-	-	-	-	-	-	-	-	N
Mutus L	-61.84	24.81	-	SA	-61.64	24.39	-	-	-	-	-	-	-	-	-	-	N
Mutus P	-59.16	25.55	W-E	N	-	-	-	-	-	-	-	-	-	-	-	-	Y
Nikolaev J	31.59	155.42	-	SA	31.34	155.63	-	-	-	-	-	-	-	-	-	-	N
Pickering	-2.87	6.99	-	ST	-3.09	6.87	11.05	1.05	-	-	-	-	-	-	-	-	N
Planck W	-55.44	131.27	Flat	N	-	-	-	-	-	-	-	-	-	-	-	-	N
Polybius A	-23.04	27.97	-	ST	-55.19	131.42	7.56	0.35	-	-	-	-	-	-	-	-	Y
Pontecoulant A	-57.68	62.79	SE-NW	N	-	-	-	-	-	-	-	-	-	-	-	-	N
Riccioli H	1.11	284.96	-	ST	0.88	285.12	8.4	0.93	-	-	-	1.74	-	-	-	-	N
Richards	7.7	140.09	Flat	N	-	-	-	-	-	-	-	-	-	-	-	-	N
Saenger C	6.25	104.35	-	ST	6.32	104.08	8.45	0.91	6.24	104.65	13.49	-	-	-	-	-	N
Safarik H	9.53	178.54	-	SA	9.72	178.71	-	-	9.29	178.44	-	2.25	-	-	-	-	N
Sanford C	33.8	222.61	-	SA	33.93	222.25	-	-	-	-	-	-	-	-	-	-	Y
Santbech B	-24.73	41.57	-	ST	-24.47	41.59	9.4	1.15	-24.78	41.31	10.75	-	-	-	-	-	N
Schickard H	-43.52	297.66	Flat	N	-	-	-	-	-	-	-	-	-	-	-	-	N
Schliemann W	0.26	152.35	-	SA	0.52	152.25	-	-	-0.02	152.32	-	-	-	-	-	-	Y
Schwarzschild T	69.82	107.63	-	SA	70.06	108.1	-	-	69.71	106.96	-	-	-	-	-	-	Y
Sisakyan C	41.98	111.03	-	SA	42.05	111.43	-	-	-	-	-	-	-	-	-	-	Y
Spencer Jones H	11.93	168.12	-	SA	12.14	168.03	-	-	11.93	168.36	-	-	11.68	168.15	-	-	Y
Sumner G	37.42	110.41	-	SA	37.31	110.75	-	-	-	-	-	-	-	-	-	-	Y
Sundman V	11.96	266.44	-	ST	12.26	266.39	10.01	1.17	-	-	-	-	-	-	-	-	N

Simple Craters

Crater Name	Latitude (°N)	Longitude (°E)	Terrain Slope Direction	Topographic break (SA/ST/N)	Break 1				Break 2				Break 3				Layering (Y/N)	
					Latitude (°E)	Longitude (°E)	Slope (°)	STD (°)	Latitude (°E)	Longitude (°E)	Slope (°)	STD (°)	Latitude (°E)	Longitude (°E)	Slope (°)	STD (°)		
Tralles A	27.42	47.03	Flat	N	-	-	-	-	-	-	-	-	-	-	-	-	-	N
Unnamed12	56.68	152.25	-	ST, SA	56.48 (ST)	151.93 (ST)	14.54	1.63	56.71 (SA)	151.7 (SA)	-	-	-	-	-	-	-	N
Unnamed13	-46.84	167.22	-	SA	-46.59	167.4	-	-	-46.74	166.77	-	-	-47.1	167.12	-	-	-	Y
Unnamed14	64.4	172.54	-	SA	64.62	172.21	-	-	64.49	173.11	-	-	64.25	173.06	-	-	-	N
Unnamed15	66.32	175.66	-	SA	66.41	176.33	-	-	66.19	176.31	-	0.88	66.02	175.42	-	-	-	N
Unnamed17	53.45	181.38	NE-SW	N	-	-	-	-	-	-	-	1.17	-	-	-	-	-	Y
Unnamed18	8.79	181.85	-	ST	8.77	181.55	9.67	0.67	8.86	182.08	9.75	-	-	-	-	-	-	N
Unnamed20	44.43	188.7	-	SA	44.17	188.63	8.86	1.2	44.68	189	8.66	-	-	-	-	-	-	N
Unnamed21	36.54	189.65	-	ST, SA	36.31 (ST)	189.5 (ST)	-	-	36.47(SA)	189.3 (SA)	-	-	36.78 (SA)	189.48 (ST)	-	-	-	Y
Unnamed23	52.21	190.87	SE-NW	N	-	-	-	-	-	-	-	-	-	-	-	-	-	N
Unnamed24	47.24	191.06	Flat	N	-	-	-	-	-	-	-	-	-	-	-	-	-	N
Unnamed26	-60.35	192.81	-	SA	-60.45	193.32	-	-	-	-	-	-	-	-	-	-	-	N
Unnamed27	14.04	193.63	SE-NW	N	-	-	-	-	-	-	-	1.04	-	-	-	-	-	Y
Unnamed28	29.1	203.12	W-E	N	-	-	-	-	-	-	-	-	-	-	-	-	-	N
Unnamed29	-45.6	207.7	-	ST, SA	-45.45 (ST)	207.94 (ST)	8.82	2.29	-45.83 (SA)	207.91 (SA)	7.48	-	-	-	-	-	-	N
Unnamed30	32.18	208.56	NW-SE	N	-	-	-	-	-	-	-	-	-	-	-	-	-	N
Unnamed31	18.32	218.59	Flat	N	-	-	-	-	-	-	-	-	-	-	-	-	-	Y
Unnamed32	-36.9	223.52	-	ST	-36.64	223.58	13.89	1.89	-	-	-	-	-	-	-	-	-	N
Unnamed35	-1.9	224.98	Flat	N	-	-	-	-	-	-	-	-	-	-	-	-	-	N
Unnamed39	-1.36	235.66	-	ST	-1.59	235.81	9	0.47	-	-	-	-	-	-	-	-	-	Y
Unnamed4	62.73	127.2	W-E	N	-	-	-	-	-	-	-	1.67	-	-	3.37	0.92	-	N
Unnamed40	-65.74	237.77	-	SA	-66.03	237.58	-	-	-65.5	237.44	-	2.29	-	-	-	-	-	N
Unnamed43	-20.96	241.4	-	ST	-20.83	241.14	14.19	1.9	-21.24	241.36	8.57	-	-20.73	241.48	-	-	-	N
Unnamed44	-57.76	247.29	-	ST	-57.54	247.64	15.61	1.88	-58.02	247.06	15.56	2.09	-	-	-	-	-	N
Unnamed46	71.2	253.65	-	ST, SA	71.43 (ST)	253.05 (ST)	12.71	3.12	71.05 (SA)	254.35 (SA)	-	-	-	-	-	-	-	N

Simple Craters

Crater Name	Latitude (°N)	Longitude (°E)	Terrain Slope Direction	Topographic break (SA/ST/N)	Break 1				Break 2				Break 3				Layering (Y/N)	
					Latitude (°E)	Longitude (°E)	Slope (°)	STD (°)	Latitude (°E)	Longitude (°E)	Slope (°)	STD (°)	Latitude (°E)	Longitude (°E)	Slope (°)	STD (°)		
Unnamed47	41.01	254.34	-	ST	40.75	254.45	8.94	0.89	41.22	254.51	12.11	-	-	-	-	-	-	N
Unnamed48	64.8	262.34	-	ST, SA	64.64 (ST)	262.78 (ST)	8.47	0.57	65.05 (SA)	262.24	-	-	-	-	-	-	-	N
Unnamed5	-56.22	127.57	-	ST	-56.29	127.11	11.23	0.8	-	-	-	-	-	-	-	-	-	N
Unnamed50	37.16	268.41	-	SA	37.1	268.73	-	-	36.86	268.34	-	-	-	-	-	-	-	N
Unnamed6	62.15	132.1	-	ST, SA	61.9 (ST)	131.98 (ST)	14.29	1.74	62.2	131.56	-	-	-	-	-	-	-	N
Unnamed8	23.62	137.65	-	SA	23.4	137.44	-	-	-	-	-	-	-	-	-	-	-	N
Unnamed9	44.52	139.37	-	SA	44.28	139.27	-	-	-	-	-	-	-	-	-	-	-	N
van den Bergh P	29.2	199.81	-	SA	29.43	199.87	-	-	-	-	-	-	-	-	-	-	-	N
Ventris B	-2.22	158.08	-	SA	-2.15	158.34	-	-	-2.45	158.25	-	-	-	-	-	-	-	N
Vestine A	36.01	94.57	-	SA	36.04	94.92	-	-	-	-	-	-	-	-	-	-	-	N
Vetchinkin P	7.06	130.56	-	ST	7.25	130.41	8.51	1.74	-	-	-	-	-	-	-	-	-	N
Viviani N	3.49	116.5	-	SA	3.3	116.34	-	-	-	-	-	-	-	-	-	-	-	N
Vlacq A	-51.28	39	-	SA	-51.25	39.44	-	-	-	-	-	-	-	-	-	-	-	Y
von Bekesy F	52.8	137.04	-	SA	53.1	137.16	-	-	52.81	136.52	-	-	52.55	136.78	-	-	-	Y
W. Bond B	65.03	7.51	Flat	N	-	-	-	-	-	-	-	-	-	-	-	-	-	N
Wargentín D	-51.03	294.7	Flat	N	-	-	-	-	-	-	-	-	-	-	-	-	-	N
Wurzelbauer A	-35.74	344.58	-	SA	-36.04	344.55	-	-	-	-	-	-	-	-	-	-	-	N

Craters with localized slumps

Crater Name	Latitude (°N)	Longitude (°E)	Terrain Slope Direction	Topographic break (SA/ST/N)	Break 1				Break 2				Break 3				Layering (Y/N)
					Latitude (°E)	Longitude (°E)	Slope (°)	STD (°)	Latitude (°E)	Longitude (°E)	Slope (°)	STD (°)	Latitude (°E)	Longitude (°E)	Slope (°)	STD (°)	
Barocius M	-42.45	19.48	-	ST	19.14	-42.58	-	-	-	-	8.5	1.32	-	-	-	-	N
Bell J	19.88	265.88	-	ST	265.81	19.6	-	-	8.86	1.84	-	-	-	-	-	-	N
Bode	6.7	357.54	SE-NW	N	357.82	6.9	-	-	9.13	0.55	-	-	-	-	-	-	Y
Coriolis S	0.1	169.66	-	SA	169.5	-0.15	-	-	-	-	-	-	-	-	-	-	N
Dreyer R	8.49	94.47	Flat	N	-	-	-	-	-	-	-	-	-	-	-	-	N
Fryxell	-21.25	258.34	-	SA	258.46	-21	-	-	-	-	-	-	-	-	-	-	Y
Geissler	-2.59	76.5	-	ST, SA	76.3 (ST)	-2.36 (ST)	76.66 (SA)	-2.83 (SA)	8.65	0.55	-	-	-	-	-	-	Y
Hagen Q	-50.33	133.29	-	ST	133.46	-50.59	-	-	12.05	1.82	-	-	-	-	-	-	N
Hahn A	29.66	69.72	W-E	N	-	-	-	-	-	-	-	-	-	-	-	-	Y
Hahn B	31.37	76.97	N-S	N	-	-	-	-	-	-	-	-	-	-	-	-	N
Harkhebi T	40.04	95.31	Flat	N	-	-	-	-	-	-	-	-	-	-	-	-	N
Hatanaka Q	25.99	235.34	-	ST, SA	235.02	26.01	235.64	25.94	10.33	1.21	-	-	-	-	-	-	N
Hommel J	-53.53	27.87	Flat	N	-	-	-	-	-	-	-	-	-	-	-	-	N
Kekule M	12.05	221.97	-	ST	221.67	12.23	-	-	9.93	1.72	-	-	-	-	-	-	N
Korolev V	-1.21	197.94	-	ST	201.41	-0.78	-	-	12.13	1.84	-	-	-	-	-	-	Y
Korolev Y	-0.5	201.53	-	ST	201.41	-0.79	-	-	8.47	3.21	-	-	-	-	-	-	N
la Condamine A	54.43	329.8	-	ST	329.56	54.7	-	-	10.92	1.87	-	-	-	-	-	-	Y
Leucippus K	27.27	244.49	NW-SE	N	-	-	-	-	-	-	-	-	-	-	-	-	Y
Leuschner Z	5.24	250.43	NE-SW	N	-	-	-	-	-	-	-	-	-	-	-	-	Y
Mairan A	38.63	321.21	-	ST	321.21	38.34	-	-	7.01	0.33	-	-	-	-	-	-	Y
Olbers B	6.84	285.79	-	SA	286.32	6.69	-	-	-	-	-	-	-	-	-	-	N
Parenago Z	28.96	250.71	-	ST	250.91	29.2	-	-	8.46	0.4	-	-	-	-	-	-	N
Poincare C	-54.59	168.7	-	ST	169.24	-54.56	-	-	7.2	1.45	-	-	-	-	-	-	Y
Rayleigh B	29.05	88.5	W-E	N	-	-	-	-	-	-	-	-	-	-	-	-	Y
Schwarzschild Q	66.24	108.83	-	ST	108.12	66.14	108.77	65.97	17.09	2.41	9.16	0.61	-	-	-	-	N

Craters with localized slumps

Crater Name	Latitude (°N)	Longitude (°E)	Terrain Slope Direction	Topographic break (SA/ST/N)	Break 1				Break 2				Break 3				Layering (Y/N)	
					Latitude (°E)	Longitude (°E)	Slope (°)	STD (°)	Latitude (°E)	Longitude (°E)	Slope (°)	STD (°)	Latitude (°E)	Longitude (°E)	Slope (°)	STD (°)		
Sharp A	47.63	317.32	-	ST	317.71	47.52	-	-	12.95	0.66	-	-	-	-	-	-	-	N
Stetson N	-43.2	239.57	-	ST	239.32	-43.47	-	-	10.53	1.28	-	-	-	-	-	-	-	Y
Swann C	52.9	114.28	-	SA	113.94	52.67	-	-	-	-	-	-	-	-	-	-	-	N
Theon Junior	-2.41	15.79	-	ST	15.53	-2.56	15.9	-2.14	10.44	1.5	7.1	1.1	-	-	-	-	-	N
Theon Senior	-0.81	15.42	W-E	N	-	-	-	-	-	-	-	-	-	-	-	-	-	N
Unnamed16	34.92	176.71	-	ST	176.36	35.01	-	-	14.48	2.09	-	-	-	-	-	-	-	N
Unnamed33	15.15	224.18	-	ST	223.88	15.03	-	-	9.09	1.92	-	-	-	-	-	-	-	N
Unnamed36	-44.87	225.13	-	ST	224.75	-44.96	-	-	Not visible	-	-	-	-	-	-	-	-	N
Unnamed7	44.88	134.77	-	ST	135.02	44.57	134.74	45.19	12.42	1.59	11.01	0.45	-	-	-	-	-	N
Van de Graaff C	-26.43	172.81	-	ST	173.04	-26.16	-	-	8.39	1.31	-	-	-	-	-	-	-	Y

CHAPTER 5 CONCLUSION

From the geologic investigation of 244 15-20 km diameter lunar impact craters that fall within the simple-to-complex transition, we conclude that target properties are the primary factors behind the observed morphological variations within the diameter range. However, there were cases in which morphological differences existed for craters in very similar targets, so we cannot rule out impactor properties as a cause for some of our observations though target properties are the premier variables governing morphological variations in the craters.

5.1 Target Properties

[1] Simple craters are confined to the highlands and complex craters dominate the mare. This is because the mare are composed of solidified basaltic lava flows that are possibly interlayered with regolith produced in the interim between flows. The layering could have resulted in vertical strength heterogeneity that drove the destabilization of the transient cavity and its collapse, resulting in complex craters at smaller diameters in the mare. The highlands crust is non-layered and therefore provides more stability to the transient cavity thereby favoring simple crater morphologies.

[2] The results from the study of co-existence of simple craters and craters with localized slumps in the highlands suggest regional topographic variations within the crust. The simple craters formed from impacts on flat or gradually sloping surfaces or degraded rims and terraces of pre-existing craters. The majority of the degraded structures created subtle topographic discontinuities that were found to slope in the opposite direction from the slope of the later craters' walls. Consequently, mass wasting was initiated outside the cavity after the deposition of ejecta along

the slope of the discontinuity. This led to the elongation of the rim in the downhill direction along with lack of localized slumped material inside the crater and hence a simple crater morphology. Most craters with localized slumps were observed to superpose sharp topographic breaks such as well-developed rims and terraces of pre-existing craters. The majority of the remaining 35% of these craters were formed on terrains with similar topographic variation as the simple craters (gradually sloping surfaces or subtle topographic breaks). The gradual slopes, the sharp and subtle breaks served as potential slopes whose aspect matched that of the adjacent craters' walls. The transient cavity walls around this uphill rim sector potentially got over steepened and experienced collapse leading to the accumulation of localized slumped material, broadening of the floor and asymmetry in the shape of the rim.

[3] We found eight deep simple craters (whose minimum d/D exceeds the sum of 0.200 and uncertainty in d/D) around the mare-highlands boundaries. These locations are characterized with the highest porosities on the lunar surface. We conclude that high porosity played a significant role in producing the deep craters. The observations that support our conclusion are: higher frequencies of deep simple craters surrounding the deep 15-20 km diameter craters as compared to the frequencies of deep simple craters in proximity to the normally deep 15-20 km craters, the rise in abundance of deeper craters with increase in porosity, the positive correlation of wall slope with d/D and porosity, the similarity in rim heights of the deep and normally deep craters and the negative correlation of crater floor diameter with d/D but independence of floor diameter with respect to wall slope. Most of the kinetic energy from impact on a porous highlands surface was consumed in compaction of the target material. The remaining energy was utilized in excavation of the material. But the compaction left behind a permanent volume that caused the formation of

a deep, elongated simple crater. Increased compaction with rise in porosity yielded in craters with greater depths.

5.2 Impactor Properties

Based on the results of investigation in all three studies, there are three cases for which we propose the contribution of impactor properties to the morphological diversity observed in lunar craters within the 15-20 km diameter range:

[1] We encountered an elliptical crater in the highlands, that potentially formed from an oblique impact (impact angle of 12° or less) as reported by previous numerical modeling and experimental studies on oblique impacts.

[2] Based on previous studies on impact melt generation, the detection of visible impact melts on the floors of selected 27% of simple craters and around the cavities of most simple craters reflects that the impact velocities (and hence impact energies) were sufficiently large to melt the impacted regions of the highlands crust.

[3] Only eight out of 61 simple craters in the high porosity terrains were found to be deep. Therefore, it is possible that impacts on locally higher porosity surfaces within these terrains produced the deep craters. Another possibility is that a larger penetration depth during contact and compression due to an unusual impactor property such as high-velocity impact, a high-density impactor and/or a near-vertical impact could have enhanced the depth generated from compaction of the porous target and therefore generated craters with larger—than-normal depths.